

Dissipation and ringing of CRT deflection coils

Harberts, D.W.

Published: 01/01/2001

Document Version

Publisher's PDF, also known as Version of Record (includes final page, issue and volume numbers)

Please check the document version of this publication:

- A submitted manuscript is the author's version of the article upon submission and before peer-review. There can be important differences between the submitted version and the official published version of record. People interested in the research are advised to contact the author for the final version of the publication, or visit the DOI to the publisher's website.
- The final author version and the galley proof are versions of the publication after peer review.
- The final published version features the final layout of the paper including the volume, issue and page numbers.

[Link to publication](#)

General rights

Copyright and moral rights for the publications made accessible in the public portal are retained by the authors and/or other copyright owners and it is a condition of accessing publications that users recognise and abide by the legal requirements associated with these rights.

- Users may download and print one copy of any publication from the public portal for the purpose of private study or research.
- You may not further distribute the material or use it for any profit-making activity or commercial gain
- You may freely distribute the URL identifying the publication in the public portal ?

Take down policy

If you believe that this document breaches copyright please contact us providing details, and we will remove access to the work immediately and investigate your claim.

Dissipation and Ringing of CRT Deflection Coils

CIP-DATA LIBRARY TECHNISCHE UNIVERSITEIT EINDHOVEN

Harberts, Dirk W.

Dissipation and ringing of CRT deflection coils / by Dirk W. Harberts. -
Eindhoven : Technische Universiteit Eindhoven, 2001.

Proefschrift. - ISBN 90-386-1810-7

NUGI 832

Trefw.: beeldbuizen / transformatoren / elektrische machines ;
verliezen / trillingen / passieve elektrische netwerken.

Subject headings: cathode-ray tubes / transformers / power
consumption / circuit oscillations / lumped parameter networks.

©Philips Electronics N.V. 2001

The cover shows a pair of CRT deflection coils wound with Ringing-Free Wire
on a pile of conventional coils and copper wires (photographed by FotoMedia,
Eindhoven).

Printed by Ponsen & Looijen BV, Wageningen.

Dissipation and Ringing of CRT Deflection Coils

PROEFSCHRIFT

ter verkrijging van de graad van doctor aan de
Technische Universiteit Eindhoven, op gezag van de
Rector Magnificus, prof.dr. M. Rem, voor een
commissie aangewezen door het College voor
Promoties in het openbaar te verdedigen
op woensdag 7 maart 2001 om 16.00 uur

door

Dirk Willem Harberts

geboren te 's-Gravenhage

Dit proefschrift is goedgekeurd
door de promotoren:

prof.dr.ir. P.C.T. van der Laan
en
prof.dr.ir. A.J.A. Vandenput

Voor Renate, Tom & Jacqueline
Voor mijn ouders
Voor Grootje

The work described in this thesis has been carried out at Philips Display Components Eindhoven as part of the R&D program.

Summary

The Cathode-Ray Tube (CRT) is the predominant display device for televisions and computers. Essentially, it is a glass tube in which electrons are accelerated towards a screen which is covered with a phosphor layer that emits light when hit by electrons. Deflection coils generate a time-dependent magnetic field to deflect the electrons such that images are written on the screen. The research documented in this thesis examines the two most important high-frequency phenomena in these coils: dissipation and ringing.

Dissipation is the conversion of electrical energy into heat. Ringing is caused by high-frequency electromagnetic oscillations in the deflection coils and results in an annoying pattern of alternating lighter and darker vertical bars at the left-hand side of the screen. This thesis develops both the theory and the measuring methods that enable designers of CRT deflection coils to reduce dissipation and to suppress ringing.

Dissipation and ringing are strongly related. Physical phenomena that contribute to the dissipation also determine the damping of ringing. Circuit models that describe dissipation can be extended to describe ringing as well. Furthermore, the same (impedance) measurements can be used to analyze both dissipation and ringing.

For both dissipation and ringing, experimental results are presented in this thesis which cannot be explained with conventional theory. For instance, the reduction in dissipation by subdividing the wires into thinner ones was measured to be less than expected from existing theoretical models. To explain these results, we introduced the theory of the ‘interwire proximity effect’ in which eddy currents flow in loops formed by parallel wires with which a coil is wound. These eddy currents cause a non-uniform distribution of the currents over the parallel wires and thus a higher dissipation.

Although ringing is one of the most common complaints from circuit designers of computer monitors, not much has been published about ringing in deflection yokes in the open literature and no adequate measuring methods were available. In this thesis new theoretical models as well as new measuring

methods for ringing are presented.

Using these measuring methods, both existing and new techniques to suppress ringing are evaluated. The most promising new technique found in this study is to include weakly conductive material in the frame coils. As a practical realization, carbon-black particles are included in one of the outer layers of the frame-coil wires. This Ringing-Free Wire is successfully implemented in industry.

Samenvatting

De kathodestraalbuis (CRT) is de meest gebruikte technologie om beelden weer te geven voor televisies en computers. In essentie is het een glazen buis waarin elektronen versneld worden naar een scherm dat bedekt is met een laag fosfor die licht geeft wanneer die door elektronen wordt getroffen. Afbuigspoelen genereren een tijdsafhankelijk magnetisch veld om de elektronen zodanig af te buigen dat beelden op het scherm worden geschreven. Het in dit proefschrift beschreven onderzoek omvat de twee meest belangrijke hoogfrequente verschijnselen in deze spoelen: dissipatie en "ringing".

Dissipatie is de omzetting van elektrische energie in warmte. Ringing wordt veroorzaakt door hoogfrequente oscillaties in de afbuigspoelen en resulteert in hinderlijke verticale strepen aan de linkerzijde van het beeldscherm. In dit proefschrift worden theorie en meetmethoden beschreven die ontwerpers van afbuigspoelen in staat stellen de dissipatie te verminderen en ringing te onderdrukken.

Dissipatie en ringing zijn nauw verbonden. Fysische verschijnselen die bijdragen aan de dissipatie, bepalen ook de onderdrukking van ringing. Netwerkmodellen die dissipatie beschrijven, kunnen uitgebreid worden om ringing te beschrijven. Verder kunnen dezelfde (impedantie)metingen gebruikt worden om zowel dissipatie als ringing te analyseren.

Voor zowel dissipatie als ringing worden experimentele resultaten gepresenteerd in dit proefschrift die niet verklaard kunnen worden met de conventionele theorie. Zo blijkt bijvoorbeeld dat de vermindering in dissipatie kleiner is dan verwacht op grond van bestaande theoretische modellen wanneer de draden in dunnere draden worden onderverdeeld. Om deze meetresultaten te verklaren, hebben we de theorie van het "interwire proximity effect" geïntroduceerd. Hierin worden wervelstromen opgewekt in een lus gevormd door de parallelle draden waarmee een spoel is gewikkeld. Deze wervelstromen veroorzaken een ongelijkmatige verdeling van de stromen over de parallelle draden, hetgeen resulteert in een hogere dissipatie.

Alhoewel ringing één van de meest gehoorde klachten is van ontwerpers

van computer monitoren, is er niet veel over ringing in afbuigspoelen gepubliceerd en zijn er tot nu toe geen geschikte meetmethodes beschikbaar. In dit proefschrift worden nieuwe theoretische modellen en nieuwe meetmethodes voor ringing gepresenteerd.

Met deze meetmethodes zijn zowel bestaande als nieuwe technieken geëvalueerd om ringing te onderdrukken. De meest belovende nieuwe techniek die in dit onderzoek is gevonden, is het aanbrengen van zwak geleidend materiaal in de beeldspoelen. Als een praktische toepassing zijn roetdeeltjes ingesloten in één van de buitenste lagen van de beeldspoeldraden. Deze "Ringing-Free Wire" wordt nu met succes toegepast in de industrie.

Contents

Summary	vii
Samenvatting	ix
1 Introduction	1
1.1 Subject of this thesis	1
1.2 Cathode-Ray Tube	3
1.3 Deflection Yoke	3
1.4 Deflection coil	5
1.5 Historical overview	7
1.6 Organization of this thesis	8
2 Low-frequency behavior	9
2.1 Introduction	9
2.2 Quasi-static magnetic behavior	9
2.2.1 Deflection in a uniform magnetic field	10
2.2.2 Description of the magnetic field	11
2.3 Low-frequency electric behavior	13
2.3.1 Circuit model of the frame coils	13
2.3.2 Drive circuit for the frame coils	13
2.3.3 Circuit model of the line coils	13
2.3.4 Drive circuit of the line coils	16
2.4 Summary and conclusions	19
3 Dissipation	21
3.1 Introduction	21
3.2 Literature on dissipation	22
3.3 Deflection energy	23
3.4 Loss phenomena	26
3.4.1 Ohmic losses in a solid wire	26

3.4.2	Eddy-current losses in a solid wire	27
3.4.3	Losses in multi-parallel solid wires	36
3.4.4	Eddy-current losses in litz wires	38
3.4.5	Dielectric losses	40
3.4.6	Eddy-current losses in the ferrite core	42
3.4.7	Magnetic power loss in the ferrite core	43
3.5	Dissipation for non-sinusoidal signals	44
3.5.1	Dissipation due to the frame current	45
3.5.2	Dissipation due to the line current	45
3.6	Experimental results	48
3.6.1	15" CMT deflection yokes	49
3.6.2	17" CMT line-coil pairs	50
3.7	Reduction of dissipation	63
3.7.1	Fixed coil thickness	63
3.7.2	Variable coil thickness	64
3.8	Summary and conclusions	67
4	Description of ringing	69
4.1	Introduction	69
4.2	The ringing problem	70
4.3	Literature on ringing	71
4.4	Measuring ringing	72
4.4.1	The optical frequency response	73
4.4.2	Differential-mode and common-mode ringing	77
4.4.3	The magnetic frequency response	81
4.4.4	Impedance characteristics	86
4.5	Equivalent circuit models	90
4.5.1	Equivalent circuit models for differential-mode ringing	91
4.5.2	Equivalent circuit model for common-mode ringing	105
4.5.3	Quality factor for ringing	111
4.6	Summary and conclusions	114
5	Prediction of ringing	117
5.1	Introduction	117
5.2	The physics of circuit models	118
5.3	Physical models for solenoids	120
5.3.1	Inductance	120
5.3.2	Capacitance	121
5.3.3	Resistance	127
5.3.4	Discussion	128

5.4	Experimental results	129
5.4.1	Impedance characteristics of single line coils	131
5.4.2	Impedance characteristics of line-coil pairs	132
5.4.3	Impedance characteristics of deflection yokes	133
5.4.4	Discussion	134
5.4.5	Magnetic Frequency Responses of 17" CMT DYs	136
5.4.6	Magnetic Frequency Responses of 15" CMT DYs	138
5.5	Summary and conclusions	139
6	Suppression of ringing	141
6.1	Introduction	141
6.2	Literature on the suppression of ringing	142
6.3	Suppression of DM line-coil ringing	142
6.3.1	Change the line-drive electronics	143
6.3.2	Bi-directional winding of the line coils	144
6.3.3	Shunt to the line coils	148
6.3.4	Taps in the line coils	149
6.3.5	Distributed damping of the line coils	151
6.3.6	Evaluation	156
6.4	Suppression of DM frame-coil ringing	156
6.5	Suppression of common-mode ringing	157
6.5.1	Change the drive electronics	157
6.5.2	Common-mode suppression choke	157
6.5.3	Taps in the frame coils	158
6.5.4	Distributed damping of the frame coils	159
6.5.5	Ring-free wire	160
6.6	Summary and conclusions	165
7	Conclusions	167
	Appendices	171
A	The diffusion equation	171
B	Proximity loss	173
C	Bessel functions	177
	Bibliography	179
	List of symbols	196

Subject index	201
Dankwoord	206
Curriculum vitae	209

Chapter 1

Introduction

1.1 Subject of this thesis

The Cathode-Ray Tube (CRT) still dominates the market for displays in television receivers and computer monitors despite the huge effort to develop new display devices. Alternative devices, such as liquid-crystal displays and plasma displays, have been coming up for more than 25 years, but cannot beat the price/performance ratio of the CRT up to now.

The CRT market is still growing. The total world market for CRTs will increase from 264 million units in 1998 to 339 million units in 2004 [1]. Although CRTs have been in use for more than 100 years now, still fascinating phenomena in CRTs are being studied in order to improve their performance. Development and production of high-quality CRTs are expected to continue at least for the coming decade.

The research documented in this thesis examines the two most important phenomena in CRT deflection coils related to high-frequency effects: dissipation and ringing. Dissipation is the conversion of electrical energy into heat. Ringing is caused by high-frequency electromagnetic oscillations in the deflection coils and results in an annoying pattern of alternating lighter and darker vertical bars at the left-hand side of the screen. This thesis shows how these two effects can be measured and predicted. It describes how these effects are caused by physical phenomena, how to model them, how to measure them and how to reduce them. This enables designers of deflection yokes to optimize their designs such that the high-frequency behavior is acceptable.

Dissipation and ringing are strongly related. Physical phenomena that contribute to the dissipation also determine the damping of ringing at higher frequencies. Circuit models that describe the dissipation can be extended to

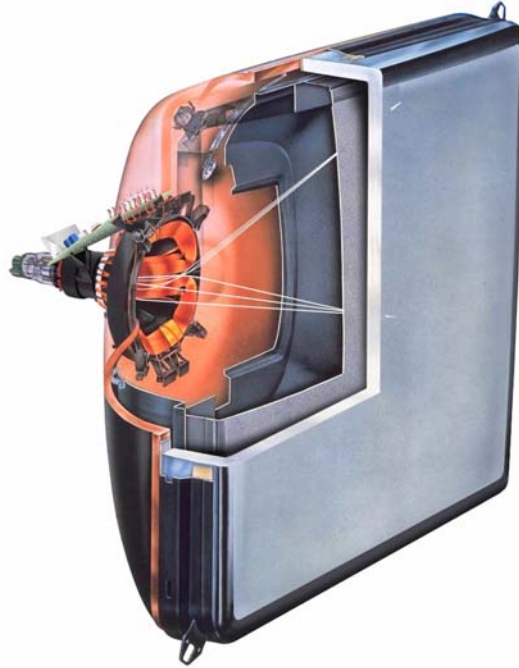


Figure 1.1: A cutaway drawing of a Cathode-Ray Tube.

circuit models that describe ringing.

To improve the high-frequency behavior of deflection yokes, designers need a theoretical framework to systematically explore options for improvement as well as measuring methods to evaluate the impact of these options. In this thesis, both theory and measuring methods are developed to reduce dissipation and to suppress ringing.

The theory results in system models, electric circuit models and physical models. System models give an insight into effects more quickly, but lack the quantitative relation to the design parameters. Physical models provide quantitative relations between circuit model parameters and coil design parameters, but are much more complex. Electric circuit models are a compact representation of physical models. In this thesis we will show how the parameters of circuit models can be derived from impedance measurements to predict both dissipation and ringing.

This thesis does not discuss ray-trace models or the design of the quasi-static magnetic fields which determine the electron-optical behavior. Those models are covered in depth by other authors (see Chapter 2).

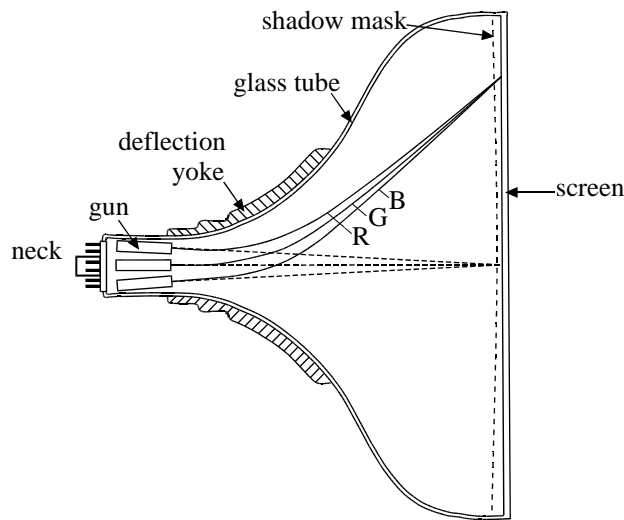


Figure 1.2: Sketch of a top view of a CRT showing how the red (R), green (G) and blue (B) electron beams are deflected across the screen.

1.2 Cathode-Ray Tube

Figure 1.1 shows the construction of a modern CRT and Fig. 1.2 shows a schematic drawing of a top view. Basically, a CRT consists of a glass tube with vacuum inside. The screen is covered with phosphor dots that generate light when hit by electrons. In both Television Tubes (TVTs) and in Computer Monitor Tubes (CMTs), color images are built up with a regular arrangement of phosphor dots in the three primary colors, red, green and blue. An image is generated by three electron beams that write horizontal lines along the screen. Holes in the shadow mask allow only electrons of the ‘red’ beam to reach the dots that generate red light, while the green and blue phosphor dots can only be addressed by electrons of the ‘green’ and ‘blue’ beams, respectively.

The picture information is modulated onto the beam currents. Confined in three separate beams, the electrons are first generated and accelerated in the gun area by an electric field. Subsequently, the beams are deflected by the magnetic deflection field which is generated by the deflection yoke.

1.3 Deflection Yoke

Without the magnetic field of a Deflection Yoke (DY), the electrons would only hit the center of the screen. The magnetic field deflects the electrons when they move from the electron gun in the neck of the tube towards the

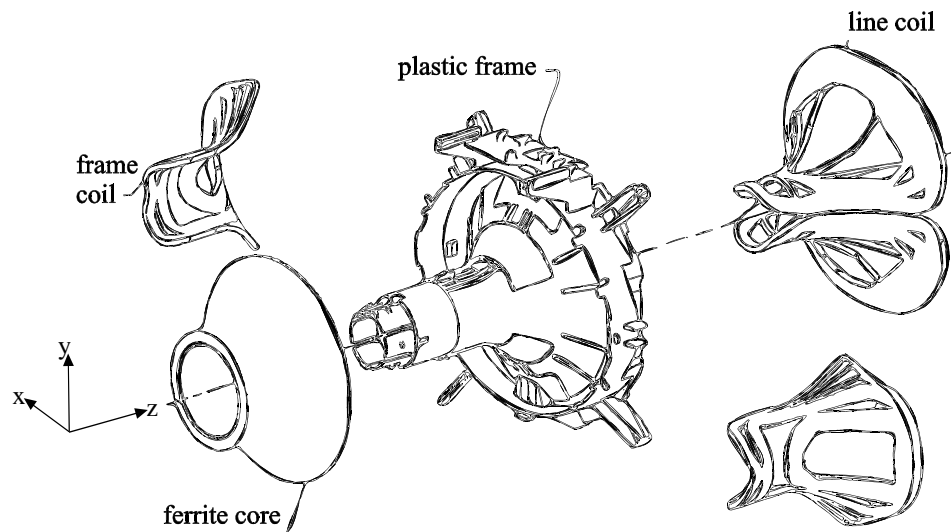


Figure 1.3: Exploded view of a deflection yoke seen from the side of the gun. The screen would be at the right.

front screen.

The magnetic deflection field is varied over time to move the beams from the left-hand side of the screen to the right-hand side. When the beams reach the right-hand edge of the screen, the electron beams are cut off and the magnetic deflection field is reversed. If the electron beam were not cut off, one would be able to observe how the spot quickly moves back to the left-hand side again. Horizontal lines are scanned by applying a time-dependent vertical magnetic field. This field is generated by the so-called ‘line coils’. The ‘line current’ through these coils varies with a ‘line frequency’ of 16 kHz for television sets up to 128 kHz for computer monitors.

At a much lower rate, the beams are deflected from the top of the screen to the bottom. The resulting image is called a frame and the coils causing the vertical deflection are called ‘frame coils’. The ‘frame current’ through these coils varies with a ‘frame frequency’ of 50 Hz for television sets up to 120 Hz for computer monitors.

Figure 1.3 shows an exploded view of a typical deflection yoke. Essentially, a deflection yoke consists of a pair of line coils, a pair of frame coils, a plastic frame and a ferrite core. The line coils are mounted at the inside of a plastic frame, and the frame coils are mounted at the outside. The plastic frame does not only provide the mechanical support of the deflection coils, but also ensures electrical insulation between line and frame coils. The cone-shaped ferrite core is placed over the frame coils. It confines the magnetic field

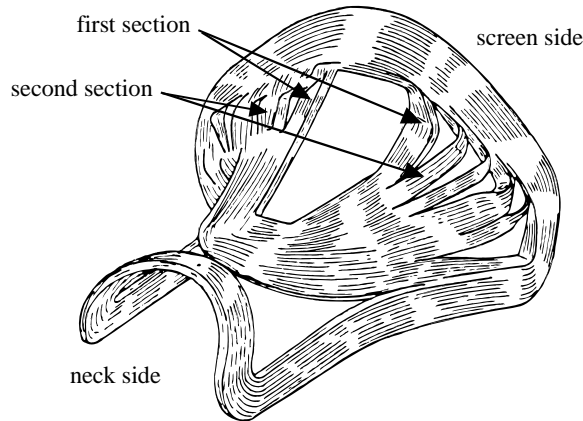


Figure 1.4: Schematic drawing of a single deflection coil. The coil is wound from the inside outwards in a relatively thin layer, typically 3 mm thick. It is divided into various sections both at the screen side and at the neck side.

generated by both the line and frame coils to a smaller volume. This results in a substantial decrease of the power required to drive the coils. Often, other components are included in the deflection yoke for further modification of the magnetic field, such as magnets and pieces of magnetic permeable materials. Usually also electric circuits are added for controlling the drive currents.

The quality of a deflection yoke is often characterized by the following errors measured at the front-side of the screen:

- geometry errors, measured as the distance between the actual position of a green dot and the aimed position;
- convergence errors, measured as the distances between the centers of gravity of the three color spots at specified positions at the screen;
- landing errors, measured as the distance between the center of gravity of a phosphor dot and the center of gravity of the part of the beam that was aimed at that dot.

1.4 Deflection coil

The shape of a deflection coil is determined by the required electron-optical performance and the shape of the glass cone and neck. Deflection coils generally have the shape of a saddle or mussel and accurately fit around the neck and the adjoining, trumpet-shaped widening part of the tube.

A deflection coil consists of several turns of a bundle of wires in parallel. Each wire has a copper core with a few layers around it. From inside outwards, these layers are an insulation layer, a heat bonding layer and a lubrication layer. The lubrication layer consists mainly of paraffin wax.

The distribution of the turns in the coils have a great influence on the distribution of the magnetic field. The turns of the coil are distributed over a number of sections which are separated by open spaces, see Fig. 1.4. By moving turns from one section to another when winding the coils, the distribution of the magnetic field can be easily adjusted.

The coils are wound on an automatic winding machine [2]. This machine includes a ‘winding mandrel’ consisting of two parts having opposed surfaces which bound a space, the shape of which corresponds to the constraining inner and outer surfaces of the coil. A bunch of winding wires is wound through the ‘winding gap’ between the two mandrel parts. One part of the mandrel is detachable from the other for the removal of the wound coil.

The inner section of a single deflection coil is wound first. As soon as the number of turns required for the first section is obtained, two, symmetrically opposed pins are extended into the winding space, approximately perpendicular to the mandrel surface. The first turn of the next section is wound around these pins so that open spaces are created in the vicinity of these pins. After the required number of turns of the second section is reached, another pair of pins is extended into the winding space around the second section in an analogous manner.

When all sections are wound, the coil is pressed into its final shape. Finally the coil is heated by a large current through the wires so that the heat bonding layer melts and forms a strong adhesive bond that holds the wires together.

For each change in a CRT, such as the size of the screen or even the curvature of the screen, a new coil has to be developed. Often the shape of the coil has to change then and a new winding mandrel is required. The development of such a mandrel takes a lot of time and is very expensive. Once a design has been made, it is practically impossible to change the shape of the coil again for reducing undesired high-frequency effects like dissipation and ringing. In fact, only the wire type can be changed then, but even this already has a strong effect on the quality of the picture at the front of the screen. An accurate prediction of the high-frequency effects is therefore very important to the designers of CRT deflection coils.

1.5 Historical overview

The development of deflection coils is strongly connected to the development of the CRT itself (see e.g. [3–8]).

In 1896, F. Braun [9] was the first person who applied a set of coils for horizontal and vertical deflection to use the CRT as a kind of display device. In those days, the deflection coils were simple solenoids. The first electronic television devices were developed in the 1920's at RCA [10]. Their deflection coils already looked like modern coils, i.e. two pairs of flat saddle-shaped coils that fit tightly around the neck of a tube [11–14].

In the first monochrome CRTs, iron shells were used around the coils to increase the strength of the magnetic field. A significant improvement was the development of ferrite material in the 1940's. Ferrite cores completely replaced the iron cores in the first color CRTs [15, 16].

In color CRTs, the three electron beams have to be deflected such that they arrive at the same position on the screen. This requires a much more complicated deflection system than for monochrome CRTs. In 1957, the design and analysis of deflection coils for color CRTs was significantly improved by Haantjes and Lubben [17, 18]. They developed the third-order aberration theory, in which the magnetic field is expanded in a power series around the axis of the CRT. Furthermore, they showed that the design of a color CRT deflection system is strongly simplified by placing the three guns next to each other. This 'in-line' system is used in all modern CRT designs. The third-order theory was further extended to the fifth order by Kaashoek [19] in 1968.

To reduce the depth of CRTs, the deflection angle was increased from 90° to 110° in the 1970's [20–23]. Design and analysis of the magnetic field became very difficult for these large deflection angles [24, 25] and dynamic adjustments were needed. The development of pin-shooting winding technology [26] and the development of the 'multipole theory' [27, 28] enabled Philips in 1980 to further improve the design so that dynamic adjustments were no longer needed.

A deflection yoke is designed with dedicated electron-optical simulation programs. This design has always strongly relied on the measurement of the magnetic fields [29–31], which is very time consuming. A major breakthrough in the development speed was reached by the introduction of computer simulation programs to calculate the magnetic fields of CRT deflection coils [32–38] and to design the coil winding moulds [39].

A recent overview of the design considerations of modern CRT deflection coils is given by Dasgupta [40, 41].

1.6 Organization of this thesis

As an introduction, Chapter 2 summarizes the basic electromagnetic concepts and describes the quasi-static magnetic behavior and the low-frequency electric behavior of CRT deflection coils.

In Chapter 3, the limits of the quasi-static modeling become apparent when the dissipation in the deflection coils is considered. The dissipation is not only caused by drive currents, but also by eddy currents, so that the dissipation increases with the frequency of the drive currents. From basic laws of physics, formulae are derived to relate the dissipation to design parameters. These formulae provide a quantitative explanation of the measured results and make it possible to develop predictive design tools.

Chapter 4 explains how high-frequency oscillations cause ‘ringing’ problems, visible on the CRT screen. With a four-terminal system model, the so-called differential-mode and common-mode oscillations are described. Various methods are presented to measure each of these modes. Adequate results are obtained by measuring the variation in light intensity at the front-side of the screen. An easier and faster measuring method is obtained by measuring the amplitude of the alternating magnetic field as a function of frequency. The optical frequency response measured in this manner and the magnetic frequency response are very similar and can both be related to the measured impedance characteristics of the deflection coils with the help of circuit models. These circuit models enable us to characterize the experimental results by only a few circuit parameters.

In Chapter 5, we try to relate these circuit parameters to the design parameters of the deflection coils. First, literature on relatively simple solenoids is reviewed and expressions for the inductance, the resistance and the capacitance are derived. Subsequently, experimental results are presented for single line coils as well as for complete deflection yokes. Although the expressions cannot explain the experimental results accurately, they give an understanding of the basic relations between ringing and the geometry of the coil and the geometry of the coil wires.

Options to suppress ringing are explored in Chapter 6. Technologies that damp the high-frequency oscillations adequately also result in a significant dissipation at lower frequencies in the line coils. In the frame coils, however, it is possible to apply techniques that suppress ringing but hardly increase the dissipation.

Finally, in Chapter 7 the most important conclusions are summarized.

Chapter 2

Low-frequency behavior

2.1 Introduction

This chapter gives a brief description of aspects of the low-frequency electromagnetic behavior of CRT deflection coils that are relevant for the high-frequency behavior. Simple analytical models give a first-order description of the low-frequency electromagnetic behavior as a starting point for high-frequency models in the remainder of this thesis.

The quasi-static magnetic behavior and the low-frequency electric behavior are described in Sections 2.2 and 2.3, respectively. In these sections, it is described how the magnetic field varies in space and time. Together with the layout of the coil, the spatial variation of the magnetic field as well as the waveform and amplitude of the line and frame currents are the main factors that determine the dissipation and ringing.

2.2 Quasi-static magnetic behavior

Traditionally, the effort in the design of deflection coils has been focused on the quasi-static behavior. Although currents and fields are continuously varied during operation, the behavior of a CRT is called quasi-static when the waveform of the currents and the resulting front-of-screen picture quality do not change with either the line or frame frequency.

In this section, first a quasi-static model of magnetic deflection is described in which the required variation of the magnetic field in time and space follows from the principles of magnetic deflection and the basic parameters of a deflection yoke. Subsequently, electric circuit models are introduced to describe the key elements of the quasi-static electromagnetic behavior.

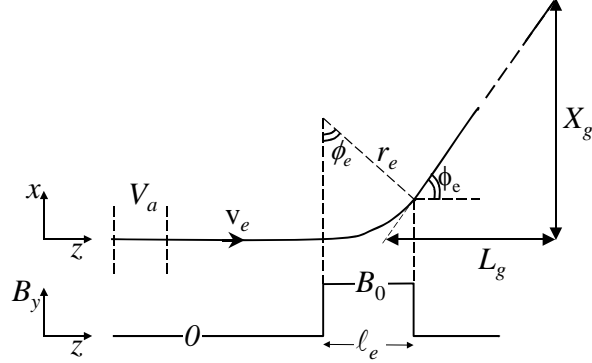


Figure 2.1: Simple model for horizontal deflection.

2.2.1 Deflection in a uniform magnetic field

The relation between the deflection angle and the strength of the magnetic field can be determined with the simplified model of the CRT deflection system shown in Fig. 2.1.

In the gun area, an electron with charge e and mass m_e is accelerated by the electric field due to the voltage difference V_a between anode and cathode. In a non-relativistic approach, the velocity v_e of the electrons follows from the transformation from potential energy eV_a to kinetic energy:

$$\frac{1}{2}m_e v_e^2 = eV_a \quad (2.1)$$

Subsequently, the electrons enter the magnetic field of the deflection coils, which field (in y -direction) is perpendicular to the plane of drawing of Fig. 2.1. For a simple analytic derivation, the magnetic flux density \vec{B} with amplitude B_0 is taken constant over some length ℓ_e . The trajectory of the electrons follows from Newton's law $\vec{F} = m_e d\vec{v}_e/dt$ and Lorentz' law $\vec{F} = e\vec{v}_e \times \vec{B}$ which causes the electrons to follow a circular trajectory with radius

$$r_e = \frac{1}{B_0} \sqrt{\frac{2m_e V_a}{e}} \quad (2.2)$$

As long as $\ell_e < r_e$, the angle ϕ_e at which the beam leaves the magnetic field, is given by

$$\sin \phi_e = \ell_e / r_e \quad (2.3)$$

The horizontal deflection distance X_g at the screen is given by

$$X_g = L_g \tan \phi_e \quad (2.4)$$

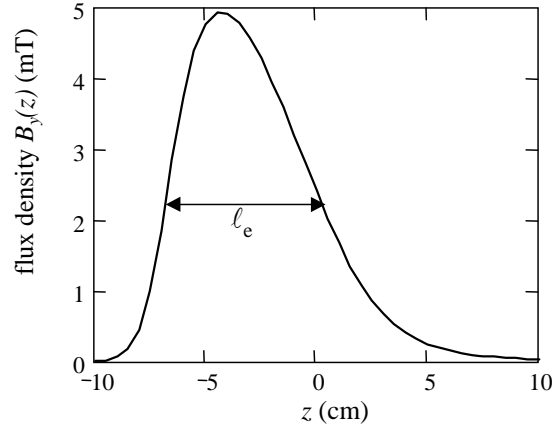


Figure 2.2: The amplitude of the flux density of the line field along the (z -)axis of a 17" CMT deflection yoke.

in which L_g is the distance between the center of the screen and the deflection point defined in Fig. 2.1.

Surprisingly, this simple model calculates the trajectories quite well. The result is close (within 1%) to that of more accurate models for horizontal deflection if the following expression for the effective length ℓ_e is used [42]:

$$\ell_e = \frac{1}{B_{y,\max}} \int_{-\infty}^{\infty} B_y(z) dz \quad (2.5)$$

in which $B_{y,\max}$ is the largest value of the vertical component $B_y(z)$ of the magnetic flux density along the z -axis. A similar expression can be given for the effective length of the vertical deflection. Figure 2.2 shows a typical variation of the flux density along the z -axis generated by the line coils, and the effective length ℓ_e calculated with Eq. 2.5. The point $z = 0$ on the z -axis is related to the outer diameter of the glass tube.

It is clear that for the design of actual deflection yokes, where a high accuracy is required (within 0.01%), the analysis is much more complex. It is common practice to develop deflection yokes with dedicated simulation and design computer programs [33].

2.2.2 Description of the magnetic field

The function of the magnetic field is to deflect the electron beams such that the beams scan the screen in both horizontal and vertical direction. The first

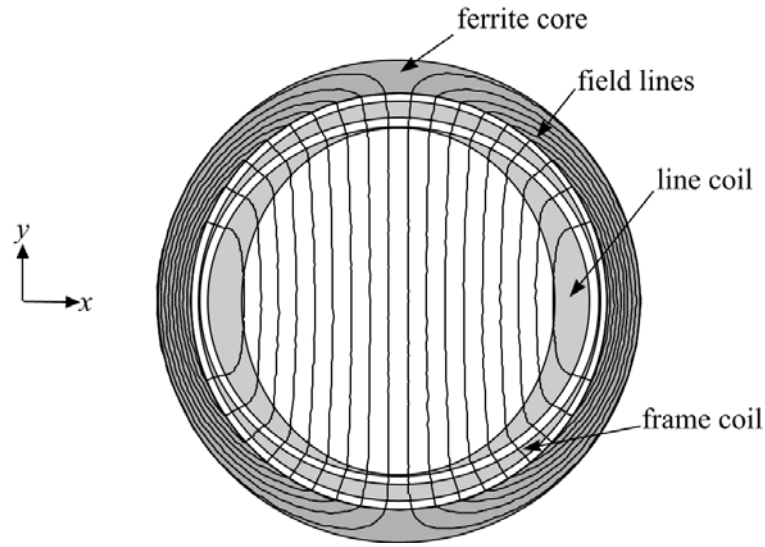


Figure 2.3: Schematic drawing of the line field through a cross section of the deflection yoke. The outer cylinder indicates the ferrite core. The moonshape area's represent the coil area's. Note the curvature of the line field in the line coils as a result of the line current. The frame current is zero in this case.

concern is that the geometry of the picture is good. This is usually checked by generating a grid of horizontal and vertical lines at the screen with a pattern generator. Furthermore, in color CRTs three electron beams have to be deflected such that they hit the screen at the same position. To achieve this so-called convergence, the deflection coils are designed to generate a specific inhomogeneous magnetic field.

In the next chapters we will see that to calculate the high-frequency behavior, the magnetic field at the location of the wires has to be known. At low frequencies, the spatial variation of the magnetic field follows from the quasi-static electron-optic design which determines the front-of-screen performance. Figure 2.2 shows a typical variation of the flux density along the z -axis generated by the line coils. Figure 2.3 shows the field lines in an idealized cross-section in which the current density in some part of the line coil along the circumference varies with the cosine of the angle between the horizontal axis and the line that connects the center of the coil with that part.

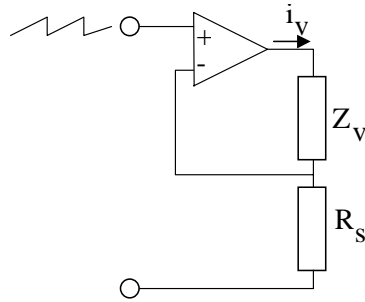


Figure 2.4: Schematic diagram of frame drive circuit.

2.3 Low-frequency electric behavior

This section discusses some simplified circuit models of the deflection coils and drive circuits to describe how the coil currents change in time. A more detailed description of the drive circuits has been given by several authors (e.g. [43, 44]). In the next chapters, we will see that high-frequency effects as dissipation and ringing are strongly determined by the time-dependent behavior of the coil currents and the magnetic field.

2.3.1 Circuit model of the frame coils

Since the current through the frame coils varies relatively slowly, typically at a rate of 50-120 Hz, it is usually sufficient to model the frame coils by a single resistance in series with the frame coil inductance. For a pair of frame coils connected in series, a typical value of the resistance is about $5\ \Omega$ and a typical value of the inductance is 5 mH.

2.3.2 Drive circuit for the frame coils

The frame current is adequately described as a saw-tooth shape. A typical frame coil drive circuit is presented in Fig. 2.4. The frame coil is driven by an amplifier with current feedback provided by a small sensing resistance R_s . During the scan, the impedance of the inductance of the frame coils is small compared to the dc resistance of these coils. Consequently, the impedance Z_v of the frame coil is adequately modeled by a single resistance.

2.3.3 Circuit model of the line coils

Since the line frequency is relatively high - 16 kHz for TVTs up to 128 kHz for CMTs - the line current is to first order determined by the inductance

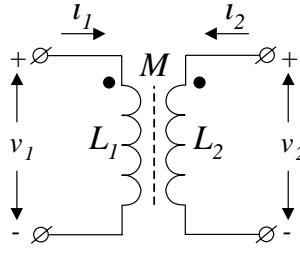


Figure 2.5: A coupled coil pair.

only. In this section, an analytical expression will be derived for the time dependence of the line current. Because of the complex shape of the coils, the inductance L is hard to determine analytically. Computer programs are commonly applied for this [45, 46].

Although the coils in a pair are coupled magnetically, they can be modeled by a single inductance at low frequencies. To explain this, Fig. 2.5 shows the voltages and currents in such a pair of coupled coils with inductances L_1 and L_2 and mutual inductance M .

The following set of coupled equations gives the relation between voltages and currents:

$$\begin{aligned} v_1 &= j\omega L_1 i_1 + j\omega M i_2 \\ v_2 &= j\omega M i_1 + j\omega L_2 i_2 \end{aligned} \quad (2.6)$$

The coils in a coil pair can be connected in series or in parallel as illustrated in figure 2.6. When the coil pairs are connected in series, the series impedance $Z_s = v_s/i_s$ follows by substituting $v_s = v_1 + v_2$ and $i_s = i_1 = i_2$:

$$Z_s = j\omega L_s \quad (2.7)$$

with

$$L_s = L_1 + L_2 + 2M \quad (2.8)$$

When $L_1 = L_2 = L$, this reduces to

$$L_s = 2(1 + k_L)L \quad (2.9)$$

in which the coupling constant k_L is defined by

$$k_L = M/L \quad (2.10)$$

When the coils are not coupled at all, the coupling constant has its minimum value $k_L = 0$. The maximum value $k_L = 1$ occurs when the coils are maximally

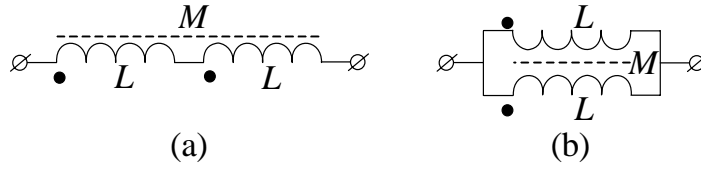


Figure 2.6: A pair of coils can be connected (a) in series or (b) in parallel.

coupled, i.e. when the magnetic flux generated by one coil is completely enclosed by the second coil.

When the coil pairs are connected in parallel, the parallel impedance $Z_p = v_p/i_p$ follows by substituting $v_p = v_1 = v_2$ and $i_p = i_1 + i_2$:

$$Z_p = j\omega L_p \quad (2.11)$$

with

$$L_p = \frac{L_1 L_2 - M^2}{L_1 + L_2 - 2M} \quad (2.12)$$

When $L_1 = L_2 = L$, this reduces to

$$L_p = \frac{1}{2}(L + M) \quad (2.13)$$

or

$$L_p = \frac{1}{2}(1 + k_L)L \quad (2.14)$$

An important consequence is that the ratio between the series inductance L_s and the parallel inductance L_p of the line-coil pair is $L_s/L_p = 4$, for every value of k_L .

Circuit designers specify the total inductance of a line-coil pair because this determines the maximum (flyback) voltage that their circuit components have to withstand. Consequently, a different value for the inductance of a single coil is required when the two coils in a line-coil pair are connected in parallel than when they are connected in series. Assuming that the inductance is proportional to the square of the number of turns with which each coil is wound, we conclude that, to obtain the same total inductance of a line-coil pair, the number of turns has to be twice as large when the single coils are connected in parallel than when they are connected in series.

When the line coils are connected in parallel, typically about 40 turns are required for each coil to obtain the required inductance. Shooting in a single pin one turn later - the smallest change that can be made when winding a coil (see page 6) - results already in a significant change in front-of-screen

performance. The change would be unacceptably large when the total number of turns was only 20 which would be the case when the coils were connected in series. Therefore line coils are connected in parallel in almost every deflection yoke.

A second reason to connect the line coils in parallel, is that for the same overall dc resistance of the line-coil pair, which is also specified by circuit designers, only half the number of parallel wires is required when the coils are connected in parallel than when the coils are connected in series.

Finally note that, in general, coils cannot easily be removed from a deflection yoke. To determine the coupling constant k_L , one can interchange the interconnections of one of the parallel coils and measure the overall inductance again. In a similar way as above, it can be shown that the overall inductance value of these ‘anti-parallel’ coils equals $L_{ap} = \frac{1}{2}(1 - k_L)L$. The coupling constant k_L then follows from

$$k_L = \frac{1 - L_{ap}/L_p}{1 + L_{ap}/L_p} \quad (2.15)$$

As an example the inductances of 17" CMT deflection coils were measured. The inductance of a single line coil mounted in the deflection yoke was $L = (190.0 \pm 0.1) \mu\text{H}$. The inductance of a pair of such line coils in parallel was $L_p = (123.0 \pm 0.1) \mu\text{H}$ and when the connections of one of the parallel line coils was interchanged the inductance dropped to $L_{ap} = (66.8 \pm 0.1) \mu\text{H}$. Substitution in Eq. 2.14 yields $k_L = 0.295 \pm 0.002$ and substitution in Eq. 2.15 yields $k_L = 0.296 \pm 0.001$, which illustrates that both approaches result in the same value for k_L .

2.3.4 Drive circuit of the line coils

The line current is much more important for the dissipation and ringing than the frame current because the line frequency is several orders of magnitude higher than the frame frequency.

For large deflection angles, the deflection distance along the screen is not linearly proportional to the magnetic field (see Eqs. 2.2-2.4). The shape of the drive current is adapted to compensate for this effect by means of a capacitance in series with the line coil. This adaptation is known as S-correction since the shape of the current as function of time resembles an ‘S’.

The time dependence of the line current is calculated by analyzing the driving circuit. Figure 2.7 shows the basic principle of a line-drive circuit. In this figure, L_h is the inductance of the line coil, C_s the S-correction

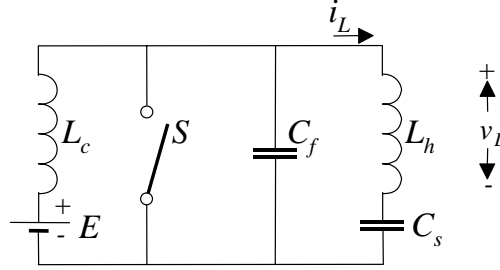


Figure 2.7: Simplified circuit diagram of the line drive circuit.

capacitance and C_f the flyback capacitance. The purpose of the choke L_c is to prevent that the supply voltage E is short circuited by the switch. We assume that L_c is so large ($L_c \gg L_h$) that its influence on the behavior can be neglected. In practice, the switch S usually is a combination of a transistor and a diode. At the line frequency, the dc resistance of the deflection coils is very small compared to their reactance. Therefore, we omit it in the following analysis.

During flyback the switch is open and the current oscillates with the flyback frequency

$$\omega_{fb} = 1/\sqrt{L_h C'_f} \quad (2.16)$$

with $C'_f = C_s C_f / (C_s + C_f)$. In practice C_s is much larger than C_f , so that $C'_f \approx C_f$. Note that the duration t_{fb} of the flyback is only half a period: $t_{fb} = \pi/\omega_{fb}$.

The line scan is started by closing the switch. This changes the resonance frequency to the scan frequency

$$\omega_{sc} = 1/\sqrt{L_h C_s} \quad (2.17)$$

If we introduce the flyback ratio p of the flyback time t_{fb} and the line signal period T by

$$p = t_{fb}/T \quad (2.18)$$

the sawtooth current waveform of Fig. 2.8 is obtained by closing the switch at time $t = -\frac{1}{2}(1-p)T$ and opening again at time $t = \frac{1}{2}(1-p)T$. This line current is described by

$$i_L(t) = \begin{cases} I_{sc} \sin(\omega_{sc} t) & \text{during line scan} \\ -I_0 \sin(\omega_{fb} t - \beta) & \text{during flyback} \end{cases} \quad (2.19)$$

where I_0 denotes the amplitude of the line current. This signal is repeated with the line frequency

$$\omega_\ell = 2\pi/T \quad (2.20)$$

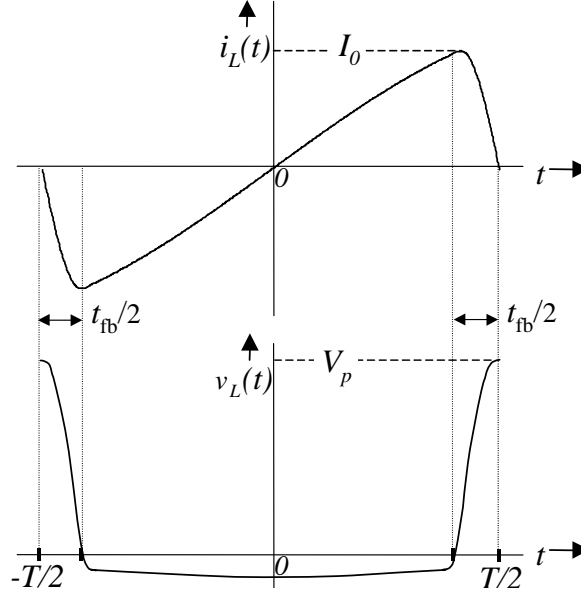


Figure 2.8: Line-coil current $i_L(t)$ and voltage $v_L(t)$ as a function of time t .

The voltage $v_L(t)$ across the line coil is determined by this line current by $v_L(t) = -L di_L(t)/dt$.

If we take $i(T/2) = 0$, the constant β is given by

$$\beta = \pi \omega_{fb} / \omega_\ell \quad (2.21)$$

The constant I_{sc} follows from the continuity of current at time $t = \frac{1}{2}(1-p)T$:

$$I_{sc} = \frac{\sin(p\beta)}{\sin \alpha} I_0 \quad (2.22)$$

with

$$\alpha = \pi (1-p) \omega_{sc} / \omega_\ell \quad (2.23)$$

Continuity of the derivative of the current in $t = \frac{1}{2}(1-p)T$ is obtained when

$$\omega_{sc} \tan(p\beta) = -\omega_{fb} \tan \alpha \quad (2.24)$$

i.e., when α , β and p comply with the following implicit relation:

$$\frac{1}{\tan(p\beta)} = \frac{\alpha}{\beta} \frac{1}{p-1} \frac{1}{\tan \alpha} \quad (2.25)$$

The flyback ratio p is usually 0.18. This value was chosen during the early years of television. For compatibility this value has been maintained up to

now. Practical values of α and β depend on the deflection angle. Practical values are $\alpha = 1.1$ for TVTs with 110° deflection angle and $\alpha = 0.82$ for CMTs with 90° deflection angle [47]. Subsequently, the value for β follows from Eq. 2.25.

Fourier expansion

Especially for the dissipation, the frequency content of the line current plays an important role. To this purpose the line current can be expanded in a Fourier series

$$i(t) = I_0 \sum_{n=1}^{\infty} a_n \sin n\omega_\ell t \quad (2.26)$$

in which the Fourier coefficients a_n are given by

$$a_n = \frac{1}{I_0 T} \int_{-T/2}^{T/2} i(t) \sin n\omega_\ell t dt \quad (2.27)$$

With Eq. 2.19 this results is [48]:

$$a_n = \frac{2}{\pi} (v_{\text{fb}}^2 - v_{\text{sc}}^2) \frac{v_{\text{fb}} \cos p\beta \sin np\pi - n \sin p\beta \cos np\pi}{(n^2 - v_{\text{fb}}^2)(n^2 - v_{\text{sc}}^2)} \quad (2.28)$$

with the relative scanning frequency

$$v_{\text{sc}} = \omega_{\text{sc}} / \omega_\ell \quad (2.29)$$

and the relative flyback frequency

$$v_{\text{fb}} = \omega_{\text{fb}} / \omega_\ell \quad (2.30)$$

Typical values of a_n are summarized in Table 2.1. Higher harmonics of the line frequency ω_ℓ contribute significantly up to about eight times the line frequency. In Chapter 3, the Fourier coefficients a_n will be used for the calculation of the dissipation.

2.4 Summary and conclusions

High-frequency effects of CRT deflection coils are neglected during the first design phases. However, the high-frequency behavior of CRT deflection coils is increasingly important because of the trend towards higher image quality. Not only the distortions become better visible at the screen, but also the distortions become stronger since the scan frequencies are increasing. The

n	a_n	
	CMT	TVT
1	0.794	0.832
2	0.331	0.321
3	0.183	0.175
4	0.105	0.101
5	0.058	0.055
6	0.029	0.027
7	0.010	0.010
8	0.004	0.003

Table 2.1: Fourier coefficients of typical CMT and TVT line-drive signals.

line frequency increases because it is the product of the number of lines per image and the number of images per second (the refresh rate), while these both have to increase to improve the image quality.

For the first conceptual design phase, simple quasi-static models for magnetic deflection and electrical models for line and frame coils are available to describe the low-frequency behavior. These models provide a starting point for modeling the dissipation and ringing in the remainder of this thesis.

The current through the frame coils varies at a rate of up to 120 Hz. At this frequency, the impedance is still fully determined by the resistance of the frame coils. Since the line frequency is relatively high (16-128 kHz), the line coil current is to first order determined by the inductance only.

The conceptual design is worked out towards hardware models with modern Computer-Aided Design (CAD) software programs that numerically calculate the main front-of-screen performance parameters such as geometry, convergence and landing errors. Also electric parameters like inductance, peak current and current shape are calculated with this software. This CAD software only considers the quasi-static behavior in which the front-of-screen performance parameters are not changed when e.g. the driving frequencies are changed. However, for higher frequencies the dynamic effects can no longer be neglected and more advanced models are required.

Chapter 3

Dissipation

3.1 Introduction

The first effect of the dynamic behavior of CRT deflection coils that becomes noticeable when the number of scan lines - and hence the line frequency - is increased, is that the dissipation increases too. Dissipation is the conversion of electrical energy into heat and manifests itself not only as a loss of electrical energy but also as a temperature rise of the coils.

Dissipation in CRT deflection coils is becoming more and more important. On the one hand customers ask for lower energy consumption in general; not only because of an increasing environmental awareness but also because a lower dissipation allows set makers to use cheaper circuit components. A large part of the dissipation of television and monitor sets is determined by the dissipation in the deflection yoke and in its drive circuits.

On the other hand, trends to improve the performance result in an increase in dissipation. Furthermore, those trends, such as larger deflection angles (120°-TVT and 100°-CMT) and higher resolution (line frequencies increasing to 128 kHz), can bring the dissipation to a level where the temperature exceeds the safety limits. To prevent this, the dissipation should be reduced by a careful design of the deflection yokes. This chapter presents the relevant models to achieve this.

As a rough indication, a 17" CMT monitor (with a line frequency of 69 kHz) takes up about 75 Watt in total, of which about 20 Watt is needed for generating and accelerating the electron beams. About 27 Watt of the remaining 55 Watt, is needed for the deflection [51]. The deflection yoke itself consumes about 12 Watt. The drive circuits that generate the line and frame

Part of this chapter has already been published in [49] and [50].

currents consume the remaining 15 Watt.

At the end of Chapter 2, we concluded that higher harmonics of the line frequency contribute up to about eight times the line frequency (see Table 2.1). With line frequencies up to 125 kHz, the consequence is that electromagnetic phenomena for frequencies up to 1 MHz play a role for dissipation.

In this chapter the dependencies of the dissipation in CRT deflection coils on various design parameters are clarified. Simple analytical models are discussed to gain insight and a short discussion deals with the main deviations from the simple models.

In Chapter 4 these models will be extended to describe phenomena that occur at even higher frequencies.

3.2 Literature on dissipation

In this chapter, we analyze the dissipation in the deflection coils. The dissipation in the drive circuits is analyzed elsewhere [52–54].

The general approach for optimizing the design of the deflection yoke for minimum deflection energy is discussed by e.g. Brilliantov [55]. The analysis of the dissipation and temperature rise in CRT deflection coils is only briefly discussed in the literature [56, 57].

A recent general review of the theory on eddy currents is given by Kriezis [58]. Analytical models for eddy-current losses are developed for simple geometries, such as cylindrical shells [59], cylindrical conductors [60, 61], systems of parallel conductors [62], insulated cables [63], foil conductors [64], thin conducting plates of various shapes [65], planar structures with spiral windings [66] and high-frequency transformers [67, 68].

For numerical calculations, many authors [69–79] have followed the approximated one-dimensional solution proposed by Dowell [80] and have improved his concepts.

The most relevant methodology for developing the theory on dissipation in coils is described in the literature on solenoids [81–85], power inductors [86–90] and various kinds of transformers [91–102]. Already for these coils with a relatively simple geometry, the winding structure greatly affects the distribution of losses within the windings [103–105]. For these applications software programs are widely used [106–112].

3.3 Deflection energy

At first thought, one could imagine that the dissipation is proportional to the energy stored in the magnetic field. A coil with inductance L_h , carrying a current I_0 contains an energy

$$E_h = \frac{1}{2} L_h I_0^2 \quad (3.1)$$

Rather than specifying this energy, it is customary to specify the ‘sensitivity’ $L_h I_{pp}^2$ of the deflection coils. With $I_{pp} = 2I_0$ it is easy to see that $L_h I_{pp}^2 = 8E_h$. Typical values for the sensitivity are $L_h I_{pp}^2 = 13$ mJ for CMT products (with 90° deflection) and $L_h I_{pp}^2 = 35$ mJ for TVT products (with 110° deflection).

The importance of the energy $\frac{1}{2} L_h I_0^2$ of the line coils is that it indeed can be correlated to the dissipation in the drive circuit. However, this energy is not the same as the dissipation! For instance, in theory the dissipation can in fact be zero if the deflection currents are generated by an oscillating system without energy loss.

In fact, the energy is lost in the resistive part of the system; both in the drive circuit and in the deflection coils. To first order we may assume that the dissipation P in the resistive parts is proportional to the line frequency ω_ℓ and the magnetic energy E_h required for deflection:

$$P \propto \omega_\ell E_h \quad (3.2)$$

but the proportionality factor and the deviations from this simple relation depend on the actual resistive losses. This will be discussed in more detail in later sections.

For higher line frequencies the dissipation in the drive circuit can be much higher than that in the deflection yoke and this is the reason why setmakers emphasize the reduction of $L_h I_{pp}^2$ rather than the reduction of the dissipation in the CRT deflection coils. However the dissipation in the deflection coils is also important as it determines the temperature of the coils during operation.

The influence of various geometry parameters can be obtained by evaluating the magnetic energy. According to Eq. 3.1 the energy is proportional to $L_h I_0^2$. This could be determined by calculating both the inductance and the required current. A more convenient way, however, is to start from the magnetic field intensities H and calculate the energy stored in the magnetic field:

$$E_h = \frac{1}{2} \mu_0 \int H^2 dV \quad (3.3)$$

in which μ_0 denotes the permeability in vacuum and V the volume. For the simple model of the previous chapter, assuming that the magnetic field is

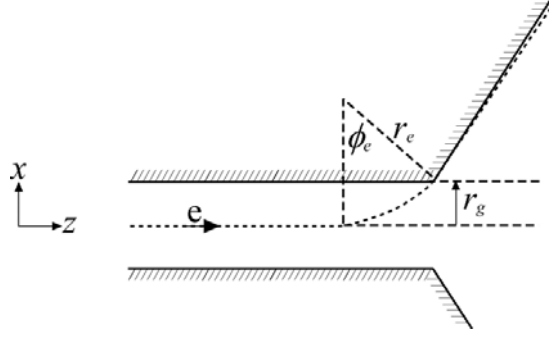


Figure 3.1: Relation between the deflection angle ϕ_e and the radius r_g in the neck of the glass cone.

confined to the area enclosed by a cylindrical ferrite core with inner radius r_c , the magnetic energy for deflecting to an angle ϕ_e follows by substituting Eq. 2.2 and Eq. 2.3 into Eq. 3.3, giving

$$E_h = \frac{m_e V_a}{\mu_0 e} \frac{\sin^2 \phi_e}{\ell_e} \pi r_c^2 \quad (3.4)$$

This result indicates that for minimum deflection energy, the effective coil length ℓ_e must be made as large as possible. However, when this length is too long, the electrons are already deflected too much in the neck area and will hit the glass tube. Figure 3.1 shows the limiting situation where the electron trajectory just touches the inner glass contour.

With the circular trajectory of our simple model it can be seen that the relation of the deflection angle ϕ_e with the inner radius r_g of the neck of the glass tube can be expressed as

$$r_g = r_e (1 - \cos \phi_e)$$

Combination with $\ell_e = r_e \sin \phi_e$ results in

$$\ell_e = r_g \frac{\sin \phi_e}{1 - \cos \phi_e} = \frac{r_g}{\tan \frac{1}{2} \phi_e} \quad (3.5)$$

Substitution in Eq. 3.4 gives the following expression for the magnetic energy [42]

$$E_h = \frac{\pi m_e}{\mu_0 e} V_a \frac{r_c^2}{r_g} \sin^2 \phi_e \tan \frac{1}{2} \phi_e \quad (3.6)$$

The relation between the horizontal deflection angle ϕ_e and the corner deflection angle ψ_e is shown in Fig. 3.2. For conventional screen sizes with

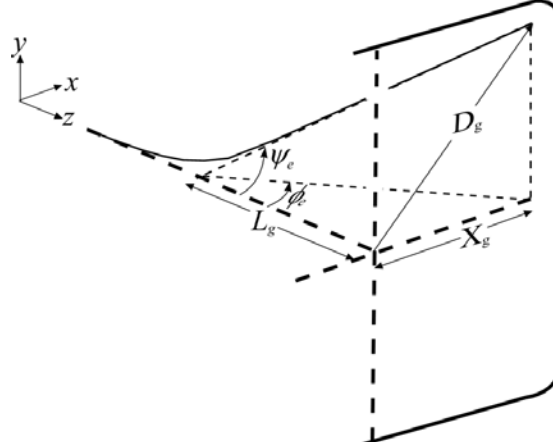


Figure 3.2: The relation between the horizontal deflection angle ϕ_e , the corner deflection angle ψ_e and the various distances D_g , X_g and L_g .

ratio 4:3 of the horizontal length and the vertical length of the screen, the relation between X_g and D_g is given by $X_g = \frac{4}{5}D_g$. With $D_g/L_g = \tan \psi_e$ and $X_g/L_g = \tan \phi_e$, we find

$$\phi_e = \arctan\left(\frac{4}{5} \tan \psi_e\right) \quad (3.7)$$

With this relation between ϕ_e and ψ_e , we introduce the auxiliary function

$$\Psi(\psi_e) = \sin^2 \phi_e \tan \frac{1}{2} \phi_e \quad (3.8)$$

so that we can write Eq. 3.6 as

$$E_h = \frac{\pi m_e}{\mu_0 e} V_a \frac{r_c^2}{r_g} \Psi(\psi_e) \quad (3.9)$$

This shows how the magnetic energy E_h , and hence also the dissipation (Eq. 3.2), depends on the anode voltage V_a , the deflection angle ψ_e , the radius r_c of the ferrite core and the radius r_g of the inside of the glass tube. The magnetic energy, for instance, increases linearly with the anode voltage. One could reduce this voltage, but then the brightness goes down and convergence errors increase due to the beam charge repulsion.

When we assume that the diameter r_c of the ferrite core is proportional to the inner glass diameter r_g , the energy E_h in Eq. 3.6 increases linearly with the neck diameter. For example, replacing a Narrow Neck (29.1 mm) by a Mini Neck (22.5 mm) reduces $L_h I_{pp}^2$ by a factor of 1.3. This has been

confirmed experimentally [57]. However, although the Mini-Neck size results in a lower dissipation than the Narrow-Neck size, often narrow-neck-designs are preferred because of a better gun performance.

The influence of the deflection angle is illustrated in Fig. 3.3, showing how the factor $\Psi(\psi_e)$ depends on the deflection angle $2\psi_e$. This figure shows that a reasonably correct approximation for this dependence for practical deflection angles is given by

$$E_h \sim \psi_e^{3.15} \quad (3.10)$$

This has been validated by measurements on comparable 25" television sets [113], where 100°-products have 40% less dissipation in the line deflection and 30% less in the frame deflection than 110°-products. Note that $(110/100)^{3.15} = 1.35$.

In the same manner it can be derived that the deflection dissipation varies with $\psi_e^{2.95}$ for wide-screen television sets in which the ratio of the horizontal length and the vertical length of the screen is 16:9.

3.4 Loss phenomena

The following physical phenomena are responsible for the dissipation in CRT deflection coils:

- Ohmic loss in the dc-resistance of the wires of the coils;
- eddy currents in the wires of the coils;
- dielectric losses in the wire insulation;
- eddy-current losses in the ferrite core;
- magnetic power losses in the ferrite core.

These phenomena will be discussed in more detail in the following sections. Unless stated otherwise, we assume that the Fourier expansion of Sect. 2.3.4 can be used. Therefore, we consider only sinusoidal currents and fields of (angular) frequency ω .

3.4.1 Ohmic losses in a solid wire

If, at low frequencies, the current $I_0 \sin \omega t$ is distributed homogeneously within a wire, the average dissipation is determined by the Ohmic loss

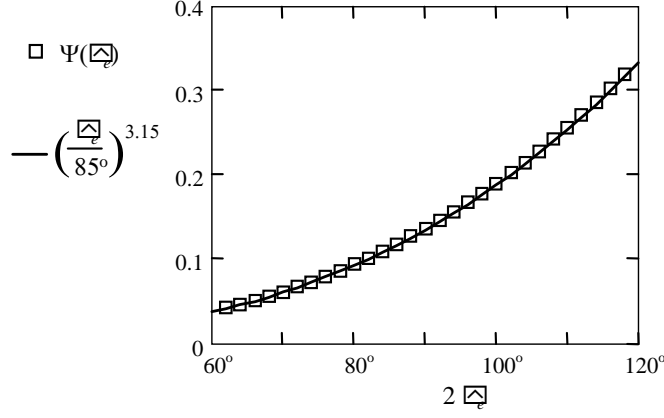


Figure 3.3: For practical deflection angles $2\psi_e$, the auxiliary function $\Psi(\psi_e)$ (squares) is proportional to $\psi_e^{3.15}$ (solid line).

$$P_{\text{dc}} = \frac{1}{2} R_{\text{dc}} I_0^2 \quad (3.11)$$

The factor $\frac{1}{2}$ follows from calculating the time average. The dc series resistance R_{dc} is proportional to the number of turns N_{turns} and the average length ℓ_{turn} of a turn. For a circular wire it follows from

$$R_{\text{dc}} = \frac{N_{\text{turns}} \ell_{\text{turn}}}{\pi a^2 \sigma} \quad (3.12)$$

in which σ denotes the conductivity and a the radius of the winding wires.

Note that the conductivity at the DY operating temperature (up to 110 °C) has to be used rather than that at room temperature. The conductivity decreases rapidly with temperature, according to [114]:

$$\sigma(T) = \frac{\sigma_0}{1 + \alpha_0(T - T_0)} \quad (3.13)$$

in which σ_0 and α_0 are the conductivity and temperature coefficient for copper at temperature T_0 . At $T_0 = 20$ °C, $\sigma_0 = 5.8 \cdot 10^7 \Omega^{-1}\text{m}^{-1}$ and $\alpha_0 = 0.00396$. Note that the dc-resistance of copper at 100 °C is more than 30% higher than at 20 °C.

3.4.2 Eddy-current losses in a solid wire

When the resistance of the line coil is measured as a function of frequency, it turns out that the resistance is a constant, R_{dc} , for frequencies below

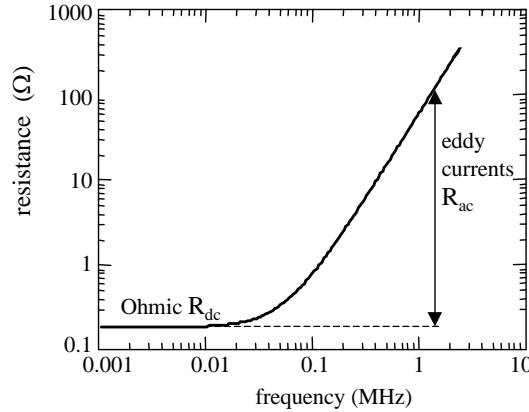


Figure 3.4: The resistance increases with the frequency.

about 1 kHz, while the resistance increases strongly for higher frequencies, as illustrated in Fig. 3.4. This increase is caused by eddy-current losses.

In eddy-current analysis, usually two simplified models are considered (see Fig. 3.5):

- (1) a wire carries an alternating current without any external magnetic field. The alternating current will set up an alternating magnetic field that induces eddy currents in the wire. As a result the current distribution in the wire is changed, causing crowding of the current near the surface of the wire. The total current in the wire remains the same. Since the local dissipation is proportional to the square of the current density, the dissipation increases. This ‘*skin effect*’, however, results in relatively low losses. An excellent description of the skin effect is given by Casimir [115–117].
- (2) in an alternating external magnetic field, a wire is considered through which no other currents flow than eddy currents. The external field can be generated by a large number of distant wires, as e.g. in a frame coil which is affected by the high-frequency varying magnetic field of the line coil. An important configuration is that in which the external field is caused by nearby other wires. This is known as the ‘*proximity effect*’ [91, 118, 119]. In fact, in a deflection yoke the contributions of all wires add to a rather uniform field that cuts the wires almost perpendicularly. Therefore, calculations assuming a uniform external field already gives valuable insight into the effects in this configuration.

In the remainder of this section we will show how expressions for the dissipation caused by the skin effect and the proximity effect follow from

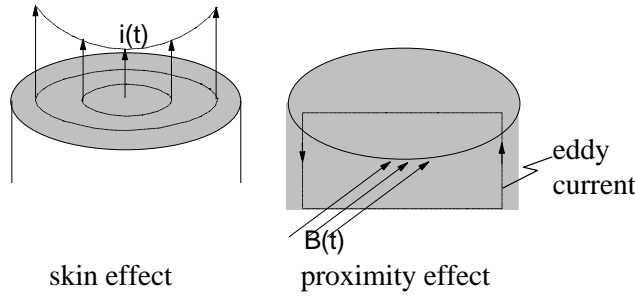


Figure 3.5: Skin effect versus proximity effect.

Maxwell's equations. At the end of this section (at page 35), we will discuss the combination of the skin effect and the proximity effect.

Skin depth

The skin effect follows from the *diffusion equation* (derived from Maxwell's equations in Appendix A):

$$\nabla^2 \vec{E} = i\omega\mu\sigma \vec{E} \quad (3.14)$$

To introduce the important concept of 'skin depth', we solve the diffusion equation in a metal occupying the positive z -space. If the current density j_x is uniform and of angular frequency ω on the surface, j_x is a function of z only, according to:

$$\frac{\partial^2 j_x}{\partial z^2} = i\omega\mu\sigma j_x \quad (3.15)$$

the solution of this equation is

$$j_x = ce^{-z\sqrt{i\omega\mu\sigma}} + de^{z\sqrt{i\omega\mu\sigma}} \quad (3.16)$$

in which the constants c and d follow from the boundary conditions. If j_x is zero when $z = \infty$ then $d = 0$. Since $\sqrt{i} = (1 + i)/\sqrt{2}$ the following expression for the real part of j_x is found:

$$\text{Re}(j_x) = j_0 e^{-z/\delta} \cos(\omega t - z/\delta) \quad (3.17)$$

Both the phase change with z and the exponential decrease of the amplitude of j_x depend on the characteristic distance, the so-called *skin depth*

$$\delta = \sqrt{\frac{2}{\omega\mu\sigma}} \quad (3.18)$$

Since Eq. 3.18 has been derived directly from the general diffusion formula Eq. 3.14, it represents the depth of penetration of many physical quantities, notably that of electric fields in conductors.

For copper at room temperature, $\sigma = 5.8 \cdot 10^7 \text{ } \Omega^{-1}\text{m}^{-1}$ so that the skin depth as function of frequency $f = \omega/2\pi$ is given by

$$\delta = \frac{6.6 \cdot 10^{-2}}{\sqrt{f}} (\text{m}) \quad (3.19)$$

Skin effect in a wire

To calculate the skin effect in a wire, we consider a current in a wire without any external magnetic field. The wire has radius a and length ℓ and carries an alternating current with amplitude $j_z(r)$ and frequency ω along the z -axis. The configuration has symmetry around the axis, so that the current density depends only on the distance r . Consequently, the diffusion equation, Eq. 3.14, reduces in cylindrical coordinates to

$$\frac{\partial^2 j_z(r)}{\partial r^2} + \frac{1}{r} \frac{\partial j_z(r)}{\partial r} = i\omega\mu\sigma j_z(r) \quad (3.20)$$

The solution of this ‘Bessel differential equation’ which is bounded for $r=0$, is the Bessel function $J_0(kr)$ (see Appendix C):

$$j_z(r) = cJ_0(kr) \quad (3.21)$$

with

$$k^2 = -i\omega\mu\sigma \quad (3.22)$$

The constant c follows from the amplitude I_0 of the total current through the cross-section of the wire:

$$\int_0^a j_z(r) \cdot 2\pi r dr = I_0 \quad (3.23)$$

This results in

$$j_z(r) = \frac{kJ_0(kr)}{2\pi aJ_1(ka)} I_0 \quad (3.24)$$

in which $J_1(ka)$ denotes the Bessel function of the first kind of order one (see Appendix C).

To calculate the dissipation P of a current density with amplitude j_z in a metal with conductivity σ , we must use the effective value of the real part $\text{Re}(j_z)$ of j_z and integrate it over the volume V :

$$P = \frac{1}{\sigma} \int \overline{\{\text{Re}(j_z)\}^2} dV \quad (3.25)$$

in which the bar denotes that the time average has to be taken. For our calculations, it is more convenient to evaluate the following equivalent expression instead:

$$P = \frac{1}{2\sigma} \int j_z \cdot j_z^* dV \quad (3.26)$$

where j_z^* denotes the conjugate of j_z .

Substitution of the current (Eq. 3.24) yields

$$P_{\text{skin}} = \frac{\ell}{2\sigma} \int_0^a \left(\frac{kI_0}{2\pi a} \frac{J_0(kr)}{J_1(ka)} \right) \left(\frac{kI_0}{2\pi a} \frac{J_0(kr)}{J_1(ka)} \right)^* 2\pi r dr \quad (3.27)$$

in which ℓ denotes the length of the wire. With the identities presented in Appendix C, this can be reduced to

$$P_{\text{skin}} = \frac{\ell I_0^2}{2\pi a^2 \sigma} \operatorname{Re} \left(\frac{ka}{2} \frac{J_0(ka)}{J_1(ka)} \right) \quad (3.28)$$

Similar to the dc resistance (Eq. 3.11), the equivalent skin resistance is introduced as

$$R_{\text{skin}} = \frac{2P_{\text{skin}}}{I_0^2} \quad (3.29)$$

so that

$$R_{\text{skin}} = R_{\text{dc}} \operatorname{Re} \left(\frac{ka}{2} \frac{J_0(ka)}{J_1(ka)} \right) \quad (3.30)$$

in which the dc resistance R_{dc} of the wire is given by $R_{\text{dc}} = \ell/(\pi a^2 \sigma)$. The second factor in Eq. 3.30 is called the skin loss factor $f_{\text{skin}}(a/\delta)$ which depends on the ratio of wire radius a and skin depth δ :

$$R_{\text{skin}} = R_{\text{dc}} f_{\text{skin}}(a/\delta) \quad (3.31)$$

For numerical evaluation of the skin loss factor, we write the argument ka with the definition of k^2 (Eq. 3.22) and that of the skin depth δ (Eq. 3.18) as

$$ka = (1 - i)x \quad (3.32)$$

with

$$x = a/\delta \quad (3.33)$$

The skin loss factor

$$f_{\text{skin}}(x) = -\operatorname{Re} \left(\frac{[1 - i]x}{2} \frac{J_0([1 - i]x)}{J_1([1 - i]x)} \right) \quad (3.34)$$

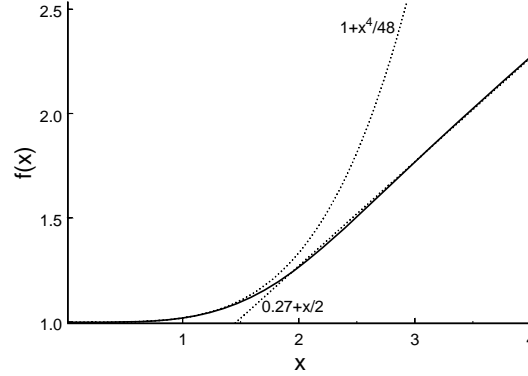


Figure 3.6: Low-frequency and high-frequency approximations of the skin loss factor $f_{\text{skin}}(x)$.

is shown in Fig. 3.6 as a function of x .

For low frequencies where $a < 1.5\delta$, Eq. 3.30 can be approximated by

$$R_{\text{skin}} = \left(1 + \frac{a^4}{48\delta^4}\right) R_{\text{dc}} = \left(1 + \frac{\mu^2 \sigma^2 a^4}{192} \omega^2\right) R_{\text{dc}} \quad (3.35)$$

For high frequencies where $a > 2\delta$, Eq. 3.30 can be approximated by

$$R_{\text{skin}} = \left(0.27 + \frac{a}{2\delta}\right) R_{\text{dc}} = \left(0.27 + a\sqrt{\frac{\mu\sigma\omega}{8}}\right) R_{\text{dc}} \quad (3.36)$$

Note that some authors, e.g. Küpfmüller [120], sometimes use a slightly different expansion.

In this section we have first calculated the dissipation and then derived an expression for the equivalent skin resistance. In the following sections we follow a similar approach for the proximity effect. For the skin effect only, several authors (e.g. [120]) follow a shorter approach by noting that the voltage difference along the surface of a wire with length ℓ can be represented as the product of the current I_0 through an impedance of resistance R_{skin} and series inductance L_{skin} :

$$I_0(R_{\text{skin}} + j\omega L_{\text{skin}}) = \ell E \quad (3.37)$$

With Ohmic law $j = \sigma E$ and the expression (Eq. 3.24) for the current, it follows directly that

$$R_{\text{skin}} = \text{Re} \left(\frac{k\ell}{2\pi a\sigma} \frac{J_0(ka)}{J_1(ka)} \right) = R_{\text{dc}} \text{Re} \left(\frac{ka}{2} \frac{J_0(ka)}{J_1(ka)} \right) \quad (3.38)$$

which is identical to Eq. 3.30. We also find

$$L_{\text{skin}} = \text{Re} \left(\frac{1}{j\omega} \frac{k\ell}{2\pi a\sigma} \frac{J_0(ka)}{J_1(ka)} \right) = R_{\text{dc}} \text{Re} \left(\frac{ka}{2j\omega} \frac{J_0(ka)}{J_1(ka)} \right) \quad (3.39)$$

Our approach has the advantage that the analysis of the proximity effect — in the following section — can be done in a similar manner. This allows for a combined analysis of the interaction of the skin effect and the proximity effect.

In practice, the skin effect is very small in deflection coils and can be neglected. For example, 17'' CMT line coils are usually wound with solid wires with a copper diameter $2a = 0.236$ mm. At a typical line frequency of 64 kHz, the skin depth $\delta = 0.26$ mm. With the low-frequency approximation, Eq. 3.35, we find that the skin effect increases the resistance by only a factor of 1.001. Even at the eighth harmonic (see Sect. 2.3.4), the resistance would only increase by a factor of 1.05. Impedance measurements (Sect. 3.6.2) show an increase which is at least an order of magnitude higher. In fact, the skin effect is negligible compared to the proximity effect.

Proximity effect

The alternating magnetic field induces eddy currents in each wire, see Fig. 3.5. This effect is called the proximity effect because in many cases the magnetic field is caused by other wires in the proximity of that wire. In a deflection yoke the total magnetic field due to all wires has to be considered.

In Appendix B the following expression is derived for the proximity loss in a wire with conductivity σ , radius a , and length ℓ with its axis perpendicular to an external varying field with amplitude H_0 and frequency ω :

$$P_{\text{prox}} = -\ell \frac{2\pi}{\sigma} H_0^2 \text{Re} \left(\frac{ka J_1(ka)}{J_0(ka)} \right) \quad (3.40)$$

in which the Bessel functions $J_0(ka)$ and $J_1(ka)$ are defined in Appendix C.

With the definition of k^2 (Eq. 3.22) and that of the skin depth δ (Eq. 3.18), the argument ka can be expressed as a simple function of the radius a of the cylinder and the skin depth δ by

$$ka = (1 - i) \frac{a}{\delta} \quad (3.41)$$

The proximity loss can then be written as

$$P_{\text{prox}} = \ell \frac{2\pi}{\sigma} H_0^2 g \left(\frac{a}{\delta} \right) \quad (3.42)$$

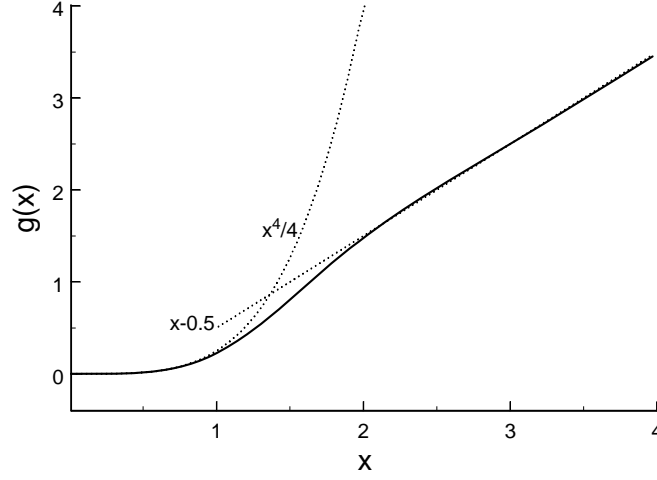


Figure 3.7: The proximity loss factor $g(x)$ and its low-frequency and high-frequency approximations as function of $x = a/\delta$.

The proximity loss function

$$g(x) = -\text{Re} \left([1 - i] x \frac{J_1([1 - i] x)}{J_0([1 - i] x)} \right) \quad (3.43)$$

is shown in Fig. 3.7.

As illustrated in Fig. 3.7 the following two approximations can be used:

$$g\left(\frac{a}{\delta}\right) \approx \frac{a}{\delta} - \frac{1}{2} \quad \text{for } a > 2\delta \quad (3.44)$$

and

$$g\left(\frac{a}{\delta}\right) \approx \frac{1}{4} \left(\frac{a}{\delta}\right)^4 \quad \text{for } a < \delta \quad (3.45)$$

Substitution of Eq. 3.18 for the skin depth δ gives

$$g\left(\frac{a}{\delta}\right) \approx \frac{1}{16} a^4 \omega^2 \sigma^2 \mu^2 \quad \text{for } a < \delta \quad (3.46)$$

If this low-frequency approximation is substituted in the expression for the dissipation (Eq. 3.42), we find

$$P_{\text{prox,lf}} = \ell \frac{\pi}{8} \sigma a^4 \omega^2 B_0^2 \quad (3.47)$$

This equation shows that, as long as the frequency is not too high:

- the proximity losses increase quadratically with the frequency of the magnetic field

- these losses can be reduced by reducing the magnetic field perpendicular to the wires or by dividing the wires into thinner wires.

If the proximity loss P_{prox} is generated by the magnetic field due to a current with amplitude I_0 , the proximity loss manifests itself as an apparent increase in resistance of the wires through which I_0 flows. We introduce the equivalent proximity resistance as

$$R_{\text{prox}} = \frac{2P_{\text{prox}}}{I_0^2} \quad (3.48)$$

so that

$$R_{\text{prox}} = \ell \frac{4\pi}{\sigma} \frac{H_0^2}{I_0^2} g\left(\frac{a}{\delta}\right) \quad (3.49)$$

For low frequencies, we find by substituting Eq. 3.46 and the expression for the skin depth (Eq. 3.18):

$$R_{\text{prox,lf}} = \ell \frac{\pi}{4} \sigma a^4 \omega^2 \frac{B_0^2}{I_0^2} \quad (3.50)$$

Clearly, the low-frequency approximation is valid as long as $a < \delta$, but it loses its validity already for slightly larger values. This can be important for non-sinusoidally varying magnetic fields such as those (saw-tooth like) in deflection coils, where according to the Fourier expansion contributions of higher frequencies can play an important role. Furthermore, the high-frequency approximation will be valid for the high-frequency oscillations to be discussed in Chapter 4.

In this thesis, we consider only eddy currents due to a magnetic field perpendicular to the wires. Kaden ([121], page 23) also calculated the dissipation in wires when the magnetic field is in parallel to the wire axis. The resulting losses are then a factor of two lower than those found in our case.

Combination of skin effect and proximity effect

As pointed out by Ferreira [122, 123] orthogonality exists between skin effect and proximity effect when the applied magnetic field due to other conductors is assumed to be uniform over the conductor cross-section. This permits decoupling of the two effects and simplifies calculation significantly. Designating the skin effect and proximity effect current densities $j_s(r, \phi)$ and $j_p(r, \phi)$, respectively, the dissipation equation (Eq. 3.26) becomes

$$P = \frac{1}{2\sigma} \int \{j_s(r, \phi) + j_p(r, \phi)\} \{j_s^*(r, \phi) + j_p^*(r, \phi)\} dV \quad (3.51)$$

When the external magnetic field is perpendicular to the conductor in the direction $\phi = 0$, the induced current $j_p(r, \phi)$ is an uneven function of ϕ :

$$j_p(r, -\phi) = -j_p(r, \phi) \quad (3.52)$$

whereas the skin current does not vary with ϕ . So it is an even function of ϕ :

$$j_s(r, -\phi) = j_s(r, \phi) \quad (3.53)$$

When carrying out the integration over ϕ in Eq. 3.51, we find canceling contributions for $+\phi$ and $-\phi$ for both the products $j_s(r, \phi)j_p^*(r, \phi)$ and $j_p(r, \phi)j_s^*(r, \phi)$. However, both the products $j_s(r, \phi)j_s^*(r, \phi)$ and $j_p(r, \phi)j_p^*(r, \phi)$ give always positive contributions. Consequently, Eq. 3.51 can be written as

$$P = \frac{1}{2\sigma} \int \{j_s(r, \phi)j_s^*(r, \phi) + j_p(r, \phi)j_p^*(r, \phi)\} dV \quad (3.54)$$

or

$$P = P_{\text{skin}} + P_{\text{prox}} \quad (3.55)$$

The dissipation P of the combined skin effect and proximity effect is simply the sum of the skin effect losses P_{skin} and the proximity effect losses P_{prox} .

3.4.3 Losses in multi-parallel solid wires

Up to now, we have only considered the eddy-current losses in a single wire. CRT deflection coils, however, are always wound with a bundle of several wires in parallel. For N_p wires in parallel, the total dissipation is N_p times the dissipation in each wire.

It is generally assumed that the parallel wires pile up more or less at random when the coils are wound, so that the individual wires carry the same current I_0/N_p and experience the same magnetic field H_0 , when I_0 denotes the amplitude of the total current and H_0 the amplitude of the magnetic field through the bundle of parallel wires.

The dc dissipation is determined by the Ohmic loss and follows from Eq. 3.11 and Eq. 3.12:

$$P_{\text{dc}} = \frac{1}{2} R_{\text{dc}} I_0^2 \quad (3.56)$$

in which the dc series resistance R_{dc} of N_p parallel wires, each with radius a and conductivity σ , is given by:

$$R_{\text{dc}} = \frac{N_{\text{turns}} \ell_{\text{turn}}}{N_p \pi a^2 \sigma} \quad (3.57)$$

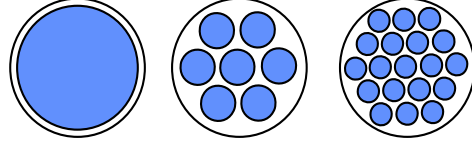


Figure 3.8: Cross-sections of a 300- μm solid wire and 7 \times 125- μm and 19 \times 71- μm litz wires.

where N_{turns} gives the number of turns and ℓ_{turn} the average length of a turn.

In a similar manner, it can be shown that the contribution to the equivalent resistance of the skin effect follows from Eq. 3.31:

$$P_{\text{skin}} = P_{\text{dc}} f_{\text{skin}}\left(\frac{a}{\delta}\right) \quad (3.58)$$

and that the losses due to the proximity effect are

$$P_{\text{prox}} = N_{\text{p}} N_{\text{turns}} \ell_{\text{turn}} \frac{2\pi}{\sigma} H_0^2 g\left(\frac{a}{\delta}\right) \quad (3.59)$$

For low frequencies, we find by substituting Eq. 3.46 and the expression for the skin depth (Eq. 3.18):

$$P_{\text{prox,lf}} = \frac{\pi}{8} N_{\text{p}} N_{\text{turns}} \ell_{\text{turn}} \sigma a^4 \omega^2 B_0^2 \quad (3.60)$$

Note that the number N_{p} of parallel wires has an opposite effect on the losses due to the skin effect and the losses due to the proximity effect. The Ohmic losses and the losses due to the skin effect are lower when more wires are used in parallel because the current through each wire is lower. The losses due to the proximity effect, however, are larger then since all wires experience the same magnetic field so that the proximity losses in each wire remains the same, independent of the number of parallel wires.

In CRT deflection coils, the number N_{p} of parallel wires cannot be chosen freely. The copper area A_{cross} of the total cross-section of the coil is determined by the available space and cannot be changed once the design of the deflection yoke is fixed. When we neglect the thickness of the insulation layers, the copper area of the cross-section is given by

$$A_{\text{cross}} = \pi a^2 N_{\text{p}} N_{\text{turns}} \quad (3.61)$$

This constraint results in the following expression for the dc resistance R_{dc} of a coil with a cross-section A_{cross} , wound with N_{turns} turns of average length ℓ_{turn} :

$$R_{\text{dc}} = \frac{\ell_{\text{turn}}}{\sigma A_{\text{cross}}} N_{\text{turns}}^2 \quad (3.62)$$

In this case the dc resistance is to first order proportional to the square of the number of turns. It is therefore also proportional to the inductance.

When we apply the same constraint to the losses due to the proximity effect (Eq. 3.59), we find:

$$P_{\text{prox}} = 2\ell_{\text{turn}} \frac{A_{\text{cross}}}{a^2\sigma} H_0^2 g\left(\frac{a}{\delta}\right) \quad (3.63)$$

showing that for a fixed cross-section, the proximity losses do not vary with the number of turns because the number of parallel wires has to be adapted accordingly.

If the low-frequency approximation Eq. 3.46 is substituted for $g(a/\delta)$, we find the following expression for the losses due to the proximity effect in wires of radius a in a fixed cross-section A_{cross} when $a < \delta$:

$$P_{\text{prox,lf}} = \frac{1}{8} \ell_{\text{turn}} A_{\text{cross}} \sigma a^2 B_0^2 \omega^2 \quad (3.64)$$

in which the constitutive relation $B_0 = \mu H_0$ is used.

3.4.4 Eddy-current losses in litz wires

The eddy currents in the wires can be reduced by using thinner wires. But then, of course, the number of parallel wires has to be increased to obtain the same cross-section of the coil. However, in the winding equipment of CRT deflection coils, the number of parallel wires is limited to about 10. Further reduction in the diameter of the copper wires can then only be handled by combining several copper wires into a litz wire [124–130], see Fig. 3.8. The main disadvantage of litz wires is that they are more expensive than solid wires. To avoid confusion in our analysis between litz wires and the separate copper wires within a litz wire, we use the following convention in the remainder of this thesis: *a wire consists of one or more copper strands surrounded by insulation, which can be handled as a single item by e.g. a winding machine.* This also applies to a solid wire.

Proximity effect in litz wires

Litz wires are introduced to reduce the losses due to the proximity effect. However, litz wires result in lower losses in a restricted frequency range only [131]. For the dc losses at low frequencies, this is quite obvious as the copper cross-section of a set of litz wires is smaller than the copper cross-section of a set of solid wires.

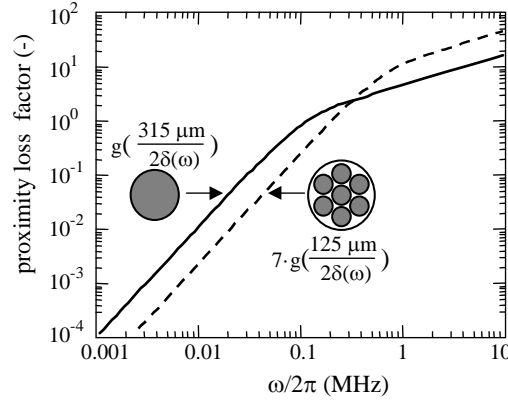


Figure 3.9: The proximity loss factor as a function of frequency for a $1 \times 315\text{-}\mu\text{m}$ solid wire and a $7 \times 125\text{-}\mu\text{m}$ litz wire assuming the same external magnetic field.

For high frequencies, we have to consider that the thicker a wire, the lower the frequency where the high-frequency approximation of the proximity loss factor is valid. The high-frequency approximation, Eq. 3.44, increases much more slowly with frequency than the low-frequency approximation Eq. 3.46. Figure 3.9 compares the proximity loss factor as a function of frequency for a $1 \times 315\text{-}\mu\text{m}$ solid wire and a $7 \times 125\text{-}\mu\text{m}$ litz wire, assuming that each strand experiences the same external magnetic field as the solid wire. For low frequencies, the proximity loss factor of the litz wire is much lower than that of the solid wire. For frequencies above 2 MHz, however, the losses in the $7 \times 125\text{-}\mu\text{m}$ litz wire are larger than the losses in the $1 \times 315\text{-}\mu\text{m}$ solid wire.

Some authors (e.g. [130, 132]) make a distinction between the internal proximity effect between the strands of a litz wire on one hand and the external proximity effect between separate litz wires on the other hand. However, in CRT deflection coils this distinction is not possible since the proximity effect is caused by the combined magnetic field of both adjacent strands and more remote strands.

The interstrand skin effect

Up to now, we have considered only eddy currents in a single copper conductor. If various copper wires run in parallel such as in litz wires, the currents through each individual copper strand can be different. The currents tend to flow more in the outer strands than in strands closer to the center of the litz wire.

This so-called interstrand skin effect is similar to the skin effect in a single

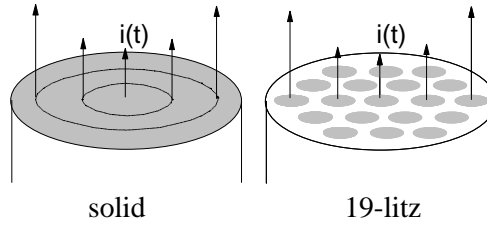


Figure 3.10: Interstrand skin effect across the whole litz wire.

solid wire. As illustrated in Fig. 3.10, a solid wire can be considered as a bunch of strands that are packed together very closely. In a stranded litz wire, the currents through the parallel strands flow as if they were part of a solid wire [133], see Fig. 3.10. In fact, this effect already occurs for a set of three parallel wires, as explained by Casimir [115].

The interstrand skin effect can be reduced by using twisted litz rather than stranded litz. In stranded litz, the outer copper strands change positions but remain on the outside for the entire length of the wire. In twisted litz, the positions of the copper strands in the litz wire are changed in such a way that within some length each strand can be found at any position in the cross-section.

The disadvantage of a twisted litz, however, is that it requires more space. To interchange a strand near the axis of the wire with a strand at the outside, it is necessary to increase the distances between the strands locally. This would make the wire thicker at that position than at other positions unless a thick insulation layer would be applied. Another alternative would be to make the distances between the strands larger than the thickness of the strands. Both options would result in an unacceptable increase in thickness of the coils.

Another disadvantage of twisted litz is that it is more expensive than stranded litz. For these reasons, stranded litz is used rather than twisted litz in modern deflection yokes.

The impact of the interstrand skin effect on the dissipation depends on the ratio between the current through the wires and the magnetic field through the wires. So, this ratio depends on the geometry of the coils. It determines whether the interstrand skin effect or the proximity effect dominates the dissipation.

3.4.5 Dielectric losses

In addition to the losses in the conductive parts of the deflection yoke, dielectric losses in non-conductive parts also contribute to the total dissipation.

pation; for instance in the insulating layers of the coil wires. The behavior of dielectrics is described by the permittivity ϵ in Maxwell's equations. In the general characterization of lossy dielectrics, a complex permittivity is introduced [132]:

$$\epsilon = \epsilon' - i\epsilon'' \quad (3.65)$$

A detailed description of the various phenomena that contribute to the dielectric losses is presented by Murphy [134–136]. More concise discussions can be found in most textbooks on dielectrics [137–139]. The simplest phenomenological model is that a part of the polarization reacts with some delay to changes in the field intensity due to some relaxation processes such as electronic or atomic displacement and rotation.

In practice, this simple relaxation model is too simple and experimental values for ϵ' and ϵ'' are used. Often, the ratio of ϵ'' and ϵ' is denoted as $\tan \delta$:

$$\tan \delta_\epsilon = \epsilon''/\epsilon' \quad (3.66)$$

where also $\tan \delta_\epsilon$ can vary with the frequency. The relaxation effect results in a phase shift δ_ϵ between the field strength and the dielectric displacement. This phase shift corresponds to certain losses, the dielectric losses, and therefore δ_ϵ is called the loss angle.

Usually, $\tan \delta_\epsilon$ is measured on separate samples of the dielectric material. Rather than taking the geometry of the dielectric material into account, simply the capacitance C is measured. Measurements taken on most dielectrics show that in a wide frequency band $\tan \delta_\epsilon$ is only weakly dependent on the frequency [140].

An alternative to the complex permittivity is to model the dielectric losses by a (frequency-dependent) resistance R_ϵ in parallel to the capacitance, with the value

$$R_\epsilon = \frac{1}{\omega C \tan \delta} \quad (3.67)$$

Practical values for CRT deflection coils are $C = 50$ pF and $\tan \delta_\epsilon = 10^{-3}$. For a 84 kHz line frequency, $R_\epsilon = 1/(2\pi \cdot 84 \cdot 10^3 \cdot 50 \cdot 10^{-12} \cdot 10^{-3}) = 4 \cdot 10^7 \Omega$. This value is much higher than the highest value of the real part of the impedance of the line coils below 10 MHz. This indicates that the dielectric losses are negligible compared to the total losses in a deflection yoke. Increasing the dielectric losses is therefore a method to damp electromagnetic oscillations in the coils. This will be discussed in the next chapter.

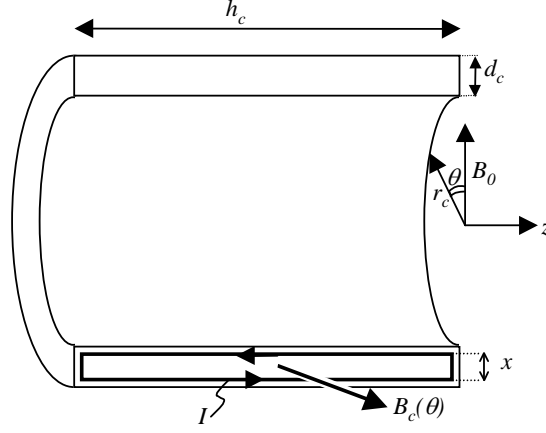


Figure 3.11: Simplified geometry of the ferrite core to estimate the eddy current loss in the ferrite core.

3.4.6 Eddy-current losses in the ferrite core

In this section we show that the dissipation due to eddy currents in the ferrite core can be neglected because of the high resistance of the ferrite material.

A detailed analysis would be quite cumbersome due to the complicated shape of the ferrite core and the non-uniformity of the magnetic flux inside. Therefore, we follow a very simple model and apply the low-frequency approximation of Sect. 3.4.2 to estimate the losses.

We model the ferrite core as a cylinder with height h_c , inner radius r_c and thickness d_c , as shown in Fig. 3.11. We assume that the height of the cylinder is much larger than its thickness. Furthermore, we assume a dipole magnetic field in the deflection area perpendicular to the axis of the ferrite core. The amplitude of the magnetic flux $B_c(\theta)$ inside the ferrite core then varies with the cosine of the angle θ to the direction of the magnetic field in the deflection area:

$$B_c(\theta) = B_c \cos \theta \quad (3.68)$$

To simplify the calculations, we take $B_c(\theta)$ uniform across the thickness d_c of the ferrite core.

The magnetic flux varies in time. For simplicity, we assume that the induced current flows along nested rectangles. Consider such a rectangle at distance $x/2$ from the center of the ferrite shell (see Fig. 3.11). The area enclosed by the rectangle is approximately $h_c x$. According to Faraday's law, the alternating magnetic flux through this area induces a voltage

$$V_{\text{ind}}(t) = \omega B_c(\theta) h_c x \sin \omega t \quad (3.69)$$

The current dI in a volume element around the rectangle with length h_c , width $r_c d\theta$, thickness dx and conductance σ is given by

$$dI(t) = \frac{\sigma r_c d\theta dx}{2h_c} V_{\text{ind}}(t) \quad (3.70)$$

Subsequently, the dissipation $dP(t) = V_{\text{ind}}(t)dI(t)$ in this volume element is given by

$$dP(t) = V_{\text{ind}}^2(t) \frac{\sigma r_c}{2h_c} d\theta dx = \frac{1}{2} \sigma r_c \omega^2 h_c x^2 B_c^2 \cos^2 \theta \sin^2 \omega t d\theta dx \quad (3.71)$$

The time average of $\sin^2 \omega t$ equals $\frac{1}{2}$. The total dissipation $P_{\text{c,eddy}}$ due to eddy currents in the ferrite core is found by substituting $V_{\text{ind}}(t)$ and integrating x from 0 to d_c and θ from 0 to 2π :

$$P_{\text{c,eddy}} = \frac{\pi}{12} \sigma r_c \omega^2 B_c^2 h_c d_c^3 \quad (3.72)$$

Substituting practical values $\sigma = 1 \text{ } \Omega\text{m}$, $\omega/2\pi = 69 \text{ kHz}$, $h_c = 5 \text{ cm}$, $d_c = 7 \text{ mm}$, $r_c = 3 \text{ cm}$, $B_c = 25 \text{ mT}$ yields $P_{\text{c,eddy}} = 16 \text{ mW}$. This is indeed negligible compared to the total dissipation found in the deflection yoke.

3.4.7 Magnetic power loss in the ferrite core

In modern deflection yokes, the ferrite cores usually consist of a soft ferrite material like 3C2 ($\text{MnZnFe}_2\text{O}_4$) and 2A2 ($\text{MgZnFe}_2\text{O}_4$) which have a large saturation induction, a small coercive force, a large initial permeability, a large maximum permeability, and small magnetic power loss [141, 142].

The magnetic power loss, excluding the eddy-current loss, depends on both the amplitude $|B_c|$ of the flux density in the ferrite core and the line frequency ω_ℓ . Steinmetz [143] proposed the following empirical formula for the magnetic power loss p_{magn} per unit volume:

$$p_{\text{magn}} = k_m \omega_\ell^\eta |B_c|^\xi \quad (3.73)$$

The proportionality factor k_m varies strongly with the temperature T . For practical conditions of deflection yokes ($10 \text{ mT} < |B_c| < 100 \text{ mT}$, $10 \text{ kHz} < \omega_\ell/2\pi < 100 \text{ kHz}$, $25 \text{ }^\circ\text{C} < T < 100 \text{ }^\circ\text{C}$), $\xi = 2.8$ for MnZn ferrites (e.g. 3C2) and $\xi = 2.0$ for MgZn ferrites (e.g. 2A2). For both ferrite types, $\eta = 1.1$.

For sine wave signals in 3C2 ferrite, $k_m = 0.31 \text{ kJs}^{0.1}\text{T}^{-2.8}\text{m}^{-3}$ (measured at $\omega_\ell/2\pi = 100 \text{ kHz}$, $B_c = 20 \text{ mT}$ and $T = 85 \text{ }^\circ\text{C}$ [144]). In practice, the sinusoidal data is also applied to saw-tooth shaped signals, simply by substituting the

line frequency in the Steinmetz equation. It is observed that for a typical ferrite the dissipation depends primarily on the total peak-to-peak excursion of the flux density and only to a minor extent on the waveform or its symmetry [142]. The resulting estimates of magnetic losses are generally sufficiently accurate.

The magnetic power loss of the entire ferrite core is calculated by integrating p_{magn} over the volume of the material. In cylindrical coordinates (r, θ, z) this yields

$$P_{\text{core}} = k_m \omega_\ell^\eta \iiint |B_c(r, \theta, z)|^\xi r d\theta dr dz \quad (3.74)$$

Figure 2.3 presents a simple model to calculate the loss in a round ferrite core. We assume that the flux density does not vary across the wall thickness, although we know that this assumption is not valid [145]. A simple dipole field results in an amplitude $B_c(r, \theta, z)$ of the flux density which varies along the circumference with the angle θ , according to

$$B_c(r, \theta, z) = \left| \hat{B}_c(z) \cos \theta \right| \quad (3.75)$$

in which the maximum flux density $\hat{B}_c(z)$ follows from the conservation of flux

$$r_c(z) B_0(z) = d_c(z) \hat{B}_c(z) \quad (3.76)$$

in which $r_c(z)$ denotes the inner radius of the ferrite core, $d_c(z)$ the difference of the outer and inner radius of the ferrite core, and $B_0(z)$ the flux density in air at position z . The flux density is assumed to be constant along the $\theta = 0$ plane. Substitution of Eqs 3.75 and 3.76 in Eq. 3.74 yields

$$P_{\text{core}} = \omega_\ell^\eta k_m \iiint \left| \frac{r_c(z)}{d_c(z)} B_0(z) \cos \theta \right|^\xi r d\theta dr dz \quad (3.77)$$

In CMTs, usually 3C2 ferrite cores are used. Practical values for a 17" CMT are $B_0 = 5$ mT, $r_c = 3$ cm, $h_c = 5$ cm, and $d_c = 7$ mm. For 69 kHz this results in an estimate for the magnetic power loss in the ferrite core of $P_{\text{core}} = 1$ Watt.

3.5 Dissipation for non-sinusoidal signals

Up to now we have considered only the dissipation for sine wave signals, but actually the currents and hence the magnetic fields in CRT deflection coils

vary in a more complicated manner in time. In general, the dissipation of the deflection coils can be calculated by multiplying the current $i(t)$ and voltage $v(t)$ of the coil during operation and averaging this over the period T of the signal:

$$P = \frac{1}{T} \int_0^T i(t)v(t)dt \quad (3.78)$$

3.5.1 Dissipation due to the frame current

The frame current is described accurately by a simple saw-tooth signal. The resistance of the frame coil equals its dc-resistance R_{frame} for practical frame frequencies (50-100 Hz). Consequently, the voltage $v(t)$ across the frame coil is simply the product of the frame current and R_{frame} . For an ideal saw-tooth current with amplitude i_{frame} , it follows from Eq. 3.78 that the dissipation is given by

$$P_{\text{frame}} = \frac{1}{3} R_{\text{frame}} i_{\text{frame}}^2 \quad (3.79)$$

3.5.2 Dissipation due to the line current

The line frequency is much higher than the frame frequency; typically it is 16 kHz for television applications and 64 kHz for computer monitors. At these frequencies, the ac resistance can no longer be neglected.

The dissipation for non-sinusoidal but repetitive signals can be calculated from the amplitudes of the Fourier components of the line current [146, 147]. In this Fourier analysis we assume that the set of voltages and currents is linear and we thus neglect the non-linear effects such as the hysteresis loss.

If the repetition frequency is ω_ℓ , both current and voltage are expanded in Fourier series [148]:

$$i(t) = I_0 \sum_{n=1}^{\infty} a_n \sin n\omega_\ell t \quad (3.80)$$

$$v(t) = I_0 \sum_{n=1}^{\infty} a_n R(n\omega_\ell) \sin n\omega_\ell t + I_0 \omega_\ell \sum_{n=1}^{\infty} n a_n L(n\omega_\ell) \cos n\omega_\ell t \quad (3.81)$$

where we wrote the impedance of the coils at frequency $n\omega_\ell$ as the sum of a frequency-dependent resistance $R(n\omega_\ell)$ and the reactance of a frequency-dependent inductance $L(n\omega_\ell)$.

With the orthogonality relations

$$\int_0^{2\pi} \sin n\phi \sin m\phi d\phi = \begin{cases} \pi & \text{if } m = n \\ 0 & \text{if } m \neq n \end{cases} \quad (3.82)$$

and

$$\int_0^{2\pi} \sin n\phi \cos m\phi d\phi = 0 \quad (3.83)$$

Eqs. 3.78, 3.80 and 3.81 are combined into

$$P = \frac{1}{2} I_0^2 \sum_{n=1}^{\infty} a_n^2 R(n\omega_\ell) \quad (3.84)$$

It is convenient to express the resistance $R(n\omega_\ell)$ as the sum of a dc and an ac part:

$$R(n\omega_\ell) = R_{\text{dc}} + R_{\text{ac}}(n\omega_\ell) \quad (3.85)$$

with $R_{\text{ac}}(0) = 0$. The dissipation can then be written as the sum of the dissipation in the dc resistance and the dissipation in the ac resistance:

$$P = P_{\text{dc}} + P_{\text{ac}} \quad (3.86)$$

with

$$P_{\text{dc}} = \frac{1}{2} I_0^2 R_{\text{dc}} \sum_{n=0}^{\infty} a_n^2 \quad (3.87)$$

and

$$P_{\text{ac}} = \frac{1}{2} I_0^2 \sum_{n=1}^{\infty} a_n^2 R_{\text{ac}}(n\omega_\ell) \quad (3.88)$$

To determine the dissipation, both the amplitude and the Fourier coefficients of the drive current are needed. The amplitude can be measured easily with a current probe. The Fourier coefficients could be determined by sampling the current and by applying a (Fast) Fourier Transform. However, this is not very convenient in practice and usually only the current amplitude is measured while the Fourier coefficients are derived from the theoretical description of the frame signal and the line signal given in Sect. 2.3.2 and Sect. 2.3.4.

Measuring method

The frequency-dependent resistance is most easily determined by measuring the impedance $Z(\omega)$ of the line coils as a function of frequency ω with an impedance analyzer. However, such an impedance characteristic shows a large resonance peak due to the parasitic capacitance between the line-coil wires. In Chapters 4 and 5 we will analyze these distributed capacitances in much more detail, but already in this section we need to consider this capacitance as it would lead to significantly larger values of the dissipation.

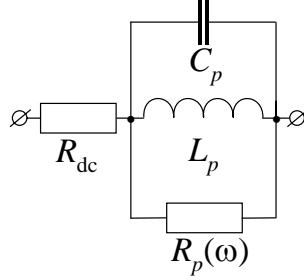


Figure 3.12: To first order, the distributed capacitances between the wires can be modeled by a capacitance C_p parallel to the line coil inductance L_p and a frequency-dependent resistance $R_p(\omega)$.

To first order, the distributed capacitances between the wires are modeled by a capacitance C_p parallel to the line coil inductance L_p and a frequency-dependent resistance $R_p(\omega)$, as shown in Fig. 3.12. In Chapter 4, we will show that also measurements at higher frequencies can be adequately fitted by this lumped RCL model.

The impedance $Z(\omega)$ of this lumped model in series with the dc resistance R_{dc} is given by

$$Z(\omega) = R_{dc} + \left[\frac{1}{R_p(\omega)} + \frac{1}{j\omega L_p} + j\omega C_p \right]^{-1} \quad (3.89)$$

Consequently, the equivalent parallel resistance is easily calculated from the measured impedance values:

$$R_p(\omega) = \left[\operatorname{Re} \left(\frac{1}{Z(\omega) - R_{dc}} \right) \right]^{-1} \quad (3.90)$$

Note that we have put R_{dc} outside the parallel RCL branch. In fact, from a physical point of view we could also have put it in series with the inductance such that C_p would be in parallel to the series arrangement of L_p and R_{dc} . Both models give a good fit of the experimental results, but with R_{dc} outside the parallel RCL branch, our analytical analysis results in more compact expressions.

When we replace the simple coil inductance in the drive circuit of the line coil, shown in Fig. 2.7, by this lumped RCL model, it is clear that the lumped capacitance C_p is in parallel to the flyback capacitance in this circuit. It is therefore sufficient to consider only the current through the inductance L_p . If the current through L_p is a sine wave with frequency ω , the dissipation in the parallel resistance $R_p(\omega)$ is the same as when the current flows through a

line-coil wires		$2a$	$2r_o$
dimensions	type	(μm)	(μm)
19×71 μm	litz	71	433
7×100 μm	litz	100	375
7×125 μm	litz	125	450
236 μm	solid	236	284
280 μm	solid	280	333
300 μm	solid	300	353
315 μm	solid	315	370
355 μm	solid	355	413

Table 3.1: Nominal copper diameters ($2a$) and overall diameters ($2r_o$) of several wire types used in the experiments. The notation 19×71 μm refers to a litz wire with 19 strands of 71- μm diameter each.

simple frequency-dependent resistance $R_{ac}(\omega) = (\omega L_p)^2 / R_p(\omega)$. Substitution of Eq. 3.90 yields

$$R_{ac}(\omega) = (\omega L_p)^2 \operatorname{Re} \left(\frac{1}{Z(\omega) - R_{dc}} \right) \quad (3.91)$$

With Eq. 3.88, this enables us to calculate the dissipation from the measured impedances.

The magnetic field of the line coils does not only generate losses in the line-coil wires, but also in the frame-coil wires. With the measurement method described above, we find the total sum of all these losses. To determine e.g. the eddy-current losses in the frame coils only, we measure the total dissipation with and without frame coils. The eddy-current loss in the frame coils is obtained by subtracting the dissipation of the deflection yoke without frame coils from the dissipation of the deflection yoke with frame coils.

3.6 Experimental results

To validate the theory on the dissipation of CRT deflection coils presented in the previous sections of this chapter, a number of experiments have been carried out. In each experiment, a set of deflection yokes has been made with different wire types. Table 3.1 lists the copper diameter and the overall outer diameter of the different wire types that we used in our experiments.

The geometry of each coil was kept the same when changing the wire type by adjusting the number of parallel wires in such a way that the coil

line coil wire	frame coil wire	line		frame		total
		P_{dc} (W)	P_{ac} (W)	P_{dc} (W)	P_{ac} (W)	P_{tot} (W)
$6 \times 300 \mu\text{m}$	$4 \times 300 \mu\text{m}$	2.5	23.3	1.3	14.6	41.6
$5 \times (7 \times 125 \mu\text{m})$	$3 \times (7 \times 125 \mu\text{m})$	2.6	7.1	1.2	2.7	13.6
$5 \times (19 \times 71 \mu\text{m})$	$3 \times (19 \times 71 \mu\text{m})$	2.9	4.3	1.6	0.7	9.4

Table 3.2: Dissipation in line and frame coils of a 15" CMT deflection yoke for various wire types, calculated from the measured impedance characteristic. Each line coil has 49 turns; each frame coil has 106 turns. The line frequency is 125 kHz.

volume remained about the same. In this way the magnetic field is the same throughout the coils and differences in dissipation can be only accounted for by the changes in the type of wire. The measurements were repeated on identical deflection yokes from which the frame coils were removed. The dissipation of each deflection yoke was determined with Eq. 3.87, Eq. 3.88 and Eq. 3.79 from the measured dc resistance of the pair of frame coils and from the measured impedance characteristic of the pair of line coils.

First the dissipation of set of 15" CMT deflection yokes was determined. The results are briefly described in Section 3.6.1. Since the results cannot be directly understood from the theory, a more elaborate series of experiments was carried out with a set of 17" CMT deflection yokes. The results are presented and analyzed in Sect. 3.6.2. The reason for changing from 15" CMT to 17" CMT was simply the availability of winding equipment in our laboratory.

3.6.1 15" CMT deflection yokes

A number of 15" CMT deflection yokes were manufactured that differed in wire type only [49]. The three wire types of Fig. 3.8 have been used in both line and frame coils. The first one is a 300- μm solid wire and the others are 7 \times 125- μm and 19 \times 71- μm litz wires. The notation 5 \times (7 \times 125- μm) indicates that the coils are wound with five litz wires that consists of seven copper strands of 125- μm diameter each. In a similar way, 6 \times 300- μm refers to six parallel wires, each with a single copper strand of 300- μm diameter. We will use this notation in the remainder of this thesis.

The impedance characteristics have been measured for all the prototypes with a HP 4192A LF Impedance Analyzer. The dissipation values at $\omega_\ell/2\pi=125$ kHz, calculated from the impedance measurements, are summarized in Table 3.2.

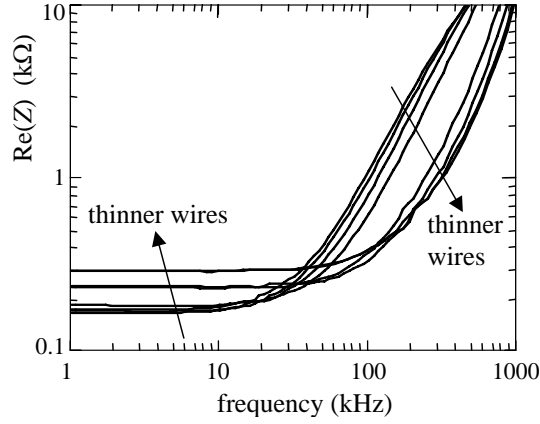


Figure 3.13: The real part of the measured impedance characteristic of the 17" CMT line-coil pairs (with ferrite core) for the wire types listed in Table 3.1.

If we assume, to first order, that the cross-section of the coils remains the same for the three types of wire, the low-frequency proximity loss model (Eq. 3.64) predicts that the ac losses scale with the square of the wire diameter. Indeed the ac losses in the frame coil scale roughly with the square of the wire diameter. However, the ac losses in the line coil are reduced much less at the smaller diameters than expected from the proximity loss model. Whereas this model predicts a dissipation reduction by a factor of $(125/71)^2 = 3.1$ when the $7 \times 125\text{-}\mu\text{m}$ litz is replaced by the $19 \times 71\text{-}\mu\text{m}$ litz wire, the ac losses in the line coils are reduced by only a factor of $7.1/4.3 = 1.7$. This indicates that the ac losses in the line coil are not merely proximity losses. Since this finding is in contrast to our expectations, we will analyze the dissipation in the line coils in more detail.

3.6.2 17" CMT line-coil pairs

To study the dependence of the dissipation on the choice of line-coil wires in more detail, 17" CMT deflection yokes were made without frame coils. So, the samples consisted of a pair of line coils and a 3C2 ferrite core. The line coils were connected in parallel as in normal 17" CMT products. Their geometry was identical to normal production coils.

Table 3.1 lists the copper diameter and the overall outer diameter of the seven different wire types that we used in our experiments. The number of wires in parallel has been adjusted to keep the coil volume about the same. This was necessary to keep the geometry of the coils the same.

line-coil wires	a (μm)	N_p (-)	L (μH)	R_{dc} ($\mu\Omega$)	β ($10^{-12} \Omega s^2$)
$5 \times (19 \times 71 \mu\text{m})$	35.5	95	123.9 ± 1.3	284 ± 4	8 ± 2
$8 \times (7 \times 100 \mu\text{m})$	50.0	56	122.5 ± 0.4	228 ± 3	11 ± 3
$5 \times (7 \times 125 \mu\text{m})$	62.5	35	122.7 ± 0.2	231 ± 4	13 ± 4
$13 \times 236 \mu\text{m}$	118.0	13	122.7 ± 0.7	182 ± 9	40 ± 3
$10 \times 280 \mu\text{m}$	140.0	10	124.2 ± 0.5	167 ± 3	57 ± 3
$8 \times 315 \mu\text{m}$	157.5	8	123.8 ± 0.5	163 ± 3	70 ± 4
$6 \times 355 \mu\text{m}$	177.5	6	123.3 ± 1.0	171 ± 5	80 ± 2

Table 3.3: Results of fitting $Z(f) = R_{dc} + \beta f^2 + j2\pi fL$ to the measured impedance characteristic of 17" CMT line-coil pairs with various wire types at 20°C. For each coil the number of turns is 38. The number of parallel wires is adapted to keep the same coil volume. The coils are fixed in a deflection unit with a 3C2 yoke ring, but without frame coils. The spread is three times the standard deviation calculated from measuring five identical samples.

For each wire type, five identical stripped deflection yokes were made consisting of a line-coil pair, fitted in a plastic frame and a regular 3C2 ferrite core. By repeating the measurements on the five identical samples, the measuring spread could be determined experimentally.

Experimental results

Figure 3.13 shows the real part of the measured impedance characteristic of the 17" CMT line-coil pairs (with the ferrite core) for the wire types listed in Table 3.1. For frequencies below 1 kHz, this real part of the impedance is equal to the dc resistance within the measuring accuracy. For frequencies above 10 kHz the real part of the impedance increases rapidly with frequency due to eddy-current losses. The imaginary part is fully determined by the inductance according to $\text{Im}(Z(\omega)) = \omega L$ for frequencies up to a few hundred kHz. Both the real part and the imaginary part change rapidly with frequencies above 1 MHz due to resonance between the inductance and capacitances of the coil windings. For dissipation, only frequencies up to 1 MHz are of interest since the harmonics of the line-scan current at higher frequencies are very small (see Table 2.1). The effects at higher frequencies will be studied in more detail in Chapters 4, 5 and 6.

For frequencies below 10 kHz the resistance decreases with the copper diameter because thicker copper wires have relatively less insulating material

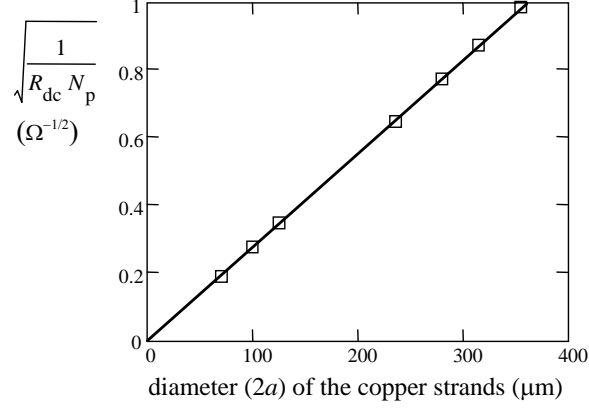


Figure 3.14: The measured dc resistance of the line-coil pairs as a function of the radius of the copper wires.

so that more copper is put in the same coil volume. For frequencies above 100 kHz the resistance increases with the copper diameter because the eddy-current losses increase rapidly with the copper diameter.

From the impedance characteristics, a number of key parameters can be determined, such as the inductance L and the dc resistance R_{dc} . The experimental results are presented in Table 3.3. In the first three columns, the composition of the wire bundle is given. For instance, a $5 \times (19 \times 71 \mu m)$ bundle consists of $N_p = 5 \times 19 = 95$ parallel copper strands, each with radius $a = 35.5 \mu m$. In the last three columns, the experimental results are listed with a spread of three times the standard deviation calculated from the experimental results from five identical samples. As expected the inductance L hardly changes when the wire type is changed since coil shape and number of turns are kept the same.

If the measured values of the dc resistances, R_{dc} in Table 3.3, are multiplied by the number of parallel copper strands N_p , the resistance $R_{dc} N_p$ per strand is obtained. Figure 3.14 shows that $\sqrt{1/R_{dc} N_p}$ increases linearly with the diameter $2a$ of a strand. Consequently, the dc resistance ($R_{dc} N_p$) per strand decreases quadratically with the diameter of the strand, as expected. The total dc resistance of the line-coil pairs, wound with N_p parallel copper strands of radius a , was therefore described by Eq. 3.12:

$$R_{dc} = \frac{N_{turns} \ell_{turn}}{N_p \pi a^2 \sigma} \quad (3.92)$$

with $\ell_{turn} = 15.6$ cm, using $\sigma = 5.8 \cdot 10^7 \Omega^{-1} m^{-1}$ and $N_{turns} = 38$.

For relatively low frequencies (below 150 kHz), the real part of the

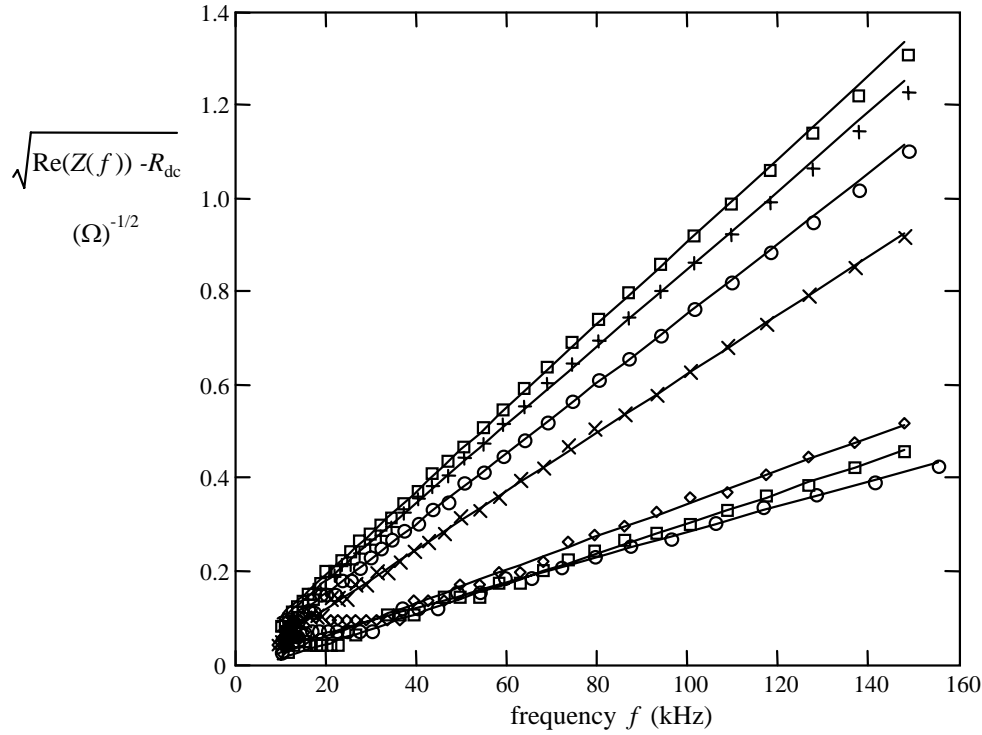


Figure 3.15: The increase in resistance as a function of frequency of the 17" CMT line-coil pairs for various wire types at 20°C; from top to bottom: 6×355 μm (\square), 8×315 μm (+), 10×280 μm (\circ), 13×236 μm (\times), 5×(7×125 μm) (\diamond), 8×(7×100 μm) (\square) and 5×(19×71 μm) (\circ).

impedance increases quadratically with frequency. For our set of 17" CMT coils, the experimental results are shown in Fig. 3.15. This shows how $\sqrt{\text{Re}(Z(f)) - R_{\text{dc}}}$, i.e. the square root of the increase in the real part of the impedance, varies with the frequency f for various types of line-coil wires. The lines show the least-squares fit with

$$\text{Re}(Z(f)) = R_{\text{dc}} + \beta f^2 \quad (3.93)$$

The fitting coefficients β are listed in Table 3.3.

Since we expected β to increase with $N_p a^4$ (Eq. 3.50 for proximity losses), we have tried to fit the data to $N_p a^4$. Note that although we have adjusted the number of parallel wires to keep the cross area of the coil and hence $N_p a^2$ about the same, a slight variation in $N_p a^2$ was inevitable due to the amount of insulating material which is larger when thinner wires are used.

As shown in Fig. 3.16, the results for the four solid wires could indeed be

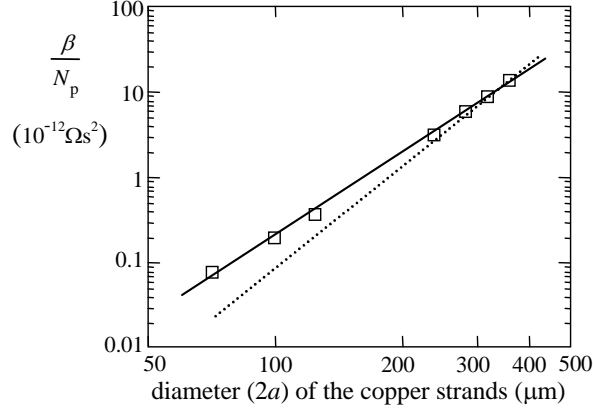


Figure 3.16: The coefficient β (squares) found from impedance measurements on 17'' CMT coils with 7 different wire types. The dotted line $\beta/N_p = 1.52 \cdot 10^{-8} a^4$ is fitted to the four upper measuring points. To fit all seven measuring points, a different (solid line) $\beta/N_p = 16.0 \cdot 10^{-12} a^{3.23}$ had to be used.

fitted adequately by

$$\beta_{\text{solid}} = 1.52 \cdot 10^{-8} N_p a^4 \quad (3.94)$$

However, the losses in the three samples with litz wires - as expressed by the coefficient β - are larger than expected from the results found with the samples with solid wires when assuming a $\beta \propto N_p a^4$ proportionality. As shown in Fig. 3.16 the coefficients β of all our samples are fitted by

$$\beta = 16 \cdot 10^{-12} N_p a^{3.23} \quad (3.95)$$

in which the radius a of the copper strands is given in meters. This confirms the results for the 15'' CMT samples, as it shows that the dissipation does not increase with $N_p a^4$, i.e. with a^2 when N_p is adjusted ($\propto a^{-2}$) to maintain a constant area of the cross-section of the coil. The dependence of the dissipation on the wire radius is much weaker than expected from theory.

Analysis

In order to explain this unexpected result we revert to the detailed analysis of the proximity effect in Sect. 3.4. Rather than using the limiting case of the low-frequency approximation, we revert in this analysis to the full frequency dependence as described by the proximity loss function.

As a first step, we have fitted this proximity loss function $g(a/\delta(f))$, defined by Eq. 3.43 as a function of the copper radius a and the skin depth

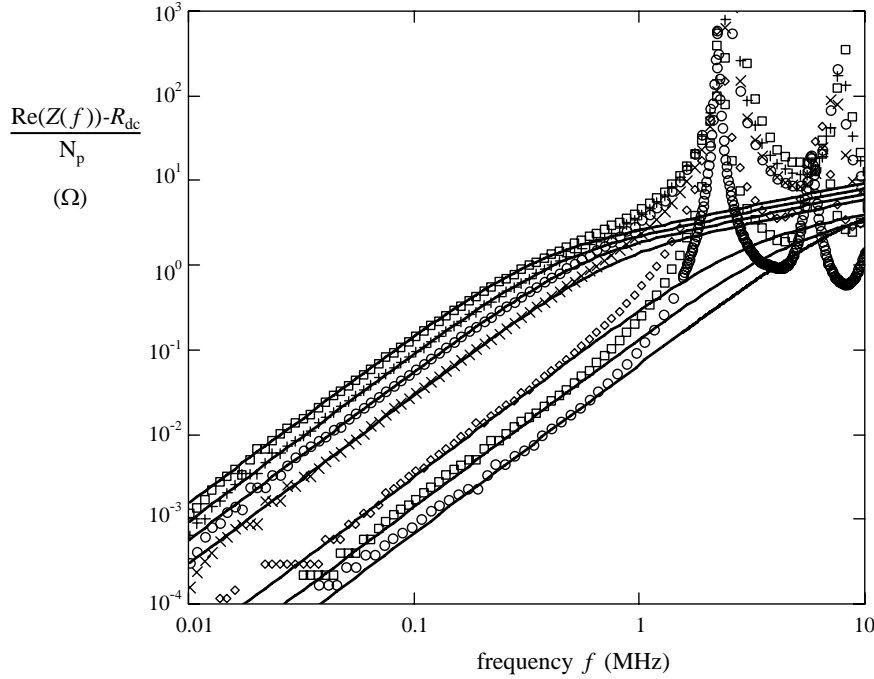


Figure 3.17: The increase in resistance as a function of frequency of the 17'' CMT line-coil pairs for various wire types. The different symbols mark the measuring results for different wire types; from top to bottom: $6 \times 355 \mu\text{m}$ (\square), $8 \times 315 \mu\text{m}$ ($+$), $10 \times 280 \mu\text{m}$ (\circ), $13 \times 236 \mu\text{m}$ (\times), $5 \times (7 \times 125 \mu\text{m})$ (\diamond), $8 \times (7 \times 100 \mu\text{m})$ (\square) and $5 \times (19 \times 71 \mu\text{m})$ (\circ). The solid lines represent the proximity loss function $g(a/\delta(a))$ multiplied by a fitting constant $c_{\text{prox}}(a)$ for each wire radius a .

δ (Eq. 3.18), to the increase in the resistive part of the impedance $Z_a(f)$ for each used value of a :

$$\text{Re}(Z_a(f)) = R_{\text{dc}}(a) + c_{\text{prox}} N_p g\left(\frac{a}{\delta(f)}\right) \quad (3.96)$$

Note that c_{prox} is related to β found in the previous section. Using the low-frequency approximation $g(a/\delta) = \frac{1}{4}(a/\delta)$ (Eq. 3.50) and Eq. 3.18 for the skin depth δ it is easy to show that

$$c_{\text{prox}} = \frac{4}{\pi^2 \mu^2 \sigma^2 a^4} \beta \quad (3.97)$$

Figure 3.17 shows the measured increase in resistance per copper strand as a function of frequency up to 10 MHz. The solid lines show $c_{\text{prox}} g(a/\delta(f))$ for the seven wire types. The proximity loss function was calculated from Eq. 3.43

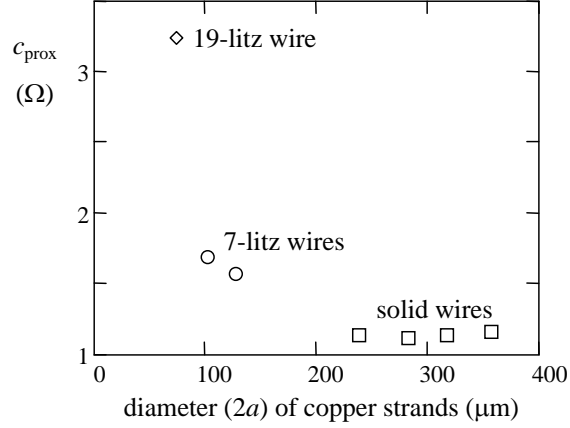


Figure 3.18: The ratio c_{prox} with which the proximity loss function $g(a/\delta(f))$ is fitted to the resistive part of the impedance characteristic, for various diameters ($2a$) of the copper strands. The squares indicate the results for the solid wires, the circles those of the 7-litz and the diamond the result for the 19-litz wires.

and depends only on the radius a of the copper strands. Because the figure has logarithmic scales, multiplication by c_{prox} corresponds to a shift in vertical direction. The values for c_{prox} were chosen so that $c_{\text{prox}}g(a/\delta(f))$ fitted the experimental results for frequencies below 200 kHz. At higher frequencies, resonances result in higher values of the impedance. These resonances will be analyzed in more detail in Chapter 4.

The values for c_{prox} found from this fitting process can be expected to depend on the amplitude $H_0(x)$ of the magnetic field along the wires. If x denotes the length from the start of a wire, we expect from our theoretical analysis (Eq. 3.49) that

$$c_{\text{prox}} = \ell \frac{4\pi}{\sigma} \frac{\int \{H_0(x)\}^2 dx}{I_0^2} \quad (3.98)$$

Figure 3.18 shows that for the four solid wires, with diameter $2a > 200 \mu\text{m}$, the fitting factor c_{prox} is approximately constant. This is consistent with the theory on proximity losses and the $\beta \propto N_p a^4$ proportionality. However, for the litz wires, c_{prox} turns out to be much larger and varies with the diameter $2a$ of the copper strands. This is not predicted by Eq. 3.98 when we use the assumption of Sect. 3.4 that the magnetic flux density through the copper strands does not depend on the diameter of a copper strand. Clearly, this assumption is not valid.

line-coil wires	a (μm)	N_p	$R_{\text{dc}}(100^\circ\text{C})$ ($\mu\Omega$)	$\beta_{100^\circ\text{C}}$ ($10^{-12} \Omega s^2$)
$5 \times (19 \times 71 \mu\text{m})$	35.5	95	373 ± 8	10 ± 2
$8 \times (7 \times 100 \mu\text{m})$	50.0	56	296 ± 3	13 ± 4
$5 \times (7 \times 125 \mu\text{m})$	62.5	35	302 ± 6	15 ± 5
$13 \times 236 \mu\text{m}$	118.0	13	247 ± 4	34 ± 3
$10 \times 280 \mu\text{m}$	140.0	10	218 ± 3	50 ± 4
$8 \times 315 \mu\text{m}$	157.5	8	215 ± 8	59 ± 4
$6 \times 355 \mu\text{m}$	177.5	6	223 ± 6	63 ± 9

Table 3.4: Results of fitting $\text{Re}(Z(f)) = R_{\text{dc}}(100^\circ\text{C}) + \beta_{100^\circ\text{C}} f^2$ to the measured impedance characteristic of 17'' CMT line coil pairs with various wire types at 100°C . For each coil the number of turns is 38.

Temperature dependence

Furthermore, we have repeated the impedance measurements on the same 17'' CMT samples at a higher temperature (100°C). The idea behind this measurement is that for frequencies between 20 kHz and 1 MHz the eddy current effects for thin wires ($< 125 \mu\text{m}$) are in the low-frequency range ($a < \delta$), while they are in the high-frequency range ($a > 2\delta$) for the bundle diameter (which we estimated to be $900 \mu\text{m}$).

The dependence of the losses - and of the corresponding resistances - is different in the low-frequency range from that in the high-frequency range. The theory in Sect. 3.4.2 showed that in the low-frequency range (where $a < \delta$) the equivalent resistances due to the proximity effect and the skin effect are proportional to the conductivity σ and hence inversely proportional to the temperature T (see Eqs. 3.13, 3.35, 3.50):

$$\begin{aligned} R_{\text{prox,lf}} &\propto \sigma \propto T^{-1} \\ R_{\text{skin,lf}} &\propto \sigma \propto T^{-1} \end{aligned} \quad (3.99)$$

This dependence is different in the high-frequency range ($a > 2\delta$). To first order we find from Eqs. 3.13, 3.36, 3.44, 3.49:

$$\begin{aligned} R_{\text{prox,hf}} &\propto \sigma^{-1/2} \propto \sqrt{T} \\ R_{\text{skin,hf}} &\propto \sigma^{-1/2} \propto \sqrt{T} \end{aligned} \quad (3.100)$$

With a steady flow of hot air, the 17'' CMT line-coil pairs with a 3C2 ferrite core were heated up to $T = (100 \pm 2)^\circ\text{C}$. By measuring the dc resistance of the line coils we verified that this temperature was reached and maintained

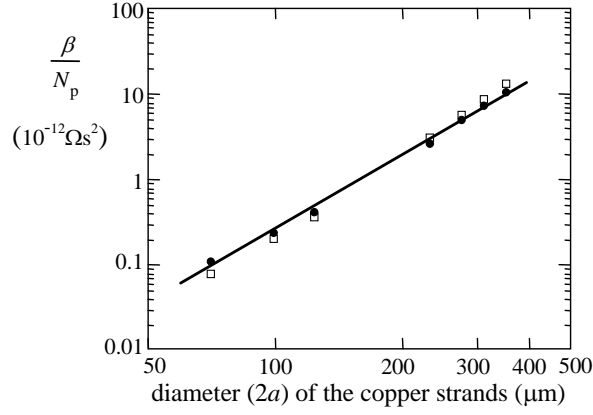


Figure 3.19: The coefficient β as a function of the diameter of the copper strands at 100 °C (●) and 20 °C (□) calculated by fitting βf^2 to the increase in the real part of the impedance characteristics. The solid line is fitted to the 100 °C (●) values by $\beta/N_p = 0.7 \cdot 10^{-12} a^{2.9}$.

for at least one hour. Subsequently we measured the impedance characteristic and fitted the resistive part between 20 kHz and 150 kHz with $\text{Re}(Z(f)) = R_{\text{dc}(100^\circ\text{C})} + \beta_{100^\circ\text{C}} f^2$ (Eq. 3.93). The fitting results at this temperature for the line coils with the seven different wire types are presented in Table 3.4.

The seven coefficients $\beta_{100^\circ\text{C}}$ in this table are fitted by

$$\beta_{100^\circ\text{C}} = 0.7 \cdot 10^{-12} N_p a^{2.9} \quad (3.101)$$

in which the radius a of the copper strands is given in meters.

In actual applications, the temperature of the line coils varies between 70 °C and 110 °C, depending on the temperature of the television set or the computer monitor in which the coils are used. Therefore Eq. 3.93 with Eq. 3.101 gives a practical expression for the losses in actual applications.

Figure 3.19 compares the fitting coefficients β at $T=100^\circ\text{C}$ with those at $T=20^\circ\text{C}$ (which were shown earlier in Fig. 3.16). This figure shows that the ac losses are reduced for the four larger diameters, while they are increased for the smaller diameters. This increase cannot be explained by the low-frequency skin and proximity effects.

Current measurements

When looking for a possible explanation, we also measured the distribution of the currents over the copper strands. One of the indications that led us to this measurement is that we concluded in Sect. 3.6.1 that the ac losses in the

frame coil increase as expected with the wire diameter, whereas the ac losses in the line coil are reduced much less for the smaller diameters than expected from the proximity-loss model. The main difference between line and frame coils in this respect is that a high-frequency current flows only through the line coils.

Note that the wires pile up more or less at random when a CRT deflection coil is being wound so that the wires have no fixed position with respect to each other along the coil. This random nature leads to the assumption that the current is evenly distributed over the parallel copper strands in a bundle.

To check this assumption, we measured the currents through the separate litz wires and the currents through the individual copper strands within a litz wire of a 17" CMT sample with $8 \times (7 \times 100\text{-}\mu\text{m})$ wires. Again we used a 17" CMT deflection yoke without frame coils. The pair of line coils were connected to a Fluke PM5128A sine wave generator and the currents were measured with a Tektronix A603 current probe in combination with a Tektronix AM503B current probe amplifier and a scope. The accuracy of the readings is $\pm 5\%$.

In the case of a 10-kHz sine wave, the current through each of the eight parallel litz wires was the same within the measuring accuracy. Also the current through each of the seven copper strands was the same (equal to one seventh of the current through a litz wire).

In the case of a 500-kHz sine wave, however, the currents differed strongly among both the litz wires as well as among the copper strands within a single litz wire. For the 8 litz wires in one of the coils, we measured 15, 13, 13, 11, 5.8, 5.8, 4.4 and 1.4 mA respectively. We splitted the litz wire with the largest current into the 7 copper strands, and measured currents of 3.0, 2.7, 2.6, 1.9, 1.7, 1.6, and 1.4 mA.

Evaluation

The experimental results can be partly explained by the interstrand skin effect (see page 39). In Sect. 3.4.4 we described that in CRT deflection coils stranded litz is used, in which the outer copper strands change positions but remain on the outside for the entire length of the wire. We already mentioned as disadvantage of this stranded litz type that the inner strands carry a lower current than the outer strands, similar to the skin effect in a single conductor. The reason is that in a litz wire the copper strands are electrically connected at the two ends. A net magnetic flux through the area enclosed by a pair of copper strands will result in a current, which flows in opposite directions in the two strands. In a straight bundle of copper strands in a litz wire, without external magnetic field, a net magnetic flux between the inner wire and each

of the outer wires is generated by the currents through the copper strands themselves. The extra current induced by this net magnetic flux decreases the current in the center strand(s) and increases the current in the outer strands. Consequently, a larger current will flow through a copper strand at the outside of a litz wire than through a copper strand near the center of the litz wire.

At 500 kHz, the skin depth $\delta = 93 \mu\text{m}$. To estimate the influence of the interstrand skin effect, we consider a solid copper wire with the same outer copper diameter $2a$ as a single ($7 \times 100 \mu\text{m}$) litz wire. Including internal insulation material between the copper strands, this equivalent copper diameter is $2a = 330 \mu\text{m}$. With Eq. 3.24 for the current density due to the skin effect, we calculated the ratio of the current density $j_z(a)$ near the surface and the current density $j_z(0)$ near the center of a solid wire with radius a . The result $\text{Re}(j_z(a))/\text{Re}(j_z(0)) = 1.8$ corresponds reasonably well to the maximum ratio $3.0/1.4 = 2.1$ of the measured currents in the copper strands in a litz wire.

In the same way, the differences among the parallel litz wires can be partly explained by an interwire skin effect in which we model the eight parallel litz wires by straight parallel copper strands in a fixed configuration. For the bundle of $8 \times (7 \times 100 \mu\text{m})$ wires we assume an overall copper diameter $2a = 1.0 \text{ mm}$. Since this diameter is much larger than the skin depth at 500 kHz, $\delta = 93 \mu\text{m}$, the current in an inner strand can easily be an order of magnitude smaller than the current in an outer strand, as measured.

However, the measured resistance at 500 kHz is much larger than predicted by either the interstrand skin effect or the interwire skin effect. At 20°C , the real part of the measured impedance of a pair of line coils with $7 \times 100 \mu\text{m}$ litz wires at 500 kHz is $R(500 \text{ kHz}) = 2.4 \Omega$. This is more than ten times the dc resistance $R_{\text{dc}} = 0.23 \Omega$. Using Eq. 3.30, we estimate that this ratio should be only $R(500 \text{ kHz})/R_{\text{dc}} = 1.2$ for the interstrand skin effect (with $2a = 330 \mu\text{m}$) and $R(500 \text{ kHz})/R_{\text{dc}} = 2.9$ for the interwire skin effect (with $2a = 1 \text{ mm}$). Clearly, our simplified model of the interstrand or interwire skin effect in long parallel straight wires without external magnetic fields cannot explain the experimental results.

The differences in currents through the various copper strands is measured to be much larger than predicted by the interskin and interwire skin effect.

A possible explanation is shown in Fig. 3.20. In CRT deflection coils, the magnetic field through a bundle of copper strands is not only generated by the current through that local part of the copper strands only, but also by currents through other copper strands and - even stronger - by currents through the same copper strands but in different turns. Also the magnetization of the

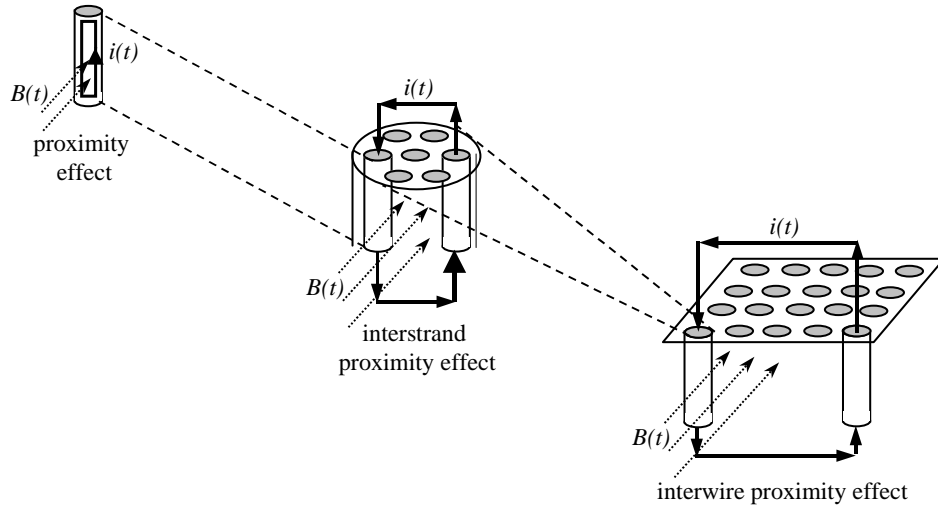


Figure 3.20: A comparison of the proximity effect, the interstrand proximity effect and the interwire proximity effect. The *proximity effect* describes the eddy currents $i(t)$ inside a single copper strand induced by a magnetic flux through this strand. The *interstrand proximity effect* describes such an induced current $i(t)$ through different copper strands in a litz wire that are electrically connected at the ends. The *interwire proximity effect* describes the current induced in a loop formed by different wires in parallel.

ferrite core results in stronger magnetic fields. If the copper strands are not twisted adequately, some net magnetic flux through the surface enclosed by those copper strands will result in additional currents through those copper strands. If the copper strands are part of the same litz wire, we call this effect the ‘interstrand proximity effect’, otherwise we call it the ‘interwire proximity effect’. In CRT deflection coils, the interstrand proximity effect is probably much smaller than the interwire proximity effect because stranded litz is used in which the outer copper strands rotate around the center strand along the wire. The various wires in a bundle, on the other hand, are not twisted sufficiently. A stronger twist of these wires can probably reduce the interwire proximity effect significantly.

Finally, note that the interwire proximity effect in a bundle of wires also explains why the dissipation increases with temperature for the smaller diameters in Fig. 3.19, since we are dealing here with the high-frequency range as the radius of the bundle is much larger than the skin depth ($a > 2\delta$, see page 57).

Discussion

In CRT deflection coils, a complicated mix of various kinds of eddy currents can occur. In fact, this distinction in various kinds of eddy currents is a simplification of the complicated physical phenomena described by Maxwell's equations. Since these equations are difficult to solve, the analytical analysis is simplified by considering straight wires in two configurations with simple boundary conditions.

In the first configuration, we assume that a net current is flowing through the copper wires while no external magnetic field is present. The effects that occur in this case are called skin effects.

In the second configuration, an external magnetic field is considered and we assume that no net current is flowing, i.e. no external current or voltage supplies are connected. The effects that occur in this case are called proximity effects.

In Sect. 3.4.2 we described the skin effect and proximity effect in a single copper wire. In Sect. 3.4.4 we showed that in litz wires the interstrand skin effect can change the distribution of the currents over the parallel copper strands. Usually the strands in a wire are stranded sufficiently, so that the interstrand proximity effect, in which an external magnetic field would drive a current to circulate through parallel strands, is negligible. Because the coils are wound with a bundle of parallel wires which are electrically connected at the terminals of the coils, also the interwire skin effect and the interwire proximity effect across parallel wires in a bundle can give a significant contribution to the total dissipation.

The interstrand proximity effect can be reduced by using stranded litz, in which the outer copper strands change positions but remain on the outside for the entire length of the wire. This does not reduce the interstrand skin effect. To reduce this interstrand skin effect, twisted litz has to be used in which the positions of the copper strands in the litz wire are changed in such a way that within some length each strand can be found at any position in the cross-section.

In a similar way, the interwire proximity effect can be reduced by using stranded wires, in which the outer wires change positions but remain on the outside for the entire length of the bundle. To reduce the interwire skin effect, stranding is not sufficient and the wires have to be twisted such that the positions of the wires in a bundle are changed in such a way that each wire can be found at any position in the cross-section of the coil.

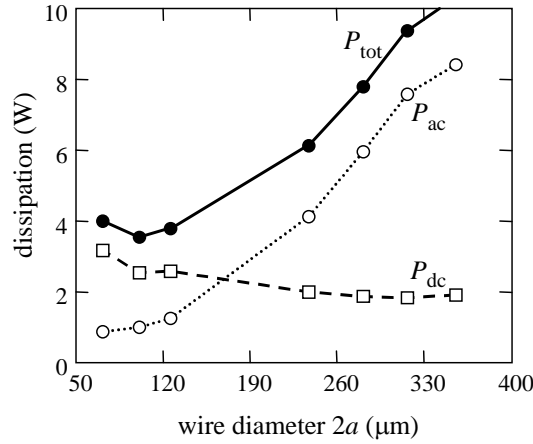


Figure 3.21: The dc dissipation P_{dc} (\square), the ac dissipation P_{ac} (\circ) and their sum P_{tot} (\bullet) in 17" CMT line coils as a function of the diameter $2a$ of the copper strands. The values are calculated from the measured impedance characteristics, assuming a saw-tooth shape deflection current with an amplitude of 5.3 A and a line frequency of 69 kHz.

3.7 Reduction of dissipation

In this section we will discuss options to reduce the dissipation in two different situations. First we will consider the case in which the geometry of the coil is completely fixed. Subsequently, we consider the case in which the overall shape of the coil is fixed, determined by the electron-optical design as described in Chapter 2, but in which the thickness of the coil can still be changed.

3.7.1 Fixed coil thickness

Once the coil design is completely fixed, the thickness of the coil cannot be changed anymore as it is determined by the winding equipment.

At a first glance, one could think that reduction of the dissipation is simply a matter of using thinner wires. However, the thinner the wires, the more insulation material has to be used. Every insulating layer around each copper strand has about the same thickness, irrespective of the wire diameter. Consequently, less copper fits in the same volume of the coil when thinner wires are used so that the dc resistance and hence the dc drive current losses will increase.

In CRT deflection coils, the area A_{coil} of the total cross-section of the coil is determined by the winding equipment and cannot be changed once the

design of the coil is fixed. To first order, it is proportional to the number of turns N_{turns} , the number of parallel copper strands N_p and the outer radius a_r of each strand including insulation:

$$A_{\text{coil}} = \zeta \pi a_r^2 N_p N_{\text{turns}} \quad (3.102)$$

in which the fraction ζ of the total coil volume filled by the copper wires depends on how tightly the wires are packed.

In general, the use of thicker wires results in lower dc losses and higher ac losses. This is illustrated by Fig. 3.21, which shows the dc dissipation P_{dc} and the ac dissipation P_{ac} and their sum for the 17" CMT line coils which were analyzed in Sect. 3.6.2. These coils have identical geometry, but are wound with different wire types. The values of P_{dc} follow from the dc resistance (Table 3.3) with $P_{\text{dc}} = \frac{1}{2} R_{\text{dc}} I_0^2$. The amplitude of the current is $I_0 = 5.3$ A. The values of P_{ac} were calculated from the measured impedance characteristics (at 20 °C) as described in Sect. 3.5.2 for a line frequency of 69 kHz. From Fig. 3.21 we conclude that at this line frequency, the lowest dissipation for the investigated 17" CMT coils is found when (7×100-μm) litz wires are used.

When a lower line frequency is considered, the dc dissipation will be the same but the ac dissipation will be lower. The lowest value of the total dissipation will therefore be obtained by using a thicker wire type.

A practical design strategy to reduce the dissipation when the thickness of the coil is fixed, is the following:

- measure the dc dissipation P_{dc} and the ac dissipation P_{ac}
- if $P_{\text{ac}} > P_{\text{dc}}$ then use thinner copper wires;
- if $P_{\text{dc}} > P_{\text{ac}}$ then use thicker copper wires.

As discussed at page 62, further reduction of the dissipation is often possible by stranding or twisting the copper strands.

3.7.2 Variable coil thickness

In an earlier design phase, before the final winding tools are ordered, the thickness of the coil can be changed slightly. In this section we will assume that the wire diameter $2a$ is fixed and that only the number N_p of parallel wires is varied to change the thickness of the coil.

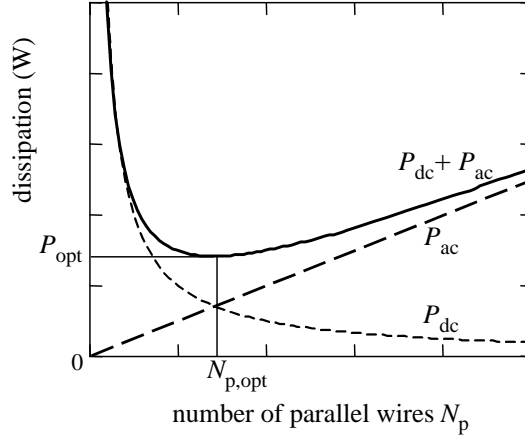


Figure 3.22: The dc dissipation P_{dc} and ac dissipation P_{ac} and their sum as a function of the number of parallel wires N_p .

According to Eq. 3.57, the dissipation due to the drive currents through the dc-resistance of the coil wires can be written as

$$P_{dc} = c_0/N_p \quad (3.103)$$

with $c_0 = N_{\text{turns}}\ell_{\text{turn}}I_0^2/(2\pi a^2\sigma)$.

Although theory predicts that the dissipation due to eddy currents varies with $N_p a^4 \omega^2$ (Eq. 3.47), we found experimentally that the dissipation is proportional to $N_p a^{2.9} \omega^2$ (Eqs. 3.93 and 3.101). Using this last result, we propose the following expression for the dissipation due to the induced eddy currents:

$$P_{ac} = c_1 N_p a^3 \omega^2 \quad (3.104)$$

in which c_1 is proportional to I_0^2 and depends on the conductivity σ and the length ℓ_{turn} of the turns.

For the remainder of this analysis, we assume that both c_0 and c_1 are constant. The total dissipation $P = P_{dc} + P_{ac}$ is then given by

$$P = \frac{c_0}{N_p} + c_1 N_p a^3 \omega^2 \quad (3.105)$$

This dependence on the number of parallel wires is illustrated in Fig. 3.22.

Differentiation with respect to N_p shows that the minimum dissipation is obtained when the number of parallel wires equals

$$N_{p,\text{opt}} = \frac{1}{\omega} \sqrt{\frac{c_0}{a^3 c_1}} \quad (3.106)$$

The minimum dissipation is then given by

$$P_{\text{opt}} = 2\omega\sqrt{a^3c_0c_1} \quad (3.107)$$

Of course the number of wires has to be an integer in reality. Therefore, the closest integer value has to be chosen. Although the analytical expressions for the constants c_0 and c_1 already give a qualitative indication of their values, in practice the actual values of these constants are determined by measuring the resistance of the line coils as a function of frequency, with and without the presence of the frame coils.

From measured P_{dc} and P_{ac} values, the number of parallel wires to achieve the minimum dissipation can also be estimated with

$$N_{\text{p,opt}} = N_{\text{p}}\sqrt{P_{\text{dc}}/P_{\text{ac}}} \quad (3.108)$$

The corresponding dissipation follows from

$$P_{\text{opt}} = 2\sqrt{P_{\text{dc}}P_{\text{ac}}} \quad (3.109)$$

These two expressions are easily validated by substituting Eq. 3.103 and Eq. 3.104 in Eq. 3.106 and Eq. 3.107.

A practical design strategy to reduce the dissipation is

- measure the dc dissipation P_{dc} and the additional ac dissipation P_{ac}
- if $P_{\text{ac}} > P_{\text{dc}}$ then reduce the number of parallel wires;
- if $P_{\text{dc}} > P_{\text{ac}}$ then increase the number of parallel wires.

The results above have been derived for a purely sinusoidal signal. Periodic signals of different shape have to be expanded in a Fourier series. When the magnetic field $H(t)$ is expanded conform Eq. 2.26 as

$$H(t) = H_0 \sum_{n=1}^{\infty} a_n \sin n\omega_{\ell}t \quad (3.110)$$

the expression 3.105 for the total dissipation has to be replaced by

$$P = \sum_{n=1}^{\infty} a_n^2 \left\{ \frac{c_0}{N_{\text{p}}} + c_1 N_{\text{p}} a^3 n^2 \omega_{\ell}^2 \right\} \quad (3.111)$$

Differentiation with respect to N_{p} shows that the minimum total dissipation is obtained when the number of parallel wires is given by

$$N_{\text{p,opt}} = \frac{1}{\omega_{\ell}} \sqrt{\frac{c_0}{a^3 c_1} \frac{\sum_n a_n^2}{\sum_n (na_n)^2}} \quad (3.112)$$

when we still assume that the wire diameter $2a$ is fixed.

In practice, it is often sufficient to estimate the optimum number of wires with Eq. 3.108.

3.8 Summary and conclusions

Dissipation in CRT deflection coils is becoming increasingly important. On the one hand customers ask for lower overall energy consumption. On the other hand, trends to improve the performance result in an increase in the energy stored in the magnetic field required for deflection. This energy depends on the geometry of the deflection yoke but also on system choices such as the anode voltage, line frequency, flyback ratio, overscan, deflection angle, and the geometry of the neck of tube. Part of this energy is lost in the resistive part of the system; both in the drive circuit and in the deflection yoke.

The largest part of the dissipation in a deflection yoke is caused by dc losses of the drive current in the copper wires and by the proximity effect due to the large magnetic field through the copper wires. Other loss phenomena, such as hysteresis loss in the ferrite core, the skin effect and dielectric loss phenomena, turn out to have a much smaller contribution and can be neglected to first order.

The losses due to the proximity effect are reduced by using several thinner wires in parallel, rather than a single thick wire. If the number of wires becomes too high to handle, litz wires are used.

However, our experimental results indicate that the reduction in dissipation by using litz wires rather than solid wires is less than expected from the theory on the proximity effect alone. The measured dissipation of the line coils can be well understood as the result of an interwire proximity effect in a bundle of parallel wires that depends on the total diameter of the bundle, instead of on the diameter of the separate conductors. The net magnetic flux through the surface enclosed by pairs of wires causes additional currents to flow, which affect the distribution of the currents over the parallel wires. This directly results in a higher dissipation.

It is clear that most of the measures to reduce the dissipation lead to higher costs. Some evident examples are the use of litz wires instead of solid wires and the use of thicker yoke rings. Measures with less impact on the cost price have to be taken during the first conceptual design phase where e.g. the coil shape, coil length and copper volume are defined. The largest contribution to the reduction of dissipation can be achieved by measures at

system level, such as by decreasing the anode voltage and the deflection angle. In later design phases, the winding tools are fixed and the shape of the coils cannot be changed anymore. In fact, then only the wire diameter and the number of parallel wires may be changed.

Chapter 4

Description of ringing

4.1 Introduction

In the previous chapter, we have analyzed dissipation over a frequency range up to 1 MHz. Up till now, we did not take into account the capacitances between the coil wires. These capacitances may result in high-frequency electromagnetic oscillations in the deflection coils with resonant frequencies typically between 1 and 10 MHz.

The main purpose of this chapter is to provide a deeper understanding of these high-frequency oscillations which also show up in the magnetic fields of the deflection coils. We will address various aspects of describing this so-called ringing phenomenon, such as measuring and modeling the oscillations. In our analysis we will use the concepts of magnetic deflection which we introduced in Chapter 2 as well as the models for the dissipation which we analyzed in Chapter 3. Understanding these concepts and models proves to be essential to finding and optimizing ways for effectively damping the high-frequency oscillations which will be described in Chapters 5 and 6.

The structure of this chapter is the following. First, the ringing problem is described in Sect. 4.2. Subsequently, the literature on ringing is discussed in Sect. 4.3. Various methods to measure ringing are described in Sect. 4.4. Circuit models are introduced in Sect. 4.5 to describe and predict the magnetic frequency response from the measured impedance characteristics. Finally, we use the new models to fit the experimental results, both from the impedance measurements and from the frequency-response measurements.

Part of this chapter has already been published in [149].

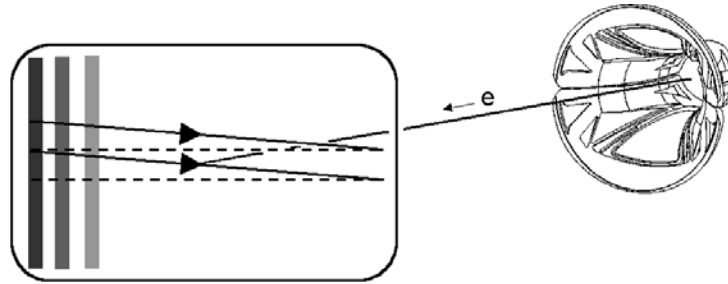


Figure 4.1: High-frequency oscillations in the deflection yoke result in vertical bars at the left hand side of the screen. This annoying effect is called ringing.

4.2 The ringing problem

If no precautions are taken, many CRTs would display a gradually decaying pattern of alternating lighter and darker vertical bars at the left-hand side of the screen, see Fig. 4.1. This phenomenon is called ringing. Ringing is one of the most common complaints from circuit designers of computer monitors. Although ringing problems can be prevented by a good design of the electronic circuits, computer-monitor designers are more and more reluctant to change their circuits. Because unexpected ringing problems require urgent action of application engineers, preventive measures in the design of the deflection coils are desirable. This justifies the detailed study carried out in this thesis.

Figure 4.1 illustrates the ringing problem. Ringing is caused by high-frequency electromagnetic oscillations in the deflection coils. To explain this, we have to realize that images on both television screens and computer-monitors screens are produced by electron beams writing lines from the left-hand side to the right-hand side of the screen. As explained in Chapter 2, this horizontal deflection is obtained by a gradually varying magnetic field generated by the line coils. At the end of each line, the current through the line coils is quickly reversed. In the mean time, the magnetic field for vertical deflection has changed such that the next horizontal line is written below the previous one.

The quick reversal of the currents in the line coils, however, can excite electromagnetic oscillations which are superimposed on the line deflection field. This causes the scanning to speed up and to slow down at the pace of the ‘ringing frequency’. This ringing frequency is typically two orders of magnitude higher than the line frequency. A typical ringing frequency for CMTs is about 5 MHz; the maximum line frequency in modern applications is 128 kHz.

When the beam moves slower, more electrons hit the screen per unit area,

which results in a brighter image. When the electron beam moves faster, less electrons hit the screen per unit area, which results in a darker image. Since the oscillation is excited in the same way by each flyback, this results in the superposition of vertical bars on the left-hand side of the picture. Especially in a uniformly white image, these ringing bars are quite annoying.

Sometimes, the ringing phenomenon causes a deviation in the vertical deflection direction on a line written in the horizontal deflection direction. This ‘serpentino’ kind of ringing is not discussed further, because more often the ringing phenomenon causes a deviation in the velocity at which a line is written in the horizontal direction.

4.3 Literature on ringing

To the best of our knowledge, not much has been published about ringing in deflection yokes in the open literature. Ringing is usually only briefly mentioned when describing a new type of deflection yoke [146, 150–152]. Only T. Murakami [153] and A. Zegers [154] presented a more detailed analysis, but both authors do not provide a link between front-of-screen appearance of ringing and the physical phenomena that affect the high-frequency behavior of CRT deflection coils. In Chapter 6, we will see that more references can be found in the patent literature in which various solutions are proposed. However, in this patent literature, no detailed analysis of the ringing problem can be found.

Many more papers have been published about the high-frequency behavior of specific transformers. An overview of several significant articles is given by Urling et al. [155]. Different equivalent circuit models have been set up to model various kinds of transformers taking into account the parasitic capacitances [?, 67, 156–171], as well as different methods for calculating the values of a lumped-component equivalent circuit from the impedance measurements [172–181]. For several transformer topologies, the model parameters can be calculated by a Finite-Element Analysis (FEA) tool [182–187]. We have not found a description in literature of such an approach to calculate the equivalent circuit model for CRT deflection coils.

Unfortunately, the proposed equivalent circuits and their parameters are very specific for the shape and technology of the modeled transformers and are not simply applicable to CRT deflection coils. Note that the overall geometry as well as the individual wire positions of CRT deflection coils differ strongly from customary transformers.

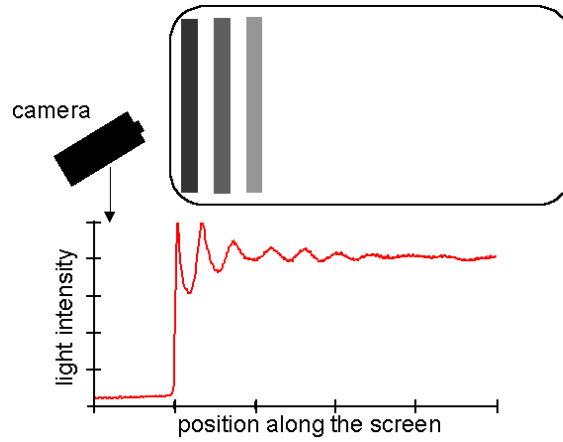


Figure 4.2: Front-of-screen ringing measuring setup.

4.4 Measuring ringing

Ringing is usually measured by recording the light intensity along the screen, as illustrated in Fig. 4.2. A dark bar corresponds to a low value, while a bright bar corresponds to a high value of the light intensity. In this way, also the decay of the ringing is adequately measured. In fact, this setup measures the time response since the horizontal position of the scan varies almost linearly in time.

A first measure for ringing is the decay of the light intensity at the left edge of the screen. Frequently, the measured decay has an exponential shape. Figure 4.3 presents the key ringing parameters to describe the ringing phenomenon for such an exponential decay: the amplitude a_r , the angular ringing frequency ω_r , and the decay time τ_r .

This conventional front-of-screen measuring method has as main disadvantage, that the results depend strongly on the drive circuit. Ringing is especially induced by steep switching transients. The main driving force for ringing is the non-ideal switching behavior of the drive circuit. Consequently, the ringing is different for different drive circuits.

Although the front-of-screen measuring method is valuable for the end inspection to test the overall quality of a television set or computer monitor, this method is less suitable to evaluate the ringing properties of a deflection yoke itself in interaction with future drive circuits.

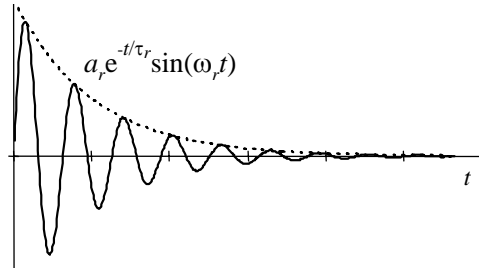


Figure 4.3: Key ringing parameters.

4.4.1 The optical frequency response

The conventional measuring method is just one of the many ways for determining the ringing characteristics of a deflection yoke. Figure 4.4 shows three different methods that are commonly used in system analysis. The first one corresponds to the conventional measuring method, in which the output depends strongly on the input signal, i.e. the flyback pulse. In fact, it is a convolution of the input signal with the pulse response of the system. In CRTs both the driving force and the resonant behavior depend on the drive circuit.

If the input pulse is short enough, the output is the pulse response which is obtained in the second method. In this method, a very short pulse is applied to the system and the response is measured as a function of time. For simple resonating systems, this pulse response is the product of a sine wave signal and an exponential decay with time constant τ_r . Unfortunately, it is difficult to apply a well defined sharp voltage pulse to a deflection yoke connected to a drive circuit, due to the large inductance of the coils and the characteristics of the drive circuit.

A third, more useful, method for characterizing oscillating systems is shown in the bottom part of Fig. 4.4. In the most elementary setup, a sine wave of constant amplitude is applied at the input and the amplitude of the output signal is measured. The plot of this amplitude as a function of frequency is the so-called frequency response.

In fact, the pulse response and the frequency response are each others Fourier transform. For our evaluations, however, it is more interesting to determine the center frequency (ω_r) and the width ($\Delta\omega$) of each resonance peak. The center frequency corresponds to the oscillating (ringing) frequency. The width at half the maximum of the frequency response is related to the decay time of the pulse response. The sharper the resonance peak, the more severe ringing problems occur.

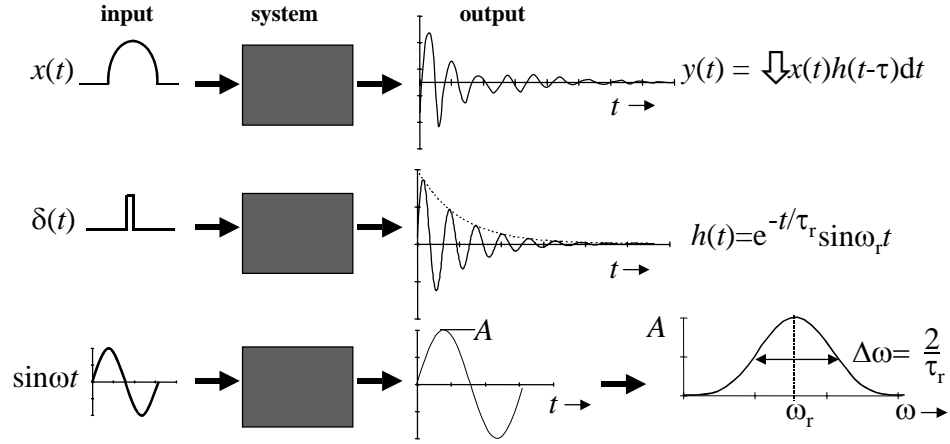


Figure 4.4: Time response and frequency response measuring methods.

A practical implementation of the frequency-response measurement is shown in Fig. 4.5. A sine wave voltage source is connected in series with the line coil and the line drive circuit. During scanning the line drive circuit is adequately modeled by a closed switch, as described in Sect. 2.3.4. The sine wave signal is started again at the start of every horizontal line scan. The frequency of the sine wave can typically be varied between 1 and 10 MHz.

The sine wave voltage source results in a small sine wave current superimposed on the large saw-tooth shaped current through the line coils. Internal oscillations increase the amplitude of the sine wave current. While the main current deflects the electron beams from the left-hand side of the screen to the right-hand side, the sine wave current results in increasing and decreasing again the deflection velocity with which the electron beams scan along the screen.

To first order, the front-of-screen light intensity is inversely proportional to the deflection velocity. The optical result of the additional sinusoidal current is a large number of vertical bars along the entire screen. With a camera in front of the screen, we measure the modulation depth of the bars along the screen. This modulation depth m is defined as

$$m = \frac{S_{\max} - S_{\min}}{S_{\max} + S_{\min}} \quad (4.1)$$

where S_{\max} and S_{\min} denote the maximum and minimum light intensity, respectively.

We assume that the light intensity $S(X_g)$ is inversely proportional to the

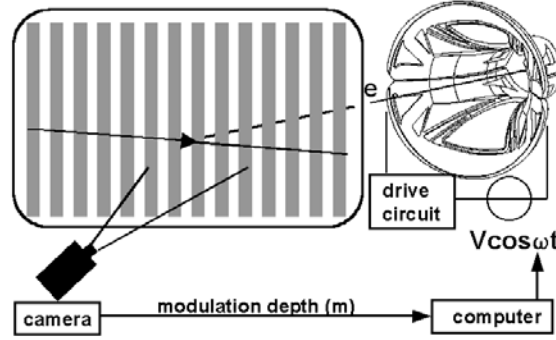


Figure 4.5: Optical frequency response measuring setup.

scanning velocity $v(X_g)$ at screen position X_g :

$$S(X_g) \approx \frac{\alpha}{v(X_g)} \quad (4.2)$$

Although this is certainly wrong for $v(X_g) = 0$, this is a reasonable assumption for practical values of $v(X_g)$. The proportionality factor α depends on the tube geometry and voltages and is considered constant in our analysis. If the maximum scan velocity is $v_{\text{scan}} + v_{\text{extra}}$ and the minimum scan velocity is $v_{\text{scan}} - v_{\text{extra}}$, the following expression results for the modulation depth m :

$$m = \frac{v_{\text{extra}}}{v_{\text{scan}}} \quad (4.3)$$

We consider v_{scan} constant in our analysis. To first order, the deflection $X_g(t)$ is proportional to the magnetic flux density $B(t)$, with proportionality constant γ :

$$X_g(t) = \gamma B(t) \quad (4.4)$$

An alternating magnetic flux density $B_{\text{extra}}(t)$, superimposed on the main deflection field, modulates the scan velocity v_{scan} with an amplitude

$$v_{\text{extra}} = \gamma \frac{dB_{\text{extra}}(t)}{dt} \quad (4.5)$$

Again to first order, we assume that the magnetic flux density $B_{\text{extra}}(t)$ is generated by a current $i(t)$ through a deflection coil with N_{turns} turns around an effective area A_L :

$$B_{\text{extra}}(t) = L \frac{i(t)}{N_{\text{turns}} A_L} \quad (4.6)$$

The proportionality constant is the inductance L of the deflection coil.

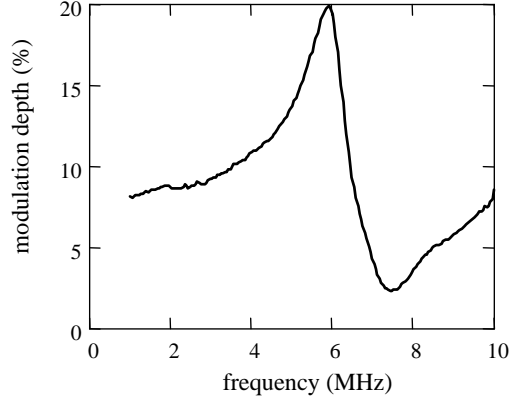


Figure 4.6: Measured optical frequency response, showing the modulation depth m as function of frequency for a 17'' CMT.

Since the voltage across an inductance is $v_L = -L di(t)/dt$, we find

$$v_{\text{extra}} = \gamma \frac{\hat{v}_L}{N_{\text{turns}} A_L} \quad (4.7)$$

where \hat{v}_L denotes the amplitude of the voltage across the inductance.

Substitution in Eq. 4.3 results in

$$m(\omega) = \kappa \frac{\hat{v}_L(\omega)}{N_{\text{turns}} A_L} \quad (4.8)$$

in which the constant κ depends on the geometry and a.o. the anode voltage. According to Eq. 4.8, the modulation depth is proportional to the voltage across the coil that generates the magnetic deflection field. We will use this relation in Sect. 4.4.3 and 4.4.4 to develop alternative measuring methods.

Figure 4.6 shows a typical result. The modulation depth as function of frequency presents the optical frequency response. In this example, the ringing frequency is about 5.8 MHz and the bandwidth is 1.5 MHz. The absolute values of the modulation depth depends of course on the amplitude of the sine wave voltage source (which is 15 V in this example) and the amplitude of the line current (which is 5 A in this example).

The advantage of the optical frequency-response measuring method is that various ringing frequencies of the deflection coils can be identified, irrespective of the transient behavior of the components in the drive circuit. By measuring somewhere in the middle of the screen, the influence of transients originating from the drive circuit is negligible.

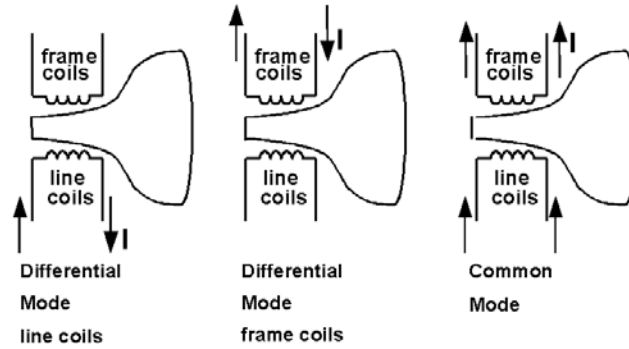


Figure 4.7: The three ringing modes.

4.4.2 Differential-mode and common-mode ringing

An additional advantage of the optical frequency-response measuring method is that it allows for separate analysis of various ringing modes as shown in Fig. 4.7. The system of CRT deflection coils is considered as a four-terminal system.

The concepts of differential-mode and common-mode currents are well known in the field of Electromagnetic Compatibility (EMC) [188, 189]. They conveniently characterize the various ringing modes. In the Differential-Mode (DM), currents flow in different directions in the coil leads with no net current in the common direction. In the Common-Mode (CM), a net current flows in a common direction in the leads, with no net current in the different directions.

If we consider in a symmetric situation two coil leads with currents i_1 and i_2 respectively, the DM current i_{dm} and the CM current i_{cm} are defined by [190]:

$$i_{\text{dm}} = (i_1 - i_2)/2 \quad (4.9)$$

and

$$i_{\text{cm}} = i_1 + i_2 \quad (4.10)$$

We distinguish:

- differential-mode ringing through the line coils;
- differential-mode ringing through the frame coils;
- common-mode ringing through line and frame coils.

A differential-mode ringing current through the line coils, superimposed on the sawtooth line current, can be excited by the sharp end of the flyback

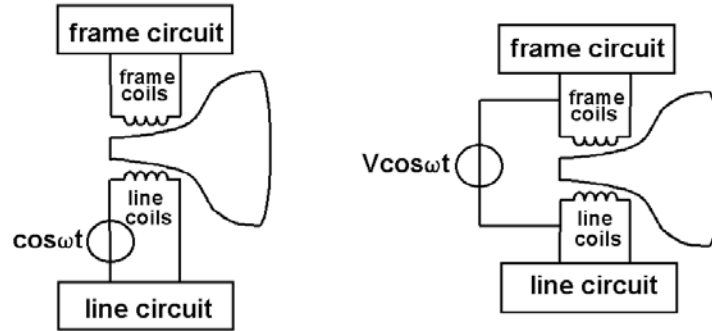


Figure 4.8: Measuring setup of differential-mode (left) and common-mode (right) ringing.

voltage generated by the line drive circuit. Similarly, a differential-mode frame coil current flows through the frame coils. Here an extra ringing current through the frame coils can also be excited by the sharp end of the flyback voltage generated by the line drive circuit due to the capacitive coupling between line and frame coils.

Because the common-mode ringing turns out to be the major cause of ringing in many applications, we explain this ringing mode in more detail. In a deflection yoke, the line coils are close to the frame coils. For higher frequencies, the (displacement) current can pass through the parasitic capacitance between the line and frame coils. In that manner, the common-mode currents flows in both line and frame coils and can return through the drive circuits. The common-mode ringing can be excited by the switching characteristics of an additional correction circuit in the ground lead of the line coils. Another important configuration that results in common-mode ringing problems is the presence of a significant impedance in the ground leads of the drive circuits.

In practice, the situation is more complicated because a differential-mode current can excite a common-mode current and vice versa. For instance, the voltage generated by a differential-mode current through the line coils can give rise to a common-mode current through the frame coils and, via the parasitic capacitance, also through the line coils. Furthermore, a differential-mode current in the line coils can also produce a differential-mode current in the frame coils as a result of their mutual magnetic coupling.

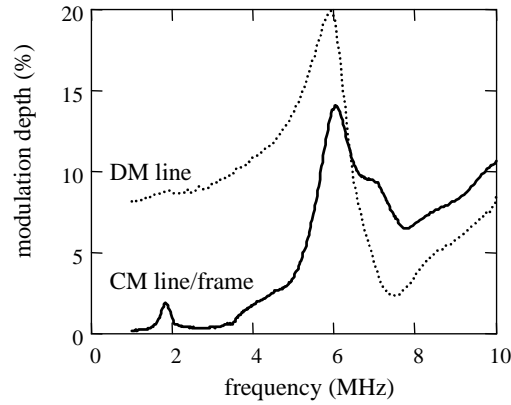


Figure 4.9: Experimental results of common-mode and differential-mode measurements of the optical frequency response of a 17" CMT sample, showing the modulation depth as a function of frequency.

Measuring principle

The principle of the setup for measuring the optical frequency response for differential-mode ringing of either line or frame coils has already been shown in Fig. 4.5. Figure 4.8 (right) shows how the common-mode ringing is measured. The test voltage produces a current that passes the capacitance between line and frame coils and that flows through both line and frame coils. Note that oscillations in the frame coils also result in vertical bars at the screen as the oscillating currents flow through (parts of) the line coils as well. The electrical circuits in the measuring setup are described in more detail in [49].

Figure 4.9 shows both the differential-mode optical frequency response of the line coils and the common-mode optical frequency response of a 17" CMT. Again note that the absolute values of the modulation depth depend on the amplitude of the voltage source. From the figure we conclude that a differential-mode current of the line coils has a resonance frequency of 5.9 MHz. The common-mode current oscillates at 1.8 MHz and 6.0 MHz. This corresponds very well to observed ringing frequencies in computer monitors. In practice the low-frequency resonance is often more annoying than the high-frequency one because it has a longer decay time.

Circuit interaction

The optical frequency-response measuring method is not only used to analyze deflection yokes, but also to analyze the interaction of the deflection yoke with the drive circuit. This allows circuit designers to optimize their circuits

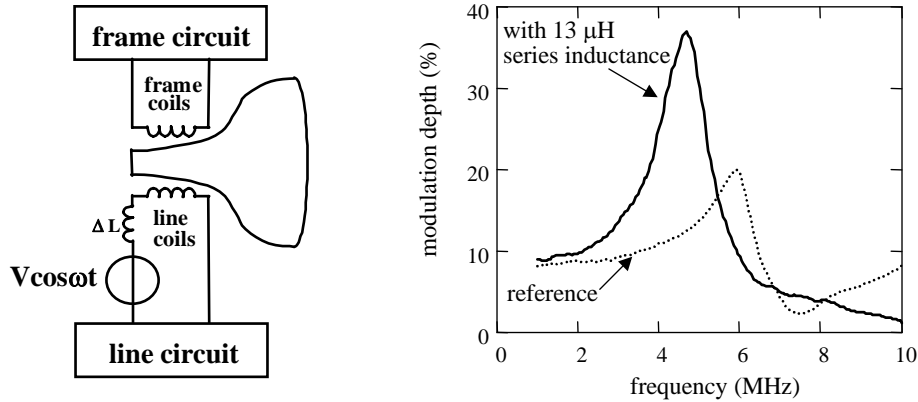


Figure 4.10: Effect of a series inductance on ringing, measured with the differential-mode optical frequency response measuring method.

in terms of a lower ringing level.

A simple illustration of the influence of the circuits is the inclusion of a series inductance in the line leads, to model long or ill-positioned wires. A $13\text{-}\mu\text{H}$ coil was added in series to a $123\text{-}\mu\text{H}$ line coil a $17''$ CMT deflection yoke. This value, 10% of the line inductance, is chosen to be larger than found in practical circuits, to see the effect more clearly. The measured results are shown in Fig. 4.10. Clearly, the combination is much more sensitive to ringing than the circuit without the series coil. The frequency response is much higher with the series coil than without.

Furthermore, the optical frequency-response measuring method can be used to analyze the effectiveness of ringing suppression measures. One of these measures is to include a common-mode rejection choke in the leads of the frame coils. This option will be explained in more detail in Sect. 6.3.4. It is presented here just to illustrate the use of the measuring method. Figure 4.11 shows the results of adding the choke. Clearly the choke suppresses the low-frequency resonance peak completely while also the high-frequency peak is reduced strongly.

Summarizing, a new measuring method has been presented for optically measuring the ringing characteristics of deflection yokes. The advantages of the optical frequency-response measuring method are the following:

- the ringing sensitivity can be characterized independently of the switching properties of the drive circuit components
- the interaction with the drive circuit can be studied systematically

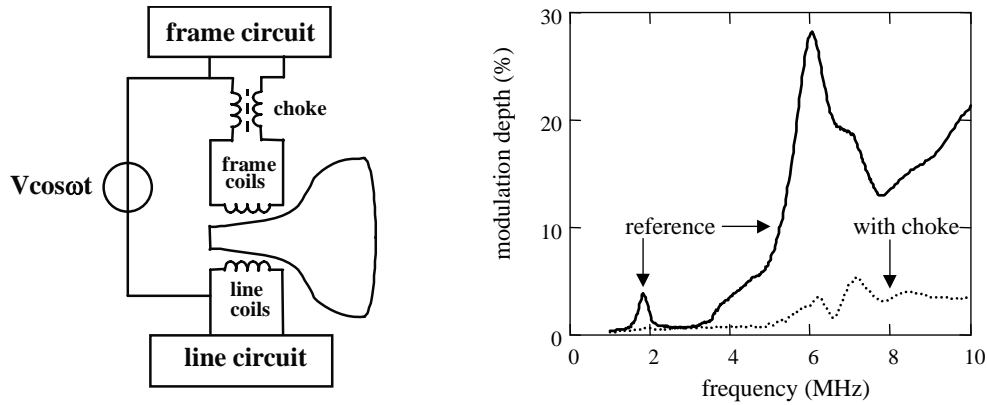


Figure 4.11: Effect of a common-mode rejection choke, measured with the common-mode optical frequency response measuring method.

- the concepts of differential-mode ringing and common-mode ringing have been introduced. These modes can be measured separately.
- the effectiveness of ringing suppression can be quantified from the measured width of the frequency response.

4.4.3 The magnetic frequency response

The optical frequency-response measuring method has many advantages and has been successfully applied for the analysis of many problems. A disadvantage, however, is that the measuring setup is quite complicated. A highly skilled operator is required to manage the settings of the camera, tube supply voltages, deflection yoke drive currents and computer control.

A much simpler, faster and cheaper measuring setup is obtained by measuring the magnetic field of the deflection yoke rather than the optical modulation depth. In general, the results are somewhat different from the optical experimental results, but we will show in this section that in practice the measured Magnetic Frequency Response (MFR) is similar enough to the optical frequency response to be useful in our analysis.

The concept of the MFR measuring setup is based on front-of-screen observations in the optical frequency-response measuring setup. There, we saw that the vertical bars are visible over the entire height for the differential mode. We therefore concluded that a large pick-up coil in the center of the deflection yoke would be a good choice to measure the magnetic frequency response of differential-mode oscillations.

For the common-mode however, the bars are observed to change phase

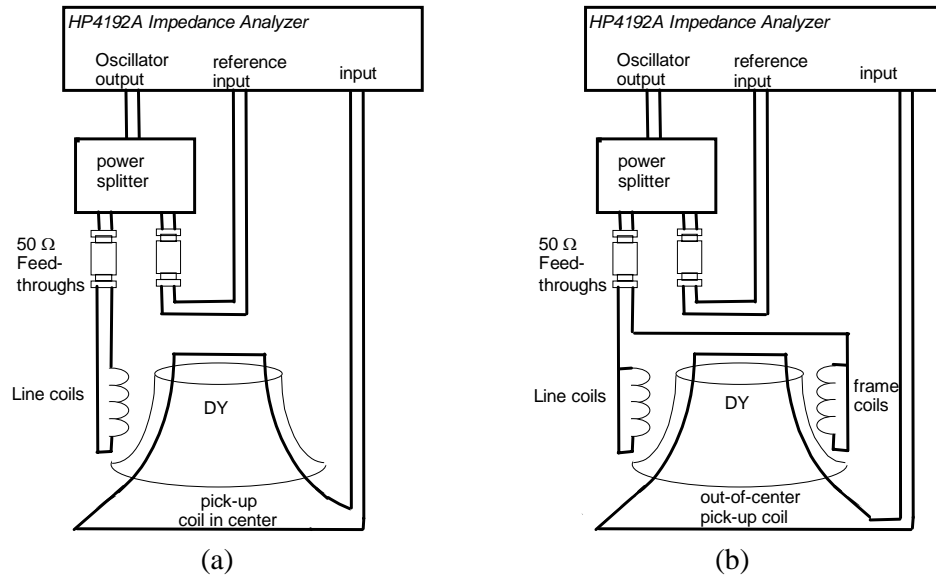


Figure 4.12: Schematic diagrams of the measuring setups for (a) the Differential-Mode Magnetic (DMM) frequency response and (b) the Common-Mode Magnetic (CMM) frequency response.

from the top to the bottom of the screen. On the upper half of the screen, the modulation depth decreases when the bars are traced from the top of the screen to the middle. In the center horizontal line of the screen, the modulation was no longer visible. Further down, the modulation increased again except that dark and bright bars were interchanged. The differential-mode pick-up coil in the x -plane of the deflection yoke cannot measure the common-mode ringing. In this case we use a large pick-up coil close to one of the line coils to measure the magnetic frequency response of common-mode oscillations.

Both pick-up coils were mounted in a glass cone to ensure a correct geometrical alignment of the coils to the deflection yoke to be measured.

In the next two sections we will describe the setups to measure the magnetic frequency response for the differential-mode and the common-mode in more detail.

Differential-mode magnetic frequency response

Figure 4.12a gives a schematic diagram of the Differential-Mode Magnetic (DMM) frequency-response measuring setup. Basically it consists of a large pick-up coil and a spectrum analyzer for which we have used an HP4192A

Impedance Analyzer. The oscillator output of a spectrum analyzer is connected to a power splitter which divides the signal in two parts. One part drives the line coils. The other part is connected to the reference input. The 50- Ω feedthroughs are included to ensure a constant load of the oscillator. The signal input of the spectrum analyzer is connected to a large pick-up coil in the x -plane of the deflection coils.

In contrast to the optical frequency response setup, no large sawtooth currents flow through the line and frame coils. In the DMM setup, the maximum voltage is only 1 V, whereas in the optical frequency-response measuring setup voltages up to 1500 V occurred (during flyback). This makes the DMM setup much more safe for operators than the optical frequency response setup.

The key design consideration was to develop a magnetic measuring setup that gives results in close agreement to the more elaborate optical measuring setup. At first sight, the principles seem quite different. However, both pick-up voltage and the optical modulation depth are proportional to the time derivative of the magnetic flux (see Sect. 4.4.1).

Also the high-frequency driving configuration is similar to that in the optical setup. The impedances ωL of the line and frame coils are much higher than 50 Ω so that the driving source in the DMM set up can be considered as a simple sine wave voltage of constant amplitude. This was also the case in the optical measuring setup (Fig. 4.8).

After some experimentation we have designed a pick-up coil that just fits in the inner side of a glass cone with maximum active area, i.e. in the rear extended towards the gun area and at the front extended up to the level where signals did no longer increase. To obtain reproducible experimental results, the pick-up coil was fixed on the inner side of a glass cone. In fact, a 15" CMT cone was used. This is also suitable for 17" CMT and 21" CMT measurements because these designs have the same cone shape.

Normally, glass cones are covered with weakly conductive layers, the so-called soft-flash and aquadag layers, but no differences in the experimental results were found when cones were used with or without these layers.

Typical experimental results for a 17" CMT are shown in Fig. 4.13. Comparison to Fig. 4.10 shows that the magnetic frequency response is very similar to the optical frequency response.

The measuring setup for the differential-mode magnetic frequency response of the frame coil is very similar to that of the line coil presented above and will not be discussed here. The measurement of the common-mode frequency response is somewhat different and will be discussed in the next section.

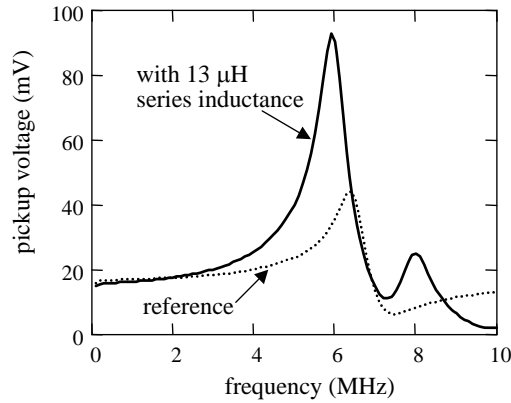


Figure 4.13: The DMM frequency response of a 17" CMT before (thick line) and after (thin line) adding a 13- μ H inductance in series to the line coil.

Similar to what we discussed for the optical frequency response, the magnetic frequency-response measuring method can also be used to analyze the interaction of the deflection yoke with the drive circuit. Figure 4.13 shows the measured magnetic frequency response before and after adding a 13- μ H inductance in series to the 123- μ H line coil. The experimental results are similar to those obtained with the optical frequency-response measuring method, as presented in Fig. 4.10, except that a second resonance peak near 8 MHz appears in the magnetic frequency response which is not seen in the optical frequency response.

Common-mode magnetic frequency response

In contrast to the differential-mode ringing field, the common-mode ringing field cannot be measured with a large pick-up coil in the x -plane of the deflection yoke because the common-mode ringing usually results in a zero field near the axis (corresponding to a quadrupole field). Therefore, an additional out-of-center pick-up coil had to be developed as well.

Figure 4.12b gives a schematic diagram of the Common-Mode Magnetic (CMM) frequency-response measuring setup. The common-mode ringing is measured by forcing the sinusoidal current through both the line coils and frame coils. The two line leads are connected to ground (to reduce the capacitive crosstalk between line coils and pickup coil), while the two frame leads are connected to the oscillator output.

Typical experimental results for a 17" CMT are shown in Fig. 4.14a. An enlarged detail of the first resonance peaks is shown in Fig. 4.14b. Comparison

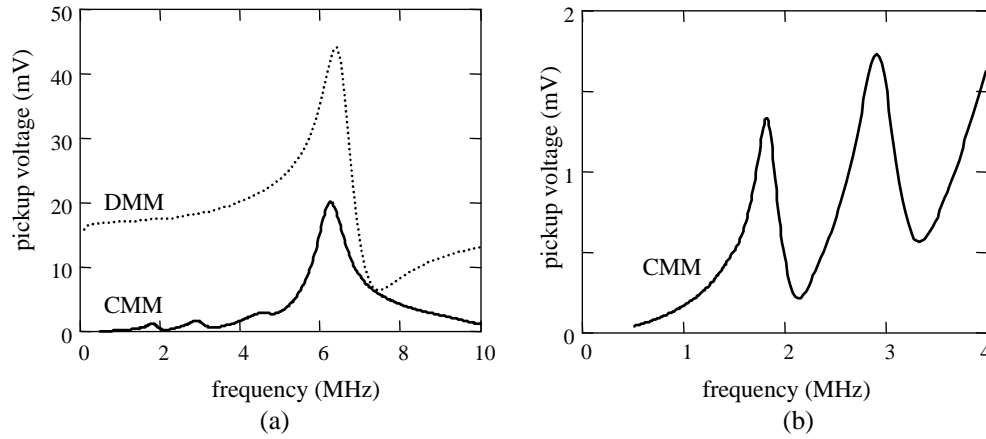


Figure 4.14: (a) Experimental results of common-mode and differential mode measurements on the magnetic frequency response of a 17'' CMT sample, showing the pick-up voltage as function of frequency. (b) Enlarged detail of the common-mode magnetic frequency response measurement.

to Fig. 4.9, shows that the common-mode magnetic frequency response is similar to the optical frequency response, except that more resonance peaks are found.

Measuring setup for the magnetic frequency response

The pickup coils consist of a single-turn wire loop of $7 \times 125\text{-}\mu\text{m}$ litz wire with twisted leads. The resonance peak of this pick-up coil is much higher than 10 MHz, which is our maximum measuring frequency. More turns result in lower resonance peaks of the pick-up coil. Two turns already lower the resonance peak to about 10 MHz which is not acceptable for our measurements.

Figure 4.15 shows the geometry of the pickup coils in detail and Fig. 4.16 shows photographs of the measuring setup.

The ringing frequencies and the bandwidths are accurately measured with the magnetic frequency-response measuring method. However, the heights of various ringing modes can differ from those found in the optical frequency response method. This can be explained by the fact that the intensity of the oscillating field changes along the z-axis of the deflection yoke. The magnetic measurement measures the average over a larger (pickup) area, whereas the contributions to the optical measuring results depend on how and where the electron beams traverse these fields.

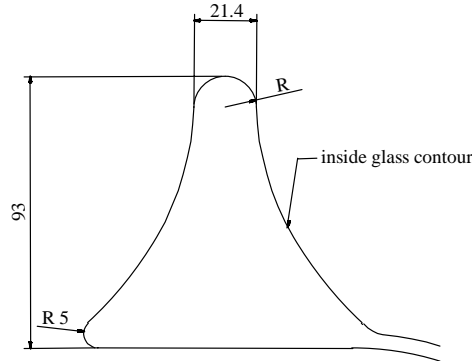


Figure 4.15: Geometry of the simple pickup coil, placed in the x -plane of the glass cone with the sides against the inside (15" CMT) glass contour.

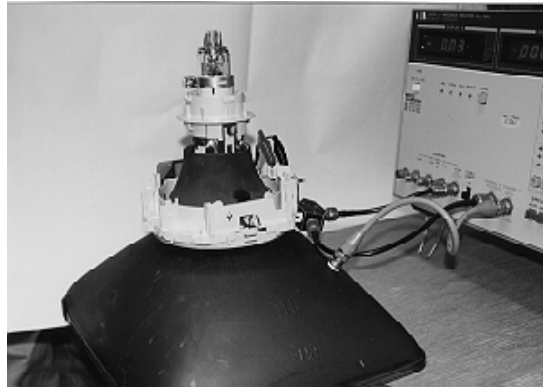
Compared to the optical frequency-response measuring method, the Magnetic Frequency Response (MFR) measuring method is easier, safer, faster and the measuring setup is simpler and less expensive. Another advantage of the MFR method is that it allows for measurements in various regions in the deflection yoke, allowing for distinction in e.g. flare, middle and neck regions.

However, the disadvantage of the MFR method is that the relative amplitudes of various ringing modes can differ from those found in the optical frequency-response measuring method. This is no serious drawback, since the main application of the measuring method is to evaluate the effectiveness of ringing suppression techniques.

4.4.4 Impedance characteristics

Up to now we have described the measurement of the ringing performance of a deflection yoke by either the optical or magnetic frequency response. This is already adequate for measuring the ringing performance, but it gives no physical understanding about how to improve on ringing. To improve this understanding, we will derive electrical circuit models in Sect. 4.5 from which the previous experimental results on the frequency response can be derived. This approach enables us to describe the performance in terms of a small number of circuit components with fixed values. Subsequently, in Chapter 5 we will show how the values of the components in the circuit models are related to the geometry of the coils.

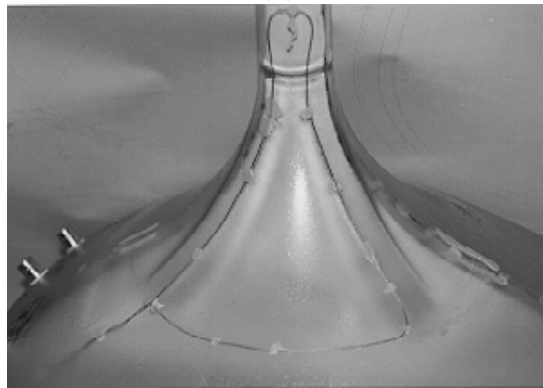
An easy and quick measuring method to determine the dynamic behavior of a deflection yoke is to measure the impedances of the line and frame coils



(a)



(b)



(c)

Figure 4.16: Photographs of (a) the magnetic measuring setup, (b) the pick-up coil in the center of the cone, and (c) the out-of-center pickup coil against the inner side of the glass cone.

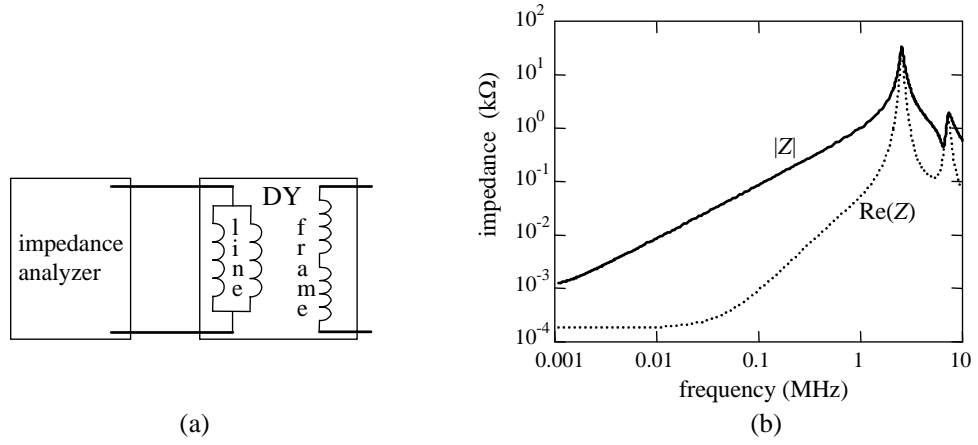


Figure 4.17: Differential-Mode Impedance (DMI) (a) measuring setup and (b) typical measuring results: amplitude and real part (dotted line) of the measured line-coil impedance of a 17" CMT deflection yoke as a function of frequency.

as functions of frequency. In contrast to the more straightforward optical and magnetic ringing measuring methods, the impedance measuring method is not restricted to complete deflection yokes, but can also be applied to characterize the ringing characteristics of individual line coils or individual frame coils. This allows for a more detailed analysis of the ringing phenomenon, e.g. when studying the influence of spread in the positions of the wires, the wire characteristics and/or the coil processing.

Most impedance measuring equipment translate the impedance Z to a resistance R with a series inductance L :

$$Z = R + j\omega L \quad (4.11)$$

However, especially for the high-frequency characteristics of deflection yokes it is important to note that the measured 'resistance' values are determined for a large part by e.g. eddy-current losses. Circuit models based on physical insights are helpful for the interpretation.

In the remainder of this section, we will discuss the setup for measuring

- the Differential-Mode Impedance (DMI);
- the Common-Mode Impedance (CMI).

In Sect. 4.5 we will present electrical circuit models which can be fitted to these impedances.

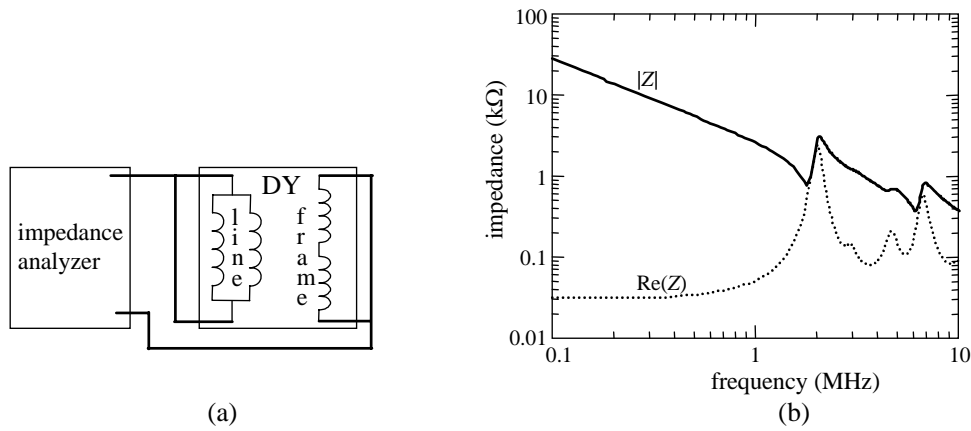


Figure 4.18: Common-Mode Impedance (CMI) characteristic (a) measuring setup and (b) typical measuring results: amplitude and real part (dotted) of the measured common-mode impedance as a function of frequency.

Differential-mode impedance

Figure 4.17a shows the basic principle of the Differential-Mode Impedance (DMI) measuring setup, in which the impedance is measured between the two line coil leads only. Although in real application circuits, the two frame coils can be short-circuited for high frequencies, in practice the measured impedance characteristics do not differ significantly when the two frame coil connections are short-circuited or not.

To obtain results as close as possible to the results obtained with the optical frequency response and the magnetic frequency-response measuring setups, we measure the line coil impedance on the fully assembled deflection yoke. Figure 4.17b shows a typical measuring result of both the amplitude of the impedance and the real part of the impedance for the line coils of a 17" CMT, measured with a HP4192A impedance analyzer up to 10 MHz. The two resonance peaks have at first sight no clear relation to the frequency responses described in the previous sections. In Sect. 4.5, we will elaborate on this relation and we will show how the frequency response can be calculated from the impedance characteristic.

In principle, the impedance between the two frame coil leads can be measured in the same way. However, in many deflection yokes a frame balance potentiometer is connected in parallel with the two frame coils. Because this provides a relatively low impedance parallel path for the high-frequency currents, no resonance peaks are observed. Of course, it is possible to remove the frame balance potentiometer and other resistances in parallel to the frame

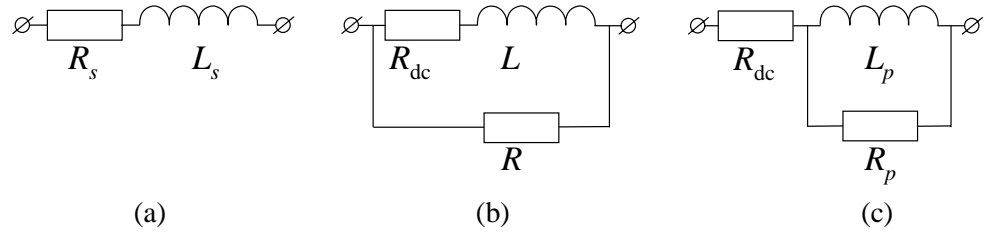


Figure 4.19: Alternative equivalent circuits to model the low-frequency behavior of CRT deflection coils.

coil, but this will not be discussed further in this thesis because this provides no new insights and is not relevant for normal operation.

Common-mode impedance

Important is also the Common-Mode Impedance (CMI) between the line coil and the frame coil leads. Figure 4.18a presents a schematic diagram of the measuring setup and Fig. 4.18b shows a typical result for the amplitude $|Z|$ and the real part $\text{Re}(Z)$ of the impedance. For frequencies up to 1 MHz the impedance looks like a simple capacitance, typically of about 60 pF. Near 2 MHz the first oscillation is measured. Again at first sight, the relation to the measured frequency-response is not obvious. In Sect. 4.5 we will elaborate on this relation.

4.5 Equivalent circuit models

The objective of this section is to present equivalent circuit models that can be fitted to the impedance characteristics presented in the previous section. Subsequently, we will derive the frequency response which should be close to the response obtained with either the optical frequency response or with the magnetic frequency-response measuring method.

Furthermore these circuit models allow for circuit analysis and optimization. Sophisticated CAD circuit design tools such as Spice [191] are commonly used in circuit design. However, for line-deflection drive circuits, the high-frequency behavior cannot be predicted yet, due to the lack of circuit models that describe the high-frequency behavior of deflection yokes. Furthermore, no link to front-of screen performance is available in the literature, yet.

This section presents circuit models for the description of high-frequency oscillations in CRT deflection coils. This enables CRT circuit designers to use circuit simulation programs to predict the high-frequency behavior of

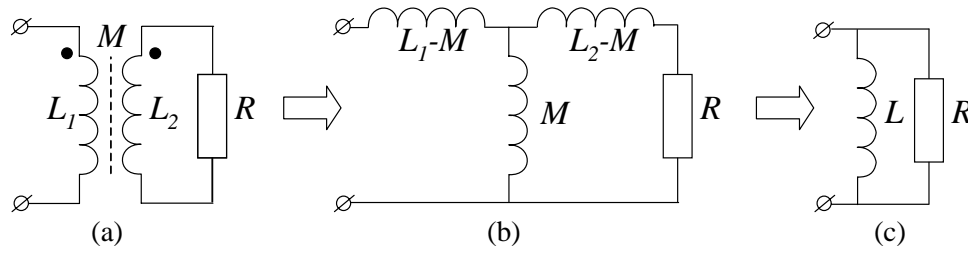


Figure 4.20: Eddy currents can be modeled as a transformer (a), which can also be represented by a T-equivalent model (b). When $L = L_1 = L_2 = M$, this reduces to a parallel arrangement of L and R (c).

the interaction between the deflection yoke and the drive circuit. Note that although these models are primarily of interest to circuit designers of television and computer-monitor sets, they are possibly also useful for transformer designers [170]. Circuit models for high frequencies are not only useful for analyzing how to reduce ringing in deflection yokes, but they also help to improve the cooperation of designers of deflection yokes with designers of drive circuits.

The structure of this section is the following. First, some conventional low-frequency circuit models are described and the basic principles for an electrical description of damped RCL oscillations are reviewed. Subsequently, new high-frequency circuit models are introduced. We will show that the oscillating currents that cause the front-of-screen ringing problem, can be adequately modeled by series of RCL circuits. Finally, some simulation results and experimental results are presented.

4.5.1 Equivalent circuit models for differential-mode ringing

At this stage it is useful to have a closer look at the equivalent circuit model of a pair of line coils. Various equivalent circuits can be used to simulate an inductor [192]. In Chapter 2 we introduced a single inductance as equivalent circuit model for a pair of line coils. In Chapter 3 we extended this inductance with a series resistance R_s to describe the eddy current losses. This equivalent circuit, shown in Fig. 4.19a, was suited well for describing the power loss, but the disadvantage is that the resistance R_s depends strongly on the frequency. This makes this circuit model difficult to use in regular circuit simulation programs.

To first order, the losses can also be modeled by a fixed series resistance R_{dc} and a fixed resistance R_p parallel to the inductance. The resistance R_{dc} models the dc Ohmic losses and the resistance R_p models the eddy current

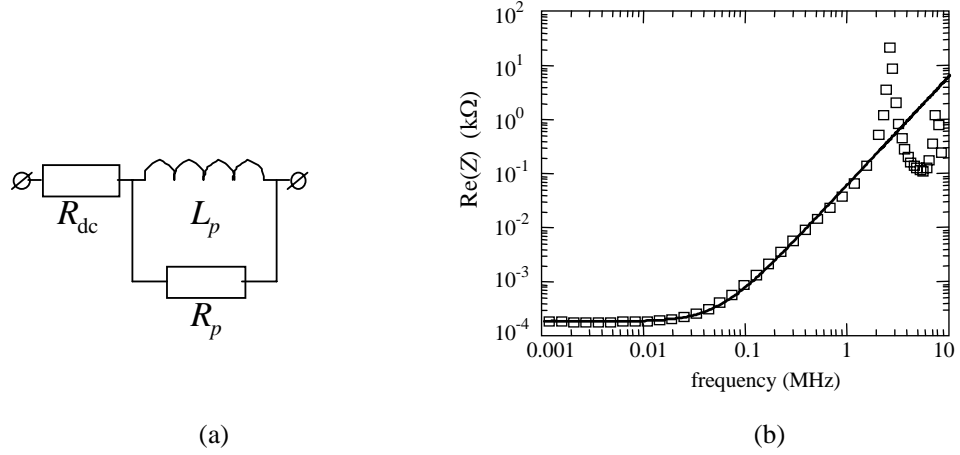


Figure 4.21: (a) a simple parallel RL model; (b) comparison of the measured real part of the impedance of 17'' CMT line coils with $13 \times 236 \mu\text{m}$ wires (squares) with a fit to this model.

losses.

The resistance R_p can be connected either across the series arrangement of the inductance and the dc resistance as shown in Fig. 4.19b, or across the inductance only as shown in Fig. 4.19c. For the parallel inductance L_p the same value is chosen as for the series inductance L_s . Some authors prefer the one while others prefer the other arrangement. For our analysis it is not relevant where we locate the dc resistance and we use the equivalent circuit shown in Fig. 4.19c since this circuit is easier to analyze. In this circuit, the losses are modeled by a fixed series resistance R_{dc} and a fixed resistance R_p parallel to the inductance.

The reason why a parallel resistance is a more convenient choice than a series resistance is related to the physics of eddy currents. In fact we could model eddy currents by a transformer in which the intended current flows through the primary side of the transformer, as shown in Fig. 4.20a. The magnetic field generated by the primary inductance L_1 , induces currents in a resistive material; in our case the resistance is located in parts of the copper wires themselves, but it could also be in some other conductive material in the neighborhood, such as e.g. gun parts. The induction of current through a resistive material can be modeled by a mutual coupling M with a secondary coil L_2 of the transformer with a resistive load R . When $L_1 = L_2 = M$, this circuit can be reduced to a parallel arrangement of an inductance and a resistance indeed, as shown in Fig. 4.20c.

The impedance $Z(\omega)$ of the equivalent circuit shown in Fig. 4.19c is given

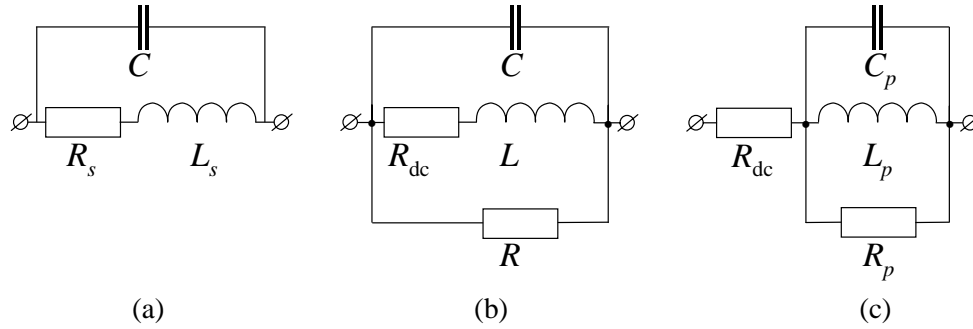


Figure 4.22: Alternative equivalent circuits to model ringing of CRT deflection coils.

by

$$Z(\omega) = R_{dc} + \frac{R_p}{1 + (R_p/\omega L_p)^2} + j\omega L_p \frac{1}{1 + (\omega L_p/R_p)^2} \quad (4.12)$$

For low frequencies, when $\omega L_p < R_p$, the real part is approximated by

$$R_{lf} = R_{dc} + \frac{\omega^2 L_p^2}{R_p} \quad (4.13)$$

This quadratic dependence on the frequency is in agreement with the low-frequency approximation of both the skin effect and the proximity effect (see Sect. 3.4.2).

The impedance of the line coils of a 17" CMT with $13 \times 236\text{-}\mu\text{m}$ wires has been measured with an HP4116A frequency analyzer. The real part of the impedance is shown in Figure 4.21. This figure illustrates that practical experimental results of frequency-dependent resistance can be adequately fitted with this model. With an impedance $L_p = 124\text{ }\mu\text{H}$, a value $R_p = 9.8\text{ k}\Omega$ is found in this case.

For frequencies above 500 kHz, the real part of the impedance no longer increases quadratically with the frequency. For proximity losses this is clear from Eq. 3.49. Consequently, the impedance of the line coils can no longer be modeled by a fixed resistance parallel to the inductance.

Although the RL model gives a close fit of the impedance characteristic for frequencies below 500 kHz and is suited for modeling the dissipation, it does not describe ringing.

In the same way, the capacitances in the coil can be modeled by a parallel capacitance in the equivalent circuit model. Again we have a number of choices, as shown in Fig. 4.22. The electrical properties of the line coils can be described by all of these circuit models, but the parameter values will be

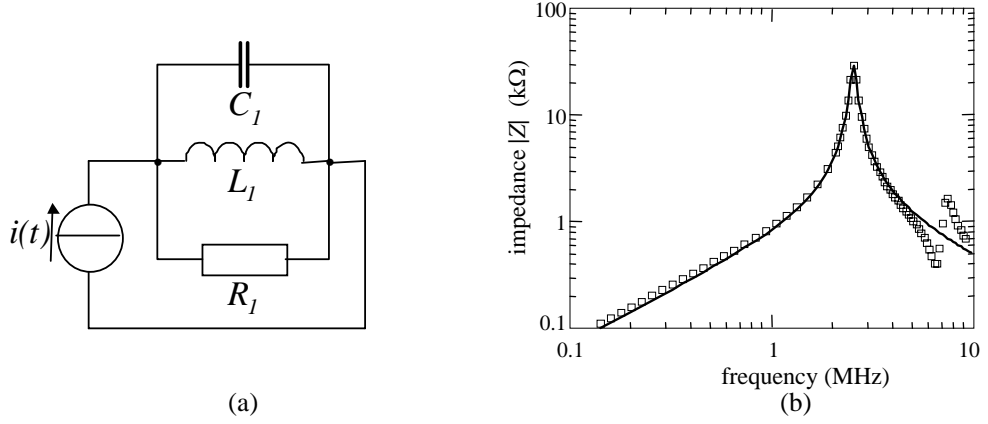


Figure 4.23: (a) the single-*RCL* model; (b) comparison of the measured impedance characteristic (squares) of 17'' CMT line coils with $13 \times 236\text{-}\mu\text{m}$ wires with a fit of the single-*RCL* model.

different in general and will be frequency dependent. We choose for the circuit in which the three components are simply in parallel (Fig. 4.22c), because this circuit is the easiest to analyze analytically. With this circuit, a convenient description with fixed parameter values can be obtained in a certain frequency range.

We follow a pragmatic approach. We propose a simple equivalent circuit model which we can easily analyze analytically and validate that this equivalent circuit model accurately describes the impedance characteristic up to 10 MHz with fixed parameter values.

Single-*RCL* model

Impedance measurements deviate from the impedance predicted by the *RL* model due to the parasitic capacitances of the deflection coils. For higher frequencies, the measured impedance is adequately fitted to the single-*RCL* model shown in Fig. 4.23a.

To first order, the impedance $Z(\omega)$ of the line-coil pairs is modeled by a lumped circuit model with a fixed capacitance C , parallel to both a fixed inductance L and a resistance R . Although the value of this parallel resistance actually varies slightly with frequency, we will see that a fixed value of R already results in a useful description of the impedance.

The impedance of this parallel *RCL* model is given by

$$Z_{RCL}(\omega) = \left(\frac{1}{R} + \frac{1}{j\omega L} + j\omega C \right)^{-1} \quad (4.14)$$

Figure 4.23b shows a comparison between the experimental results and a least-squares fit with this lumped RCL model to the impedance characteristic of the line coils of a 17" CMT with 13×236-μm wires. The fitting parameters are $R = 27.7 \text{ k}\Omega$, $C = 35 \text{ pF}$ and $L = 111 \text{ }\mu\text{H}$.

To make fitting easier, Eq. 4.14 is rewritten as

$$Z_{RCL}(\omega) = \frac{R}{1 + jQ\left(\frac{\omega}{\omega_o} - \frac{\omega_o}{\omega}\right)} \quad (4.15)$$

with $Q = R\sqrt{C/L}$ and $\omega_o = 1/\sqrt{LC}$. For fitting to $|Z_{RCL}(\omega)|$, we use 2π times the peak frequency f_o of the first peak of the impedance characteristic as a first guess for ω_o . Furthermore, we use the peak value of the impedance characteristic as a first guess for R . As a first guess for Q , the ratio $f_o/\Delta f$ is used in which Δf denotes the width of the impedance characteristic $|Z_{RCL}(\omega)|$ at $1/\sqrt{2}$ of the peak value.

Damped RCL parallel oscillation

In this section, we summarize the basic principles of the damped oscillation of the parallel RCL circuit shown in Fig. 4.23a for a damped oscillation, i.e. for $\omega_o^2 - \tau^{-2} > 0$ with $\tau = 2RC$ and $\omega_o = 1/\sqrt{LC}$.

After a sharp current pulse with amplitude \hat{i} and duration Δt , the voltage across a parallel RCL circuit is given by

$$v(t) = \frac{\hat{i}\Delta t}{C} e^{-t/\tau} \left\{ \cos(\omega_r t) + \frac{1}{\omega_r \tau} \sin(\omega_r t) \right\} \quad (4.16)$$

with damped resonance frequency $\omega_r = \sqrt{\omega_o^2 - \tau^{-2}}$. From Eq. 4.16 we see that the voltage oscillates with frequency ω_r and that the amplitude of this oscillation drops exponentially with decay time τ .

The ratio

$$Q = \frac{1}{2}\omega_o\tau = R\sqrt{C/L} \quad (4.17)$$

is called the quality factor of the parallel RCL circuit. The higher its value, the longer the decay of the oscillation takes.

Unfortunately, the single- RCL model is not suited to describe ringing of CRT deflection coils. As described in Chapter 2, the line drive circuit is to first order modeled by a closed switch in series with a dc voltage during

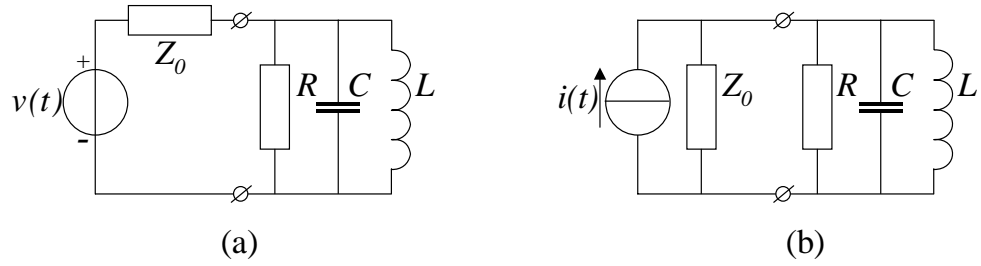


Figure 4.24: The drive circuit is modeled by (a) a voltage source v_0 and series impedance Z_0 , or its Norton equivalent (b) a current source v_0/Z_0 and parallel impedance Z_0 .

the time that the electron beams scan along the screen. This closed switch imposes a short-circuit parallel to the RCL circuit so that no oscillations can occur.

In the following two sections we explore two possibilities to extend the single- RCL model such that ringing can be explained:

- a) include the impedance of the drive circuit;
- b) extend the single- RCL model to a more complex model.

a) Influence of the impedance of the drive circuit

The first possibility to extend the single- RCL model such that ringing becomes possible, is to include the impedance of the drive circuit.

During the time that the electron beams scan the screen, we model the drive circuit by a voltage source v_0 with a series output impedance Z_0 , see Fig. 4.24a. This circuit is easily analyzed by modeling the drive circuit by its Norton equivalent, i.e. a current source $i_0 = v_0/Z_0$ with a parallel output impedance Z_0 (see e.g. [132], page 179), as shown in Fig. 4.24b. We consider the following two simplified cases:

- i. the output impedance Z_0 is a pure resistance;
- ii. the output impedance Z_0 is a pure inductance.

i. The output impedance Z_0 is a pure resistance In the Norton equivalent circuit, the output resistance R_0 is in parallel to the resistance R of the RCL circuit. These two resistances can be replaced by a single resistance $R' = R_0 R / (R_0 + R)$ and the circuit of Fig. 4.23a results with

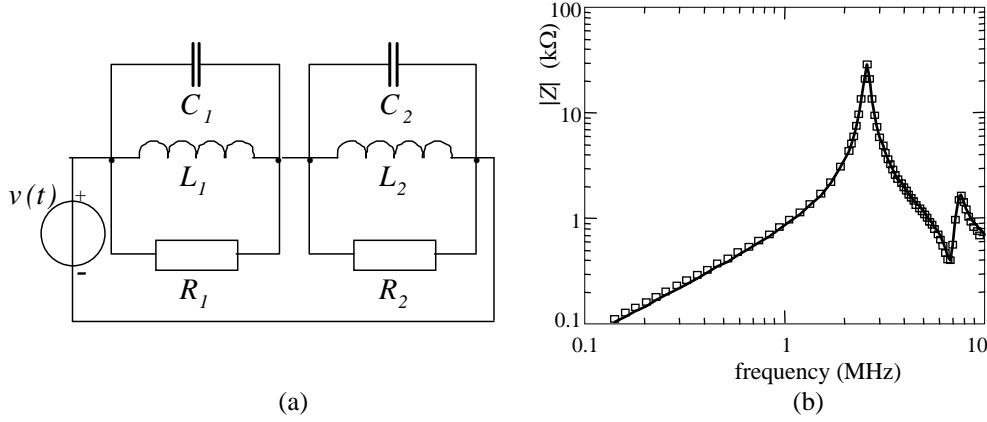


Figure 4.25: (a) the two- RCL -sections circuit model for differential-mode ringing; (b) comparison of the measured impedance characteristic (squares) with a fit of the two- RCL -sections model. The impedance was measured of a the line coils of a 17''CMT with $13 \times 236\text{-}\mu\text{m}$ wires.

$i_0 = v_0/R_0$. As analyzed in Sect. 4.5.1, this circuit oscillates with frequency $\omega_r = \sqrt{(LC)^{-1} - (2R'C)^{-2}}$.

With the fitting parameters $L = 111\text{ }\mu\text{H}$ and $C = 35\text{ pF}$ of the measured impedance, shown in Fig. 4.23b, a resonance frequency of 2.5 MHz results. Since in practical applications a resonance frequency of 5 to 6 MHz is measured for the differential-mode line-coil ringing, we conclude that the ringing is not modeled adequately by a single RCL model driven by a source with a resistive output impedance.

ii. The output impedance Z_0 is a pure inductance In the Norton equivalent circuit, the output inductance L_0 is in parallel to the inductance L of the RCL circuit. The two inductances can be replaced by $L' = L_0 L / (L_0 + L)$ and the circuit of Fig. 4.23a results with $i_0 = v_0 / (\omega L)$. This circuit oscillates with frequency $\omega_r = \sqrt{(L'C)^{-1} - (2RC)^{-2}}$.

Especially at higher frequencies, long leads introduce inductance. Furthermore, capacitors in the drive circuit are no longer purely capacitive. However, even if we would assume a total series inductance of $L_0 = 1\text{ }\mu\text{H}$, we end up with a predicted resonance frequency above 25 MHz. Since this is much higher than the frequencies found in practical applications, we conclude that also a single RCL model driven by a source with a purely inductive output impedance can not explain the observed ringing.

b. Two-*RCL*-sections model

Another possibility to model ringing is to use a more complicated model of the CRT deflection coils than the single-*RCL* model. In fact, we have already an indication that ringing is mainly caused by internal oscillations in the deflection coils rather than by the impedance of the leads, because we measured a similar resonance curve in the magnetic frequency-response measuring setup as in the optical frequency-response measuring setup. In the optical frequency-response measuring setup a drive circuit is used with about 1 m long interconnections, whereas in the magnetic frequency-response measuring setup the deflection yoke was directly driven by the HP4192A Impedance Analyzer with only 10 cm leads and no drive electronics.

A better model to describe differential-mode line-coil ringing is obtained by further analyzing the impedance of the line coil as function of frequency. In the measured impedance characteristic of the line coils of a 17" CMT, Fig. 4.17b, we clearly see two resonance peaks. The first resonance peak in the measured impedance characteristic is adequately described by the simple *RCL* model, but that model does not describe the second resonance peak. This brings us to the idea to try two *RCL* combination in series, as suggested by Foster [193, 194], see Fig. 4.25a.

Figure 4.25b shows the measured impedance of the line coils of 17" CMT together with a fit to this new two-*RCL*-sections model. The fitted curve is close to the measured impedance from 1 to 10 MHz including the first two resonance peaks. The fitting parameters are:

$$\begin{aligned} R_1 &= 27.7 \text{ k}\Omega; & R_2 &= 1.4 \text{ k}\Omega \\ L_1 &= 111 \text{ }\mu\text{H}; & L_2 &= 2.7 \text{ }\mu\text{H} \\ C_1 &= 35 \text{ pF}; & C_2 &= 179 \text{ pF} \end{aligned}$$

In fact, the two-sections-*RCL* model should be extended with a dc resistance in series. Otherwise the model has a zero impedance for low and very high frequencies. This series resistance is also mandatory in circuit simulation programs. For our analytical ringing analysis, however, we omit this series resistance because it is much smaller than the impedance of the *RCL* branches for frequencies above 100 kHz and because it strongly simplifies our analysis. Later on, we will analyze the effect of including a series impedance by circuit simulation and we will see that the total response is still dominated by the damped sine wave that we find in our simplified analysis.

In the remainder of this section we will derive the optical (and thus also the magnetic) frequency response with the two-*RCL*-sections model. First we show that the currents in this model oscillate and we will calculate the resonance frequency and the decay time. Subsequently, we derive the front-

of-screen performance in more detail.

In Sect. 4.4.1 we showed that the optical front-of-screen performance is related to the voltage across the coil that generates the magnetic field for deflection. To derive the optical frequency response of the two-*RCL*-sections model of Fig. 4.25a, we need to calculate how the voltages across the two *RCL* branches depend on the drive signal. We model the drive circuit for ac signals as a closed switch during the time that electron beams scan the screen (Sect. 2.3.4).

We calculate the voltage v_1 across inductance L_1 . The voltage v_2 across inductance L_2 is simply found by interchanging indices 1 and 2. The impedance $Z_1(\omega)$ of a parallel R_1, C_1, L_1 circuit is given by

$$Z_1(\omega) = \left(\frac{1}{R_1} + \frac{1}{j\omega L_1} + j\omega C_1 \right)^{-1} \quad (4.18)$$

and a similar expression is obtained for $Z_2(\omega)$ as function of R_2, C_2 , and L_2 .

If we define the transfer function $H_1(\omega)$ as the ratio between the voltage $v_1(\omega)$ across L_1 and the voltage $v_0(\omega)$ across the network, then

$$H_1(\omega) = \frac{v_1(\omega)}{v_0(\omega)} = \frac{Z_1(\omega)}{Z_1(\omega) + Z_2(\omega)} \quad (4.19)$$

The analysis is simplified by introducing the following parameters:

$$R_r = \frac{R_1 R_2}{R_1 + R_2} \quad (4.20)$$

$$L_r = \frac{L_1 L_2}{L_1 + L_2} \quad (4.21)$$

$$C_r = C_1 + C_2 \quad (4.22)$$

and

$$\sigma_1 = \frac{1}{2R_1 C_1}, \quad \sigma_2 = \frac{1}{2R_2 C_2}, \quad \sigma_r = \frac{1}{2R_r C_r} \quad (4.23)$$

$$\alpha_1 = 1/\sqrt{L_1 C_1}, \quad \alpha_2 = 1/\sqrt{L_2 C_2}, \quad \alpha_r = 1/\sqrt{L_r C_r}$$

$$\omega_1 = \sqrt{\alpha_1^2 - \sigma_1^2}, \quad \omega_2 = \sqrt{\alpha_2^2 - \sigma_2^2}, \quad \omega_r = \sqrt{\alpha_r^2 - \sigma_r^2}$$

where e.g. α_1 denotes the undamped oscillating frequency and ω_1 the damped oscillating frequency of the $R_1 C_1 L_1$ circuit.

With these notations, the transfer function $H_1(\omega)$ can be written as

$$H_1(\omega) = \frac{C_1}{C_r} \frac{\omega_2^2 + (\sigma_2 + j\omega)^2}{\omega_r^2 + (\sigma_r + j\omega)^2} \quad (4.24)$$

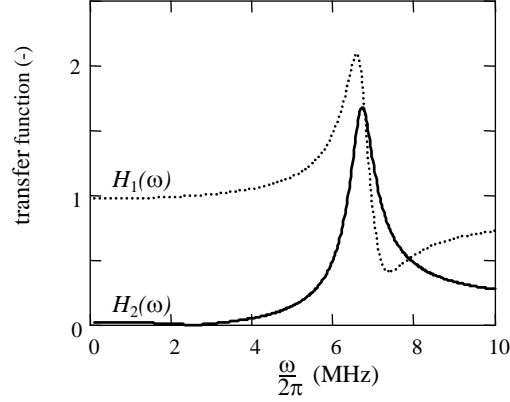


Figure 4.26: The absolute values of the transfer functions $H_1(\omega)$ and $H_2(\omega)$ as functions of frequency.

From a similar calculation we find for the transfer function $H_2(\omega)$, the ratio between the voltage $v_2(\omega)$ across L_2 and the voltage $v_0(\omega)$ across the network:

$$H_2(\omega) = \frac{C_2}{C_r} \frac{\omega_1^2 + (\sigma_1 + j\omega)^2}{\omega_r^2 + (\sigma_r + j\omega)^2} \quad (4.25)$$

The voltage $v_1(t)$ across L_1 after applying a short rectangular pulse with value \hat{v} during a very short period of time Δt to the network, is calculated with the inverse Fourier transformation¹ after modeling the pulse by a Dirac pulse. The result for $t > 0$ is

$$v_1(t) = 2\hat{v}\Delta t \frac{C_1}{C_r} (\sigma_2 - \sigma_r) (\cos \omega_r t + q_2 \sin \omega_r t) e^{-\sigma_r t} \quad (4.26)$$

with

$$q_2 = \frac{\sigma_2 - \sigma_r}{2\omega_2} + \frac{\omega_2^2 - \omega_r^2}{2\omega_2(\sigma_2 - \sigma_r)} \quad (4.27)$$

This describes a damped oscillation with frequency ω_r , decay time $1/\sigma_r$ and amplitude a_r given by

$$a_r = 2v_0\Delta t \frac{C_1}{C_r} (\sigma_2 - \sigma_r) \sqrt{1 + q_2^2} \quad (4.28)$$

¹Using the identities ([195], Chapter 29) that the inverse Fourier transform of $\frac{1}{(a+j\omega)^2+b^2}$ is $\frac{1}{b}e^{-at} \sin(bt)$ and that the inverse Fourier transform of $\frac{j\omega+a}{(a+j\omega)^2+b^2}$ is $e^{-at} \cos(bt)$.

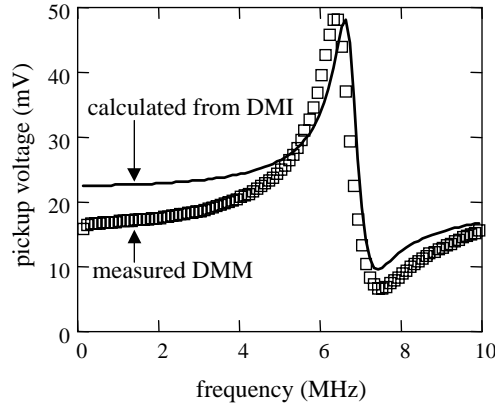


Figure 4.27: The measured Differential-Mode Magnetic (DMM) frequency response of a 17'' CMT (squares) and the transfer function $|H_1(\omega)|$ calculated from the best possible fit of the two- RCL -sections model to the measured Differential-Mode Impedance (DMI) characteristic.

Experimental results

As we showed in Fig. 4.25b, the two- RCL -sections model could be properly fitted to the differential-mode impedance characteristic of a 17'' CMT sample with $13 \times 236\text{-}\mu\text{m}$ line-coil wires. Figure 4.26 shows the absolute values $|H_1(\omega)|$ and $|H_2(\omega)|$ of the transfer functions with parameters fitted to the impedance characteristic.

Comparison of Fig. 4.26 to the optical frequency response, Fig. 4.9, and the magnetic frequency response, Fig. 4.14, shows that $|H_1(\omega)|$ is very similar to our measured DM magnetic frequency response, while $|H_2(\omega)|$ is very similar to the CM magnetic frequency response. Figure 4.27 shows both the Differential-Mode Magnetic (DMM) frequency response and the transfer function $|H_1(\omega)|$ calculated from the Impedance Frequency Characteristic. In this figure, the transfer function is normalized appropriately to achieve the same maximum value. This example illustrates that the resonance peak in the magnetic frequency response can be adequately predicted by the transfer function calculated from the fitting parameters of the impedance characteristic.

Furthermore, we could also choose not to use the impedance characteristic at all and directly fit the absolute value of the transfer function $H_1(\omega)$, Eq. 4.24, to the measured magnetic frequency response. The amplitude of the magnetic frequency response depends on e.g. the size and position of the pickup coil and we have to use a proportionality factor rather than the ratio

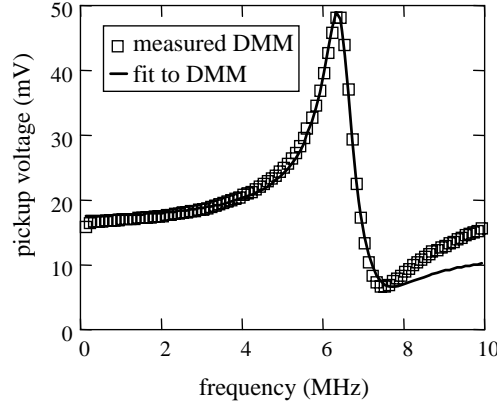


Figure 4.28: Fit of the absolute value of the transfer function $H_1(\omega)$ to the measured DM magnetic frequency response of a 17" CMT.

of C_1 and C_r :

$$H_1(\omega) \propto \frac{\omega_2^2 + (\sigma_2 + j\omega)^2}{\omega_r^2 + (\sigma_r + j\omega)^2} \quad (4.29)$$

Unfortunately, we cannot calculate all the six circuit parameters ($R_1, C_1, L_1, R_2, C_2, L_2$) from the five fitted parameters ($\sigma_2, \sigma_r, \omega_2, \omega_r, a_m$) of the fit of the frequency response.

Figure 4.28 shows that the transfer function can indeed be fitted to the measured magnetic frequency response. Table 4.1 gives a comparison between the fitted parameter values of this transfer function and the values calculated from the parameters of the fitted impedance characteristic, using Eq. 4.23. The fitting parameters, obtained from the Differential-Mode Magnetic (DMM) frequency response and the Differential-Mode Impedance (DMI) characteristic, respectively, agree quite well for the frequency parameters ω_2 and ω_r . For the damping parameters σ_2 and σ_r the results differ significantly but are still of the same order of magnitude. If we take into account that

fit to	$\sigma_2/2\pi$ (MHz)	$\sigma_r/2\pi$ (MHz)	$\omega_2/2\pi$ (MHz)	$\omega_r/2\pi$ (MHz)
DMM	0.55	0.34	7.4	6.4
DMI	0.32	0.28	7.2	6.7

Table 4.1: Comparison of the parameters fitted to the Differential-Mode Magnetic (DMM) frequency response and the parameters calculated from the six parameters of the fitted Differential-Mode Impedance (DMI) characteristic.

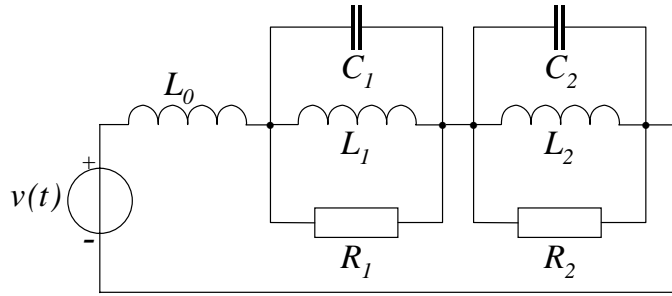


Figure 4.29: The interaction with the drive circuit is modeled by an inductance in series with the two-*RCL*-sections model.

the DMM and DMI fitting parameters are obtained by completely different measuring methods, the agreement in the corresponding fitting parameters is remarkably good.

The use of the fitting formula, Eq. 4.29, and the relation to a circuit model is a major breakthrough. In Sect. 4.4.1 we presented the measured optical frequency response but at that time we could only present the experimental results as measured data in a picture. In Sect. 4.4.3 we showed that the magnetic frequency response is very similar to the optical frequency response, but still we had to present the experimental results graphically. The analysis in the previous section enables us to characterize the frequency response by only a few fitting parameters.

Furthermore, we have derived how these parameters are related to the parameters in a circuit model. This is an important step too, because it enables us to establish a relation to the design parameters of CRT deflection coils (Sect. 5.1).

Circuit interaction

The circuit models that we developed to describe ringing of deflection yokes do not only enable us to characterize ringing under ideal drive conditions, but they also enable us to analyze the effect on ringing of all kinds of design choices for the circuit design. With circuit-simulation programs, such as Spice [191], the voltages across the inductances in our circuit models are easily calculated in either the time or the frequency domain. Because the voltage across the main part of the line coil, L_1 , is proportional to the optical modulation depth (Sect. 4.4.1), these calculations give a good indication of the front-of-screen ringing performance.

As an illustration, we discuss the impact of a series inductance on the ringing performance. Connecting leads and capacitors in the drive circuit

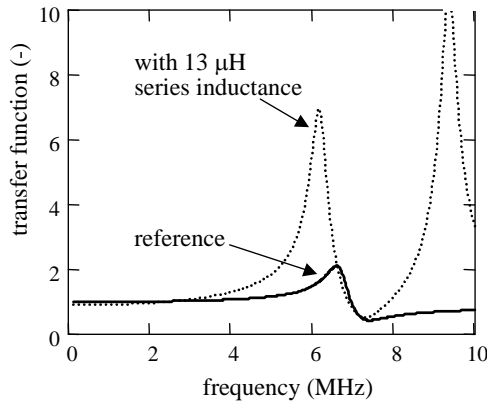


Figure 4.30: The calculated effect of a series inductance on the transfer function. The thin and thick curves show the transfer functions with and without a 13- μ H series inductance, respectively.

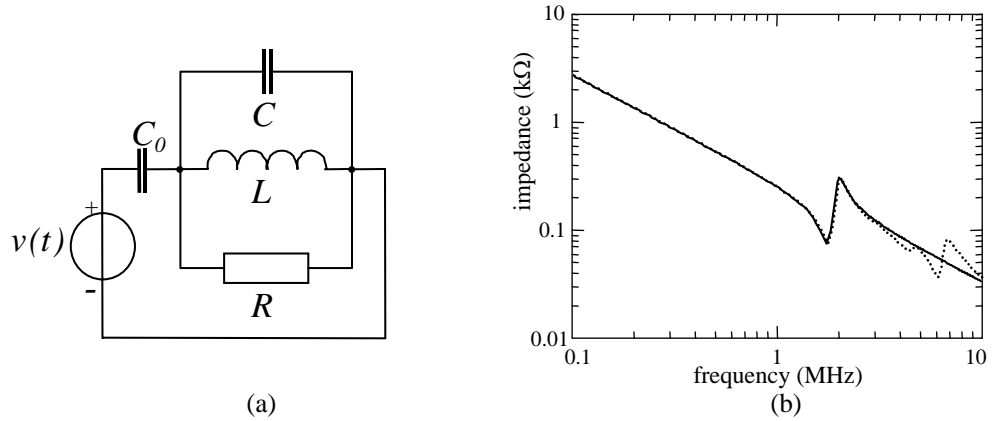


Figure 4.31: Single-*RCL* CM equivalent circuit model for common-mode ringing (a), and a comparison (b) of the impedance of its best fit (straight line) to the measured Common-Mode Impedance (CMI) (dotted line).

can be modeled by a series inductance at frequencies above 100 kHz. This inductance might have a significant impact on the ringing behavior. As an example we have both simulated and measured the impact of adding a small inductance in series with the line coil and the drive circuit on the differential-mode ringing, as shown in Fig. 4.29. The result in Fig. 4.30 is a much higher resonance peak at a somewhat lower frequency than without the series inductance, similar to the result that we have found in the magnetic frequency-response measurements, see Fig. 4.13. Clearly, a large output impedance of the drive circuit enhances ringing.

A second resonance peak appears at a higher frequency. Note that this peak was not found in the frequency-response measurements. Approximately, it corresponds to the resonance of the series inductance L_0 with the series arrangement of C_1 and C_2 . Apparently, our model is still too simple for frequencies near 10 MHz. For instance, resistances could be added in series to the capacitances in our model. However, we will not extend our two-*RCL*-sections model further, because this model allows us to describe ringing in practical cases.

4.5.2 Equivalent circuit model for common-mode ringing

In the previous section, circuit models were introduced that could be fitted successfully to the differential-mode impedance characteristic. Subsequently, from the two-*RCL*-sections model the measured differential-mode optical and magnetic frequency responses have been adequately explained.

In the following two sections, models are presented to describe the Common-Mode Impedance (CMI) characteristic as well as the corresponding optical and magnetic frequency response.

Single-*RCL* CM model

The Common-Mode (CM) current flows through the parasitic capacitance between line coils and frame coils. When we consider a single resonance peak, we introduce the circuit of Fig. 4.31a. Figure 4.31b shows the measured CM impedance characteristic and the best possible fit of the single-*RCL* CM model to these experimental results. The fitting parameters are $C_0 = 58.2$ pF, $R = 2.40$ k Ω , $C = 275$ pF and $L = 22.8$ μ H.

Similar to the previous section we define the transfer function $H_{\text{cm}}(\omega)$ as the ratio between the voltage $v_L(\omega)$ across L and the voltage $v_0(\omega)$ across the network. This transfer function can be written as

$$H_{\text{cm}}(\omega) = \frac{Z_{RCL}(\omega)}{Z_C(\omega) + Z_{RCL}(\omega)} \quad (4.30)$$

in which $Z_C(\omega) = 1/j\omega C_0$ represents the impedance of the capacitance C_0 between the line coils and the frame coils, while $Z_{RCL}(\omega)$ gives the impedance of the parallel *RCL* circuit (see Eq. 4.14).

With the notations

$$\begin{aligned}\sigma_c &= \frac{1}{2R(C_0 + C)} \\ \alpha_c &= \frac{1}{\sqrt{L(C_0 + C)}} \\ \omega_c &= \sqrt{\alpha_c^2 - \sigma_c^2}\end{aligned}\tag{4.31}$$

the transfer function $H_{\text{cm}}(\omega)$ can be written as

$$H_{\text{cm}}(\omega) = \frac{-\omega^2}{(j\omega + \sigma_c)^2 + \omega_c^2}\tag{4.32}$$

The voltage across the *RCL* circuit after applying a short rectangular pulse with value \hat{v} during a very short time Δt to the total network, is calculated by applying an inverse Fourier transformation to Eq. 4.32. The result is:

$$v_{\text{RCL}}(t) = \hat{v}\omega_c \frac{C_0}{C_0 + C} \Delta t \left\{ 2\frac{\sigma_c}{\omega_c} \cos \omega_c t + \left(1 - \frac{\sigma_c^2}{\omega_c^2}\right) \sin \omega_c t \right\} e^{-\sigma_c t}\tag{4.33}$$

This describes a decaying oscillation with frequency ω_c , decay time $\tau = 1/\sigma_c$ and initial amplitude a_c given by

$$a_c = \hat{v}(\omega_c + \sigma_c) \Delta t \frac{C_0}{C_0 + C}\tag{4.34}$$

Multi-*RCL* CM model

In the previous section we have analyzed the most simple case that gives rise to common-mode ringing. In practice, more resonance peaks are observed at higher frequencies. These can be described adequately by including more *RCL* branches in series. Figure 4.32 shows the circuit model for four ringing frequencies.

Rather than fitting the impedance of the circuit model to the measured impedance data, fitting with the real part of both impedances turns out to be a better choice. The modulation in the real part is much larger than the modulation in the absolute value of the impedance, which makes fitting to the real part much easier.

The fitting has been made with a least-squares fit to each peak in the impedance characteristic separately. Figure 4.33 shows the separate fits to the first four peaks of the real part of the measured common-mode impedance

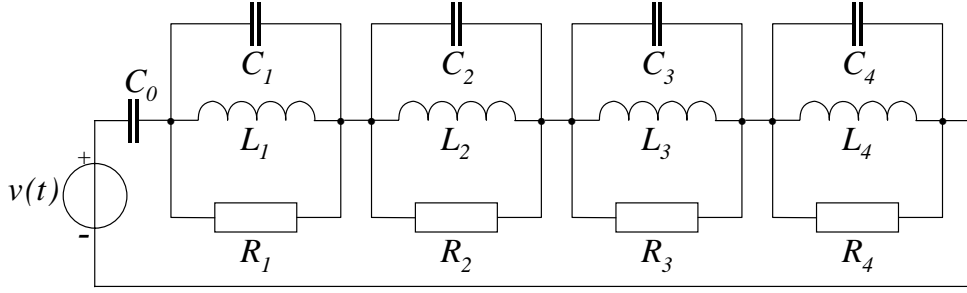


Figure 4.32: Circuit model for four common-mode ringing frequencies.

characteristic. The slope of the absolute value of the impedance $|Z|$ as a function of frequency between 1 kHz and 1 MHz, corresponds to an impedance of $C_0 = 58.2$ pF. The fitting parameters R, C, L for each peak separately are listed in Table 4.2 together with values for ω_c and σ_c calculated from these fitting parameters (using Eq. 4.31).

The analysis of the extended circuit model is similar to that for a single common-mode ringing frequency, but is not really straightforward. We work out the case of n RCL subcircuits in series with the main capacitance C_0 , because we often measure more than one resonance peak. Figure 4.32 shows the circuit model for $n = 4$.

If $Z_{RCL,i}(\omega)$ represents the impedance of each parallel $R_i C_i L_i$ circuit and $Z_C(\omega)$ represents the impedance of the capacitance C_0 , the total series impedance of the circuit is

$$Z_{\text{cm}}(\omega) = Z_C(\omega) + \sum_i Z_{RCL,i}(\omega) \quad (4.35)$$

The measured impedance characteristic $Z_{\text{cm}}(\omega)$ is shown in Fig. 4.33. The transfer function $H_{\text{cm},i}(\omega)$, the ratio between the voltage across L_i and the

CMI peak	R (Ω)	C (pF)	L (μH)	$\omega_c/2\pi$ (MHz)	$\sigma_c/2\pi$ (MHz)
1st	2400	275	22.8	1.82	0.10
2nd	144	1280	2.38	2.79	0.41
3rd	200	752	1.55	4.46	0.49
4th	551	293	1.93	6.10	0.41

Table 4.2: The R, C, L values of the separate fits to the four resonance peaks of the measured impedance characteristic and parameter values of the CM transfer function calculated from these R, C, L values.

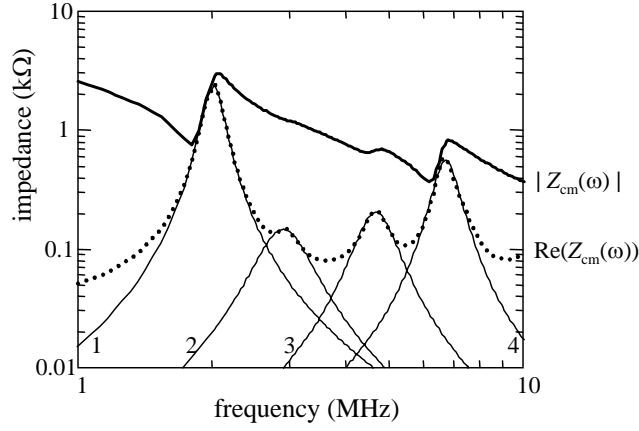


Figure 4.33: Fitting results (thin lines) to the first four peaks of the real part of the measured common-mode impedance $\text{Re}(Z_{\text{cm}}(\omega))$. For reference also the absolute value $|Z_{\text{cm}}(\omega)|$ of the impedance is shown (top line).

voltage across the network, equals:

$$H_{\text{cm},i}(\omega) = \frac{Z_{\text{RCL},i}(\omega)}{Z_{\text{cm}}(\omega)} \quad (4.36)$$

The combined effect of the various $H_{\text{cm},i}(\omega)$ is not simply found by adding them for each RCL . In Sect. 4.4.3 we showed that the impact on the front-of-screen performance depends also on the effective area and the number of turns for the resonant part of the coil. Because the effective area and the number of turns of these parts of the coil - that contribute to the ringing - are not known, we introduce the proportionality factor $\alpha_{\text{cm},i}$ to obtain the total transfer function

$$H_{\text{cm},\text{T}}(\omega) = \sum_i \alpha_{\text{cm},i} H_{\text{cm},i}(\omega) \quad (4.37)$$

Figure 4.34 shows the absolute values of the transfer functions $H_{\text{cm},i}(\omega)$ calculated from the common-mode impedance characteristic. If we compare these curves with the measured magnetic frequency response in Fig. 4.14, we see a clear similarity between the transfer functions derived from the common-mode impedance characteristic, and the MFR except for the first transfer function $H_{\text{cm},1}(\omega)$. Based on this, we substitute $\alpha_{\text{cm},1} = 0$ and $\alpha_{\text{cm},2} = \alpha_{\text{cm},3} = \alpha_{\text{cm},4} = 1$ in Eq. 4.37. Figure 4.35 shows the absolute value of the resulting sum $H_{\text{cm},2} + H_{\text{cm},3} + H_{\text{cm},4}$ as a function of frequency, calculated from the common-mode impedance characteristic. The resulting curve looks similar to the measured common-mode magnetic frequency response in Fig. 4.14.

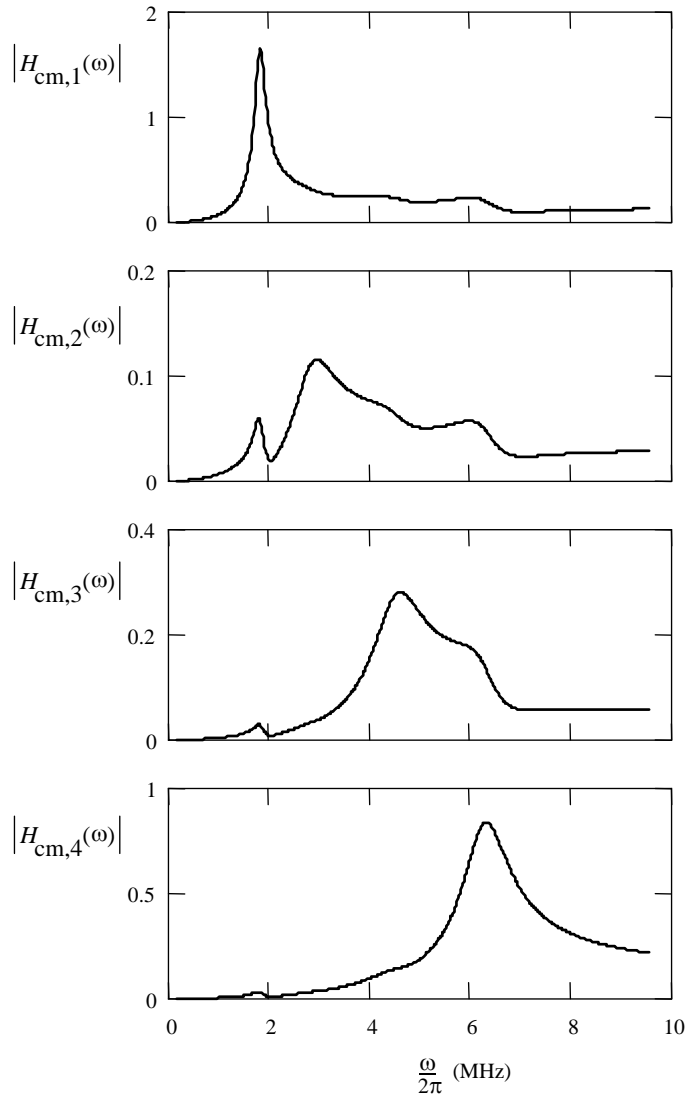


Figure 4.34: The absolute values of the separate transfer functions successively calculated from the common-mode impedance characteristic.

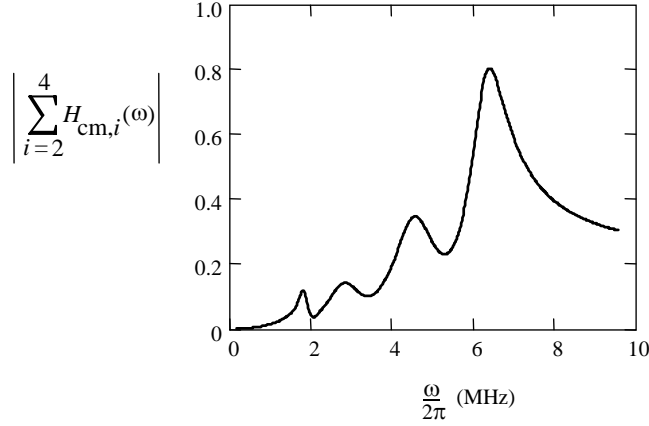


Figure 4.35: The absolute value of the total transfer function as a function of frequency, obtained by adding the separate transfer functions calculated successively from the 2nd, 3rd and 4th resonance peaks in the common-mode impedance characteristic.

Notice that each of the three transfer functions $H_{\text{cm},2}$, $H_{\text{cm},3}$ and $H_{\text{cm},4}$ has at least two resonance peaks. They all contribute to the first resonance peak near 1.8 MHz of the total transfer function.

A possible explanation for the choice $\alpha_{\text{cm},1} = 0$ is that $H_{\text{cm},1}(\omega)$ describes the effect of a coil current which produces an additional magnetic field perpendicular to the line magnetic field so that it is not seen by the pick-up coil which is only sensitive in the direction of the line magnetic field. Obviously, the transfer functions $H_{\text{cm},2}$, $H_{\text{cm},3}$ and $H_{\text{cm},4}$ describe the effect of coil currents which produce magnetic fields parallel to the line magnetic field.

Experimental results

In the previous section we have shown how circuit parameters of a model with four *RCL* subcircuits in series with the main capacitance C_0 can be fitted to the measured common-mode impedance characteristic. With those fitted circuit parameters and an appropriate choice for the relevance of the four subcircuits for ringing, we derived a total transfer function which is very similar to the measured Common-Mode Magnetic (CMM) frequency response.

Alternatively, we can also directly fit the derived expressions for the transfer function to the measured CMM frequency response without using impedance measurements.

The common-mode transfer function Eq. 4.32 can be used to fit the

peak	$\omega_c/2\pi$ (MHz)	$\sigma_c/2\pi$ (MHz)	α_{cm} (mV)
1st	1.75	0.11	0.16
2nd	2.83	0.16	0.20
3rd	4.49	0.47	0.60
4th	6.20	0.27	1.80

Table 4.3: Parameter values of the CM transfer function fitted to the separate four resonance peaks of the measured magnetic frequency response.

separate peaks of the measured CMM frequency response, shown in Fig. 4.14. Figure 4.36 presents the curves fitted successively to the first four ringing peaks. This figure shows that the CMM frequency response can be reasonably described reasonably by the transfer function Eq. 4.32.

Table 4.3 presents the values of the fitting parameters of the magnetic frequency response (Eq. 4.32) to the first four peaks. The results are very similar to the values in Table 4.2 which were calculated after fitting the parameters to the impedance characteristic. This illustrates again that with our theory it is sufficient to measure either the (magnetic or optical) frequency response or the impedance characteristic of the deflection yoke. With each of these different experimental results, we can adequately predict the results obtained with the other methods.

4.5.3 Quality factor for ringing

For the characterization of the ringing performance of a deflection yoke, it is advantageous to have a single figure of merit for the quality of the deflection yoke with respect to ringing. Such a figure is not in common use yet, but is needed to quantify the ringing performance. Up to now, the ringing quality could not be quantified and subjective quality evaluations were required for the front-of-screen ringing.

We propose to use the quality factor Q given by Eq. 4.17, defined for the parallel RCL circuit in Sect. 4.5.1, in which we substitute the R, C, L of that part of the circuit responsible for the considered ringing frequency. The lower the value of Q , the lower the sensitivity to ringing.

In the following two sections we work out this proposal for differential-mode and common-mode ringing and show how this quality factor can be determined from either optical frequency response, the magnetic frequency response or the impedance measurements.

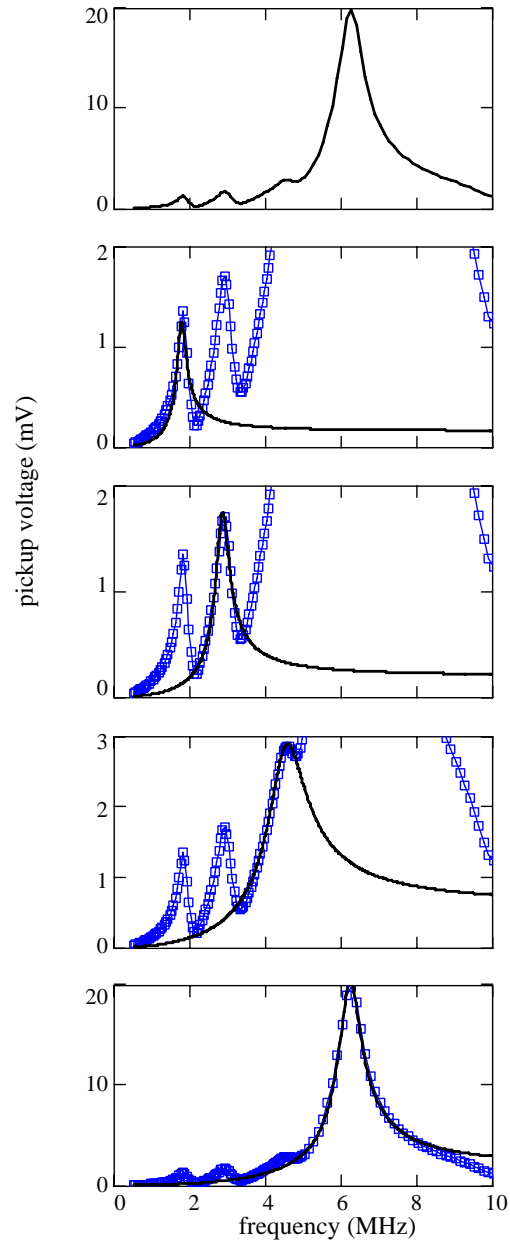


Figure 4.36: Curves fitted to the first four ringing peaks of the measured Common-Mode Magnetic (CMM) frequency response. The figure at the top shows the measured CMM response. The figures below show the fitted curves (solid lines) to the measuring results (squares). All figures have the same horizontal scale, but have different vertical scales.

Quality factor for differential-mode ringing

In Sect. 4.5.1 we introduced the two- RCL -sections model to describe differential-mode ringing. Once the parameters of this model have been fitted to the differential-mode impedance characteristic, the quality factor

$$Q_r = R_r \sqrt{C_r / L_r} \quad (4.38)$$

is easily calculated by substituting the fitted values for R_1, C_1, L_1 and R_2, C_2, L_2 in the expressions (Eqs. 4.20, 4.22 and 4.21) for R_r, C_r and L_r . The lower the value of Q_r , the lower the sensitivity to differential-mode ringing will be.

The quality factor Q_r can also be calculated from the optical frequency response or the magnetic frequency response. With the definitions of σ_r and ω_r (Eq. 4.23) we can write Q_r (Eq. 4.38) as

$$Q_r = \frac{1}{2} \sqrt{1 + \frac{\omega_r^2}{\sigma_r^2}} \quad (4.39)$$

From the DMM frequency response, an estimate for the quality factor can be obtained from the frequency f_{\max} at which the frequency response has its maximum and the width Δf of the curve at $1/\sqrt{2}$ of the maximum height (see Fig. 4.37) with the following expression:

$$Q_r \approx \frac{1}{2} \sqrt{1 + \left(\frac{2f_{\max}}{\Delta f} \right)^2} \quad (4.40)$$

If $Q_r \gg 1$, this reduces to $Q_r \approx f_{\max} / \Delta f$.

Without additional measures to reduce ringing, most line-coil pairs show ringing with a quality factor of about 10. For instance, the differential-mode magnetic frequency response shown in Fig. 4.37a has a quality factor of $Q_r = 9.5$.

Quality factor for common-mode ringing

We follow the same approach as in the previous section for deriving the quality factor for common-mode ringing. Again, once the parameters of our circuit model have been fitted to the impedance characteristic, the CM quality factor

$$Q_c = R \sqrt{C / L} \quad (4.41)$$

is easily calculated for each resonance peak by substituting the fitted values for R, C, L . The lower the value of Q_c , the lower the sensitivity to common-mode ringing will be.

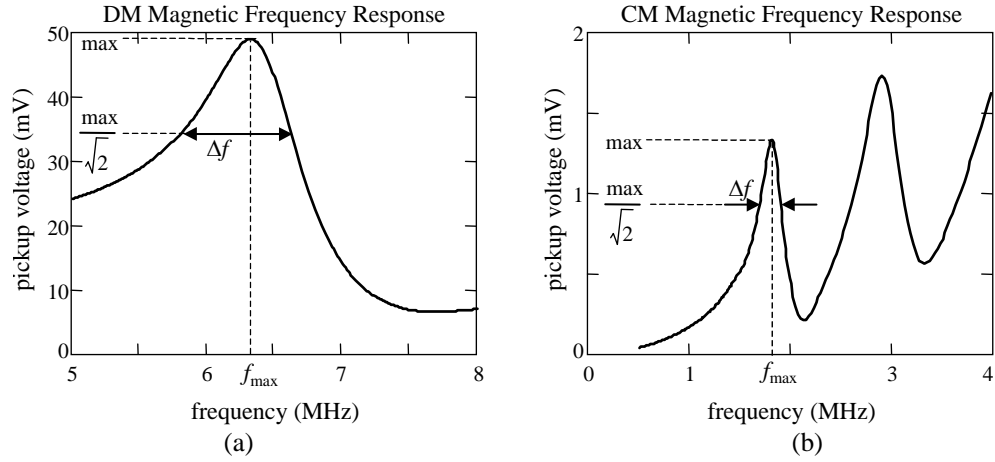


Figure 4.37: An estimate for the quality factor can be found for either (a) the differential-mode magnetic frequency response, or (b) the common-mode magnetic frequency response, from the maximum frequency f_{\max} and the width Δf at $1/\sqrt{2}$ of the maximum value.

The quality factor Q_c can also be calculated from the optical frequency response or the magnetic frequency response. Substitution of the definitions of σ_c and ω_c (Eq. 4.31) in Eq. 4.41 results in:

$$Q_c = \frac{1}{2} \sqrt{1 + \frac{\omega_c^2}{\sigma_c^2}} \quad (4.42)$$

In a similar way as described above, an estimate for the quality factor can be obtained with Eq. 4.40 from the frequency f_{\max} at which the CMM frequency response has its maximum and the width Δf of the curve at $1/\sqrt{2}$ of the maximum height). For example, the two common-mode ringing peaks in Fig. 4.37b have a quality factor of $Q_c = 9.1$ and 8.3 , respectively

4.6 Summary and conclusions

In this chapter several methods are presented for describing ringing of deflection yokes. A straightforward method is to measure the light intensity at the screen as a function of the horizontal distance from the left-hand side of the screen. The disadvantage of this method is that the results strongly depend on the driving circuitry. This hampers a systematic analysis of the ringing problem.

Rather than using the time response, we introduced two alternative methods to measure the frequency response. In the first method we measure the optical frequency response by recording the modulation depth of the variation in light intensity at the front of the screen as a function of the frequency of a sine wave voltage source which we connected in series with the deflection yoke and the drive circuitry. In the second method we measured the magnetic frequency response by measuring the amplitude of the magnetic field with a large pick-up coil inside the deflection yoke as a function of the frequency of a drive voltage which directly drives the deflection yoke. The magnetic frequency response is very similar to the optical frequency response, but is much easier to measure. Furthermore, the advantage of the magnetic frequency-response measuring method is that no drive circuitry is used so that the experimental results represent the characteristics of the deflection yoke only, whereas in the previous methods the results also depended on the drive circuit.

Both methods to measure the frequency response of a deflection yoke allow for a more detailed analysis than the straightforward measurement of variation of light intensity on the front of a picture tube. Various ringing modes can be distinguished. Different ringing peaks are visible and also a distinction can be made between differential-mode and common-mode ringing. This distinction allows for a detailed analysis of the ringing phenomenon.

Subsequently, we introduced equivalent circuit models to describe the differential-mode ringing and the common-mode ringing. A good agreement was obtained between the measured impedance characteristics and the impedance characteristic of the equivalent circuit models by a simple fit of the circuit parameters. From the equivalent circuits we derived expressions for the transfer function which we associated with the measured frequency response. For a 17" CMT deflection yoke, the derived transfer function proved to be very similar to the measured (magnetic and optical) frequency response when we calculated the parameters from the measured impedance characteristic. The derived transfer function was also very similar to the measured frequency response when we directly fitted the parameters in the formula of the transfer function.

The analytical formula derived from the circuit models enable us to describe the ringing performance of a deflection yoke with only a small number of fitting parameters. Finally, a quality factor is introduced as a figure of merit to characterize the sensitivity for ringing.

Chapter 5

Prediction of ringing

5.1 Introduction

Up to now, we have described how ringing can be measured and characterized. Before using these methods to evaluate options to suppress ringing (Chapter 6), we use them in this chapter to assess the usefulness of existing physical models for the prediction of ringing of CRT deflection coils.

In Chapter 4 we have introduced circuit models to describe ringing. In this chapter we will try to relate the circuit parameters to geometry and material properties of the deflection coils, such as the diameters of the copper wires and the thicknesses of the insulation layers.

CRT deflection coils have a complicated shape. Due to the complex geometry of the coils an exact theoretical description is difficult to achieve. Instead, we combine theoretical and empirical models. Rather than aiming at a completely consistent description, we establish general rules based on simplified models for components and derive more specific design rules from experimental results.

The organization of this chapter is the following. We start with a description of the physics of circuit models in Sect. 5.2. Subsequently, in Sect. 5.3 we review the literature on physical parameter models of solenoids, i.e. tightly wound cylindrical coils. Even for the apparently simple shape of a solenoid, the analysis is not straightforward. Finally, in Sect. 5.4, we present experimental results to test the validity of this approach.

In Chapter 6, the information obtained from this study on the electromagnetic oscillations of solenoids and individual CRT deflection coils is used to reduce the ringing of complete deflection yokes.

5.2 The physics of circuit models

The relation between the circuit model and the configuration of the coil is not straightforward. In a circuit model, the properties of the elements are described completely in terms of currents and voltages that appear at the terminals. By making suitable approximations, it is often possible to ignore the complexity of the fields inside the object. The resulting equivalent circuit shows the interconnected components as in a graph. Such an equivalent circuit is much easier to analyze than the complicated three-dimensional reality. The drawback, however, is that a lot of detail is lost and it is difficult to find a one-to-one relation between circuit parameters and design parameters.

In Chapter 3, the eddy current loss models were derived from Maxwell's equations, but no indications for electromagnetic oscillations were given there because no electric fields were considered between the turns. The derivation from Maxwell's equations of circuit models that describe both the magnetic and electric fields, turns out to be surprisingly difficult when we also consider the interior of the coil. It is fascinating that the electromagnetic behavior of coils can be described by a circuit model at all.

One of the basic assumptions in network theory is that Kirchhoff's laws are valid. The voltage law of Kirchhoff corresponds to

$$\oint \vec{E} \cdot d\vec{\ell} = 0 \quad (5.1)$$

Only under this condition the electric field can be expressed as the gradient of a scalar potential and a capacitance can be introduced based on this scalar potential. In general, Eq. 5.1 is not valid inside coils since $\oint \vec{E} \cdot d\vec{\ell} = -\partial\Phi/\partial t$ in the presence of a time-varying magnetic flux Φ through the surface around which the integral is calculated.

However, in the special case of a pair of infinitely long parallel wires with equal currents in opposite directions, the net magnetic flux through the surface perpendicular to the wires is zero such that a local voltage difference can be defined in that plane and a capacitance can be calculated.

Furthermore, it is a common approach to still think of an electromagnetic system as an LC circuit in which the capacity section is the region where we find most of the electric field and the inductance section is that region where we find most of the magnetic field. In fact, in a capacitor the electric field is dominant and in an inductor the magnetic field is dominant, but still both field types are present in both these components.

One option to proceed is to start with Maxwell's equations and to solve the wave equations for helical structures. This approach has been followed

by several authors [196–199], but their results cannot be easily related to the circuit models that we introduced in the previous sections. Instead we follow the simplified description of Feynman ([200] Sect. 22-1) to relate the electric and magnetic fields in a coil to the voltage and current of an inductance, resistance and capacitance.

We consider a current flowing through a helical wire. The resulting magnetic field is proportional to the current. If the current changes with time, the magnetic field \vec{B} also changes. According to Faraday's law, the line integral of \vec{E} around any closed path is equal to the negative of the rate of change of the flux of \vec{B} enclosed by that path:

$$\oint \vec{E} \cdot d\ell = -\frac{d}{dt} \iint \vec{B}(t) \cdot d\vec{S} \quad (5.2)$$

This law can be applied to a path inside the wire of the coil to find the voltage between the terminals. Because electric fields are quite small inside a copper wire (since the smallest fields would produce large currents), almost the entire contribution to the line integral of \vec{E} comes from the path from terminal to terminal outside the coil. If the terminals of the coil are far enough away from the helix, we can assume that there is not much flux in the space between the leads of the coil. Consequently, this part of the integral is only weakly dependent on the path chosen and we can define the voltage difference between the two terminals. This voltage difference is

$$v = -\frac{d}{dt} \iint \vec{B}(t) \cdot d\vec{S} \quad (5.3)$$

The electric field between the terminals of the coil implies that there must be a distribution of charges in the solenoid. These charges are present at the terminals and to a lesser extent also inside the coil, located at the surface of the wires. The resulting axial electric field is many times larger than the radially dependent circumferential electric field usually associated with the time-varying axial magnetic field within the coil [201, 202].

During oscillation, the electric field varies in time 90° out of phase with the magnetic field, i.e. energy is alternatively stored in the electric field and the magnetic field. If no energy is added from outside, the oscillation decreases gradually due to losses in the copper wires.

In this simplified view, the electric field between the two terminals corresponds to a voltage across a capacitance between the two terminals and the magnetic field is caused by the current through an inductance. The losses can be modeled by a resistance added in parallel to the capacitance and the inductance. In fact, this is an arbitrary choice. The damping effect is also

found when a different resistance is placed in series with the capacitance or in series with the inductance. In Chapter 2, however, we concluded that the losses at high frequencies are mainly caused by eddy currents in the coil wires and we found that it is simpler to present these losses by a parallel resistance. For not too high frequencies, an accurate description of the eddy current losses is obtained with a fixed value of the parallel resistance whereas the value of a series resistance increases quadratically with frequency.

5.3 Physical models for solenoids

Physical models for ringing are helpful to give direction to our analysis as they give us clues on the design parameters relevant for the ringing phenomenon. In this section, we review expressions for the inductance, capacitance and resistance. We relate the inductance of a coil to the design parameters, considering only quasi-static magnetic fields. Subsequently, we relate the capacitances in the equivalent circuit to the design parameters, considering only quasi-static electric fields. Finally, we relate the parallel resistances in the equivalent circuit to the design parameters, considering e.g. the proximity effect.

5.3.1 Inductance

Advanced CAD software is available to calculate the inductance of CRT deflection coils (see references in Chapter 2). However, these CAD programs only result in a value for a single lumped inductance. They do not give much insight how the inductances of various sections of our equivalent circuit are related to design parameters.

The inductance of coils is studied extensively in literature for various geometries [203, 204], such as a single straight wire, a square loop, a circular loop and an cylindrical coil.

The apparent ‘internal’ inductance of a single straight wire with length ℓ_w follows from our analysis of the skin effect in Chapter 3 (Eq. 3.39). This gives the contribution to the inductance of the wire due to the current and thus of the magnetic flux inside the wire. For low frequencies (when the skin depth is much larger than the wire diameter), the result is ([132], page 184):

$$L_{\text{wire,lf}} = \frac{\mu_o}{8\pi} \ell_w \quad (5.4)$$

which corresponds to 50 nH/m. Of course, the current can only flow in a loop and an additional (in general much larger) contribution to the total inductance follows from the flux enclosed by the loop.

The inductance of a square loop with sides b and wire with diameter a (with $b \gg a$), excluding the apparent internal inductance of the wire, is given by

$$L_{\square} = 2b \frac{\mu_o}{\pi} \left[\ln\left(\frac{2b}{a}\right) - 1 \right] \quad (5.5)$$

The inductance of a circular loop of radius r and a wire with radius a (with $r \gg a$), excluding the apparent internal inductance of the wire, is given by ([132], page 193):

$$L_o = \mu_o r \left[\ln\left(\frac{8r}{a}\right) - 2 \right] \quad (5.6)$$

The inductance of a coil consisting of N_{turns} circular loops closely to each other, is then

$$L_{\text{coil}} = N_{\text{turns}}^2 \mu_o r \left[\ln\left(\frac{8r}{a}\right) - 2 \right] \quad (5.7)$$

For the inductance of a cylindrical coil of length ℓ_c , short compared to the radius r , empirical formulas are available. For r/ℓ_c up to 2, a simple approximate formula is ([132] page 195, [205]):

$$L_{\text{short-coil}} = \frac{\pi \mu_o r^2 N_{\text{turns}}^2}{\ell_c + 0.9r} \quad (5.8)$$

5.3.2 Capacitance

The capacitive effects in the coils are essential for the ringing of deflection coils. Models for these capacitive effects are necessary for designers to predict and to control ringing. In this section we briefly review existing models for the capacitance for various geometries.

The capacitance between two parallel wires of radius a , with length ℓ_w and axes separated by d_w can be calculated with conformal mapping ([132], page 345):

$$C_{2\text{wires}} = \varepsilon \frac{\pi \ell_w}{\cosh^{-1}\left(\frac{d_w}{2a}\right)} = \varepsilon \frac{\pi \ell_w}{\ln\left(\frac{d_w}{2a} + \sqrt{\frac{d_w^2}{4a^2} - 1}\right)} \quad (5.9)$$

assuming that the space between and around the two wires is filled with a dielectric medium with permittivity ε .

The capacitance of single-layer solenoids

The lumped capacitance of a single-layer solenoid has been extensively discussed in literature for more than a century (see e.g. the references in [206–210]). In 1934, Palermo [211] proposed to calculate the lumped capacitance of a single-layer solenoid from the energy stored in the electric field. He considered a tightly wound helix of N circular turns with radius r with the centers of adjacent wires at distance d_w . He assumed that the voltage V_L across the terminals of the solenoid is equally divided across the coil, which is true for low frequencies. Between two adjacent parallel wire segments the voltage difference is then $V_s = V_L/(N - 1)$. The energy stored in the electric field between two wire segments of length $d\ell$ equals $dW = \frac{1}{2}V_s^2 dC_{2s}$, in which the capacitance dC_{2s} between these parallel wire segments follows from the capacitance between two parallel wires, Eq. 5.9, by substituting $d\ell$ for the length ℓ_w .

The lumped capacitance C_L follows the energy equation:

$$\frac{1}{2}C_L V_L^2 = \int_0^{2\pi r(N-1)} \frac{dW}{d\ell} d\ell \quad (5.10)$$

For wires with radius a , this is easily worked out to

$$C_L = \varepsilon \frac{2\pi^2 r}{(N - 1) \cosh^{-1}\left(\frac{d_w}{2a}\right)} \quad (5.11)$$

For a series of separate insulated wire loops this expression is confirmed experimentally [212]. For single-layer solenoids, however, experimental results [213] can not be explained by Palermo's model.

In 1947, Medhurst [213, 214] presented a detailed experimental analysis of the self-capacitance of single-layer solenoids. He pointed out that besides the ‘internal’ capacitance between each pair of turns, also the ‘external’ capacitance to the nearby earth contributes significantly to the overall capacitance. Note in this context that the capacitance with respect to infinity of a sphere with radius r is already

$$C_{\text{sphere}} = 4\pi\varepsilon_0 r \quad (5.12)$$

Medhurst measured the self-capacitance for a wide range of single-layer coils, with diameters ranging from 0.67 cm to 6.36 cm and the length/diameter ratio from 0.8 to 5.0 while the number of turns varied from 10 to 636. All coils were connected to ‘earth’ at one end. He fitted his experimental results for

the lumped capacitance C_L (in pF) for coils with length ℓ_c (in cm) and radius r_c (in cm) by

$$C_L = 0.12\ell_c + 0.16r_c + 0.76r_c\sqrt{r_c/\ell_c} \quad (5.13)$$

Essentially this expression depends only on the length and radius of the solenoid. In contrast to Palermo's theory, Medhurst's expression for the capacitance does not depend on the spacing of the turns or on the wire radius. In fact, this indicates that the internal capacitance calculated by Palermo is much smaller than the external capacitance which depends only on the outer dimensions of the coil.

The capacitance of multi-layer solenoids

Many other authors consider relatively long multi-layer coils and neglect the capacitance between successive wire turns in the same layer in comparison to capacitances between different layers [94, 215–222]. This is a valid approach for relatively long coils where the voltage difference between successive turns is small compared to the voltage difference between different layers.

The capacitance between two successive layers cannot be calculated from the wire-to-wire capacitance, Eq. 5.9, because the electric field is confined to the space between the two successive layers as is the field between two parallel metal plates.

Koch [223] and Massari [224] considered the energy stored in a basic cell consisting of two wires in one layer and two wires in an adjoining layer. Both took the wire insulation into account, but Koch considered a thin dielectric layer around each wire whereas Massari considered the entire basic cell filled with a dielectric. Koch considered a layer of N_w turns on top of an identical second layer. Within a layer the turns are connected to obtain a single solenoid. The two layers are not connected galvanically to each other so that the capacitance between these two layers can be measured. After summation over all the basic cells, Koch derived the following formula of the capacitance C_ℓ between two layers:

$$C_\ell = 8\varepsilon_0 N_w \ell_{\text{turn}} \left\{ M_L + \frac{t_i}{2\varepsilon_r r_o^2} (2r_o - t_i) M_D \right\} \quad (5.14)$$

where

- ε_0 is the dielectric constant,
- ε_r is the relative dielectric constant,
- N_w is the number of turns in a single layer,
- ℓ_{turn} is the average length of a single turn,
- r_o is the outer radius of a wire including insulation,
- t_i is the thickness of the insulation layer of a wire.

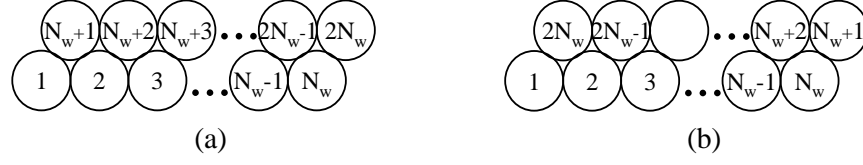


Figure 5.1: The winding direction can be the same for each layer (a), or runs in opposite directions from layer to layer (b).

M_L and M_D denote the following integrals which are solved numerically:

$$M_L = \frac{1}{2} \int_0^{\pi/6} \frac{\cos^2 \psi - \cos \psi \sqrt{\cos^2 \psi - 0.75} - 0.5}{\left\{ \cos \psi - \left(1 - \frac{t_i}{\varepsilon_r d_w} \right) \left(\sqrt{\cos^2 \psi - 0.75} + 0.5 \right) \right\}^2} d\psi \quad (5.15)$$

and

$$M_D = \frac{1}{2} \int_0^{\pi/6} \frac{\sin^2 \psi + \cos \psi \sqrt{\cos^2 \psi - 0.75}}{\left\{ \cos \psi - \left(1 - \frac{t_i}{\varepsilon_r d_w} \right) \left(\sqrt{\cos^2 \psi - 0.75} + 0.5 \right) \right\}^2} d\psi \quad (5.16)$$

The lumped capacitance of a two-layer solenoid with length ℓ_c is calculated from the capacitance C_ℓ between the two co-axial layers which can be measured after cutting the wire at the end of a layer. For the derivation of Eq. 5.14, a fixed voltage difference between the layers was assumed. In an actual coil, however, the voltage $V(x)$ between turns in adjacent layers varies with the distance x along the coil. For an infinitesimal length dx , the capacitance between the two layers is $(C_\ell/\ell_c)dx$ and the energy stored in the electric field is given by

$$W = \int_0^{\ell_c} \frac{1}{2} \frac{C_\ell}{\ell_c} \{V(x)\}^2 dx \quad (5.17)$$

On the other hand, the total energy W in the electric field should be expressed in terms of the - yet unknown - lumped capacitance C_{L2} and the voltage V_L across the terminals:

$$W = \frac{1}{2} C_{L2} V_L^2 \quad (5.18)$$

The lumped capacitance depends on the way in which the subsequent layers are interconnected. If the turns in two subsequent layers are connected in the same direction, e.g. from left to right as illustrated in Fig. 5.1a, the voltage difference will be $V_L/2$ for each pair of adjacent wire turns in the two layers. If a voltage V_L is applied to such a two-layer coil of N_w turns per

layer, the lumped capacitance follows from the energy W of the electric field between the two layers:

$$W = \frac{1}{2\ell_c} \int_0^{\ell_c} C_\ell \left(\frac{1}{2} V_L \right)^2 dx \quad (5.19)$$

The lumped capacitance C_{L2s} of the solenoid with two layers wound in the same direction (Fig. 5.1a), follows from $W = \frac{1}{2} C_{L2s} V_L^2$:

$$C_{L2s} = \frac{1}{4} C_\ell \quad (5.20)$$

However, if the turns in two subsequent layers are wound in opposite directions, as illustrated in Fig. 5.1b, the voltage difference between two adjacent wires in the two layers varies along the coil. This voltage difference $V(x)$ increases linearly with the distance x from the end of the coil where the first layer ends and where the second layer starts, i.e. $V(x) = (x/\ell_c) V_L$.

The energy of the electric field between the two layers is then

$$W = \frac{1}{2} \int_0^{\ell_c} C_\ell \left(\frac{x}{\ell_c} V_L \right)^2 \frac{dx}{\ell_c} = \frac{1}{6} C_\ell V_L^2 \quad (5.21)$$

The lumped capacitance C_{L2d} of the solenoid with two layers with turns connected in different directions (Fig. 5.1b), follows from $W = \frac{1}{2} C_{L2d} V_L^2$:

$$C_{L2d} = \frac{1}{3} C_\ell \quad (5.22)$$

For more than two layers, the lumped capacitance is calculated in a similar way. As an example, we consider the case that turns in successive layers are connected in opposite directions. Again the voltage difference at the coil terminals is denoted as V_L . If we consider N_L layers, the maximum voltage difference between two adjacent turns in two successive layers is $2V_L/N_L$. The energy of the electric field between two successive layers is then $\frac{1}{2} C_{L2d} (2V_L/N_L)^2$. For the $N_L - 1$ pairs of successive layers we thus find for the lumped capacitance C_{Lnd} of N_L layers wound in opposite directions:

$$C_{Lnd} = \frac{4}{3N_L^2} (N_L - 1) C_\ell \quad (5.23)$$

The capacitance of coils with several wires in parallel

Up to now we implicitly assumed that the coils are wound with a single solid wire. Many coils, however, are wound with several copper wires in

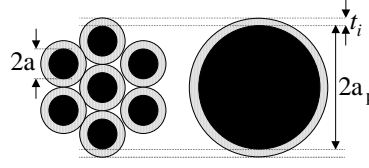


Figure 5.2: To calculate the capacitance of a coil, a litz wire is modeled by a solid wire with the same maximum overall copper diameter and the same maximum overall outer diameter.

parallel. The effect of using several copper wires in parallel when winding a coil, depends on how the parallel copper wires are positioned with respect to each other. For instance, the coil capacitance will be different when the parallel copper wires are placed next to each other, or on top of each other.

If the copper wires are assembled into a single more or less round package, as illustrated by Fig. 5.2, this resulting wire is called a litz wire. As a first order model, we assume that the parallel wires are tightly packed as in a litz wire. We follow the approach proposed by Albach [225], to model such a litz wire by a single solid wire for capacitance calculations.

To find an expression for the radius of the equivalent solid wire, we assume that the total cross-section of this wire is identical to the sum of the cross-sections of the actual wires. For the insulation thickness of the equivalent solid wire we use the same thickness t_i as the actual wires. If N_p wires are used in parallel, each with copper radius a and insulation thickness t_i , we find the following expression for the radius a_p and insulation thickness t_i given by

$$(a_p + t_i)^2 = N_p(a + t_i)^2 \quad (5.24)$$

so that

$$a_p = (a + t_i)\sqrt{N_p} - t_i \quad (5.25)$$

The thickness of CRT deflection coils is about 3 mm and only a few turns fit next to each other. If we model the CRT deflection coil by equivalent solid wires nicely wound in layers, the number of turns N_w in one layer, i.e. the number of turns that fit in the thickness w of the coil is

$$N_w = \frac{w}{2(a_p + t_i)} \quad (5.26)$$

The number of layers N_L also depends on the diameter of the equivalent wire and follows from the total number of turns N_{turns} by

$$N_L = \frac{N_{\text{turns}}}{N_w} \quad (5.27)$$

As an example of the application of the theory above, we estimate the capacitance of a single 17" CMT line coil wound with $N_{\text{turns}} = 38$ turns of $13 \times 236 \mu\text{m}$ solid wire, i.e. with $N_p = 13$, $a = 118 \mu\text{m}$, $t_i = 30 \mu\text{m}$. The thickness of the coil is $w = 3 \text{ mm}$. We find for the equivalent copper radius of the wire bundle $a_p = 0.50 \text{ mm}$ (Eq. 5.25) and outer radius $r_o = 0.53 \text{ mm}$. Furthermore, we find for the number of turns per layer $N_w = 3$ (Eq. 5.26) and for the number of layers $N_L = 14$ (Eq. 5.27). Numerical evaluation of Eqs. 5.15 and 5.16 yield $M_L = 0.841$ and $M_D = 54.8$. We estimate the average length per turn from the measured dc resistance, $R_{\text{dc}} = 0.34 \Omega$; with the expression for the dc resistance, Eq. 3.57, we find $\ell_{\text{turn}} = 29 \text{ cm}$. Assuming a dielectric constant $\epsilon_r = 3$, we finally find with Eq. 5.14 a layer capacitance $C_\ell = 175 \text{ pF}$ and with Eq. 5.23 a lumped terminal capacitance of $C_{Lnd} = 16 \text{ pF}$.

In addition to the layer capacitance, also the capacitance to the environment contributes to the lumped capacitance of the coil. If we model a line coil as a sphere with radius $r = 3 \text{ cm}$, we find with Eq. 5.12 an additional capacitance of $C_{\text{sphere}} = 3 \text{ pF}$.

The sum $C_{Lnd} + C_{\text{sphere}} = 19 \text{ pF}$ is remarkably identical to the measuring result (for C_1) which will be presented in Sect. 5.4.1 (in Table 5.1).

Clearly, the layer capacitance gives the largest contribution to the total lumped capacitance of the coil, but the capacitance to the environment cannot be neglected. In the remainder of this thesis, we will see that the ringing performance is strongly determined by this capacitance to the environment.

5.3.3 Resistance

In the previous sections we have described models for the inductance and capacitance of solenoids. The combination of these two result in high-frequency oscillations which show up in CRT deflection coils as ringing. In our analysis of the ringing phenomenon in Chapter 4, we showed that ringing is damped by the resistances parallel to the inductances. In the circuit models, the resistances parallel to the inductances represent the high-frequency losses in the deflection yoke. In Chapter 3, eddy current losses in the copper wires are identified as the main contributor to the total losses. For low frequencies ω at which the skin depth δ is larger than the wire radius a , we derived the following expression (Eq. 3.47) for the losses P_{prox} due to this proximity effect:

$$P_{\text{prox}} = \frac{\pi}{8} \sigma a^4 \omega^2 B_o^2 \ell \quad (5.28)$$

for a single wire with length ℓ and conductivity σ . Although our experimental results at the end of Chapter 3 indicate that the losses in actual deflection

coils vary approximately with a^3 rather than with a^4 , we proceed our analysis with Eq. 5.28, which is commonly used in literature.

In a coil, the total wire length ℓ is proportional to the product of the number of turns N_{turns} , the number of parallel wires N_p and the average length ℓ_{turn} of a turn. In general, the magnetic flux density B does vary along the turn and the total dissipation in the coil is given by

$$P_{\text{coil}} = \frac{\pi}{8} N_{\text{turns}} N_p \sigma a^4 \omega^2 \int_0^{\ell_{\text{turn}}} B^2(x) dx \quad (5.29)$$

If we assume for simplicity that the flux through every turn equals $B_o A_{\text{turn}}$, the amplitude V_{coil} of the voltage across the coil follows from the law of Faraday:

$$V_{\text{coil}} = N_{\text{turns}} \omega B_o A_{\text{turn}} \quad (5.30)$$

In a parallel *RCL* circuit model, with a resistance R_p parallel to the coil inductance, the dissipation is also given by

$$P_{\text{coil}} = \frac{V_{\text{coil}}^2}{2R_p} \quad (5.31)$$

If we assume that $\int_0^{\ell_{\text{turn}}} B^2(x) dx$ is proportional to $B_o^2 \ell_{\text{turn}}$, we conclude from the last three equations that

$$R_p \propto \frac{1}{a^4} \frac{A_{\text{turn}}^2}{\ell_{\text{turn}}} \frac{N_{\text{turns}}}{N_p} \quad (5.32)$$

If we consider a coil with a constant cross-section A_{cross} , we substitute $A_{\text{cross}} = \pi a^2 N_p N_{\text{turns}}$ to find

$$R_p \propto \frac{1}{a^2} \frac{A_{\text{turn}}^2}{\ell_{\text{turn}} A_{\text{cross}}} N_{\text{turns}}^2 \quad (5.33)$$

Although we have made several simplifications in deriving this expression, it gives valuable insight into the relations between the circuit parameter R_p and the various design parameters. As expected intuitively, R_p depends on the wire diameter (the first factor), the geometry of the coil (the second factor) and the number of turns (the third factor).

5.3.4 Discussion

The next step could be to combine the theoretical models for the inductance, resistance and capacitance into a model to predict the ringing of deflection coils. However, despite the good agreement between predictions and

measurements on solenoids reported in literature, it will turn out in the next section that our experimental results deviate from the predictions from the solenoid models. Therefore, we will not proceed with these theoretical models.

Apparently the models for the equivalent circuit parameters of solenoids do not accurately predict the capacitance and resistance to be used in the equivalent circuit models for CRT deflection coils. A possible explanation is that the geometry of the deflection coils differs strongly from the geometry of solenoids. Not only the shape of a deflection coil is totally different, also the magnetic field perpendicular to the wires and the electric field between the wires are very different from the situation of a solenoid.

Although the theoretical models cannot be used for an accurate quantitative predicting the ringing performance, they are still valuable as they provide an understanding and a description of the phenomena that contribute to the high-frequency performance of deflection coils. Many of the ideas that will be presented in Chapter 6 to suppress ringing, can be described qualitatively with the concepts described in the previous sections.

5.4 Experimental results

In this section, measurements of impedance characteristics of CRT deflection coils are compared to predictions from the solenoid models in the previous section.

In the previous section, theory was discussed to predict the influence of various design choices on the high-frequency performance of solenoids. In contrast to solenoids, CRT deflection coils are wound with several wires in parallel, typically 5 to 15 for line coils. Furthermore, the wires in deflection coils are not precisely positioned, but more or less randomly distributed as shown in Fig. 5.3. Clearly, a long solenoid with accurately positioned turns is not a very adequate model for a CRT deflection coil.

The methods that we have introduced in Chapter 4 to measure either the optical frequency response, the magnetic frequency response or the impedance characteristic, and the circuit models to relate the measured data, enable us to analyze systematically the influence of various design choices on the ringing performance of a deflection yoke. In this section we consider the influence of changing the wire type.

The measuring methods of the magnetic frequency response and the impedance characteristic allow us to go even further in our analysis. In contrast to the optical measuring method, they are not restricted to complete deflection yokes. These two measuring principles can also be applied to

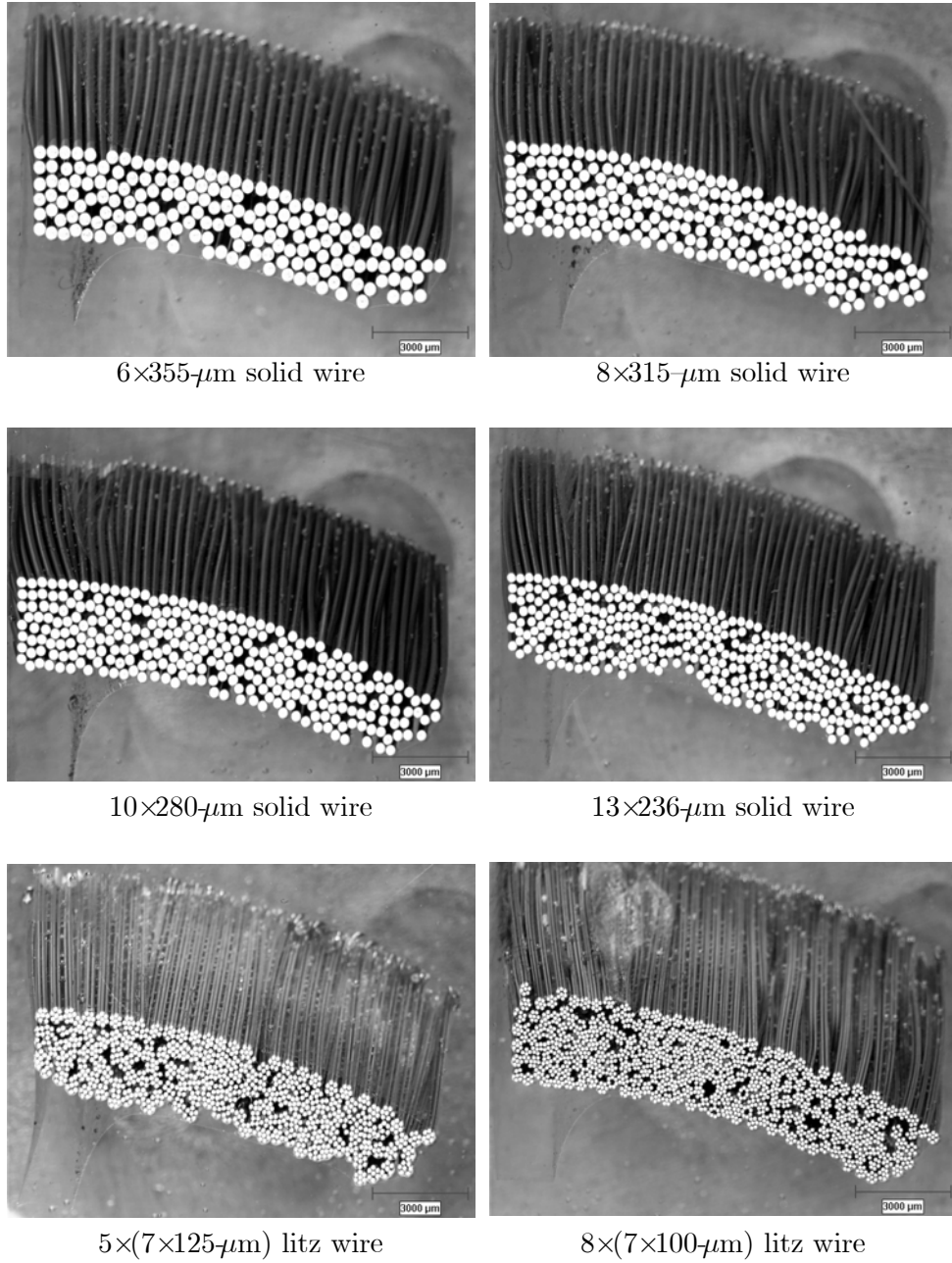


Figure 5.3: Photographs of cross-sections of 17'' CMT line coils wound with different wire types.

line-coil wires	R_{dc} (Ω)	R_1 (k Ω)	C_1 (pF)	L_1 (μ H)	R_2 (k Ω)	C_2 (pF)	L_2 (μ H)
8 \times (7 \times 100 μ m)	0.44	66	20	137	3.4	61	9.4
5 \times (7 \times 125 μ m)	0.45	60	21	140	2.2	114	5.7
13 \times 236 μ m	0.34	66	19	138	1.1	235	2.5
10 \times 280 μ m	0.31	64	18	131	4.4	51	7.8
8 \times 315 μ m	0.30	71	17	134	3.1	85	5.1
6 \times 355 μ m	0.32	82	17	135	3.0	98	4.4
spread (3s)	0.01	5	3	6	1	40	3

Table 5.1: Parameter values of the two-*RCL*-sections model fitted to the measured impedance characteristics of *single* 17'' CMT *line coils* wound with 38 turns of different wire types.

analyze the ringing performance of e.g. a line-coil pair with or without a ferrite core, a single line coil and even a part of a line coil.

In the following sections, we evaluate experimental results of:

1. impedance characteristics of single line coils;
2. impedance characteristics of line-coil pairs with ferrite core;
3. impedance characteristics of complete deflection yokes;
4. magnetic frequency responses of 17'' CMT DYs
5. magnetic frequency responses of 15'' CMT DYs

5.4.1 Impedance characteristics of single line coils

To analyze the impact of the wire type on electrical oscillations in line coils, the impedance characteristics have been measured of single line coils that have the same geometry but have different wire types. In fact, we used the same (17'' CMT Mk IIa/84 kHz) line coils (with 38 turns) as for the dissipation analysis (Sect. 3.6.2).

For each type of line-coil wire, the impedance characteristics of five identical single line coils were measured, i.e. without plastic cap or ferrite core. Table 5.1 presents the average and the spread - three times the standard deviation (*s*) for the five identical coils - of the parameters of the two-*RCL*-sections model obtained by fitting to the impedance characteristics. We have the following observations:

- the dc resistance R_{dc} for the coils made with litz wires is almost 40% higher than the dc resistance of coils made with solid wires. The reason is that the thickness of the insulation layers of the individual copper wires has to remain the same to maintain the electrical insulation. The volume taken in by the insulation layers increases when more thinner copper wires are used and consequently the copper volume becomes lower;
- the inductance L_1 is almost independent of the wire type, as expected;
- the capacitance C_1 varies only slightly with the wire type, as expected. Furthermore it is quite close to our estimate of 19 pF (see page 127);

However:

- the resistance R_1 increases slightly with the wire radius, whereas theory predicted it to decrease rapidly with increasing wire radius (Eq. 5.33);
- the values for R_2 , C_2 and L_2 vary in an unpredictable way with the wire diameter. Furthermore, the spread in the values of R_2 , C_2 and L_2 is much larger than the spread in the values of the other parameters.

Especially due to the unpredictable dependence of R_2 , C_2 and L_2 on the wire type, ringing cannot be described with the discussed theory for simple solenoids.

5.4.2 Impedance characteristics of line-coil pairs

The next step towards analyzing a complete deflection yoke is to analyze the ringing performance of a pair of line coils mounted with a 3C2 ferrite core inside a plastic cap. In fact, only frame coils have to be added at the outside of the plastic cap to obtain a complete deflection yoke. The same (17" CMT Mk IIa/84 kHz) line coils were used as in the previous section.

For each type of line-coil wire, the impedance characteristic was measured of five pairs of line coils. In each pair, two line coils were connected in parallel and were mounted in a plastic cap with a ferrite core. In fact, this is a deflection yoke without frame coils.

Table 5.2 gives the average and the spread of the parameters obtained by fitting the two- RCL -sections model to the impedance characteristics. Comparison to Table 5.1 shows that the values of the resistances R_{dc} , R_1 and R_2 for the line-coil pairs with ferrite core are about half the values for single line coils. The values of C_1 are about twice as large. This is what we

line-coil wires	R_{dc} (Ω)	R_1 ($k\Omega$)	C_1 (pF)	L_1 (μH)	R_2 ($k\Omega$)	C_2 (pF)	L_2 (μH)
$8 \times (7 \times 100 \mu m)$	0.23	50	40	116	1.5	131	4.8
$5 \times (7 \times 125 \mu m)$	0.24	36	42	119	1.7	125	5.1
$13 \times 236 \mu m$	0.18	34	36	114	1.5	132	3.7
$10 \times 280 \mu m$	0.17	36	37	114	2.1	112	4.0
$8 \times 315 \mu m$	0.16	38	35	115	1.9	112	3.7
$6 \times 355 \mu m$	0.17	41	33	113	2.2	103	3.9
spread (3s)	0.01	4	2	4	0.4	14	0.5

Table 5.2: Parameter values of the two- RCL -sections model fitted to the measured impedance characteristic of 17" CMT *line-coil pairs* made with various wire types. The coils, each with 38 turns, are fixed in a deflection yoke with a 3C2 yoke ring, but without frame coils.

expect when two coils are connected in parallel. The values of the inductances L_1 and L_2 for the line-coil pair are not half the values of the single line coils, but this can be explained by the presence of the ferrite core as well as by the coupling of the line coils (see Sect. 2.3.3).

The values of C_2 , however, changed in an unpredictable way from a single line coil to a line-coil pair with a ferrite core. Some values are larger; others are smaller. Since the ringing performance depends strongly on the value of C_2 , it is not possible to predict the ringing behavior of a deflection yoke from the ringing behavior of a single line coil.

5.4.3 Impedance characteristics of deflection yokes

Subsequently, frame coils were added to the sets analyzed in the previous section to obtain complete 17" CMT deflection yokes. Normal production frame coils were used consisting of $2 \times 250\text{-}\mu m$ and $2 \times 265\text{-}\mu m$ solid wires. Only one deflection yoke for each wire type was made and analyzed. We measured the impedance characteristics of the line coils as well as the differential-mode and common-mode magnetic frequency responses.

Table 5.3 presents the fitting parameters of the two- RCL -sections model to the differential-mode impedance characteristics of these complete 17" CMT deflection yokes. Comparison with Table 5.2 shows that by adding the frame coils:

- the value of the dc resistance R_{dc} does not change significantly, as expected;

line-coil wires	R_{dc} (Ω)	R_1 ($k\Omega$)	C_1 (pF)	L_1 (μH)	R_2 ($k\Omega$)	C_2 (pF)	L_2 (μH)
$8 \times (7 \times 100 \mu m)$	0.24	32	43	114	1.1	156	3.9
$5 \times (7 \times 125 \mu m)$	0.25	27	45	114	1.6	133	4.9
$13 \times 236 \mu m$	0.19	28	36	113	1.3	173	2.8
$10 \times 280 \mu m$	0.18	29	38	112	1.6	134	3.4
$8 \times 315 \mu m$	0.17	30	35	112	1.5	137	3.0
$6 \times 355 \mu m$	0.18	31	34	112	1.5	150	2.7

Table 5.3: Parameter values of the two- RCL -sections model fitted to the measured impedance characteristic of fully assembled 17" CMT deflection yokes with different types of line-coil wires. The line coils are fixed in a deflection yoke with a 3C2 ferrite core, with frame coils consisting of $2 \times 250 \mu m$ and $2 \times 265 \mu m$ solid wires .

- both the damping resistances R_1 and R_2 become smaller, corresponding to more damping due to additional eddy current losses in the frame-coil wires;
- the inductances L_1 and L_2 do not change significantly;
- the capacitance C_1 increases slightly by 0-5%;
- the capacitance C_2 increases by 20-30%.

Figure 5.4 shows how the fitted parameters $R_1, C_1, L_1, R_2, C_2, L_2$ vary with the wire type for a single 17" CMT line coil, a pair of line coils within a ferrite core and a complete 17" CMT deflection yoke. Clearly, the values obtained for a single line coil are not related well to the values obtained for a complete deflection yoke. The values for a pair of line coils are much closer to the values of the complete deflection yoke and have the same dependence on the wire diameter.

The capacitances change due to the presence of nearby conductors (the frame coils). The large change in C_2 makes it difficult to predict the ringing behavior of deflection yokes from the high-frequency behavior of its components, but this time the change is quite consistent.

5.4.4 Discussion

Our experiments indicate that especially the second peak in the impedance characteristic deviates strongly from the prediction for simple solenoids. In our analysis this is especially manifest as an unpredictable dependence of R_2 ,

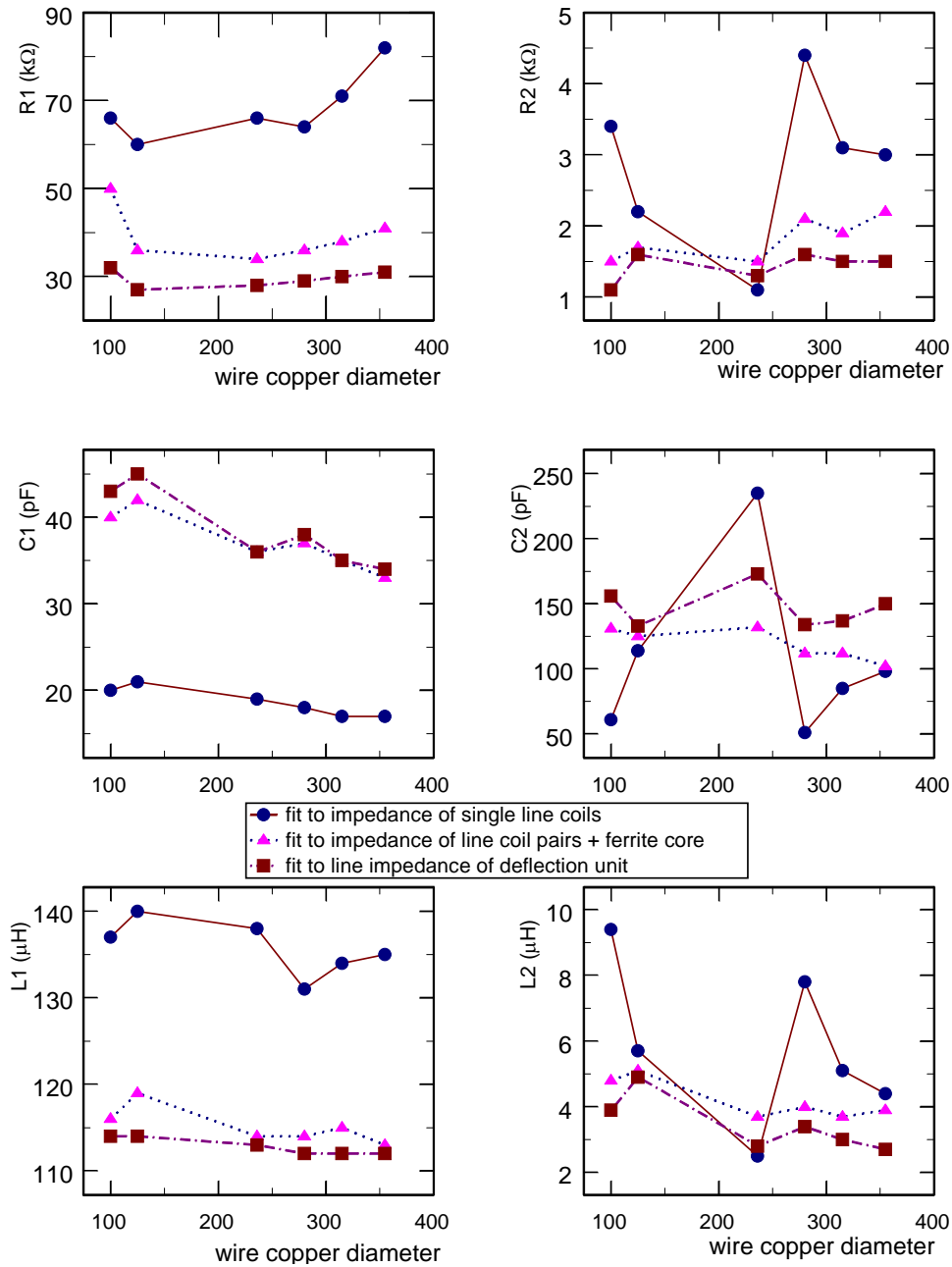


Figure 5.4: Comparison of the parameter values of the two-*RCL*-sections model fitted to the line impedance of: (●) single line coils, (▲) line-coil pairs + ferrite core, (■) line-coil pair + frame coil pair + ferrite core.

C_2 and L_2 on the wire type. One could raise the question whether theory can give us an indication where in the coil the oscillation takes place. However, this is not possible. In fact, we have reached the limits of the validity of circuit modeling since the dimensions of the coil become comparable to the wavelength at frequencies of the second resonance peak. For instance, an electromagnetic wave of 10 MHz has a wavelength of 17 m in a dielectric medium with $\varepsilon_r = 3$. The length of a wire (bundle) with which a coil is wound is about 10–15 m.

We therefore suppose that the second resonance peak in the impedance characteristic corresponds to a standing electromagnetic wave somewhere within the coil. We have verified this by measuring the strength of the alternating magnetic field at the resonance frequencies with a small pickup coil (with a diameter of 2 mm) perpendicular to the wires, which we moved over the surface of a single line coil. At frequencies near the first resonance peak, a field of constant amplitude was measured. At frequencies near the second resonance peak, however, the field varied as a single cosine along the length of the wire bundle with a higher value near the terminals than near the middle of the wire (bundle), i.e. in the middle of the coil.

Furthermore, the capacitance to the environment plays an important role and cannot be neglected. Especially when several coils are packed closely together, as in a deflection yoke, this has a strong effect on the equivalent capacitances and hence on the ringing frequencies. It is therefore necessary to measure ringing on complete deflection yokes rather than on individual coils.

5.4.5 Magnetic Frequency Responses of 17" CMT DYs

Figure 5.5 shows the differential-mode and the common-mode magnetic frequency responses for the various types of line-coil wires of the complete 17" CMT deflection yokes. Clearly, the differential-mode ringing peak shifts to higher frequencies when thicker copper wires are used in the line coils. The width of the resonance curves and hence the decay time of the time response do not vary significantly with the copper diameter.

The common-mode frequency responses show that the first three resonance peaks in the common-mode frequency response do not vary significantly when different line-coil wires are used. The fourth peak, however, varies like the peak in the differential-mode frequency response with the copper diameter of the line-coil wires.

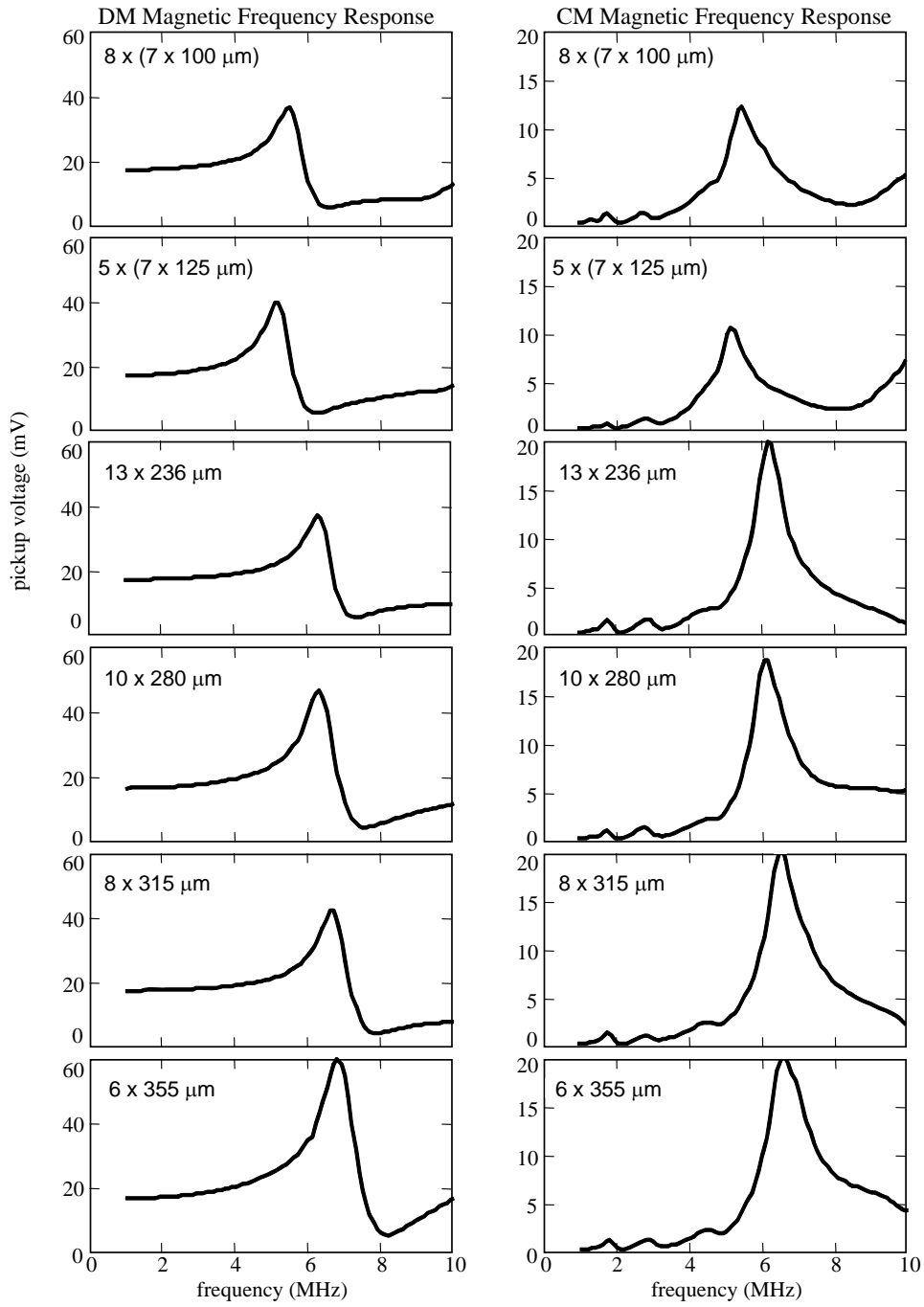


Figure 5.5: Differential-Mode (DM) and Common-Mode (CM) magnetic frequency response of a 17" CMT deflection yoke for various types of line-coil wires.

5.4.6 Magnetic Frequency Responses of 15" CMT DYs

The influence of line-coil wire on ringing of a 15" CMT DY

A similar experiment was performed for a deflection yoke of a 15" CMT. Also for this design, line coils were made with identical geometry but with different wire types. Each line coil consisted of 49 turns of either $6 \times 300\text{-}\mu\text{m}$ solid wire, $5 \times (7 \times 125\text{-}\mu\text{m})$ litz, $5 \times (19 \times 71\text{-}\mu\text{m})$ litz or $5 \times (1 \times 153 + 7 \times 106\text{-}\mu\text{m})$ litz wire. Each frame coil consisted of 106 turns of $3 \times (7 \times 125\text{-}\mu\text{m})$ litz wires.

Figure 5.6 shows the differential-mode and common-mode magnetic frequency responses of these deflection yokes. The differential-mode magnetic frequency response changes strongly with the wire type, in the same way we measured for the 17" CMT samples (Fig. 5.5). In the common-mode magnetic frequency response, the large, second, peak varies similar to the peak in the differential-mode magnetic frequency response. Because the first ringing peak in the common-mode response, near 2 MHz, is much higher for these 15" CMT samples than for the 17" CMT samples, it is even more clear to see that the first peak does not change with the line-coil wire.

Apparently, peaks in the common-mode frequency response up to about 3 MHz are caused by oscillations inside the frame coils. These frame-coil oscillations modulate the common-mode current which flows through both the frame coils and the line coils. This current through (parts of) the line coils determines the speed with which lines are written on the screen, so that these oscillations result in ringing bars at the screen (as described in Sect. 4.2).

Furthermore, we conclude that common-mode ringing at higher frequencies (above about 5 MHz) are caused by oscillations inside the line coils. These oscillations affect both the common-mode and the differential-mode currents in a similar way.

The influence of frame-coil wire on ringing of a 15" CMT DY

To investigate also the influence of the frame-coil wires on the ringing performance of a deflection yoke, several 15" CMT deflection yokes were made with identical line-coil wires, but different frame-coil wires. As shown in Fig. 5.7, this time the differential-mode frequency response hardly changed, while the common-mode resonance peak near 2 MHz shifted significantly when different frame-coil wires were used. This behavior is consistent with our explanation that this peak is caused by oscillations inside the frame coils only.

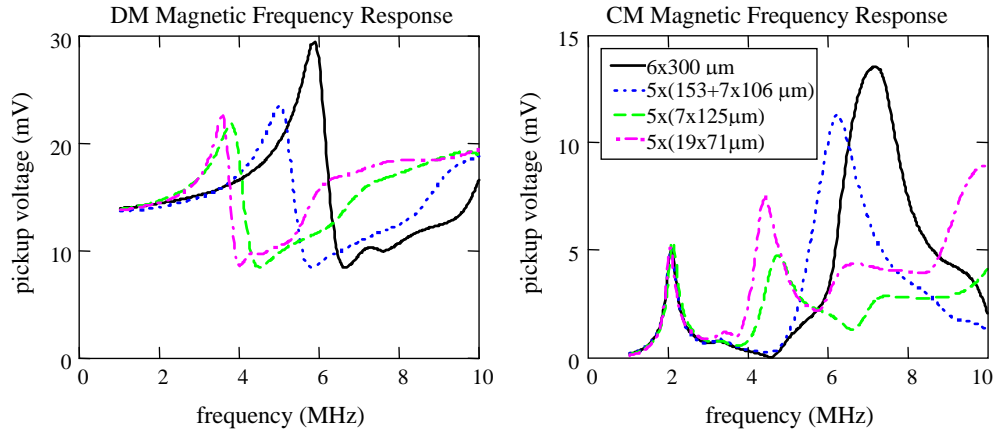


Figure 5.6: The differential-mode and common-mode magnetic frequency responses of various 15'' CMT deflection yokes with identical frame coils but with line coils made with different wire types.

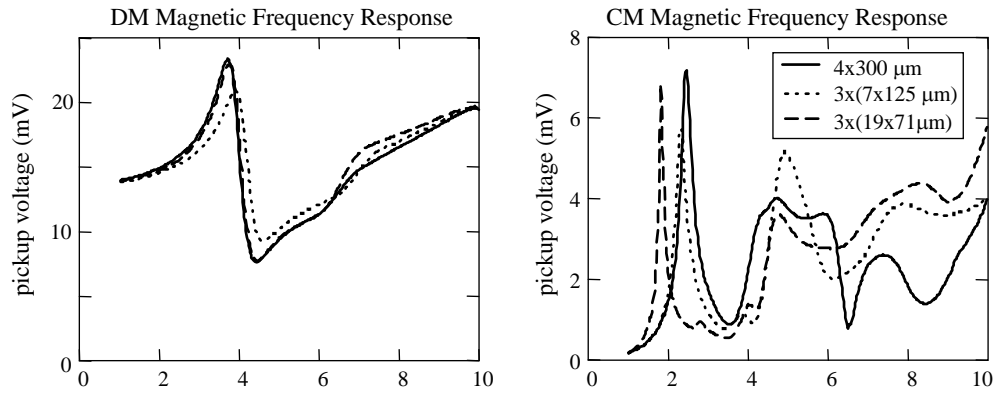


Figure 5.7: The differential-mode and common-mode magnetic frequency responses of various 15'' CMT deflection yokes with identical line coils but with frame coils made with different wire types.

5.5 Summary and conclusions

This chapter started with an overview of the theory on solenoids. Although thorough empirical validation of this theory is reported in the literature, these models turned out to be unsuitable for predicting the high-frequency behavior of deflection yokes. In particular, the prediction of ringing from the coil geometry and other design parameters of a deflection yoke is not accurate enough. A likely cause is that deflection coils have a more complicated geometry than solenoids. We cannot trust the theoretical relations between

circuit parameters and design parameters and have to rely on experimental analysis.

We presented experimental results for different wire diameters. With the methods described in Chapter 4 we measured the ringing performance of single line coils, of line-coil pairs and of complete deflection yokes. After fitting the parameters of the equivalent circuit models for various wire types we saw that especially the dependence of the capacitance on the wire type was different from the prediction by the solenoid models. Probably this is caused by the fact that the wires are positioned in a rather random way in CRT deflection coils in contrast to solenoids where successive turns are accurately positioned. This is also the reason why the spread in the position of the second peak in the impedance characteristic of single line coils, and hence the spread in the values of R_2, C_2, L_2 is quite large. Furthermore, also the capacitances to the environment of the coils probably have a strong effect.

When we changed the line-coil and frame-coil wires, we found that the common-mode ringing at frequencies below about 3 MHz are caused by oscillations inside the frame coils only. Oscillations inside the line coils affect both the common-mode and the differential-mode ringing in a similar way.

Although the theoretical models cannot be used for an accurate quantitative prediction of the ringing performance, they give a valuable qualitative description of the basic relations between ringing and the design parameters such the number of turns and the wire type of the line and frame coils. Without such a qualitative description it would be much more difficult to generate options to suppress ringing.

Chapter 6

Suppression of ringing

6.1 Introduction

In the previous chapters we have discussed how ringing of CRT deflection coils can be evaluated by measuring the frequency response. Subsequently, we have discussed various models to analyze and describe ringing. Although the theoretical models that successfully predict the oscillating behavior of solenoids do not accurately predict ringing of deflection coils, these models give us sufficient insight to generate ideas to suppress ringing. Our goal is to reduce ringing such that the effect is no longer visible on the screen.

In this chapter we apply this knowledge to explore and evaluate options to suppress ringing. A measure to reduce ringing should not hamper the primary function of deflection (Chapter 2), or result in a strong increase in dissipation (Chapter 3). We will therefore also evaluate the impact of various options to suppress ringing on both deflection and dissipation. We saw that the wire diameter has only a small impact on the ringing performance. In this chapter we will evaluate more drastic modifications of the deflection coils to reduce ringing.

The organization of this chapter is the following. First we will review the literature on the suppression of ringing in Sect. 6.2. Subsequently, we will discuss the suppression of the differential-mode line-coil ringing (Sect. 6.3), the differential-mode frame-coil ringing (Sect. 6.4) and the common-mode ringing (Sect. 6.5).

Part of this chapter has already been published in [226], [227], and [228].

6.2 Literature on the suppression of ringing

In the past, several measures have been proposed to suppress ringing. Although not much attention has been paid to ringing in the open literature, several ideas for solving the ringing problem are found in the patent literature.

Unfortunately, most of the ideas are not very useful for modern deflection coils. For instance, one proposal is to add external capacitances across each coil to obtain a balance in capacity such that the capacity relationships of the two coils are symmetrical [229–231]. In practice, this option is not used; not only because of the large spread in both the capacity of the coils and the external capacitances, but also because this option is effective only when the coils are connected in series, whereas modern line coils are connected in parallel (see Chapter 2).

Another proposal is to position the wires such that the interlayer voltage difference is reduced. Unfortunately, practical suggestions are only made for the case where frame coils are wound around the ferrite core [232]. For the double mussel coils considered in this thesis, no useful ideas are presented to reduce the voltage difference between successive layers. For this type of coils, it is proposed to electrically connect parallel wires in series [233], but this will result in an inductance that is much too large for practical applications.

More feasible proposals will be analyzed in more detail in this chapter.

6.3 Suppression of DM line-coil ringing

For the evaluation of techniques to suppress differential-mode line-coil ringing, we measured the magnetic frequency response before and after applying these techniques. Because the output impedance of the drive circuit is very important for differential-mode ringing, we have not only measured the magnetic frequency response of the deflection coils alone, but we have also measured the magnetic frequency response when a small inductance was placed in series with the line coils and the drive voltage. We assume that such a series impedance may also be present in actual drive circuits as a result of long or ill-positioned wires. To simulate the effect of such a series impedance, we measured the effect on the magnetic frequency response of including a $12\ \mu\text{H}$ series inductance. This value is 10% of the line inductance of a 17" CMT deflection yoke. It is chosen to be larger than found in practical circuits, to see the effect more clearly.

In the upcoming sections we discuss the following techniques to suppress differential-mode line-coil ringing:

1. change the line-drive electronics;
2. bi-directional winding of the line coils;
3. shunt to the line coils;
4. taps in the line coils;
5. distributed damping inside the line coils.

6.3.1 Change the line-drive electronics

The easiest way to reduce ringing is to adapt the drive electronics. A first way to deal with ringing problems is to increase the time delay between the start of the horizontal line scan and the start of the video signal of that line. Usually this delay is combined with some ‘overscan’ such that writing the video signal still starts at the left-hand border of the screen. This method is often applied to make differential-mode ringing invisible. However, the delay of the video signal has several disadvantages. First of all, the overscan results in higher power consumption due to the larger deflection angle. Furthermore, because of the delay, a higher video frequency is required during the active part of the line which may require more expensive components.

Another way to prevent ringing problems is to reduce unwanted high-frequency differential-mode currents by applying the following circuit design rules:

i. Reduce the output impedance of the drive circuit:

On page 104, we concluded that a large output impedance of the drive circuit enhances ringing. A first measure to reduce ringing, is therefore to reduce the output impedance of the drive circuit. Practical suggestions to do so are the following:

- use shorter wires, especially for connecting the deflection coils to the drive circuit;
- use components with low parasitic impedance; especially capacitors are notorious for their inductive behavior at high frequencies;
- if a diode modulator is used in series with the line drive circuit (to improve the scan linearity in horizontal direction), then the difference in switching times of the diode modulator and the main drive circuit should be short enough to prevent that the diode modulator acts like a high impedance for a short period of time.

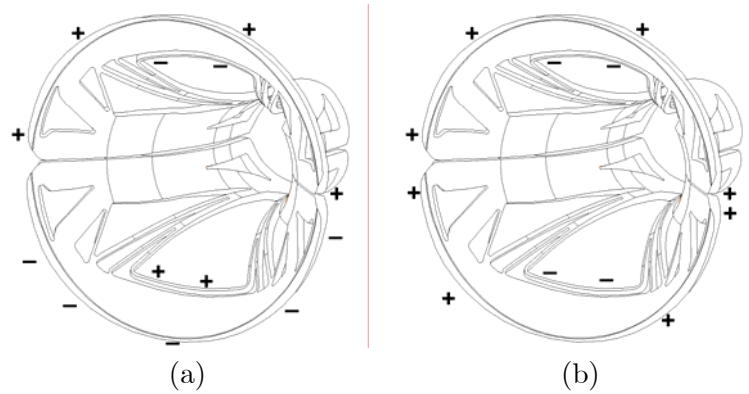


Figure 6.1: The voltage distribution along a line-coil pair is different when the line coils are wound in the same direction (a), than when they are wound in opposite directions (b).

ii. Reduce high-frequency signals generated by the drive circuit:

- minimize loop areas, especially minimize the distance between flyback capacitance and the diode;
- mount a ferrite bead around the leads of the diode or around the leads of the flyback capacitance;
- add damping resistances across auxiliary coils such as the line balance coil and the linearity coil;
- minimize crosstalk between different circuit parts, especially by decoupling the dc supply leads by means of capacitors.

These adaptations of the circuit design - although effective - will not be discussed in more detail as the purpose of this thesis is to improve the high-frequency performance of the deflection coils rather than improving the drive circuitry.

6.3.2 Bi-directional winding of the line coils

Today, almost every CMT deflection yoke has bi-directionally wound line coils, i.e. the two line coils in the deflection yoke are wound in opposite directions. These right-handed and left-handed wound coils were initially introduced to reduce the chance of dielectric breakdown [146] since it strongly reduces the

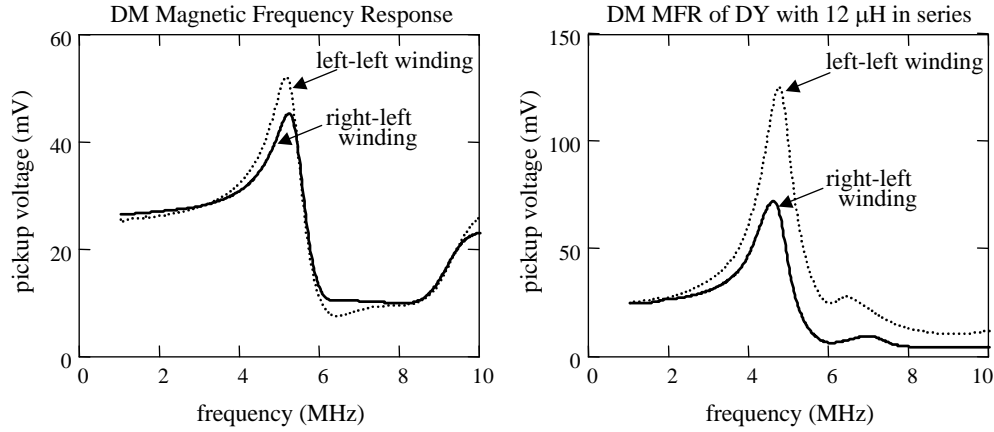


Figure 6.2: The differential-mode magnetic frequency response of a deflection yoke with the line coils wound in the same direction (dotted line) or in opposite directions (solid line). The figure at the right shows the magnetic frequency response when a $12\text{-}\mu\text{H}$ inductance is put in series with the line coils.

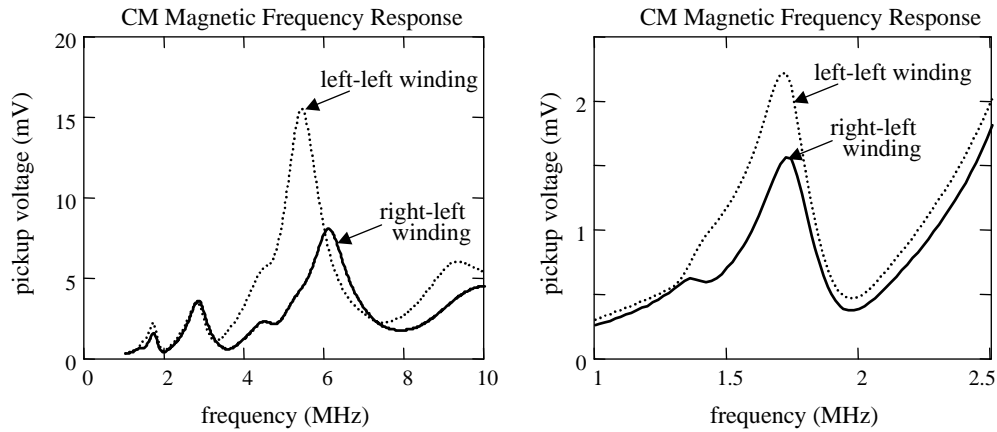


Figure 6.3: The common-mode magnetic frequency response of a deflection yoke with the line coils wound in the same direction (dotted curve) or in opposite directions (solid curve). The figure at the right shows the first peak in more detail.

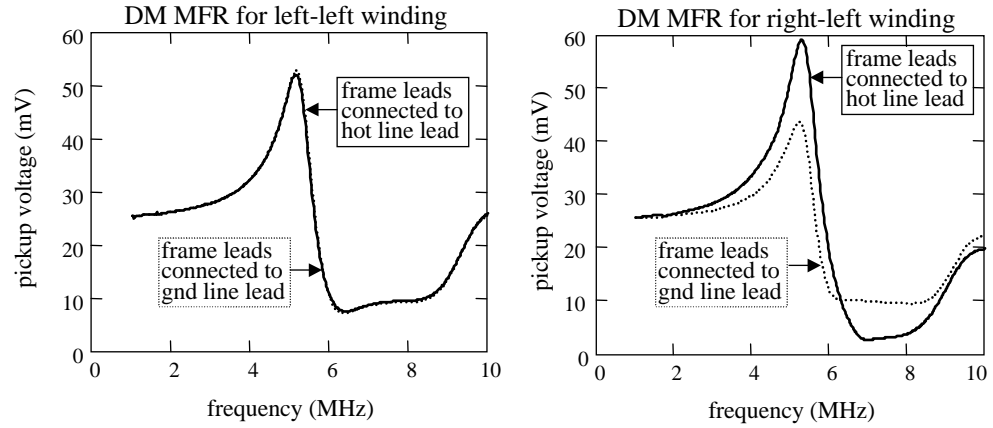


Figure 6.4: The differential-mode magnetic frequency response of a 17" CMT where both frame coil leads are connected to the 'ground' lead (dotted curve) of the line coils or to the 'hot' lead (solid curve). The first figure shows the results when the line coils are wound in the same direction. The second figure shows the results when the line coils are wound in opposite directions.

voltage difference between the outer wires of the two line coils as illustrated in Fig. 6.1.

The bi-directional winding of the line coils also results in much less ringing. Without the left/right winding technique, the capacitance between the adjacent sides of the coils has to be charged and discharged again every line scan period, whereas it remains uncharged once the winding direction of one of the coils is reversed [150]. In Sect. 5.3.2 we concluded that the ringing performance is strongly determined by the capacitance of each individual coil to its environment. The bi-directional winding technique reduces the influence of this capacitance.

Although bi-directionally wound line coils have already been in use for many years, no objective experimental results have been published about the suppressing effect on ringing. With the measuring methods introduced in Chapter 4, the effectiveness of the bi-directional winding technique can be studied in more detail by measuring the frequency response. Figure 6.2 shows the differential-mode magnetic frequency response of a 17" CMT deflection yoke with the line coils wound in the same direction (dotted line) or in opposite directions (solid line). When the two line coils are wound in opposite directions, the magnetic frequency response peaks are significantly smaller, which shows that this deflection yoke is less sensitive to ringing than when the line coils are wound in the same direction. The difference in ringing performance is much larger when a series inductance is included, as shown in

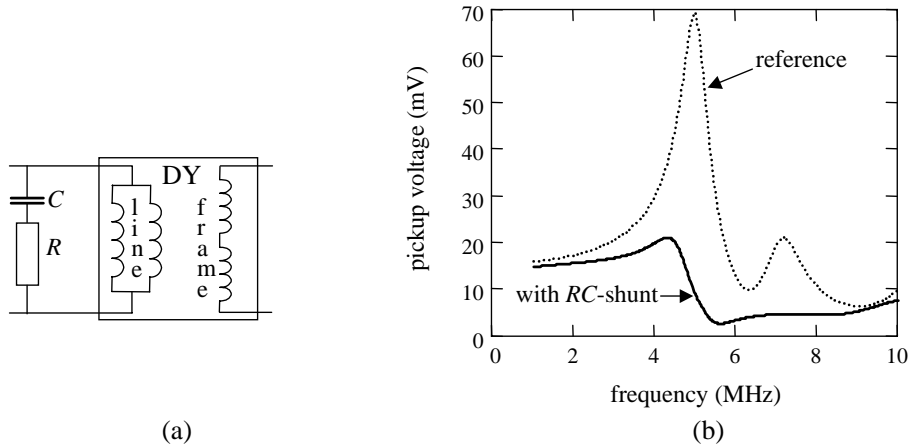


Figure 6.5: An RC shunt parallel to the line coils: (a) configuration, and (b) measured differential-mode magnetic frequency response of a 17" CMT in series with $12\ \mu\text{H}$, with (solid) and without (dotted) such an RC shunt.

the figure at the right-hand side of Fig. 6.2.

Furthermore, also the voltage difference between some parts of the line coils and the frame coils is reduced by using line coils that are wound in opposite directions. Figure 6.3 shows that the measured common-mode magnetic frequency response is strongly improved as well.

However, this winding of the line coils in opposite directions has one serious drawback: the sensitivity to ringing depends strongly on the way in which the line coils are connected. Figure 6.4a shows the measured differential-mode magnetic frequency response of a 17" CMT where both frame coil leads are connected to either the 'ground' lead of the line coils or to the 'hot' lead. Figure 6.4a shows the results when the line coils are wound in the same direction (the so-called 'left-left' winding). Clearly, there is no difference when the coils are wound in the same direction. Figure 6.4b shows the results when the line coils are wound in opposite directions ('right-left winding'). In contrast to the previous configuration, the amount of ringing depends strongly on the way in which the coils are connected. This is the reason why different deflection yokes have to be made for application circuits that apply a positive flyback voltage, and for application circuits that apply a negative flyback voltage. The ground of the circuit has to be connected to different leads of the line coils in these two concepts.

6.3.3 Shunt to the line coils

An option that is already commonly applied in practice, is to add a damping circuit in parallel to the line coils. The differential-mode line-coil ringing can be reduced by adding an RC -shunt to the line coil leads with an impedance which is much lower than the line coil impedance at ringing frequencies (above 1 MHz) and which is much higher at normal drive frequencies (up to 100 kHz). The basic principle of this arrangement is shown in Fig. 6.5a.

Practical values for the components of such a shunt are found as follows:

- the currents through the shunt should be negligible compared to the main current through the coils. Thus the impedance of the shunt at the highest significant harmonic of the drive signal should be much larger than the impedance of the coil parts. In Chapter 2, we concluded that the highest harmonic of the drive signal that contributes significantly to the dissipation is eight times the line frequency ω_ℓ . This constraint is simplified by requiring that the impedance of the capacitance is much larger than the impedance of the line-coil pair, i.e.

$$\frac{1}{8\omega_\ell C} \gg 8\omega_\ell L \quad (6.1)$$

For $L = 100 \mu\text{H}$ and $\omega_\ell = 2\pi \cdot 84 \text{ kHz}$, the requirement is that $C \ll 561 \text{ pF}$. A practical choice is $C = 220 \text{ pF}$.

- at a ringing frequency ω_r , the impedance of the resistance should be larger than that of the capacitance, or

$$R > \frac{1}{\omega_r C} \quad (6.2)$$

For $C = 220 \text{ pF}$ and $\omega_r = 2\pi \cdot 3 \text{ MHz}$, the requirement is that $R > 242 \Omega$. A practical choice is $R = 470 \Omega$.

- the ringing currents should flow more through the shunt than through the line coils. Thus the impedance of the shunt at ringing frequency ω_r should be lower than the impedance of the inductance:

$$R < \omega_r L \quad (6.3)$$

For $L = 100 \mu\text{H}$ and $\omega_r = 2\pi \cdot 3 \text{ MHz}$, the requirement is that $R < 1.9 \text{ k}\Omega$, which is already fulfilled in our case.

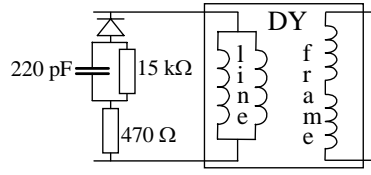


Figure 6.6: A practical configuration of an RC-shunt to the line coils.

The dissipation in the resistance is mainly caused by the flyback pulse (with a peak voltage up to 1.5 kV). By adding a diode in series such that no current flows during flyback, the dissipation in this RC -shunt is reduced significantly. Because the diode conducts again at the end of the flyback pulse, the damping circuit still catches possible sharp voltage peaks at the end of the flyback pulse. Figure 6.6 shows a practical configuration where an additional 15 kΩ resistance provides a conductive path, which is necessary for a proper functioning of the diode. We conclude that an RC -shunt is a possible method to damp the differential-mode ringing of the line coils.

Note that when a shunt circuit does reduce ringing in a certain configuration, it is an indication that the impedance of the drive circuit is too high at ringing frequencies. If the output impedance of the drive circuit would be much smaller than the impedance of the RC -shunt at the ringing frequency, much less or even no ringing reduction would be obtained. In fact, when we measure the magnetic frequency response of the deflection yoke alone, we see no change when adding a shunt in parallel because the driving voltage across the line coils remains the same. The damping effect of the shunt becomes quite clear when we add a small series inductance ($12\ \mu\text{H}$) in series with the measuring set-up. The measured magnetic frequency response (Fig. 6.5b) shows that ringing is significantly reduced but not eliminated.

Although favorable damping results are obtained with the diode-resistance-capacitance shunt to the line coils, a practical disadvantage is that the values of the shunt components have to be different for different monitor circuits due to differences in output impedances of the driving circuits. Therefore, it would be advantageous to damp the high-frequency oscillations inside the coils.

6.3.4 Taps in the line coils

A useful option to reduce the differential-mode ringing described in literature [234–240], is to connect a damping resistance to an electrical connection made inside each line coil. Each of these so-called taps is connected through a capacitance and a series resistance to the line ground. In several cases, it

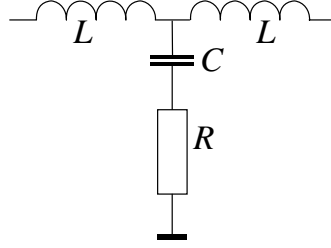


Figure 6.7: A simplified circuit diagram of the RC -tap in the line coils.

was reported that measures successful in one application turn out to make ringing even worse in another application so that additional modifications in the drive circuit are needed [241, 242]. This can be well understood with the theory presented in Chapter 4, as a distinction has to be made between the various ringing models.

Figure 6.7 shows a simplified circuit diagram of an RC -tap, assuming that the tap divides a line coil in two parts. A practical minimum value for such an inductance part is $L = 50 \mu\text{H}$.

Practical values for the components of such a tap are found in the same way as described for the shunt in the previous section:

- the currents through a tap should be negligible compared to the main current through the coils. Thus the impedance of the tap at the highest significant harmonic of the drive signal should be much larger than the impedance of the coil parts. In Chapter 2, we concluded that the highest harmonic of the drive signal is 8 times the line frequency ω_ℓ . This constraint is simplified by requiring that the impedance of the capacitance is much larger than the impedance of the coil parts

$$\frac{1}{8\omega_\ell C} \gg 8\omega_\ell L \quad (6.4)$$

For $L = 50 \mu\text{H}$ and $\omega_\ell = 2\pi \cdot 84 \text{ kHz}$, the requirement is that $C \ll 1 \text{ nF}$. A practical choice is $C = 120 \text{ pF}$.

- the ringing currents should flow more through the tap than through a coil half. Thus the impedance of the tap at ringing frequencies should be lower than the impedance of the inductance:

$$R < \omega_r L \quad (6.5)$$

For $L = 50 \mu\text{H}$ and $\omega_r = 2\pi \cdot 3 \text{ MHz}$, the requirement is that $R < 940 \Omega$.

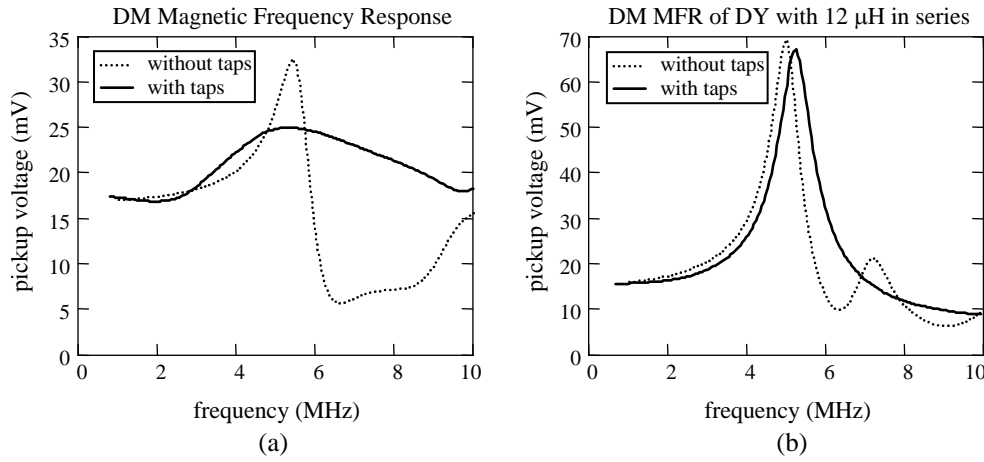


Figure 6.8: The differential-mode magnetic frequency response of a 17" CMT sample with (solid curve) and without (dotted curve) an RC -tap in each line coil, before (a) and after (b) adding a 12- μH series inductance.

- at a ringing frequency ω_r , the impedance of the resistance should be larger than that of the capacitance, i.e.

$$R > 1/\omega_r C. \quad (6.6)$$

For $C = 120 \text{ pF}$ and $\omega_r = 2\pi \cdot 3 \text{ MHz}$, the requirement is that $R > 442 \Omega$. A practical choice is $R = 470 \Omega$.

Although favorable results are reported in literature [234–240], we still found significant ringing when this option was applied in our measuring set-up when we added a small series inductance (12 μH). This was confirmed by visual front-of-screen inspection in actual monitor applications. Our measurement results, shown in Fig. 6.8, indicate that ringing of the deflection coils alone is indeed reduced by the RC -tap in each line coil. However, if ringing is enhanced by the presence of a small inductance in series with the line leads, the use of taps makes the ringing even worse.

We conclude that some ringing problems can indeed be solved by an RC -tap in each line coil, but taps are certainly no solution to all differential-mode line-coil ringing problems.

6.3.5 Distributed damping of the line coils

In theory, we could improve the damping of electrical oscillations by adding more RC -taps, as illustrated in Fig. 6.9a for a single line coil. Rather than

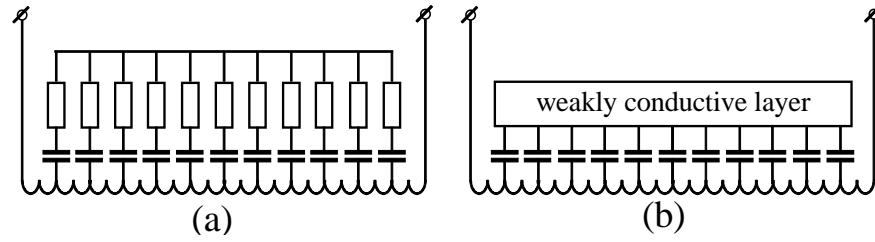


Figure 6.9: A configuration with many RC -taps in a coil (a) can be replaced by a similar coil with a conductive layer on the wires (b) in which the insulating layers of the wires act as capacitances.

damping ringing outside the deflection coils, it is more effective to damp high-frequency oscillations inside the coils. In fact, it would be worthwhile to add a resistance between each pair of coil windings. This gave us the idea to replace the separate resistors by a weakly conductive material close to the wires, as shown in Fig. 6.9b. In this new configuration, the insulating layers of the wires provide the capacitances.

We implemented the idea of distributed damping by impregnating the line coils with a weakly conductive fluid. First we applied a thin layer of carbon black particles suspended in a resin on the line coils. Later we obtained better results by impregnating the coils with a weakly conductive fluid like ATO¹, PEDOT² and Conquest³.

Typical experimental results are shown in Fig. 6.10. By impregnating the coils with controlled amounts of fluid, we could affect both the damping and dissipation. Clearly, the more conductive fluid is used, the stronger the damping of ringing, also when a 12 μH series inductance was included in the measuring set-up. However, when the damping became higher, also the dissipation increased.

From the line-impedance characteristics (Fig. 6.11) we found that, by impregnating each line coil with 0.75 ml PEDOT, the Q_r -factor of the oscillation changed from 6.8 to 3.0. Qualitatively, this reduction can be understood with the theory presented in Chapter 4 (see Eq. 4.38, in which the equivalent resistance R_r is lowered by adding resistive material in parallel to the capacitances between the coil windings).

Unfortunately, it turned out in a visual evaluation on a monitor screen, that even for $Q_r = 3.0$ the ringing is still visible. Although the ringing is significantly reduced, it is not completely suppressed.

¹AntimonyTonOxide, 6% suspension in water, (supplied by LBW BV, Eindhoven)

²PolyEthyleneDithiOThiophenepolystyrenesulphate (Bayer BV, Mijdrecht)

³Polypyrrole (supplied by DSM, Heerlen)

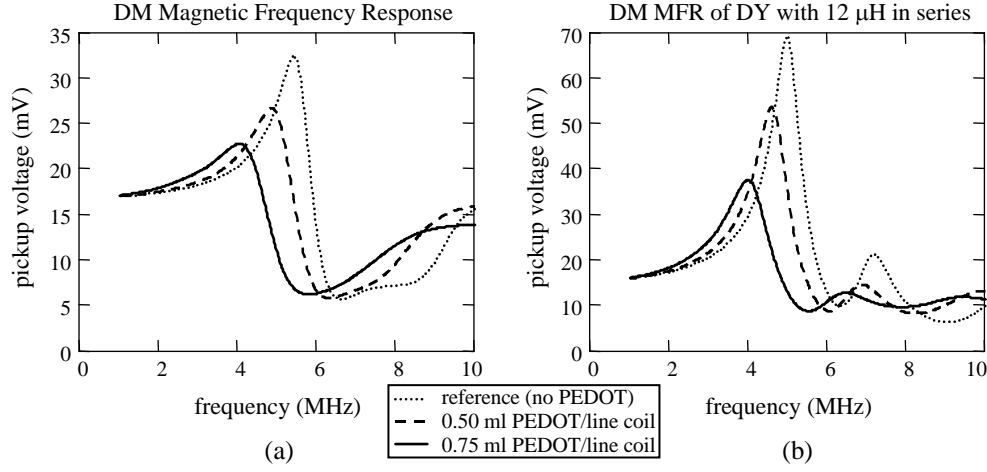


Figure 6.10: The differential-mode magnetic frequency response of a 17'' CMT for various amounts of conductive fluid (PEDOT) injected into the line coils, before (a) and after (b) adding a 12 μH series inductance.

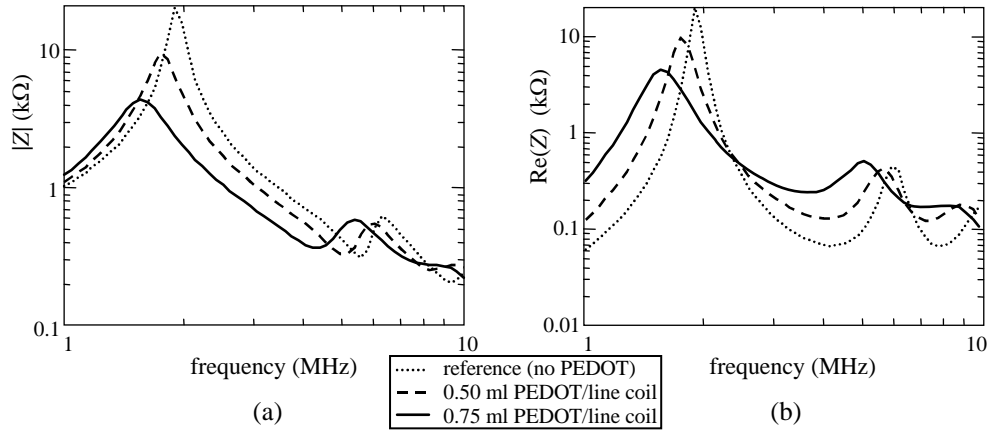


Figure 6.11: The modulus (a) and real part (b) of the line impedance of a 17'' CMT as a function of frequency for various amounts of conductive fluid (PEDOT) injected into the line coils.

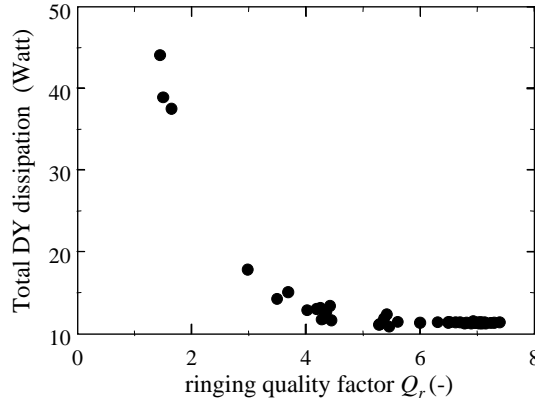


Figure 6.12: The total dissipation in a 17" CMT deflection yoke as a function of the quality factor Q_r , which quantifies the ringing performance.

Already at this level, the dissipation and hence the temperature rise became unacceptably high. With the measuring method described in Chapter 3, we found that the total dissipation in the deflection yoke changed from 11.3 Watt to 17.8 Watt. Temperature measurements showed that the temperature of the line coils rose with an additional 8 °C, while only an increase of less than 2 °C would be acceptable.

By varying the amount and concentration of the conductive fluid injected into the line coils, the relation between dissipation and ringing is determined empirically. Figure 6.12 shows the total dissipation of a 17" CMT as a function of Q_r which is a measure for ringing and which is determined from the impedance characteristic (see Chapter 3). As can be expected, the higher the suppression of ringing, i.e. the lower Q_r , the higher the dissipation.

Clearly, the technique of impregnating the line coils with a weakly conductive fluid is not practical since the dissipation becomes far too high for acceptable ringing suppression.

The problem with a conductive layer in a deflection coil is that the strong magnetic fields vary in time and induce eddy currents in such a conductive layer. These eddy currents can result in unacceptably high losses and heat generation. The challenge therefore was to develop a layer that suppresses at ringing frequencies (typically above 1 MHz), but which is not too dissipative for line frequencies (typically below 100 kHz).

An option to reduce the eddy currents is to use distinct conductive particles rather than a continuous medium of conducting material. The inclusion of conductive particles in a dielectric material leads to a strong increase of the dielectric loss, due to an increase of the interfacial polarization,

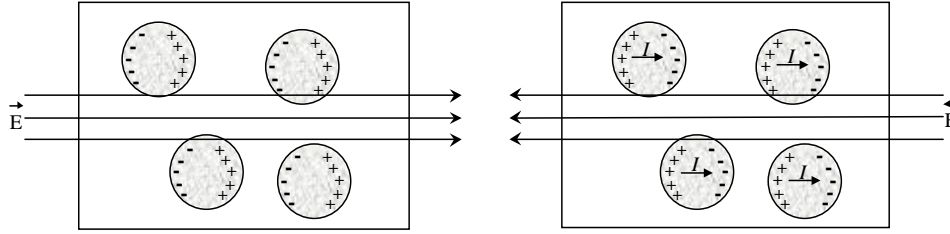


Figure 6.13: Due to an external electric field, the electric charges of weakly conducting particles accumulate at the interface with the insulating environment.

also called the Maxwell-Sillars-Wagner polarization [243–245].

The mechanism of interfacial polarization is illustrated in Fig. 6.13. Charge accumulates at the interface between the two materials in the presence of an electric field, below a certain frequency. If the electric field alternates, the polarization is reversed and consequently a current has to flow inside the particles. Because of the resistance of carbon-black this results in additional dissipation and thus damping of the electrical oscillation. These losses vary with frequency. At low frequencies the polarization follows the change of the electric field and the losses increase with frequency. At high frequencies the electric fields changes too rapidly for the polarization to build up, and the dielectric losses decrease with frequency.

The electrical properties of the compound depend on the material, the geometry and the distribution of the filler particles. Carbon black was chosen as conductive particles owing to its versatility, low cost and availability in a variety of special grades. The use of carbon black as a filler for polymers has been described extensively (see e.g. the references in [246–248]). The dielectric losses of a polymer filled with carbon-black particles is seen to increase with the amount of filler. This result has been clearly demonstrated by Yacobowicz et al. [249] for various carbon-black filled polymer materials.

We implemented this idea by using a suspension of fine carbon particles (Electrodag 109⁴). Unfortunately we found similar results as for PEDOT, i.e. a strong increase in dissipation when the concentration was high enough to get adequate suppression of ringing. In Sect. 6.5.5 we will see that, despite these results for the line coils, we succeeded in developing this technique towards an effective solution for the frame coils.

⁴Graphite suspension (supplied by Acheson BV, Scheemda)

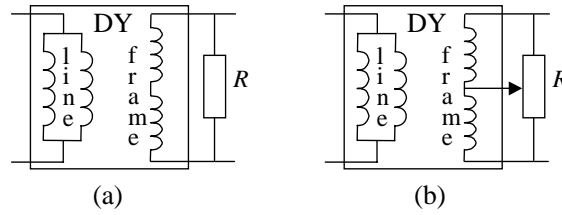


Figure 6.14: The differential-mode frame-coil ringing is adequately suppressed by either a resistance in parallel to the frame coils or (b) a potentiometer across the frame coils.

6.3.6 Evaluation

A single solution to fully suppress differential-mode line-coil ringing has not been found. A combination of different techniques is needed to obtain an adequate suppression of differential-mode ringing. For computer monitors, where ringing is most manifest, sufficient suppression is usually obtained by combining bi-directional winding of the line coils with an additional diode-resistor-capacitor shunt circuit.

Impregnating the line coils with a conductive fluid such as PEDOT also reduces the ringing level, but this quickly leads to an unacceptable increase of dissipation inside the line coils.

6.4 Suppression of DM frame-coil ringing

In fact, many of the techniques to suppress the differential-mode line-coil ringing, discussed in the previous section, can also be applied to suppress the differential-mode frame-coil ringing. In practice, however, adequate suppression is simply obtained by connecting a resistance in parallel to the frame coils (Fig. 6.14a). For many designs this is implemented either as a frame-balance potentiometer (Fig. 6.14b) which is primarily added for adjusting the difference in currents of the two frame coils.

In contrast to a similar shunt to the line coil, such a simple shunt to the frame coil does not result in significant power loss since the voltage across the frame coil is much lower than the voltage across the line coil. The maximum voltage across the frame coil is about 50 V, whereas during flyback the voltage across the line coil can raise up to 1.5 kV.

This is an effective, commonly used option to reduce the differential-mode frame-coil ringing. It has no effect on common-mode ringing and differential-mode line-coil ringing.

6.5 Suppression of common-mode ringing

Common-mode ringing is usually much more annoying than differential-mode ringing. The reason is that common-mode ringing occurs already at much lower frequencies than differential-mode ringing. For a same damping (quality factor), this results in a much longer decay time than for differential-mode ringing, so that the common-mode ringing bars are visible along a much longer distance along the screen.

In Chapter 5 we concluded that the common-mode ringing at frequencies below about 3 MHz are caused by oscillations inside the frame coils only. These have much lower resonance frequencies than the line coils because the frame coils have a much higher inductance than the line coils.

Unlike for suppressing differential-mode ringing, we only have to consider the frame coils for suppressing common-mode ringing. In the following sections we discuss the following techniques to do so:

1. change the drive electronics;
2. add a common-mode suppression choke;
3. add taps in the frame coils;
4. apply distributed damping in the frame coils.

6.5.1 Change the drive electronics

Unfortunately the option of delaying the video signal in combination with overscan is not suited to make common-mode ringing invisible because of the relatively long decay time of common-mode ringing.

In Sect. 6.3.1 various other options were presented to reduce differential-mode ringing by adapting the drive electronics. The common-mode ringing can be reduced too by similar measures in the parts of the drive electronics through which common-mode currents can flow. In addition, it is well known from the theory on Electromagnetic Compatibility (EMC) [250, 251] that common-mode currents can be prevented by avoiding currents through shared ground connections of e.g. line- and frame-drive circuitry.

6.5.2 Common-mode suppression choke

A commonly used method to suppress common-mode ringing is to increase the impedance for common-mode currents substantially by adding a common-mode suppression choke [252], see Fig. 6.15a. A practical example is shown in

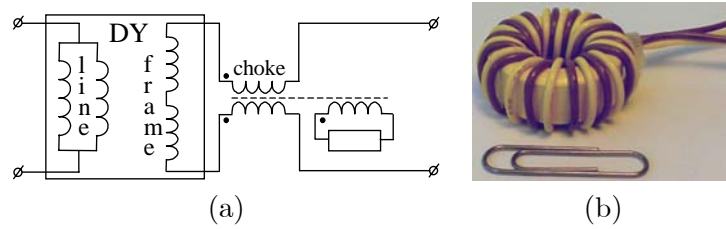


Figure 6.15: Common-mode suppression choke in the frame coil leads: circuit diagram (a) and photograph of the choke (b). The resistance and the third winding around the choke, shown in the circuit diagram, can be omitted when the ferrite losses are sufficiently high.

Fig. 6.15b. This choke consists of a low-grade ferrite toroid around which the frame coil leads are wound such that the normal (differential) currents give opposite and thus canceling magnetic fluxes inside the toroid.

The choke effectively suppresses the common-mode current without affecting the main frame drive current. This is because the magnetic fluxes in the choke caused by the common-mode currents do not cancel. By using a ferrite choke material with relatively high hysteresis losses, the common-mode ringing is efficiently damped. The damping can even be further increased by winding a third wire around the choke and by connecting this wire to a separate damping resistance. This is a very effective, and often used option to reduce common-mode ringing. It has no effect on differential-mode line-coil ringing.

A disadvantage of the common-mode suppression choke, however, is that the frame coils become ‘floating’ for high frequencies so that they can carry a high ringing voltage, invisible on the screen. At the front side of the tube the electrical fields are shielded by a (transparent) conductive coating on the front glass, but if no metal shield is present behind the tube the electrical fields may not comply with modern stray-field (the so-called ‘TCO AEF’) requirements.

Alternatively, the choke can be included in the line leads. This suppresses the common-mode ringing adequately, but this alternative has as disadvantage that the line coil inductance is increased so that a larger line voltage is required.

6.5.3 Taps in the frame coils

A practical alternative solution to suppress common-mode ringing is to make an electrical connection half way each frame coil and to connect a resistance

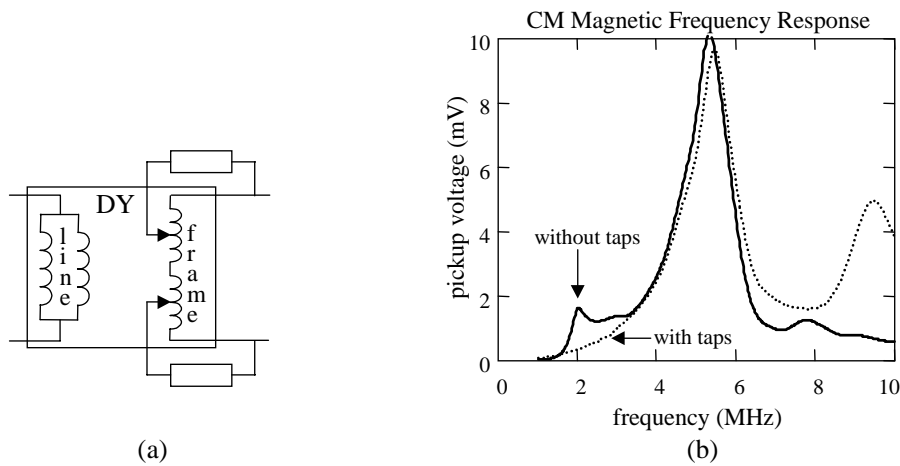


Figure 6.16: Taps in the frame coils: (a) configuration, (b) common-mode magnetic frequency response before and after adding taps in the frame coils of a 17" CMT. Note that adding taps does not change the differential-mode magnetic frequency response.

between this so-called tap and the closest frame coil lead [237–240], see Fig. 6.16a. From the theory presented in Chapter 4, it is clear that adding this resistance in parallel to a part the frame coil, and hence in parallel to the parasitic capacitance of this part, gives a stronger damping of ringing.

A capacitance can be added in series to the resistance to reduce the low-frequency leakage current, but is not really necessary. As illustrated by Fig. 6.16b taps in the frame coils effectively suppress the common-mode ringing peaks at low frequencies. As ringing at these frequencies turn out to be the major problem in real applications, taps in the frame coils are commonly applied.

6.5.4 Distributed damping of the frame coils

Similar to the suppression of differential-mode ringing of the line coils, good results were obtained by impregnating the frame coils with a weakly conductive fluid. As described in Chapter 4, adding a resistance in parallel to a coil gives a stronger damping of ringing.

Figure 6.17 shows the magnetic frequency response curves measured on 17" CMT deflection yokes in which the frame coils were impregnated with various amounts of PEDOT. The more PEDOT was used, the lower the ringing peaks and hence the stronger the suppression of the ringing. This was confirmed by front-of screen evaluation in customer sets.

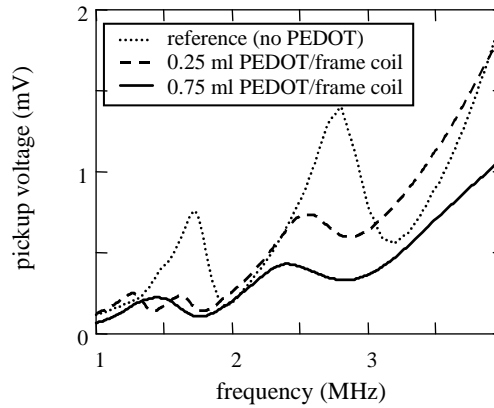


Figure 6.17: The common-mode magnetic frequency response of a 17'' CMT DY for various amounts of PEDOT impregnated in each frame coil.

Furthermore, we found that the total dissipation of the deflection yoke increased by less than 0.5 Watt, the temperature rise was unchanged within the measuring accuracy (2°C), and the change in convergence was less than $10\text{ }\mu\text{m}$. Hence this technique has been further worked out towards industrial implementation.

6.5.5 Ringing-free wire

Based on our experiments with impregnating the coils with conductive fluids, we asked our wire suppliers to include carbon-black particles in one of the outer layers of the wires [227]. This so-called Ringing-Free Wire (RFW) consists of a normal copper wire with an insulation layer plus on top the special layer with carbon-black particles, see Fig. 6.18. Both Belden BV and L&K developed such a wire. Belden BV transformed a standard wire, made with a polyurethane base coat and a polyamide bond coat, by incorporating carbon black in the bond coat [253]. A second structure has been developed by L&K. In this wire, a thin carbon black filled intermediate coat has been inserted between the base coat and the bond coat [228].

The influence of the carbon black amount on the properties of the wire has been studied [228]. Five different wire samples were prepared with various concentration of carbon black in the intermediate coat in the range [0-10% (weight)]. The properties of the wires are summarized in Table 6.1. Sample A corresponds to very low filler concentration while the sample E was made with a high carbon black amount.

Except for the electrical properties, the characteristics of the wire such as

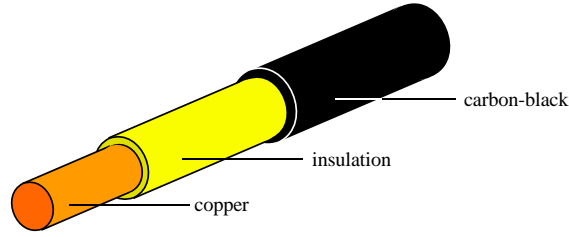


Figure 6.18: Schematic drawing of the Ringing-Free Wire, in which carbon-black particles are included in one of the outer insulating layers.

the mechanical, thermal or bonding properties are not affected by the presence of carbon black [228]. On the other hand, the insulation resistance is seen to decrease from 6 to 0.6 M Ω .cm. The breakdown voltage (ac) decreases slightly from 3.3 to 2.3 kV when the carbon black concentration is increased (from sample A to E). Such a change of the resistivity and the breakdown voltage is obviously caused by the conductive filler in the intermediate layer but the carbon black concentration is still low enough to comply with electrical insulation requirements.

We used this new wire type in the frame coils to suppress common-mode ringing.

To evaluate the effectiveness of this new technique, we first measured the impedance characteristic of the frame coils. The effect of the carbon black filled layer on the ringing effect can be seen in Fig. 6.19a where the impedance characteristics of single frame coils are presented for the different samples from Table 6.1. For low frequencies the impedance characteristics are rather similar for filled and unfilled standard wires whereas for higher frequencies impedance peaks corresponding to the ringing effect are more strongly attenuated with an increasing carbon-black concentration.

Although the losses are actually distributed along the turns of the coil,

Sample reference	A	B	C	D	E
Breakdown voltage (ac) (kV)	3.3	2.8	2.5	2.5	2.3
Insulation resistance (dc) (M Ω .cm)	6.0	2.6	0.9	0.7	0.6
Concentration (weight %)	2.0	2.5	3.0	6.0	10

Table 6.1: Properties of various carbon-black filled winding wires. For each wire the overall diameter was 0.300 ± 0.01 mm and the copper diameter was 0.259 ± 0.01 mm. Sample A was made with a very low filler concentration and sample E was made with a high carbon black amount (about 10%(wt)).

the effect on the ringing related to the dielectric loss may be quantified by fitting the two-*RCL*-sections model (Sect. 4.5.1) to the measured impedance characteristics. The fitting results are presented in Table 6.2. For sample E no second peak was seen anymore in the impedance characteristic so that the fitting of R_2, C_2, L_2 was not possible for this sample. The value of the R_1 resistance was 168 k Ω for the (unfilled) standard wire. It was found to decrease from 27 k Ω for the sample A down to 8 k Ω for the sample E presented in Fig. 6.19a. A similar trend is found for R_2 . The higher the concentration of carbon black, the lower the value of the parallel resistance and the stronger the damping of ringing. This is also clear from the value of the quality factor Q_r , calculated with Eq. 4.38 with the fitted values of R_1, C_1, L_1, R_2, C_2 , and L_2 .

The effect on ringing is also evaluated by measuring the common-mode frequency response. The measured common-mode frequency responses, shown in Fig. 6.19b, demonstrate the effectiveness of the new Ringing-Free Wire. Whereas sharp resonance peaks are measured with conventional deflection wires, a smooth frequency response is found when the new Ringing-Free Wire is used in the frame coils.

Subsequently, we have evaluated the effectiveness of this new common-mode suppression technology in various computer-monitor designs. As expected from the measured frequency-response, this technology gives a better suppression of the common-mode ringing than e.g. the common-mode suppression choke.

An alternative to varying the concentration of carbon black, is to vary the number of Ringing-Free Wires in the bundle wires with which the frame coils are wound [227]. Consequently, the number of conventional wires changes

sample	R_1 (k Ω)	C_1 (pF)	L_1 (μ H)	R_2 (k Ω)	C_2 (pF)	L_2 (μ H)	Q_r -
ref	168	14	143	19	44	112	12.9
A	27	27	154	5.2	50	193	2.9
B	21	43	155	4.2	75	220	2.7
C	20	49	153	3.7	82	222	2.5
D	15	52	156	3.2	95	216	2.3
E	8	71	165	-	-	-	-

Table 6.2: The values of parameters of the two-*RCL*-sections model, fitted to the measured impedance characteristics of single frame coils for various concentrations of carbon-black in the insulating layers of the wires.

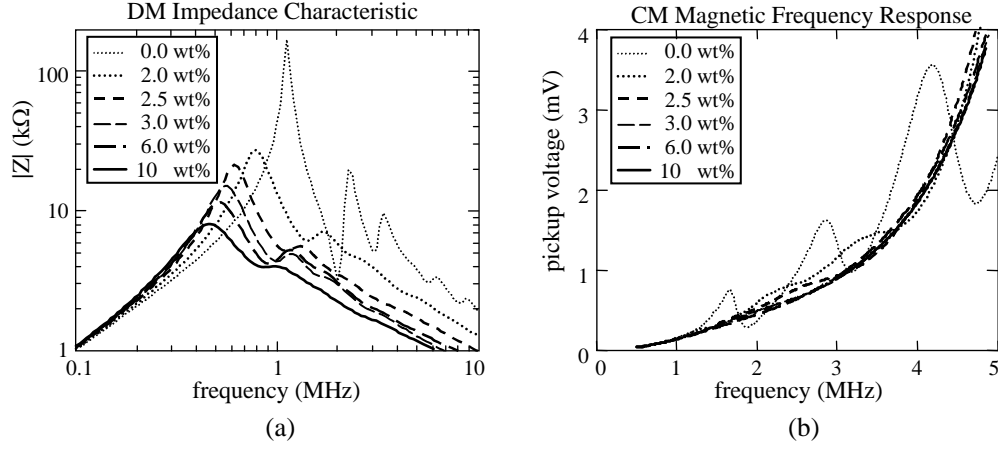


Figure 6.19: The impedance characteristic of a single frame coil (a) and the common-mode frequency response of a 17" CMT DY (b) for different concentrations of carbon black in the insulating layers of the frame-coil wires.

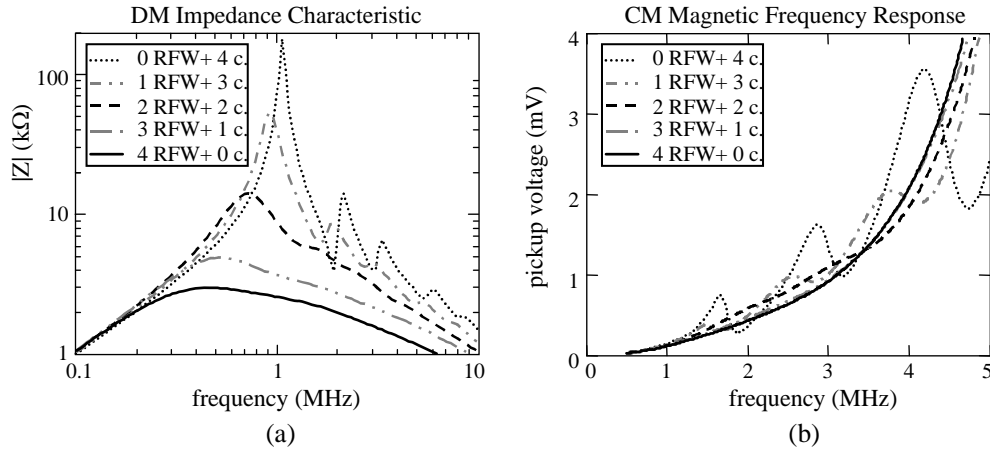


Figure 6.20: The impedance characteristic of single frame coils (a) and the common-mode frequency response of a 17" CMT DY (b) for various combinations of conventional wire ('c') and Ringing-Free Wire (RFW).

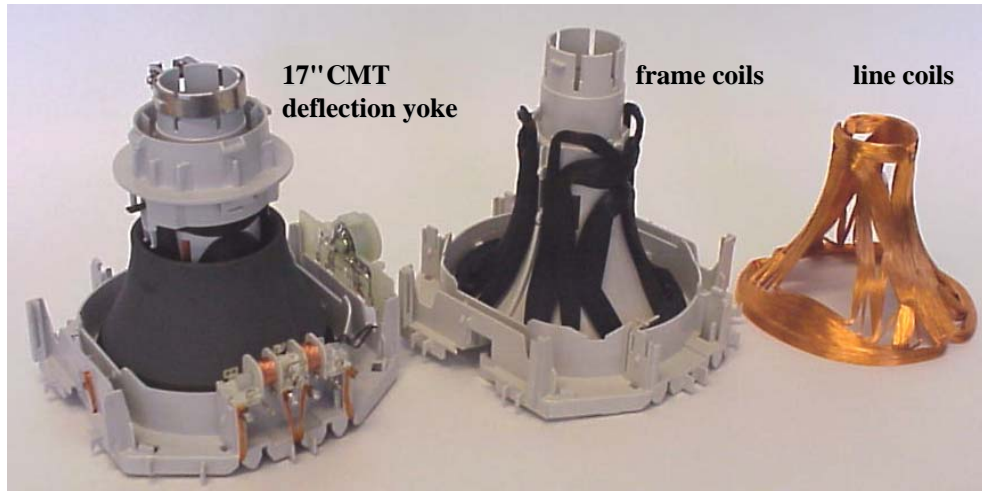


Figure 6.21: A 17" CMT with Ringing-Free Wire in the frame coils. The difference in color between the frame coils with Ringing-Free Wire and the line coils with conventional wires is more clearly to see when the ferrite core is removed.

accordingly as the total number of parallel wires should remain the same. Figure 6.20a shows the impedance characteristic of single frame coils of a 17" CMT for various combinations of conventional wire and Ringing-Free Wire. Figure 6.20 shows the corresponding common-mode magnetic frequency responses measured on 17" CMT deflection yokes with these frame coils.

A drawback of this new suppression technology could be an unacceptable dissipation as we found for the line coils. However, additional measurements on the dissipation of the deflection yoke, according to the method described in Chapter 3, showed that it increased by less than 1%. The explanation of this low increase of the loss is that the electric field between successive turns of the frame coil varies only at a low rate (50-120 Hz) where the dielectric losses are very small. The electric field of the line-coil wires varies at a much higher rate, but this electric line field is negligible in the frame coil. Furthermore, the strong magnetic field does not contribute to the dielectric losses.

In a deflection yoke, this technology is easily recognized from the black frame coils, see Fig. 6.21. For clarity, the ferrite core and the line coils are removed from a second sample so that the difference in color of the frame coils and the line coils is easily seen.

6.6 Summary and conclusions

In this chapter, various technological options to suppress ringing are evaluated by measuring the magnetic frequency response and the impedance characteristic of the deflection coils. The best suppression results are obtained by using a combination of different suppression technologies.

Differential-mode frame-coil ringing is already effectively suppressed by the potentiometer which is connected across the leads of the frame coils.

Differential-mode line-coil ringing can best be suppressed by winding the two line coils in opposite directions and by connecting an RC -damping circuit across the line coil leads. In practice, the line-coil ringing is not suppressed completely and is still visible during the first one or two millimeter at the left-hand side of the screen. This can be made invisible by applying overscan. In principle, further suppression is possible by impregnating the coils with a weakly conductive fluid such as PEDOT. In practice, however, this quickly results in an unacceptable increase of the dissipation in the line coils.

Common-mode ringing can be damped adequately by either a common-mode suppression choke in the leads of the frame coil, an RC -tap in the frame coils or by adding a weakly conductive layer to the frame coils. As a practical realization of this last option, carbon-black has been included in the bonding layer or in an additional insulating layer of the frame-coil wires. This Ringing-Free Wire is successfully implemented in industry.

Chapter 7

Conclusions

Although high-frequency effects are usually not taken into account during the first design phases of CRT deflection coils, they are becoming increasingly important. As a result of the trends towards higher image quality and shorter tubes, the deflection coils have to generate stronger magnetic fields at higher frequencies. This results in more dissipation and in more ringing.

Dissipation is the conversion of electrical energy into heat. Ringing is caused by high-frequency electromagnetic oscillations in the deflection coils and results in an annoying pattern of alternating lighter and darker vertical bars at the left-hand side of the screen.

Dissipation and ringing are strongly related. Physical phenomena that contribute to the dissipation also determine the damping of ringing. From the Fourier expansion of the drive currents, it is clear that electromagnetic phenomena for frequencies up to 1 MHz have to be considered for dissipation, while ringing occurs at even higher frequencies, typically between 1 and 10 MHz. Circuit models that describe dissipation can be extended to describe ringing. Furthermore, the same (impedance) measurements can be used to analyze both dissipation and ringing.

Dissipation

The main causes of the dissipation in a deflection yoke are dc losses of the drive current in the copper wires and proximity losses due to the large magnetic field through the copper wires. Other loss phenomena, such as hysteresis loss in the ferrite core, the skin effect in itself and dielectric loss phenomena, turn out to be less important and can be neglected.

To reduce the proximity losses in the wires, it is common practice to wind the coils with several thinner wires in parallel, rather than a few thicker

wires. The number of parallel wires is adjusted to obtain the same total copper volume. If the number of wires becomes too high to handle, litz wires are used. However, our experimental results indicate that the reduction in dissipation by using litz wires rather than thick solid wires is less than expected from the theory on the proximity effect alone. To explain this, we introduced a description with an interwire proximity effect in a bundle of parallel wires that depends on the total diameter of the bundle, instead of on the diameter of the separate conductors. The net magnetic flux through the surface enclosed by pairs of wires causes additional currents to flow. This results in a non-uniform distribution of the currents over the parallel wires, and thus in a higher dissipation.

It is clear that most of the measures to reduce the dissipation lead to higher costs. Some evident examples are the use of litz wires instead of solid wires and the use of thicker yoke rings. Measures with less impact on the cost price have to be taken during the first conceptual design phase where e.g. the coil shape, coil length and copper volume are defined. The largest contribution to the reduction of dissipation can be achieved by measures at system level, such as by decreasing the anode voltage and the deflection angle. Once, the design of the CRT is fixed, the dissipation in the deflection coils can still be reduced to some extent by adjusting the thickness of the coils. In the last design phase, when the winding tools are fixed and the shape of the coils cannot be changed anymore, only the wire type and the number of parallel wires may be changed. In general, thinner wires result in a lower dissipation. Moreover, our experimental results indicate that the dissipation can be further reduced by twisting the parallel wires in such a way that each wire assumes, to substantially the same extent, the different possible positions in the cross-section of the conductor.

Ringling

Although ringling is one of the most common complaints from circuit designers of computer monitors, not much has been published about ringling in deflection yokes in the open literature and no adequate measuring methods were available. In this thesis new theoretical models as well as new measuring methods for ringling are presented.

In addition to the existing method of recording the light intensity at the screen as a function of the horizontal distance from the left-hand side of the screen, we introduced three new alternative methods to measure ringling. In the first method we measure the optical frequency response by recording the modulation depth of the variation in light intensity at the front of the screen

as a function of the frequency of a sine-wave voltage source in series with the deflection yoke and the drive circuitry. In the second method we measure the magnetic frequency response by measuring the amplitude of the magnetic field with a large pick-up coil inside the deflection yoke as a function of frequency of a sine-wave voltage which directly drives the deflection yoke. In the third method, the impedance characteristics of the coils are measured.

The three measuring methods have complementary advantages. The advantage of the optical frequency response is that it is directly related to the conventional method of recording the light-intensity at the left-hand side of the screen. Moreover, by measuring the frequency response, various ringing modes can be analyzed separately and a distinction can be made between differential-mode and common-mode ringing. This allows for a more detailed analysis of ringing than is possible with the conventional method. The magnetic frequency response is similar to the optical frequency response, but is easier to measure. The advantage of the impedance characteristic is that it enables us to describe ringing with equivalent circuit models. With analytical formulae derived from these circuit models, a frequency response can be described with only a few fit parameters.

We presented a new theory on ringing in which differential-mode ringing and common-mode ringing are described with equivalent circuit models. A good agreement is obtained between the measured impedance characteristics and the impedance characteristic of the equivalent circuit models by a simple fit of the circuit parameters. The analytical formula derived from the circuit models enable us to describe the ringing performance of a deflection yoke with only a small number of fit parameters and to characterize the sensitivity of deflection coils for ringing with a single quality factor.

Although the quantitative prediction of ringing with these circuit models from the geometry and other design parameters of deflection coils turns out to have a limited value, these models are very helpful for understanding and describing the ringing phenomenon. Without such an understanding it would be much more difficult to generate options to suppress ringing.

Finally we have evaluated existing as well as new technological options to suppress ringing by measuring the magnetic frequency response and the impedance characteristic of the modified deflection coils. Differential-mode frame-coil ringing is effectively suppressed by the existing potentiometer which is connected across the leads of the frame coils. Differential-mode line-coil ringing can best be suppressed by winding the two line coils in opposite directions and by connecting an external damping circuit across the line coil leads. In practice, the line-coil ringing is not suppressed completely and is still visible during the first one or two millimeter at the left-hand

side of the screen. This can be made invisible by applying overscan. In principle, further suppression is possible by impregnating the coils with a weakly conductive fluid such as PEDOT. In practice, however, this quickly results in an unacceptable increase of the dissipation in the line coils.

Common-mode ringing can be damped adequately by either a common-mode suppression choke in the leads of the frame coil, resistors connected to taps in the frame coils or by adding a weakly conductive layer to the frame coils. As a practical realization of this last option, carbon-black particles are included in one of the outer layers of the frame-coil wires. This Ringing-Free Wire is successfully implemented in industry.

Appendix A

The diffusion equation

In this appendix, the ‘diffusion equation’ is derived for the electric field.

We start by giving two of Maxwell’s laws in the complex phasor notation, obtained by replacing the time derivatives by $i\omega$ (because we consider sinusoidal variations in time in linear media):

$$\vec{\nabla} \times \vec{E} = -i\omega \vec{B} \quad (\text{A.1})$$

and

$$\vec{\nabla} \times \vec{H} = \vec{j} + i\omega \vec{D} \quad (\text{A.2})$$

In these equations, \vec{B} denotes the magnetic flux density, \vec{D} the electric displacement density, \vec{E} the electric field, \vec{H} the magnetic field, and \vec{j} the electric current density.

We assume the following constitutive relations in a homogeneous and isotropic medium:

$$\begin{cases} \vec{B} &= \mu \vec{H} \\ \vec{D} &= \epsilon \vec{E} \\ \vec{j} &= \sigma \vec{E} \end{cases} \quad (\text{A.3})$$

In these equations, μ denotes the magnetic permeability, ϵ the dielectric permittivity, and σ the specific electrical conductivity

Substituting Ohm’s law, $\vec{j} = \sigma \vec{E}$, in Eq. A.2 results in

$$\vec{\nabla} \times \vec{H} = (\sigma + i\omega\epsilon) \vec{E} \quad (\text{A.4})$$

Since the divergence of any curl operator is zero, we find

$$0 = (\sigma + i\omega\epsilon) \vec{\nabla} \cdot \vec{E} \quad (\text{A.5})$$

under the assumption that both σ and ϵ are homogeneous within a conductor. We conclude that in a conductor

$$\vec{\nabla} \cdot \vec{E} = 0 \quad (\text{A.6})$$

Consequently, the charge density is zero inside homogeneous conductors. Charge can only be found at the surface of conductors.

Furthermore, by taking the curl of Eq. A.2 we obtain

$$\vec{\nabla} \times \vec{\nabla} \times \vec{E} = -i\omega(\vec{\nabla} \times \vec{B}) \quad (\text{A.7})$$

By applying the vector identity

$$\vec{\nabla} \times \vec{\nabla} \times \vec{E} = -\nabla^2 \vec{E} + \vec{\nabla}(\vec{\nabla} \cdot \vec{E}) \quad (\text{A.8})$$

and combining the result with the constitutive relations (Eq. A.3) and Maxwell's law Eq. A.2, we obtain

$$-\nabla^2 \vec{E} + \vec{\nabla}(\vec{\nabla} \cdot \vec{E}) = -i\omega\mu\sigma\vec{E} + \epsilon\mu\omega^2\vec{E} \quad (\text{A.9})$$

The second term in this expression equals zero according to Eq. A.6, so that we obtain the following differential equation for the electric field:

$$\nabla^2 \vec{E} = i\omega\mu\sigma\vec{E} - \epsilon\mu\omega^2\vec{E} \quad (\text{A.10})$$

The last term (with ω^2) can be neglected when $\omega\epsilon \ll \sigma$ so that:

$$\nabla^2 \vec{E} = i\omega\mu\sigma\vec{E} \quad (\text{A.11})$$

This is a fundamental law of propagation for many physical quantities. For instance, it is mathematically identical to the (scalar) heat conduction equation. In the same way it can be shown that the same relation holds for \vec{B} , \vec{D} , \vec{H} , \vec{j} and also for the vector potential \vec{A} which was introduced in Sect. 3.4.2.

Note that neglecting the last (ω^2) term in Eq. A.10 results in neglecting the phase difference of fields along the wire. This assumption that electric and magnetic fields propagated “instantaneously”, is called the *quasi-stationary approximation*.

Appendix B

Proximity loss

In this appendix, an expression is derived for the proximity loss in a wire due to eddy currents induced by an alternating magnetic flux density \vec{B} by solving Maxwell's equations outside and inside the wire. The total net current in the wire is assumed to be zero.

Practical calculations can be simplified significantly by introducing the magnetic vector potential \vec{A} , with

$$\vec{B} = \vec{\nabla} \times \vec{A} \quad (\text{B.1})$$

Since there are any number of vector functions whose rotation is the same we add a restriction, in this case the Coulomb gauge:

$$\vec{\nabla} \cdot \vec{A} = 0 \quad (\text{B.2})$$

Combination of Eqs. A.1, A.3, B.1 and B.2 leads to the 'Poisson equation':

$$\nabla^2 \vec{A} = -\mu \vec{j} \quad (\text{B.3})$$

Outside the conductor, in free space, both charge density and current density are zero and the Poisson equations reduce to the 'Laplace equation':

$$\nabla^2 \vec{A} = \vec{0} \quad (\text{B.4})$$

Because we consider a symmetrical case where currents only flow in the z -direction, we consider only the z -component:

$$\nabla^2 A_z = 0 \quad (\text{B.5})$$

This Laplace equation has been solved for many different geometries. For problems with cylindrical wires, evaluation in cylindrical coordinates (r, ϕ, z)

is most appropriate. If all quantities do not depend on z , it can be shown (by separation of variables) that the general solution of the Laplace equation is given by:

$$A_z(r, \phi) = a_0 + b_0 \ln \frac{r}{r_0} + \sum_{n=1}^{\infty} r^n \{a_n \cos n\phi + b_n \sin n\phi\} + \sum_{n=1}^{\infty} r^{-n} \{c_n \cos n\phi + d_n \sin n\phi\} \quad (\text{B.6})$$

An important property of this Laplace equation is the uniqueness of its solutions; two functions can only comply with the Laplace equation and the boundary conditions if the two functions are identical, i.e. only one single solution exists. We could start with the general solution given by Eq. B.6, but we can save effort by making an educated guess about the solution.

A wire is modeled as a metal cylinder with radius a and length ℓ with its axis perpendicular to an external varying field $B(t) = B_0 \cos \omega t$. The amplitude and direction of the magnetic vector potential describing the uniform external field in a point with cylindrical coordinates (r, ϕ, z) is given by

$$\vec{A}_0^{\text{ext}} = B_0 r \sin \phi \vec{e}_z \quad (\text{B.7})$$

This is easily validated by writing out $\vec{B} = \vec{\nabla} \times \vec{A}$.

According to Faraday's law of induction, the varying magnetic field inside the cylinder induces an electric field in the z -direction. Since this electric field is produced inside a conductor, currents will flow according to Ohm's law. These currents generate an additional magnetic field, also outside the cylinder. Because of symmetry conditions we expect that this additional field also varies with $\sin \phi$. We therefore try to solve the differential equations by only considering the two $\sin \phi$ -terms of Eq. B.6:

$$A_{0z} = (b_1 r + d_1 r^{-1}) \sin \phi \quad (\text{B.8})$$

At large distances, only the term $b_1 r \sin \phi$ is important which corresponds to the uniform external field of Eq. B.7, so that $b_1 = B_0$. This turns Eq. B.8 into

$$A_{0z} = (B_0 r + d_1 r^{-1}) \sin \phi \quad (\text{B.9})$$

The value of the constant d_1 follows from the boundary conditions.

Within the conductor, we make a similar educated guess for the fields. Because of the continuity of the fields at the boundary, we expect that within the wire the magnetic vector field A_z can also be written as a product of a distance-dependent part and a $\sin \phi$ -factor, and we therefore try

$$A_{1z} = F(r) \sin \phi \quad (\text{B.10})$$

Substitution in the diffusion equation (Eq. 3.14) in cylindrical coordinates gives after division by $\sin \phi$:

$$\frac{d^2 F(r)}{dr^2} + \frac{1}{r} \frac{dF(r)}{dr} + \left(k^2 - \frac{p}{r^2}\right) F(r) = 0 \quad (\text{B.11})$$

with $p=1$ and $k^2 = -i\omega\mu\sigma$. Equation B.11 is known as *Bessel's differential equation* and the solution which is bounded at $r = 0$ for $p = 1$ is known as the Bessel function $J_1(kr)$ of the first kind, see Appendix C. We can thus write:

$$F(r) = cJ_1(kr) \quad (\text{B.12})$$

and

$$A_{1z} = cJ_1(kr) \sin \phi \quad (\text{B.13})$$

where c is a constant which follows from the two boundary conditions at the surface of the wire (with $\mu_r = 1$ for copper):

1. the tangential component $B_{0\phi}$ of the magnetic field within the wire equals the tangential component $B_{1\phi}$ of the field outside the wire: $B_{0\phi} = B_{1\phi}$, for $r = a$
2. the radial component B_{0r} of the magnetic field within the wire equals the radial component B_{1r} of the field outside the wire: $B_{0r} = B_{1r}$, for $r = a$

With $\vec{B} = \vec{\nabla} \times \vec{A}$ this implies for the magnetic vector potential:

$$\begin{cases} \frac{\partial A_{0z}}{\partial r} = \frac{\partial A_{1z}}{\partial r}, & \text{for } r = a \\ \frac{\partial A_{0z}}{\partial \phi} = \frac{\partial A_{1z}}{\partial \phi}, & \text{for } r = a \end{cases} \quad (\text{B.14})$$

Substitution of Eq. B.9 for A_{0z} and Eq. B.13 for A_{1z} gives

$$\begin{cases} B_0 - d_1/a^2 = ckJ_1'(ka) \\ B_0 a + d_1/a = cJ_1(ka) \end{cases} \quad (\text{B.15})$$

where $J_1'(x) = dJ_1(x)/dx$. With the identity $xJ_1'(x) = xJ_0(x) - J_1(x)$ (see Appendix C), we find

$$c = \frac{2B_0}{kJ_0(ka)} \quad (\text{B.16})$$

and

$$d_1 = a^2 B_0 \left(\frac{2J_1(ka)}{kaJ_0(ka)} - 1 \right) \quad (\text{B.17})$$

Inside the wire we thus have found (combining Eq. B.16 and Eq. B.13):

$$A_{1z} = \frac{2}{k} B_0 \frac{J_1(kr)}{J_0(ka)} \sin \phi \quad (\text{B.18})$$

Combining the Poisson equation (Eq. B.3) with the diffusion equation (Eq. 3.14) and the definition of k (Eq. 3.22) results in

$$j_z(r, \phi) = -\frac{k^2}{\mu} A_{1z} \quad (\text{B.19})$$

So with the constitutive equation $B_0 = \mu H_0$ this can be written as

$$j_z(r, \phi) = -2H_0 k \frac{J_1(kr)}{J_0(ka)} \sin \phi \quad (\text{B.20})$$

In cylindrical coordinates $dV = \ell r d\phi dr$, so that the loss due to the proximity effect is given by

$$P_{\text{prox}} = \frac{\ell}{2\sigma} \int_{r=0}^a \int_{\phi=0}^{2\pi} j_z(r, \phi) \cdot j_z^*(r, \phi) r d\phi dr \quad (\text{B.21})$$

Substitution of the current density, Eq. B.20, gives

$$P_{\text{prox}} = \frac{\ell}{2\sigma} \int_{r=0}^a \int_{\phi=0}^{2\pi} \left\{ -2H_0 k \frac{J_1(kr)}{J_0(ka)} \sin \phi \right\} \cdot \left\{ -2H_0 k \frac{J_1(kr)}{J_0(ka)} \sin \phi \right\}^* r d\phi dr \quad (\text{B.22})$$

With the general identities $(a \cdot b)^* = a^* \cdot b^*$, $(J_p(x))^* = J_p(x^*)$ and $\int_0^{2\pi} \sin^2 \phi d\phi = \pi$ this becomes

$$P_{\text{prox}} = \ell \frac{\pi}{2\sigma} (2H_0)^2 \int_0^a k \frac{J_1(kr)}{J_0(ka)} \cdot k^* \frac{J_1(k^*r)}{J_0(k^*a)} r dr \quad (\text{B.23})$$

With the identities presented in Appendix C, this can be further reduced to

$$P_{\text{prox}} = -\ell \frac{2\pi}{\sigma} H_0^2 \text{Re} \left(\frac{ka J_1(ka)}{J_0(ka)} \right) \quad (\text{B.24})$$

Appendix C

Bessel functions

The differential equation

$$\frac{d^2 w}{dz^2} + \frac{1}{z} \frac{dw}{dz} + \left(k^2 - \frac{p}{z^2}\right)w = 0 \quad (\text{C.1})$$

is known as the ‘Bessel equation’. The solutions of this equation and their properties are well documented in regular textbooks and handbooks [254,255]. This appendix summarizes some formulae useful for Chapter 3. For sake of reference, citations to equation numbers in the handbook of Abramowitz [195] are given. The Bessel equation is given in ([195], Eq. 9.1.1).

The solution which is bounded at $z = 0$ for $p \geq 0$ is known as the Bessel function $J_p(z)$ of the first kind. It is defined as ([195], Eq. 9.1.10):

$$J_p(z) = \left(\frac{z}{2}\right)^p \sum_{k=0}^{\infty} \frac{\left(-\frac{1}{4}z^2\right)^k}{k! \Gamma(p+k+1)} \quad (\text{C.2})$$

From the definition Eq. C.2 it can be proven that ([195], Eq. 9.1.40):

$$J_p(z^*) = \{J_p(z)\}^* \quad (\text{C.3})$$

where $z^* = (x + iy)^* = (x - iy)$ denotes the complex conjugate of z .

A basic identity is ([195], Eq. 9.1.28):

$$\frac{dJ_0(z)}{dz} = -J_1(z) \quad (\text{C.4})$$

All Bessel functions $J_p(z)$ and its derivatives with integer p can be expressed in terms of $J_0(z)$ and $J_1(z)$ only. We have applied ([195], Eq. 9.1.27):

$$J_2(z) = \frac{2}{z}J_1(z) - J_0(z) \quad (\text{C.5})$$

and

$$\frac{dJ_1(z)}{dz} = J_0(z) - \frac{1}{z}J_1(z) \quad (\text{C.6})$$

Many integrals of products of Bessel functions have been published. We use ([195], Eq. 11.3.29):

$$\int_0^a (\alpha^2 - \beta^2) J_p(\alpha r) J_p(\beta r) r dr = a \{ \alpha J_{p+1}(\alpha a) J_p(\beta a) - \beta J_p(\alpha a) J_{p+1}(\beta a) \} \quad (\text{C.7})$$

To derive Eq. 3.28 from Eq. 3.27, substitute $\alpha = k$, $\beta = k^*$ and $p = 0$ in Eq. C.7 and use Eq. C.5 to get

$$\int_0^a \{k^2 - (k^*)^2\} J_0(kr) J_0(k^*r) r dr = a \{k J_1(ka) J_0(k^*a) - k^* J_0(ka) J_1(k^*a)\} \quad (\text{C.8})$$

and thus with $k^2 = -(k^*)^2$ (which follows from the definition of k^2 in Eq. 3.22) the following relation results

$$\int_0^a k \frac{J_0(kr)}{J_1(ka)} k^* \frac{J_0(k^*r)}{J_1(k^*a)} r dr = \frac{a}{2} \left\{ k^* \frac{J_0(k^*a)}{J_1(k^*a)} + k \frac{J_0(ka)}{J_1(ka)} \right\} = \text{Re} \left(ka \frac{J_0(ka)}{J_1(ka)} \right) \quad (\text{C.9})$$

To derive Eq. 3.40 from Eq. B.23, substitute $\alpha = k$, $\beta = k^*$ and $p = 1$ in Eq. C.7 to get

$$\int_0^a \{k^2 - (k^*)^2\} J_1(kr) J_1(k^*r) r dr = a \{k J_2(ka) J_1(k^*a) - k^* J_1(ka) J_2(k^*a)\} \quad (\text{C.10})$$

which can be reduced with Eq. C.5 to

$$\int_0^a k \frac{J_1(kr)}{J_0(ka)} k^* \frac{J_1(k^*r)}{J_0(k^*a)} r dr = -\frac{a}{2} \left\{ k^* \frac{J_1(k^*a)}{J_0(k^*a)} + k \frac{J_1(ka)}{J_0(ka)} \right\} = -\text{Re} \left(ka \frac{J_1(ka)}{J_0(ka)} \right) \quad (\text{C.11})$$

Bibliography

- [1] J. A. Castellano. *Trends in the global CRT market*. SID Intl. Symp. Digest Tech. Papers, pp. 356–359, 1999.
- [2] N.G. Vink, F.C.A.J. Facobs, and M.P.P. Doomernik. *Method of manufacturing a saddle-shaped deflection coil for a picture display tube*. US Patent 5,013,964, May 7 1991.
- [3] L.E. Tannas Jr. *Flat-Panel Displays and CRTs*. Van Nostrand Reinhold, ISBN 0-442-28250-8, 1985.
- [4] B. Bowers. *Television, an International History of the Formative Years*. The Institution of Electrical Engineers, ISBN 0 85296 9147, 1998.
- [5] F. Kerkhof and W. Werner. *Televisie*. Meulenhoff & Co., 1951.
- [6] T.S. Soller, M.A. Starr, and G.E. Valley. *Cathode Ray Tube Displays*. McGraw-Hill Book Company, 1948.
- [7] E.W. Herold. *History and developmment of the color picture tube*. SID Intl. Symp. Digest Tech. Papers, 15(4):141–149, 1974.
- [8] E.F. Ritz, Jr. *Progress in the theory of electron-beam deflection*. Scanning Electron Microscopy, pp. 97–108, 1984.
- [9] G. Shiers. *Ferdinand braun and the cathode ray tube*. Scientific American, 230(3):92–101, March 1974.
- [10] C.B. Jollite. *TELEVISION, a bibliography of technical papers by RCA authors 1929–1946*. RCA Review, VII(4):641–652, December 1946.
- [11] C.W. Francis. *Method for making windings*. US patent 1,396,033, Nov. 8, 1921.
- [12] M. Bowman-Manifold. *Cathode ray tube*. US patent 2,108,523, Feb. 15, 1938.
- [13] O.H. Schade. *Magnetic-deflection circuits for cathode-ray tubes*. RCA Review, IX:506–538, 1948.
- [14] O.H. Schade. *Characteristics of high-efficiency deflection and high-voltage supply systems for kinescopes*. RCA review, pp. 5–37, March 1950.
- [15] A.W. Friend. *Deflection and convergence in color kinescopes*. RCA Review, 12:612–64, 1951.

- [16] M.J. Obert. *Deflection and convergence of the 21-inch color kinescope*. RCA review, pp. 140–169, March 1955.
- [17] J. Haantjes and G.J. Lubben. *Errors of magnetic deflection, i*. Philips Res. Rep., 12:46–68, 1957.
- [18] J. Haantjes and G.J. Lubben. *Errors of magnetic deflection, ii*. Philips Res. Rep., 14:65–97, 1959.
- [19] J. Kaashoek. *A study of magnetic-deflection errors*. Thesis, Technical University Eindhoven, July 1968.
- [20] J. Kaashoek. *Deflection system design for 110° shadow-mask tubes*. Philips Electronic Applications Bulletin, 32(1):3–22, 1973.
- [21] P.G.J. Barten. *The 20AX system and picture tube*. IEEE Trans. Broadcast and TV receivers, BTR-20(1):286–292, February 1974.
- [22] P.G.J. Barten and J. Kaashoek. *Large-screen colour television with intrinsically convergent 110° deflection*. Philips Electronic Applications Bulletin, 33(2):75–87, 1974.
- [23] J. Kaashoek. *Deflection in the 20AX system*. IEEE Trans. Broadcast and TV receivers, BTR-20(1):293–298, Feb. 1974.
- [24] B.B. Dasgupta. *Theory of large angle deflection of electrons in the magnetic field inside a television tube*. RCA Review, 43(3):548–557, Sept. 1982.
- [25] B.B. Dasgupta. *An analytic method for calculating the magnetic field due to a deflection yoke*. RCA Review, 44(3):404–23, Sept. 1983.
- [26] M.C. van der Heijde. *Method of winding deflection coils for picture display tubes*. US patent 3,855,694, Dec. 24, 1974.
- [27] W.A.L. Heijnemans, J.A.M. Nieuwendijk, and N.G. Vink. *The deflection coils of the 30ax colour-picture system*. Philips Techn. Rev., Vol. 39, No. 6/7, pp. 154–171, 1980.
- [28] A.A.S. Sluyterman. *The design of deflection units for monochrome data-graphic displays*. Electronic Displays '82 and Information Display Systems, page 11, 1982.
- [29] R. Vonk. *Magnetic deflection in television picture tubes*. Philips Techn. Rev., 32(3/4):61–72, 1971.
- [30] G.A.J. van Engelsen, J.L.M. Hagen, W.A.L. Heijnemans. *An equipment for measuring the magnetic fields of television deflection coils*. Philips Techn. Rev., 39(10):277–282, 1980.
- [31] B.B. Dasgupta, J.R. Kurtrock, L.G. Doriott. *A non-destructive method of estimating the harmonic content of a yoke*. SID Intl. Symp. Digest Tech. Papers, pp. 56–59, 1986.

- [32] A. Osseyran. *Computer aided design of magnetic deflection systems*. Philips Journal of Research, 41(1):1–150, 1986.
- [33] H. Penninga. *Computer simulation of double-mussel deflection-coil winding*. Journal of the SID, 1(1):11–14, Jan. 1993.
- [34] M. Miyazawa, M. Koizumi, T. Mizuta, K. Oku, S. Shirai, and I. Yoshimi. *Development of an electron optics simulator to consider the 3-d magnetic deflection fields in CRTs*. Nuclear Instruments and Methods in Physics Research, A 363:341–346, 341–346 1995.
- [35] K. Nishimura, S. Nakata, and T. Nakagawa. *Optimization of the coil distribution of the deflection yoke for CRT*. IEEE Trans. Magn., 33(2):1848–1851, March 1997.
- [36] R.C. Alig, J.R. Fields. *Computer-aided design of electron guns and deflection yokes: A review*. Journal of the SID, (3):203–215, 1997.
- [37] T.G. Beelen, J. Penninga, R. Mulder, and P. Bingley. *DUCAD-new: A CAD-tool for designing and simulating deflection units*. Proc. IDW, pp. 425–428, 1997.
- [38] Y. Yamada, S. Makino, N. Aibara, M. Narita, and M. Kitamura. *Numerical analysis of deflection yoke*. Proc. International Display Workshops (IDW), pp. 429–432, 1997.
- [39] R.M.J. Voncken. *Simulation of Deflection Coil Winding: Theory and Verification of SWING*. Thesis University of Technology Delft, ISBN 90-386-0497-1, 1996.
- [40] B.B. Dasgupta. *Designing self-converging crt deflection yokes*. Information Display, 8(1):15–19, Jan. 1992.
- [41] B.B. Dasgupta. *Recent advances in deflection yoke design*. SID Intl. Symp. Digest Tech. Papers, pp. 248–253, 1999.
- [42] A. Boekhorst and J. Stolk. *Television Deflection Systems*. Philips Technical Library, 1962.
- [43] D. Sharples. *Designing CRT deflection*. Electronics World, pp. 472–476, June 1996.
- [44] D.M. Taub. *Analysis of line-scan output/e.h.t. generator circuit for c.r.t. displays*. Proc. IEE, 127, Pt. G(3):129–144, June 1980.
- [45] B.B. Dasgupta. *Calculation of inductance of the horizontal coil of a magnetic-deflection yoke*. IEEE Trans. Consumer Electronics, CE-28(3):455–462, Aug. 1982.
- [46] H. Miyazawa et al. *Development of inductance analysis technique for deflection yoke*. Proc. IDW, pp. 433–436, 1997.
- [47] F.H. Fleuren. *Private communication*. 1989.

- [48] A. van Dalfsen. *Private communication*. 1989.
- [49] D.W. Harberts. *The heat dissipation in Litz wires of CRT deflection coils*. J. of the SID, 5(4):323–326, 1997.
- [50] X. Zhang, H. Yin, and D.W. Harberts. *Hysteresis loss in the ferrite core of a deflection yoke*. submitted to SID Intl. Symp. Digest Tech. Papers, XXXII, 2001.
- [51] F. Tol. *Private communication*. Philips Taiwan, 2000.
- [52] J.F. Bulharowski. *Power consumption in a transformerless TV vertical output circuit*. IEEE Trans. Broadcast and TV receivers, BTR-19(1):58–64, February 1973.
- [53] W.E. Babcock and W.F. Wedam. *Practical considerations in the design of horizontal deflection systems for high-definition television displays*. IEEE Trans. Consumer Electronics, CE-29(3):334–349, August 1983.
- [54] L. Ostergaard and U.B. Jensen. *Evaluation and modelling of the power losses in the horizontal deflection circuit in televisions - with focus on the semiconductors*. Proc. European Conf. on Power Electronics and Applications (EPE), 1999.
- [55] D.P. Brilliantov and G.S. Tsykin. *Design of magnetic deflecting systems of maximum effectiveness*. Radio Engineering, 25(4):105–109, 1970.
- [56] R. Morooka, Y. Inoue, and K. Shiomi. *Analysis on reduction of the temperature rise of deflection yoke (DY)*. IEICE Trans. Electron., E78-C(7):878–884, July 1995.
- [57] J.W.J.M. Van der Heijden. *A low power 15" CMT design*. Proc. Int. Display Research Conf. EuroDisplay, pp. 145–148, October 1996.
- [58] E.E. Kriezis, T.D. Tsiboukis, S.M. Panas and J.A. Tegopoulos. *Eddy currents: Theory and applications*. Proc. IEEE, 80(10):1559–1589, 1992.
- [59] J.A. Tegopoulos and E.E. Kriezis. *Eddy current distribution in cylindrical shells of infinite length due to axial currents*. ??, pp. 1278–1294, 1970.
- [60] B.B. Dasgupta. *Anomalous skin effect in a cylindrical conductor*. Physica Status Solidi A, 91(1):235–241, Sept. 1985.
- [61] J.L. Maksiejewski. *Losses in conductors due to current surges taking the skin effect into account*. Proc. IEE, part A, 137(2):80–84, March 1990.
- [62] G.S. Smith. *Proximity effect in systems of parallel conductors*. J. Appl. Phys., 43(5):2196–2203, 1972.
- [63] K. Ferkan, M. Poloujadoff and E. Dorison. *Proximity effect and eddy current losses in insulated cables*. IEEE Trans. Power Delivery, 11(3):1171–1178, 1996.
- [64] A.J. Sinclair and J.A. Ferreira. *Optimum shape for AC foil conductors*. Proc. IEEE Power Electronics Specialist Conf. (PESC), pp. 1064–1069, 1995.

- [65] N.J. Siakavellas. *Two simple models for analytical calculation of eddy currents in thin conducting plates*. IEEE Trans. Magn., 33(3):2245–2257, 1997.
- [66] W.G. Hurley, M.C. Duffy, S. O'Reilly and S.C. Ó'Mathúina. *Impedance formulas for planar magnetic structures with spiral windings*. Proc. IEEE Power Electronics Specialist Conf. (PESC), 1:627–633, 1997.
- [67] P.F. Okyere and L. Heinemann. *An advanced SPICE-compatible model for high frequency multiwinding transformers*. Proc. IEEE Power Electronics Specialist Conf. (PESC), 1:592–597, 1999.
- [68] L. Heinemann and J. Helfrich. *Modeling and accurate determination of winding losses of high frequency transformers in various power electronics applications*. Proc. IEEE Applied Power Electronics Conf., 2:647–653, 2000.
- [69] J. Jongsma. *Minimum-loss transformer windings for ultrasonic frequencies part 1: Background and theory*. Philips Electronic Applications Bulletin, 35(3):146–163, 1978.
- [70] J. Jongsma. *Minimum-loss transformer windings for ultrasonic frequencies part 2: Design methods and aids*. Philips Electronic Applications Bulletin, 35(4):211–226, 1978.
- [71] P.S. Venkatraman. *Winding eddy current losses in switch mode power transformers due to rectangular wave currents*. Proc. of Powercon 11, Eleventh Annual Int. Power Electronics Conf., San Diego CA, pp. A.1.1–A1.9, March 1983.
- [72] B. Carsten. *High frequency conductor losses in switchmode magnetics*. Proc. of High Frequency Power Conversion, pp. 155–176, May 1986.
- [73] J.P. Vandelac and P. Ziogas. *A novel approach for minimizing high frequency transformer copper losses*. Proc. IEEE Power Electronics Specialist Conf. (PESC), pp. 355–367, 1987.
- [74] J.P. Vandelac and P.D. Ziogas. *A novel approach for minimizing high-frequency transformer copper losses*. IEEE Trans. Power Electron., 3(3):266–277, 1988.
- [75] K. Sakakibara and N. Murakami. *Analysis of high-frequency resistance in transformers*. Proc. IEEE Power Electronics Specialist Conf. (PESC), pp. 618–624, 1989.
- [76] J. Spreen. *Electrical terminal representation of conductor loss in transformers*. IEEE Trans. Power Electron., 5(4):424–429, October 1990.
- [77] R. Severns. *Additional losses in high frequency magnetics due to non ideal field distributions*. Proc. IEEE Applied Power Electronics Conf., pp. 333–338, 1992.
- [78] P.D. Evans, W.M. Chew and W.J. Heffernan. *Tensor analysis of eddy current losses in multiple winding transformers*. Proc. IEEE Power Electronics Specialist Conf. (PESC), pp. 1105–1110, 1993.

- [79] K.W.E. Cheng and P.D. Evans. *Calculation of winding losses in high frequency toroidal inductors using multistrand conductors*. Proc. IEE Electr. Power Appl., 142(5):313–322, 1995.
- [80] P.L. Dowel. *Effects of eddy currents in transformer windings*. Proc. IEE, 113(8):1387–1394, 1966.
- [81] S. Butterworth. *On the alternating current resistance of solenoidal coils*. Proc. Roy. Soc. A, A107:693–715, 1925.
- [82] S. Butterworth. *Effective resistance of inductance coils at radio frequency*. Wireless Eng., III:203–210, 309–316, 417–424, 483–492, April–August 1926.
- [83] E. Bennett and S.C. Larson. *Effective resistance to alternating currents in multilayer windings*. Trans. Amer. Inst. Elect. Eng., 59:1010–1017, 1940.
- [84] M. Gevers. *Measuring the dielectric constant and the loss angle of solids at 3000 mc/s*. Philips Technical Review, 13(3):61–70, 1951.
- [85] W.G. Hurley, W.H. Wölflé and J.G. Breslin. *Optimized transformer design: Inclusive of high-frequency effects*. IEEE Trans. Power Electron., 13(4):651–659, 1998.
- [86] M.P. Perry. *Multiple layer series connected winding design for minimum losses*. IEEE Trans. Power App. Syst., PAS-98(1):116–123, 1979.
- [87] G.L. Tawney. *Description of losses in switching power inductors*. Power Conversion International, pp. 22–26, July/August 1983.
- [88] M. Bartoli, N. Noferi, A. Reatti and M.K. Kazimierczuk. *Modelling winding losses in high-frequency power inductors*. Journal of Circuits, Systems, and Computers, 5(4):607–626, 1995.
- [89] I.T. Wallace et al. *Inductor design for high power applications with broad spectrum excitation*. Proc. IEEE Power Electronics Specialist Conf. (PESC), pp. 1057–1063, 1995.
- [90] U. Reggiani, G. Grandi, G. Sancineto, M.K. Kazimierczuk, and A. Massarini. *High-frequency behavior of laminated iron-core inductors for filtering applications*. Proc. IEEE Applied Power Electronics Conf., 2:654–660, 2000.
- [91] C.E. Hawkes, T.G. Wilson, and R.C. Wong. *Magnetic-field-intensity and current-density distributions in transformer windings*. Proc. IEEE Power Electronics Specialist Conf. (PESC), 2:1021–1030, 1989.
- [92] G.R. Skutt and P.S. Venkatraman. *Analysis and measurement of high-frequency effects in high-current transformers*. Proc. IEEE Applied Power Electronics Conf., pp. 354–364, 1990.
- [93] P.D. Evans and W.M. Chew. *Reduction of proximity losses in coupled inductors*. IEE Proc.-B, 138(2):51–58, 1991.

- [94] E. Laveuve, J.P. Keradec, and G. Meunier. *Influence of induced currents in conductors on leakage and losses in a transformer*. Electric Machines and Power Systems, 19:55–68, 1991.
- [95] A.W. Lotfi and F.C. Lee. *Two dimensional field solutions for high frequency transformer windings*. Proc. IEEE Power Electronics Specialist Conf. (PESC), pp. 1098–1104, 1993.
- [96] A. Reatti. *Winding loss optimization in a flyback converter transformer*. Proc. Power Conversion, pp. 371–382, June 1993.
- [97] K.W. Klontz. *Skin and proximity effects in multi-layer transformer windings of finite thickness*. Proc. IEEE Industry Application Society Conf. (IAS), 1:851–858, 1995.
- [98] L. Heinemann. *Simulation and design of high frequency magnetics including the skin effect, nonlinear core properties and thermal effects*. Proc. IEEE Applied Power Electronics Conf., 1:461–466, 1996.
- [99] J.G. Breslin and W.G. Hurley. *Derivation of optimum winding thickness for duty cycle modulated current waveshapes*. Proc. IEEE Power Electronics Specialist Conf. (PESC), 1:655–661, 1997.
- [100] J.M. Lopera, M.J. Prieto, F. NuÑo, A.M. Perniá and J. Sebastián. *A quick way to determine the optimum layer size and their disposition in magnetic structures*. Proc. IEEE Power Electronics Specialist Conf. (PESC), 2:1150–1156, 1997.
- [101] E. Fraga, C. Prados, and D.-X. Chen. *Practical model and calculation of AC resistance of long solenoids*. IEEE Trans. Magn., 34(1):205–212, January 1998.
- [102] R. Prieto, J.A. Cobos, O. García, P. Alou, and J. Uceda. *High frequency resistance in flyback type transformers*. Proc. IEEE Applied Power Electronics Conf., 2:714–719, 2000.
- [103] N.H. Kutkut, D.M. Kivan. *Optimal air-gap design in high-frequency foil windings*. IEEE Trans. Power Electron., 13(5):942–949, 1998.
- [104] N.H. Kutkut. *A simple technique to evaluate winding losses including two-dimensional edge effects*. IEEE Trans. Power Electron., 13(5):950–958, 1998.
- [105] N.H. Kutkut. *Minimizing winding losses in foil windings using field shaping techniques*. Proc. IEEE Power Electronics Specialist Conf. (PESC), 1:634–640, 1997.
- [106] A.F. Goldberg, J.G. Kassakian, and M. F. Schlecht. *Finite element analysis of copper loss in 1-10 MHz transformers*. Proc. IEEE Power Electronics Specialist Conf. (PESC), 2:1105–1111, 1988.
- [107] A.W. Lotfi and F.C. Lee. *Proximity losses in short coils of circular cylindrical windings*. Proc. IEEE Power Electronics Specialist Conf. (PESC), pp. 1253–1260, 1992.

- [108] N. Dai and F.C. Lee. *High-frequency eddy-current effects in low-profile transformer windings*. Proc. IEEE Power Electronics Specialist Conf. (PESC), 1:641–647, 1997.
- [109] K.R. Davey and D. Zheng. *Prediction and use of impedance matrices for eddy-current problems*. IEEE Trans. Magn., 33(4):2478–2485, 1997.
- [110] F.X. Hart. *Spreadsheet solutions for Ampere’s law problems with irregularly shaped conductors*. Am. J. Phys., 65(6):565–567, 1997.
- [111] F. Robert, P. Mathys, J. Schauwers. *Ohmic losses calculation in SMPS transformers: Numerical study of dowell’s approach accuracy*. IEEE Trans. Magn., 34(4):1255–1257, 1998.
- [112] J. Hu and C.R. Sullivan. *Analytical method for generalization of numerically optimized inductor winding shapes*. Proc. IEEE Power Electronics Specialist Conf. (PESC), 1:568–573, 1999.
- [113] H. Hogers. *Internal philips report*. TVR-45-94-HH/D512, January 1994.
- [114] T.G. Imre, W.A. Cronje, J.D. van Wyk, and J.A. Ferreira. *Experimental validation of loss calculations for a planar inductor*. Proc. IEEE Power Electronics Specialist Conf. (PESC), 1:586–591, 1999.
- [115] H.B.G. Casimir and J. Ubbink. *Het skineffect*. Philips Technisch Tijdschrift, 28(6):173–185, 1967.
- [116] H.B.G. Casimir and J. Ubbink. *Het skineffect (II) bij hoge frequenties*. Philips Technisch Tijdschrift, 28(7):206–221, 1967.
- [117] H.B.G. Casimir and J. Ubbink. *Het skin effect (III) in supergeleiders*. Philips Technisch Tijdschrift, 28(12):376–392, 1967.
- [118] R.M. Seeley. *Transformer winding design presented in programmable form*. IEEE Trans. Parts, Hybrids, and Packaging, 13(1):98–104, March 1977.
- [119] P.F. Desesquelles et G. Terracol. *Un modèle analytique monodimensionnel complet pour bobinages solénoïdaux en régime alternatif*. J. Phys. III France, 2(3):415–437, March 1992.
- [120] K. Küpfmüller. *Einführung in die Theoretische Elektrotechnik*. Springer-Verlag, 1973.
- [121] H. Kaden. *Wirbelströme und Schirmung in der Nachrichtentechnik, Zweite Auflage*. Springer-Verlag, 1959.
- [122] J.A. Ferreira. *Appropriate modelling of conductive losses in the design of magnetic components*. Proc. IEEE Power Electronics Specialist Conf. (PESC), pp. 780–785, 1990.
- [123] J.A. Ferreira. *Improved analytical modeling of conductive losses in magnetic components*. IEEE Trans. Power Electron., 9(1):127–131, 1994.

- [124] T.A.O. Gross. *Multistrand litz wire adds 'skin' to cut ac losses in switching power supplies*. Electronic Design, pp. 86–89, February 1979.
- [125] Y. Akiba, T. Futami, and T. Suda. *Litz wire*. US Patent 4,546,210, Oct. 8 1985.
- [126] H. Osinga. *Composite wire, coil and deflection unit for HF applications*. US Patent 4,692,731, Sep. 8 1987.
- [127] Y. Nakao, S. Jumonji, T. Sawamoto, and Y. Anraku. *Litz wire development*. Wire & Cable Technology International, (6):92–93, November 1997.
- [128] J. Schutz, J. Roudet, and A. Schellmanns. *Modeling litz wire windings*. Proc. IEEE Industry Application Society Conf. (IAS), 2:1190–1195, 1997.
- [129] C.R. Sullivan. *Optimal choice for number of strands in a litz-wire transformer winding*. Proc. IEEE Power Electronics Specialist Conf. (PESC), 1:28–35, 1997.
- [130] C.R. Sullivan. *Cost-constrained selection of strand diameter and number in a litz-wire transformer winding*. Proc. IEEE Industry Applications Society Conf. (IAS), 2:900–906, 1998.
- [131] M. Bartoli, N. Noferi, A. Reatti, and M.K. Kazimierczuk. *Modeling litz-wire winding losses in high-frequency power inductors*. ??, (4):1690–1696, 1996.
- [132] S. Ramo, J.R. Whinnery and T. van Duzer. *Fields and Waves in Communication Electronics*. John Wiley & Sons, ISBN 0-471-30578-2, 1994.
- [133] A.W. Lotfi, P.M. Gradzki and F.C. Lee. *Proximity effects in coils for high frequency power applications*. IEEE Trans. Magn., 28(5):2169–2171, September 1992.
- [134] E.J. Murphy and S.O. Morgan. *The dielectric properties of insulating materials*. Bell Syst. Tech. J., 16:493–512, 1937.
- [135] E.J. Murphy and S.O. Morgan. *The dielectric properties of insulating materials, part II*. Bell Syst. Tech. J., 17:640–643, October 1938.
- [136] E.J. Murphy and S.O. Morgan. *The dielectric properties of insulating materials, part III*. Bell Syst. Tech. J., 18:502–537, 1939.
- [137] C.P. Smyth. *Dielectric Behavior and Structure*. McGraw-Hill Book Company, 1955.
- [138] S. Flügge. *Encyclopedia of Physics, Vol. XVII Dielectrics*. Springer-Verlag, 1956.
- [139] R.M. Fano, L.J. Chu, and R.B. Adler. *Electromagnetic Fields, Energy, and Forces*. John Wiley & Sons, Inc., 1967.
- [140] M. Stel and E.C. Witsenburg. *Heating by means of high-frequency fields, II. capacitive heating*. Philips Technical Review, 11(8):232–240, February 1950.
- [141] Philips Components. *Data Handbook on Soft Ferrites (MA01)*. 1993.

- [142] E.C. Snelling. *Soft Ferrites: Properties and Applications*. ISBN 0-408-02760-6, Butterworth & Co. Ltd., 1988.
- [143] C.P. Steinmetz. *On the law of hysteresis*. Proc. IEEE, 72(2):196–221, February 1984. Reprinted from the American Institute of Electrical Engineers Trans., vol. 9, pp.3–64, 1892.
- [144] A. deGraft-Johnson. *Private communication*. Philips Southport, 1999.
- [145] D. Zhang and C.F. Foo. *Theoretical analysis of the electrical and magnetic field distributions in a toroidal core with circular cross section*. IEEE Trans. Magn., 35(3):1924–1931, May 1999.
- [146] D.K. Strong. *A clamshell deflection yoke (crts)*. SID Intl. Symp. Digest Tech. Papers, 26(1):41–5, 1985.
- [147] J.A. Lemus-Armas. *Electric power measurements for non-sinoidal input signals using non-simultaneous sampling*. Trans. of IEEE Instrumentation and Measurement Technology Conference (IMTC), pp. 573–576, 1992.
- [148] W.G. Hurley, E. Gath, and J.G. Breslin. *Optimizing the AC resistance of multilayer transformer windings with arbitrary current waveforms*. Proc. IEEE Power Electronics Specialist Conf. (PESC), 1:580–585, 1999.
- [149] D.W. Harberts. *Measuring ringing in CRT deflection yokes*. Proc. SID, 15:898–901, May 1999.
- [150] A. Murata, M. Sudo, T. Uba, and Y. Amano. *Deflection yoke for a trinitron 20x20 in. color CRT*. SID Intl. Symp. Digest Tech. Papers, pp. 49–52, 1989.
- [151] M. Yoshii, Y. Nakamura, and H. Inouye. *Deflection yoke for super-fine-pitch 20-in (19v) in-line color CRT (trinitron)*. SID Intl. Symp. Digest Tech. Papers, 31:205–208, 1990.
- [152] I. Yonetani, E. Tagami, M. Honda and K. Iwasaki. *17-inch new SS deflection yoke system*. National Technical Report, 38(4):35–42, Aug. 1992.
- [153] T. Murakami. *Ringing in horizontal-deflection and high-voltage television circuits*. RCA Review, March:17–44, 1960.
- [154] A. Zegers. *Suppression of ringing in colour monitor deflection circuits*. Technical Publication Philips Components, 9398 083 09011, Sept. 1994.
- [155] A.M. Urling, A. van Niemela, G.R. Skutt, and T.G. Wilson. *Characterizing high-frequency effects in transformer windings - a guide to several significant articles*. Proc. IEEE Applied Power Electronics Conf. (APEC), pp. 373–385, 1989.
- [156] L. Heinemann, R. Ullrich and H. Grotstollen. *Transfer function and calculation of parameters for high frequency multiwinding transformers*. Proc. IEEE Power Electronics Specialist Conf. (PESC), pp. 659–666, 1991.

- [157] A. van Niemela, H.A. Owen and T.G. Wilson. *Frequency-independent-element cross-coupled-secondaries model for multiwinding transformers*. Proc. IEEE Power Electronics Specialist Conf. (PESC), pp. 1261–1268, 1992.
- [158] J.M. Lopera et Al. *A complete transformer electric model, including frequency and geometry effects*. Proc. IEEE Power Electronics Specialist Conf. (PESC), pp. 1247–1252, 1992.
- [159] H.A. Owen, A. van Niemela and T.G. Wilson. *Enhanced cross-coupled-secondaries model for multiwinding transformers*. Proc. IEEE Power Electronics Specialist Conf. (PESC), pp. 1269–1276, 1992.
- [160] V.S. Sinev. *A generalized description of multi-winding transformer circuits*. Electrical Technology, (3):37–46, 1992.
- [161] L. Heinemann, R. Ullrich, B. Becker and H. Grotstollen. *State space modeling of high frequency multiwinding transformers*. Proc. IEEE Power Electronics Specialist Conf. (PESC), pp. 1091–1097, 1993.
- [162] M. Bartoli, A. Reatii, and M.K. Kaziemierczuk. *High-frequency models of ferrite core inductors*. Proc. IEEE Power Electronics Specialist Conf. (PESC), pp. 1670–1675, 1994.
- [163] F. Blache, J.P. Keradec, and B. Cogitore. *Stray capacitances of two winding transformers: Equivalent circuit, measurements, calculations and lowering*. Proc. IEEE Industrial Application Society (Denver), pp. 1211–1217, 1994.
- [164] L. Heinemann, R. Schulze, P. Wallmeier, and H. Grotstollen. *Modeling of high frequency inductors*. Proc. IEEE Power Electronics Specialist Conf. (PESC), pp. 876–883, 1994.
- [165] P. Colpo, R. Ernst, and J.P. Keradec. *Electrical modeling of HF coupled inductors supplying a double frequency inductive plasma reactor*. Proc. IEEE Applied Power Electronics Conf. (APEC), pp. 937–943, 1997.
- [166] E. Dallago, G. Sassone and G. Venchi. *High-frequency power transformer model for circuit simulation*. IEEE Trans. Power Electron., 12(4):664–670, 1997.
- [167] L. Østergaard, M. Rudnicki, and B. Bak-Jensen. *A simple two-winding model of the diode split transformer*. Proc. Int. Symp. Micromachines & Servodrives, 1998.
- [168] B. Bak-Jensen and L. Østergaard. *Estimation of the model parameters in equivalent circuit models of potential transformers*. 1999.
- [169] J. Wang et Al. *Derivation, calculation and measurement of parameter for a multi-winding transformer electrical model*. Proc. IEEE Applied Power Electronics Conf. (APEC), pp. 220–226, 1999.
- [170] P.J. Bax. *Modelling of Inductive Properties of the Line-Output Transformer; From Field-Line Pictures to Equivalent Circuits*. Ph.D. thesis Eindhoven University, ISBN 90-386-0196-4, June 1995.

- [171] L. Østergaard. *Modelling and Simulation of the Diode Split Transformer*. Ph.D. Thesis Aalborg University, ISBN 87-89179-27-7, October 1999.
- [172] C.E. Longhurst. *Stray capacitances of coils wound on mullard vinkor pot-core assemblies*. Mullard Technical Communications, 46:218–226, January 1961.
- [173] T. H. Sloane, T.G. Wilson, and H.A. Owen. *Tailoring inductor and capacitor circuit models to frequency-domain measurements*. Proc. IEEE Power Electronics Specialist Conf. (PESC), pp. 645–654, 1986.
- [174] A. van Niemela et Al. *Calculating the short-circuit impedances of a multiwinding transformer from its geometry*. Proc. IEEE Power Electronics Specialist Conf. (PESC), pp. 607–617, 1989.
- [175] A. van Niemela, H.A. Owen and T.G. Wilson. *Cross-coupled-secondaries model for multiwinding transformers with parameter values calculated from short-circuit impedances*. Proc. IEEE Power Electronics Specialist Conf. (PESC), pp. 822–830, 1990.
- [176] A. Keyhani, H. Stai, and A. Abur. *Maximum likelihood estimation of high frequency machine and transformer winding parameters*. IEEE Trans. Power Electron., 5(1):212–219, January 1990.
- [177] W.M.G. Hurley, D.J. Wilcox, and P.S. McNamara. *Calculation of short circuit impedance and leakage impedance in transformer windings*. Proc. Power Electronics Specialist Conf. (PESC), pp. 651–658, 1991.
- [178] A. Keyhani, S.W. Chua, and S.A. Sebo. *Maximum likelihood estimation of transformer high frequency parameters from test data*. IEEE Trans. Power Delivery, 6(2):858–865, April 1991.
- [179] J. Bak-Jensen et Al. *Parametric identification in potential transformer modelling*. IEEE Trans. Power Delivery, 7(1):70–76, January 1992.
- [180] B. Cogitore, J.P. Kéradec, and J. Barbaroux. *The two-winding transformer: An experimental method to obtain a wide frequency range equivalent circuit*. IEEE Trans. Instrum. and Meas., pp. 364–369, April 1994.
- [181] L. Heinemann. *A novel SPICE compatible high frequency multiwinding transformer model*. Proc. IEEE Industry Application Society Conf. (IAS), 2:929–936, 1998.
- [182] R. Asensi, J.A. Cobos, O. García, R. Prieto, and J. Uceda. *A full procedure to model high frequency transformer windings*. Proc. Power Electronics Specialist conf. (PESC), pp. 856–863, 1994.
- [183] R. Prieto, R. Asensi, J.A. Cobos, O. García and J. Uceda. *Model of the capacitive effects in magnetic components*. Proc. IEEE Power Electronics Specialist Conf. (PESC), pp. 678–683, 1995.
- [184] A. Nicolet, C. Brasseur, and E. Sire. *Computation of parasitic capacitance in conducting coils*. Proc. IEEE CEFC, page 323, 1998.

- [185] R. Prieto, V. Bataller, J.A. Cobos, and J. Uceda. *Influence of the winding strategy in toroidal transformers*. Proc. Annual Conference on the IEEE Industrial Electronics Society (IECON), 1:359–364, 1998.
- [186] R. Prieto, V. Bataller, J.A. Cobos, and J. Uceda. *Influence of the winding strategy in toroidal transformers*. Proc. Conf. IEEE Industrial Electronics (IECON), 1:359–364, 1998.
- [187] M. Feliziani and F. Maradei. *Modeling of electromagnetic fields and electrical circuits with lumped and distributed elements by the WETD method*. IEEE Trans. Magn., pp. 1666–1669, May 1999.
- [188] L.F. Casey, A.F. Goldberg and M.F. Schlecht. *Issues regarding the capacitance of 1-10 MHz transformers*. Proc. IEEE Applied Power Electronics Conf. (APEC), pp. 352–359, 1988.
- [189] J. Schutz, R. Roudet, and A. Schellmanns. *Transformer modeling in EMC applications*. Proc. IEEE Industry Application Society Conf. (IAS), 2:1005–1010, 1998.
- [190] M. van Helvoort, A. van Deursen, and P.C.T. van der Laan. *The transfer impedance of cables with a nearby return conductor and a noncentral inner conductor*. IEEE Trans. on Electromagnetic Compatibility, 37(2):301–306, May 1995.
- [191] A.B.H. Derks, N.A.J.C. Bouwman, E.E.E. Hofer, and H. Nielinger. *SPICE*. Nijgh & Van Ditmar, The Hague, ISBN 90 236 0538 1, 1985.
- [192] F. Blache, J.P. Keradec, and J.L. Schanen. *Improving electronic simulation accuracy by using new equivalent circuits for wound components*. Proc. European Conf. on Power Electronics and Application (EPE), 2:2.813–2.818, 1995.
- [193] S.A. Schelkunoff. *Representation of impedance functions in terms of resonant frequencies*. Proc. Inst. Radio Eng., 32:83–90, February 1944.
- [194] R.M. Foster. *A reactance theorem*. Bell Syst. Tech. J., 3:259–267, 1924.
- [195] M. Abramowitz and I.A. Stegun. *Handbook of Mathematical Functions*. ISBN 486-61272-4, Dover publications, Inc., New York, 1970.
- [196] H. Poritsky, P.A. Abetti, and R.P. Jerrard. *Field theory of wave propagation*. AIEE Trans. Power App. Syst., 72III:930–938, October 1953.
- [197] A.E.S. Mostafa and M.K. Gohar. *Determination of voltage, current, and magnetic field distributions together with the self-capacitance, inductance and HF resistance of single-layer coils*. Proc. Inst. Radio Eng., 41(4):537–547, 1953.
- [198] D.A. Watkins and E.A. Ash. *The helix as a backward-wave circuit structure*. J. Appl. Phys., 25(6):782–790, June 1954.
- [199] S. Sensiper. *Electromagnetic wave propagation on helical structures*. Proc. Inst. Radio Eng., pp. 149–161, February 1955.

-
- [200] R.P. Feynman, R.B. Leighton, and M. Sands. *The Feynman Lectures on Physics, Volume II*. Addison-Wesley Publishing Company, ISBN 0-201-02117-X, 1977.
- [201] N. Contaxes and A.J. Hatch. *High-frequency fields in solenoidal coils*. J. Appl. Phys., 40(9):3548–3550, August 1969.
- [202] F.S. Chute and F.E. Vermeulen. *A visual demonstration of the electric field of a coil carrying a time-varying current*. IEEE Trans. Education, 24(4):278–283, November 1981.
- [203] T. Takano, S. Hayano, and Y. Saito. *Coil impedance computation having arbitrary geometrical shape*. Proc. IEEE Power Electronics Specialist Conf. (PESC), 2:1991–1996, 1998.
- [204] A.E. Ruehli. *Inductance calculations in a complex integrated circuit environment*. IBM J. Res. Developm., 11:470–481, Sept. 1972.
- [205] H. Wheeler. *Simple inductance formulas for radio coils*. Proc. Inst. Radio Eng., 16(10):1398–1400, October 1928.
- [206] P. Drude. *Zur construction von teslatransformatoren. schwingungsdauer und selbstinduction von drahtspulen*. Ann. Phys., 9:293–339, 590–610, 1902.
- [207] W. Rietz. *über die kapazität von spulen*. Annalen der Physik, 41(8):543–569, 1913.
- [208] W. Lenz. *Berechnung der eigenschwingungen einlagiger spulen*. Ann. Phys., 43:749–809, 1914.
- [209] G. Breit. *The distributed capacity of inductance coils*. Physical Review, 18(2):133–139, 1921.
- [210] J.H. Morecroft. *Resistance and capacity of coils at radio frequencies*. Proc. Inst. Radio Eng., pp. 261–289, 1922.
- [211] A.J. Palermo. *Distributed capacity of single-layer coils*. Proc. Inst. Radio Eng., 22(7):897–905, July 1934.
- [212] G. Grandi, M.K. Kaziemierczuk, A. Massarini, and U. Reggiani. *Stray capacitances of single-layer air-core inductors for high-frequency applications*. Proc. IEEE Industry Applications Society (IAS), pp. 1384–1388, 1996.
- [213] R.G. Medhurst. *H.f. resistance and self-capacitance of single-layer solenoids (II)*. Wireless Engineer, 24:80–92, March 1947.
- [214] R.G. Medhurst. *H.f. resistance and self-capacitance of single-layer solenoids*. Wireless Eng., 24:35–43, February 1947.
- [215] H. Zuhrt. *Einfache näherungsformeln für die eigenkapazität mehrlagiger spulen*. Elektrotechnische Zeitschrift, 55(27):662–665, July 1934.
- [216] W.T. Duerdoth. *Equivalent capacitances of transformer windings*. Wireless Eng., 23:161–167, 1946.

- [217] D. Maurice and R.H. Minns. *Very-wide band radio-frequency transformers*. Wireless Eng., pp. 168–177, 209–216, June, July 1947.
- [218] N.H. Crowhurst. *Winding capacitance*. Electronic Engineering, pp. 417–421, November 1949.
- [219] J.A. Collins. *An accurate method for modeling transformer winding capacitances*. Proc. Industrial Electronics Conference, pp. 1094–1099, 1990.
- [220] R. Prieto, J.A. Cobos, O. García, and J. Uceda. *Influence of the winding strategy on the parasitics of magnetic components*. Proc. European Conf. on Power Electronics and Application (EPE), pp. 2.038–2.043, 1997.
- [221] A. Massarini and M.K. Kazimierczuk. *Self-capacitance of inductors*. IEEE Trans. Power Electron., 12(4):671–676, July 1997.
- [222] K.A. MacFayden. *Small Transformers and Inductors*. Chapman & Hall, 1953.
- [223] J. Koch. *Berechnung der kapazität von spulen, insbesondere in schalenkernen*. Valvo Berichte, 14(3):99–119, 1968.
- [224] A. Massarini, M.K. Kazimierczuk, and G. Grandi. *Lumped parameter models for single- and multiple-layer inductors*. Proc. IEEE Power Electronics Specialist Conf. (PESC), Bavena, pp. 295–301, June 1996.
- [225] M. Albach and J. Lauter. *The winding capacitance of solid and litz wires*. Proc. European Conf. on Power Electronics and Application (EPE), 2:2.001–2.005, 1997.
- [226] D.W. Harberts. *Suppression of common-mode ringing in CRT deflection yokes*. Proc. SID, 16:492–495, 2000.
- [227] D.W. Harberts, H.D. van den Berg, and R.T.M. Doedee. *Cathode ray tube comprising a deflection unit (ringing free wire)*. International Patent Application WO 99/66526, 17 June 1998.
- [228] R. Nagel, L. Danel, D.W. Harberts, J. Fournier. *Conducting layered enamelled wire to avoid ringing effect in deflection yokes of colour monitor and TV tubes*. Proc. of Electrical Insulation Conference & Electrical Manufacturing and Coil Winding Conference (EIC/EMCW), Cincinatti, November 2000.
- [229] Telefunken. *Improvements in or relating to electromagnetic deflection apparatus for television and other cathode ray tubes*. UK Patent Specification 472,834, March 30 1936.
- [230] R. Andrieu and R. Schienemann. *Magnetic coil for deviating cathode-ray tubes*. US Patent 3,337,053, Dec. 31 1940.
- [231] C.E. Tosch and R.F. Wood. *Kathodenstrahlblenkspulen*. Patentanmeldung Deutschland G12,432, Aug. 11 1953.
- [232] N. Okuyama, S. Sakurai, M. Nakahara, M. Ohsawa, and I. Niitsu. *Deflection system for a cathode ray tube*. European Patent Application 0,481,216, Sept. 11 1991.

- [233] A.H. van Tiel. *Cathode ray tube comprising a deflection system*. European Patent Application 0,547,678, Dec. 11 1992.
- [234] W. Schröder. *Ablenkspulenanordnung zur magnetischen ablenkung des elektronenstrahls in einer kathodenstrahlröhre*. Patentanmeldung Deutschland 22.7.54, March 13 1953.
- [235] J.K. Kratz and W.H. Barkow. *Deflection yokes*. US Patent 2,799,798, July 16 1957.
- [236] A. Hishimoto and S. Arai. *Saddle deflector coils for cathode ray tube*. Offenlegungsschrift DE 4026416, March 7 1991.
- [237] M. Ogasa and Y. Ono. *CRT deflection yoke with ringing suppression*. European Patent Application 0,304,200, Aug. 4 1988.
- [238] H. Akira, and S. Arai. *Deflection yoke device*. US Patent 5,008,600, Apr. 16 1991.
- [239] J.P. Fourche. *Deflection yoke with ringing suppression means*. European Patent Applications 0,480,110, Oct. 10 1990.
- [240] K. Kaneko, and T. Takemoto. *Ringing free deflection yoke*. US Patent 5,568,020, Oct. 22 1996.
- [241] G.J. Beaumont. *Anti-ringing circuit for CRT deflection yoke*. US Patent 4,272,705, June 9 1981.
- [242] M. Onozawa, M. Osawa, H. Maekawa, and K. Kito. *Horizontal deflection output circuit*. US Patent 4,707,640, Nov. 17 1987.
- [243] J.C. Maxwell. *A Treatise on Electricity & Magnetism*. Clarendon Press, 3rd edition, 1891.
- [244] W.W. Wagner. *Erklärung der dielektrischen nachwirkungsvorgänge auf grund maxwellscher vorstellungen*. Archiv für Elektrotechnik, 2(9):371–387, 1914.
- [245] W.R. Sillars. *The properties of a dielectric containing semi-conducting particles of various shapes*. J. Inst. Elec. Engrs, 80:378–394, 1937.
- [246] J. Yacubowicz, M. Narkis and L. Benguigui. *Electrical and dielectric properties of segregated carbon black-polyethylene systems*. Polymer Engineering and Science, 30(8):459–468, April 1990.
- [247] L.J. Adriaanse et Al. *High-dilution carbon-Black/Polymer composites: Hierarchical percolating network derived from hz to THz ac conductivity*. Physical Review Letters, 78(9):1755–1758, March 1997.
- [248] F. Lux. *Models proposed to explain the electrical conductivity of mixtures made of conductive and insulating materials*. J. Material Science, 28:285–301, 1993.
- [249] J. Yacubowicz, M. Narkis, and L. Benguigui. *Electrical and dielectric properties of segregated carbon black-polyethylene systems*. Polymer Eng. & Sci, 28(24):1581–1585, December 1988.

-
- [250] J.J. Goedbloed. *Elektromagnetische Compatibiliteit*. Kluwer Technische Boeken BV, ISBN 90-201-2220-7, 1991.
 - [251] C.R. Paul. *Introduction to electromagnetic compatibility*. John Wiley & Sons, Inc., ISBN 0-471-54927-4, 1992.
 - [252] A.H. van Tiel. *Cathode-ray tube with deflection system*. European Patent Application 0,313,138, Oct. 10 1988.
 - [253] F.M.P. Berghmans and W.G. Peters. *Electrical conductor*. International Patent Application WO 00/33327, 8 June 2000.
 - [254] E. Kreyszig. *Advanced Engineering Mathematics*. John Wiley & Sons, ISBN 0-471-50728-8, 1972.
 - [255] G.N. Watson. *A Treatise on the Theory of Bessel Functions*. Cambridge University Press, ISBN 0-521-48391-3, 1995.

List of symbols

To limit the length of this list, symbols that are used only in adjacent pages, have been omitted. Following each symbol and definition there is, in general, a reference (in parentheses) to the equation or the figure in which the symbol is introduced or first used.

symbol	description	unit
$\alpha_1, \alpha_2, \alpha_c, \alpha_r$	undamped oscillating frequencies (Eqs. 4.23,4.31)	s^{-1}
$\alpha_{cm,i}$	proportionality factor for transfer function (Eq. 4.37)	-
β	proportionality factor (Eqs. 3.93,3.101)	Ωs^2
δ	skin depth (Eq. 3.18)	m
$\Delta\omega$	width of resonance peak (Fig. 4.4)	rad/s
Δf	width of impedance characteristic	s^{-1}
ϵ	permittivity; in vacuum $\epsilon_0 = 8.854 \cdot 10^{-12}$	F/m
ϵ_r	relative dielectric constant	-
θ	angle with magnetic field in the deflection area	rad
μ	magnetic permeability; in vacuum $\mu_0 = 4\pi \cdot 10^{-7}$	H/m
σ	specific copper conductivity (Eq. 3.13)	$\Omega^{-1}m^{-1}$
$\sigma_1, \sigma_2, \sigma_c, \sigma_r$	damping constants (Eqs. 4.23,4.31)	s^{-1}
τ, τ_r	decay time (Fig. 4.3)	s
ϕ_e	horizontal deflection angle (Eq. 2.3)	rad
$\Psi(\psi_e)$	auxiliary function (Eq. 3.8)	-
ψ_e	corner deflection angle (Fig. 3.2)	rad
ω	(angular) frequency	rad/s
ω_o	(undamped) resonance frequency ($=1/\sqrt{LC}$)	rad/s
$\omega_1, \omega_2, \omega_r, \omega_c$	damped oscillating frequencies (Eq. 4.23,4.31)	rad/s
ω_ℓ	(angular) line frequency	rad/s
ω_{fb}	flyback frequency (Eq. 2.16)	rad/s
ω_r	(angular) ringing frequency (Fig. 4.3)	rad/s
ω_{sc}	line-scan frequency (Eq. 2.17)	rad/s
\vec{A}	magnetic vector potential	T/m
A_{coil}	total cross section of the coil (Eq. 3.102)	m^2
A_{cross}	area of cross section of a coil (Eq. 3.61)	m^2
A_L	effective area of deflection coils	m^2
A_{turn}	area of a turn (Eq. 5.30)	m^2

symbol	description	unit
a	(copper) radius of winding wire	m
a_n	Fourier coefficients of line signal (Eq. 2.28)	-
a_p	equivalent radius of a litz wire (Fig. 5.2)	m
\vec{B}	magnetic flux density, with amplitude B_0	T
$B_{\text{extra}}(t)$	additional magnetic flux density (Eq. 4.6)	T
$B_c(\theta)$	magnetic flux density in the ferrite core (Eq. 3.68)	T
C, C_1, C_2	capacitance	F
C_0	capacitance (Eq. 4.30)	F
C_ℓ	capacitance between two layers (Eq. 5.14)	F
C_L	lumped capacitance of solenoid (Eq. 5.11)	F
C_{L2s}, C_{L2d}	lumped capacitance of 2-layer solenoid (Eqs. 5.20, 5.22)	F
C_{Lnd}	lumped capacitance of multi-layer solenoid (Eq. 5.23)	F
C_p	capacitance that is parallel to an inductance (Fig. 3.12)	F
C_r	replacement value of two parallel capacitances (Eq. 4.22)	F
C_s, C_f	capacitances in drive circuit (Fig. 2.7)	F
C_{sphere}	capacitance of a sphere (Eq. 5.12)	F
\vec{D}	the electric displacement density	C/m ²
D_g	distance from screen center to corner (Fig. 3.2)	m
d_c	thickness of ferrite core (Fig. 3.11)	m
\vec{E}	electric field	V/m
E_h	energy stored in the magnetic field (Eq. 3.1)	J
e	electron charge, $1.6022 \cdot 10^{-23}$	C
f	frequency	Hz
f_o	frequency of first peak in the impedance characteristic	Hz
f_{max}	frequency of frequency-response peak (Fig. 4.37)	Hz
$f_{\text{skin}}(x)$	skin loss factor (Eq. 3.34)	-
$g(x)$	proximity loss function (Eq. 3.43)	-
\vec{H}	magnetic field intensity with amplitude H_0	A/m
$H_1(\omega), H_2(\omega)$	transfer functions of two- RCL -model (Eqs. 4.19, 4.25)	-
$H_{\text{cm}}(\omega)$	transfer function of single- RCL CM model (Eq. 4.30)	-
$H_{\text{cm},i}(\omega)$	transfer function of multi- RCL CM model (Eq. 4.36)	-
h_c	height of ferrite core (Fig. 3.11)	m
I_0	amplitude of current	A
I_{pp}	peak-to-peak value of line current ($=2I_0$)	A
I_{sc}	amplitude of line current during scan (Eq. 2.19)	A
i	complex number ($i^2 = -1$)	-
i_1, i_2	currents through inductances L_1, L_2	A
i_L	current through the line coil (Fig. 2.8)	A
i_{cm}	common-mode current (Eq. 4.10)	A
i_{dm}	differential-mode current (Eq. 4.9)	A
$J_0(x), J_1(x)$	Bessel functions	-
\vec{j}	electric current density; j_z in z -direction	A/m
k	complex wave number (Eq. 3.22)	m ⁻¹

symbol	description	unit
k_L	coupling constant (Eq. 2.10)	-
L, L_1, L_2	inductance	H
$L(n\omega_\ell)$	series inductance of line coil at frequency $n\omega_\ell$ (Eq. 3.80)	H
$L_{\text{wire,lf}}$	apparent lf inductance of straight wire (Eq. 5.4)	H
L_g	distance from deflection point to screen (Fig. 2.1)	m
L_h	inductance of line-coil pair (Fig. 2.7)	H
L_p	inductance that is parallel to a resistance (Fig. 3.12)	H
L_r	replacement of two parallel inductances (Eq. 4.21)	H
L_s	inductance that is in series with a resistance (Fig. 4.22)	H
ℓ, ℓ_w	length of wire (Eq. 5.9)	m
ℓ_c	length of coil (Eq. 5.8)	m
ℓ_e	effective coil length (Fig. 2.1)	m
ℓ_{turn}	average length of a turn (Eq. 5.14)	m
M	mutual inductance (Eq. 2.6)	H
M_D, M_L	constant (Eqs. 5.15,5.16)	-
m	modulation depth (Eq. 4.1)	m^{-1}
m_e	electron rest mass, 9.109510^{-31}	kg
N_L	number of layers in solenoid (Eq. 5.23)	-
N_p	number of parallel wires	-
$N_{p,\text{opt}}$	number of parallel wires for minimum loss (Eq. 3.106)	-
N, N_{turns}	number of turns	-
N_w	the number of turns per layer (Eq. 5.14)	-
n	number of harmonic of line frequency	-
P	dissipation	W
P_{ac}	dissipation in the ac-resistance (Eq. 3.88)	W
P_{dc}	dissipation in the dc-resistance (Eq. 3.87)	W
P_{opt}	minimum dissipation (Eq. 3.107)	W
P_{tot}	total dissipation in line and frame coils	W
$P_{\text{c,eddy}}$	eddy-current loss in ferrite core (Eq. 3.72)	W
P_{coil}	total dissipation of a coil (Fig. 5.29)	W
P_{core}	magnetic dissipation in the ferrite core (Eq. 3.74)	W
P_{dc}	dc dissipation (Eq. 3.11)	W
P_{prox}	proximity loss (Eq.3.40,3.47)	W
P_{skin}	dissipation due to skin effect (Eq. 3.28)	W
p	ratio of flyback time and signal period (Eq. 2.18)	-
p_{magn}	magnetic power loss per unit volume (Eq. 3.73)	W/m^3
Q, Q_r, Q_c	quality factor for ringing ((Eqs. 4.17,4.38,4.41)	-
R, R_1, R_2	resistance	Ω
$R(n\omega_\ell)$	resistance of line coil at frequency $n\omega_\ell$ (Eq. 3.81)	Ω
$R_{\text{ac}}(\omega)$	ac part of resistance (Eqs. 3.85,3.85)	Ω
R_{dc}	dc series resistance (Eq. 3.12)	Ω
R_{lf}	low-frequency approximation of resistance (Eq. 4.13)	Ω
R_p	resistance that is parallel to an inductance (Fig. 3.12)	Ω
R_{prox}	proximity resistance (Eq. 3.48,3.50)	Ω

symbol	description	unit
R_r	replacement of two parallel resistances (Eq. 4.20)	Ω
R_s	resistance (in series with an inductance) (Fig. 4.22)	Ω
r	radius	m
r_c	inner radius of ferrite core (Fig. 3.11)	m
r_e	radius of circular electron trajectory (Eq. 2.2)	m
r_g	inner radius of tube neck (Fig. 3.1)	m
r_o	overall radius of a wire including insulation (Eq. 5.14)	m
T	temperature	$^{\circ}\text{C}$
T	repetition period of line signal	s
t	time	s
t_{fb}	duration of the fly-back (Fig. 2.8)	s
t_i	thickness of the insulation layer of a wire (Eq. 5.14)	m
V	volume	m^3
V_a	anode voltage (Fig. 2.1)	V
V_{coil}	voltage across a coil (Fig. 5.30)	V
$V_{\text{ind}}(t)$	voltage induced by magnetic flux (Eq. 3.69)	V
v_1, v_2	voltages across inductances L_1, L_2	V
v_e	velocity of electrons (Fig. 2.1)	m/s
v_{extra}	modulation of scan velocity (Eq. 4.5)	m/s
v_{scan}	average scan velocity (Eq. 4.3)	m/s
$v(X_g)$	scan velocity along the screen (Eq. 4.2)	m/s
v_L	voltage across inductance L	V
\hat{v}_L	amplitude of voltage across L (Eq. 4.7)	V
w	thickness of a coil	m
X_g	horizontal deflection distance along screen (Fig. 3.2)	m
$Z(\omega)$	impedance as a function of frequency ω	Ω
$Z_1(\omega)$	impedance of a parallel R_1, C_1, L_1 circuit (Eq. 4.18)	Ω
$Z_C(\omega)$	impedance of capacitance C	Ω
$Z_{RCL}(\omega)$	impedance of parallel RCL circuit (Eq. 4.14)	Ω
$Z_{RCL,i}(\omega)$	impedance of parallel $R_i C_i L_i$ circuit (Eq. 4.37)	Ω
z	distance along the axis of a deflection yoke	m

Subject index

- AC resistance, 46
- Anode voltage, 10
- Antimonytonoxide, 152
- ATO, *see* AntimonyTonOxide
- Bessel function, 30, 175
- Bi-directional winding, 144
- CAD, *see* Computer-Aided Design
- Capacitance
 - fly-back, 17
 - parallel, 47
 - S-correction, 17
 - solenoid, 121
- Carbon black, 155, 160
- Cathode-ray tube, 1, 3
- Circuit
 - interaction, 79, 96, 103, 143
 - model, 90
 - for common-mode ringing, 105
 - for differential-mode ringing, 91
 - Single-*RCL* model, 94
 - single-*RCL* CM, 105
 - simulation, 103
- CM, *see* Common-Mode
- CMI, *see* Common-Mode Impedance
- CMM, *see* Common-Mode Magnetic
- CMT, *see* Computer Monitor Tube
- Coil
 - bi-directional winding, 144
 - cross area, 64, 129
 - development, 7
 - history, 7
 - impregnating, 151
 - length, 24
 - literature, 6
 - Mussel, 5
 - Saddle, 5
 - sections, 6
 - series/parallel, 15
 - shape, 5
 - taps, *see* Taps
 - turns, 6
- Common-mode
 - current, 77
 - impedance, 90
 - magnetic frequency response, 84
 - suppression choke, 157
- Computer monitor tube, 3
- Computer-aided design, 20
- Conductive fluid, 152
- Conductivity, 171
- Conquest, 152
- Convergence, 5
- Copper
 - conductivity, 27, 30
 - cross area, 37
 - diameters, 48
 - temperature dependency, 27
 - wire, 6
- Corner deflection angle, 24
- Coulomb gauge, 173
- Coupling constant, 14
- CRT, *see* Cathode-Ray Tube
- Current
 - density, 171
 - distribution, 58
- Damped oscillation, 95
- DC resistance, 27, 91
 - of copper, 27
 - of multi-parallel wires, 37

- Decay time, 72
- Deflection, 3, 7, 10
 - angle, 7, 10, 19, 21
 - coil, *see* Coil
 - distance, 24, 75
 - energy, 23
 - point, 11
 - wire
 - see* Wire, 6
 - yoke, 3
- Dielectric displacement, 41
- Dielectric losses, 40, 155
- Differential-mode
 - current, 77
 - impedance, 89
 - magnetic frequency response, 82
- Displacement density, 171
- Dissipation, 21
 - due to magnetic power loss, 43
 - due to dielectric losses, 40
 - due to frame current, 45
 - due to line current, 45
 - due to proximity effect, 33, 61
 - due to skin effect, 31, 60
 - for non-sinusoidal signals, 44
 - in ferrite core, 42, 43
 - in litz wire, 38
 - in multi-parallel wires, 36
 - in solid wire, 26
 - measuring method, 46
 - of 15" CMT, 49
 - of 17" CMT line-coil pairs, 50
 - reduction, 63
- Distributed damping, 151
- DM, *see* Differential-Mode
- DMI, *see* Differential-Mode Impedance
- DMM, *see* Differential-Mode Magnetic
- DY, *see* Deflection yoke
- Eddy current loss
 - in ferrite core, 42
 - in litz wires, 35, 38
 - in solid wire, 27
- Effective length, 11
- Electric
 - circuit model, *see* Circuit model
 - field, 171
- Electromagnetic compatibility, 157
- Electron
 - beams, 3
 - charge, 10
 - gun, 3, 10, 26
 - mass, 10
 - trajectory, 10, 24
 - velocity, 10
- Electron-optical design, 7
- EMC, *see* ElectroMagnetic Compatibility
- Equivalent parallel resistance, 47
- FEA, *see* Finite-Element Analysis
- Ferrite
 - core, 4, 7
 - eddy currents, 42
 - cylinder, 24
 - magnetic power loss, 43, 44
 - material, 43
- Finite-element analysis, 71
- Fly-back, 17
 - capacitance, 17
 - frequency, 17
 - ratio, 17, 18
 - time, 17
 - voltage, 78
- Fourier
 - expansion, 19, 45, 66
- Frame, 4
 - balance potentiometer, 90
 - coil, 4, 13
 - impedance, 13
 - inductance, 13
 - resistance, 13
 - current, 13
 - drive circuit, 13
 - frequency, 4
- Frequency response, 73
- Frequency-dependent
 - inductance, 45
 - resistance, 45
- Front-of-screen
 - convergence errors, 5

- geometry errors, 5
- ringing measuring, 72
- Geometry errors, 5
- Glass tube, 3
- Horizontal deflection, 10
 - angle, 24
- Hysteresis loss, 43
- Impedance
 - analyzer, 82
 - characteristic, 86
 - of a deflection yoke, 134
 - of line-coil pairs, 133
 - of drive circuit, 96, 103, 143
- Impregnation, 151
- In-line system, 7
- Inductance
 - calculation, 20
 - frame coil, 13
 - line coil, 16
 - mutual, 14
 - of circular loop, 121
 - of square loop, 121
 - parallel, 47
 - solenoid, 120
- Interfacial polarization, 155
- Interstrand
 - proximity effect, 61
 - skin effect, 39, 59
- Interwire
 - proximity effect, 61
 - skin effect, 60
- Kirchhoff, 118
- Landing, 5
- Laplace equation, 173
- Line
 - coil, 4
 - inductance, 16
 - mutual inductance, 14
 - pair, 14
 - series/parallel, 15
 - current, 4, 13, 17
 - fourier expansion, 19
 - drive circuit, 16
 - frequency, 4, **17**
 - period, 17
 - scan, 3, 17
- Literature
 - on CRT deflection coils, 7
 - on dissipation, 22
 - on ringing, 71, 142
- Litz wire, 38, 126
 - stranded, 40, 59, 62
 - twisted, 40, 59, 62
- Loss angle, 41
- Loss phenomena, 26
- Lubrication layer, 6
- Lumped *RCL* model, 47
- Magnetic
 - deflection, *see* Deflection
 - energy, 23, 24
 - field, 4, 6, 10, 11, 171
 - calculation, 7
 - flux density, 171
 - power loss, 43
 - vector potential, 173
- Magnetic frequency response, 81
 - common-mode, 84
 - differential-mode, 82
 - measuring setup, 85
- Mandrel, 6
- Maxwell equations, 118
- Maxwell-Sillars-Wagner polarization, 155
- Measuring method
 - for dissipation, 46
 - for ringing
 - conventional, 72
 - impedance characteristic, 86
 - optical frequency response, 79, 85
- MFR, *see* Magnetic Frequency Response
- Mini Neck, 26
- Modulation depth, 74
- Multi-parallel wire, 126
- Mussel coil, 5
- Mutual inductance, 14
- Narrow Neck, 26

- Ohmic loss, 26
- Optical frequency response, 73
 - measuring setup, 79
- Orthogonality relations, 45
- PA, *see* PolyAmide
- Parallel
 - coils, 15
 - impedance, 15
 - inductance, 15
 - resistance, 91
 - wires, 36, 37, 62
- Parallel wires, 61
- Pedot, 152
- Permeability, 23, 171
- Permittivity, 41, 171
- Phasor notation, 171
- Phosphor dots, 3
- Pick-up coil, 85
- Picture quality, 6
- Pin-shooting, 6, 7
- Plastic frame, 4
- Poisson equation, 173
- Polyamide bond coat, 160
- Polyurethane base coat, 160
- Power dissipation
 - due to proximity effect, 176
- Proximity effect, 28, 33
 - interstrand, 61
 - interwire, 61
 - with skin effect, 35
- Proximity loss, 33, 176
 - for low frequencies, 34
 - function, 34
 - in multi-parallel wires, 37
- Pulse response, 73
- PUR, *see* PolyURethane
- Quality factor
 - of *RCL* circuit, 95
 - of common-mode ringing, 113
 - of differential-mode ringing, 113
- Quasi-static behavior, 9, 20
- Quasi-stationary
 - approximation, 172
- Recursive relation, 18
- Resistance
 - ac, 46
 - dc, 27
 - due to skin effect, 35
 - frame coil, 13
 - frequency-dependent, 45
 - parallel, 47
 - solenoid, 127
- Resonance peak, 73
- RFW
 - see* Ringing-Free Wire, 160
- Ringing, 70
 - amplitude, 72
 - decay time, 72
 - frequency, 72
 - key parameters, 72
 - measuring method, 72
 - of a deflection yoke, 133
 - of line-coil pairs, 132
 - of single line coils, 131
 - physics, 118
 - prediction, 117
 - quality, *see* Quality factor
 - suppression, 141
- Ringing-free wire, 160
- S-correction, 16
- Saddle coil, 5
- Scan
 - frequency, 17
- Sensitivity, 23
- Series inductance, 15
- Shadow mask, 3
- Shunt, 148
- Simulation programs, 7, 11
- Single-*RCL* CM model, 105
- Single-*RCL* model, 94
- Skin
 - depth, 29
 - effect, 28–31
 - with proximity effect, 35
 - inductance, 32
 - loss factor, 31
 - resistance, 31

- for high frequencies, 32
 - for low frequencies, 32
- Solenoid
 - capacitance, 121
 - inductance, 120
 - multi-layer, 123
 - resistance, 127
 - short, 121
 - single-layer, 122
- Steinmetz' law, 43
- Strand, 58
- Stranded litz, 40, 59
- Taps
 - in frame coils, 158
 - in line coils, 80, 149
- Television tube, 3
- Temperature dependency
 - of copper, 27
 - of dissipation, 57
- Transfer function
 - common-mode, 105
 - differential-mode, 99
- Transformers, 71
- TVT, *see* Television tube
- Twisted litz, 40, 59
- Two-*RCL*-sections model, 98
- Wide-screen television, 26
- Winding
 - machine, 6
 - mandrel, 6
 - moulds, 7
 - process, 6
- Wire, 6
 - copper, 6, 27, 30, 37
 - dimensions, 48
 - heat bonding layer, 6
 - insulating layer, 6, 64
 - litz, 38
 - lubrication layer, 6
 - multi-parallel, 36
 - type, 131

Dankwoord

Het schrijven van een proefschrift is een energievervlindende activiteit. Ik heb er erg van genoten, maar ik ben me ervan bewust dat het onmogelijk was geweest zonder de sterke steun van mijn gezin, mijn collega's en de leiding van Philips Display Components.

Allereerst wil ik Renate, Tom en Jacqueline bedanken voor hun begrip voor de invloed die het schrijven op ons gezinsleven had. Naast hen, wil ik ook mijn ouders en mijn oma "Grootje" bedanken voor hun stimulans vanaf mijn prille jeugd om natuurkunde en elektronica te verkennen. Ik denk nog altijd met veel plezier aan de proefjes die ik toen kon doen en de hulp die ze mij daarbij gaven.

Ik ben Meijndert van Alphen dankbaar voor het aannemen van mij in zijn toenmalige groep in Display Components om aan die onderwerpen te werken die uiteindelijk tot dit proefschrift hebben geleid. Mijn voormalige collega's Mark Vrinten en Ewoud Vreugdenhil wil ik bedanken voor hun stimulans om daadwerkelijk te starten met het schrijven van dit proefschrift. Het management van Philips Display Components Eindhoven, en in het bijzonder Cees Admiraal en Bas Zeper dank ik voor de toestemming en de steun die ik heb gekregen.

De collega's van de modelshop ben ik zeer erkentelijk voor het wikkelen van de spoelen, het samenstellen van de deflektie units en hun hulp bij het uitvoeren van mijn experimenten.

Verder wil ik de mensen bedanken die het manuscript grondig hebben doorgelezen en mij met hun positieve kritiek geholpen hebben de leesbaarheid van dit proefschrift aanzienlijk te verbeteren. In het bijzonder wil ik daarbij bedanken: Ferrie Aalders, Meijndert van Alphen, Martijn Dekker, Frank van Horck, Karel Kuijk, Daniëlle Palmen en Tjerk Spanjer. Veel dank ook aan prof.dr.ir. A.J.A. Vandenput, prof.dr.ir. J.H. Blom en prof.dr. A.G. Tjhuis voor hun konstruktieve kritische opmerkingen en plezierige discussies.

Tenslotte, maar niet in het minst, wil ik mijn leermeester professor Piet van der Laan heel hartelijk bedanken voor de vele intensieve, vaak langdurige,

maar altijd plezierige discussies gedurende de afgelopen twee jaar. Ik heb er veel van geleerd en ik heb er veel van genoten. Bedankt!

Curriculum vitae

Dick Harberts is geboren op 26 december 1960 te 's-Gravenhage. Van 1973 tot 1979 volgde hij het VWO op scholengemeenschap Simon Stevin in zijn geboortestad. In 1979 begon hij de studie Technische Natuurkunde aan de Technische Universiteit Delft, waar hij in mei 1984 het diploma van Natuurkundig Ingenieur behaalde.

Van mei 1984 tot november 1985 vervulde hij zijn militaire dienst als marineofficier gedetacheerd bij het Fysisch en Elektronisch Laboratorium in Den Haag met theoretisch en experimenteel onderzoek aan de voortplanting van geluid in de oceaan.

In 1985 startte hij bij het Natuurkundig Laboratorium van Philips in Eindhoven in de groep "CAD for VLSI", waarin hij onder andere werkte aan software voor het lokaliseren van verschillen in elektrische netwerken ("netlist comparison") en het ontwerpen en bedraden van geïntegreerde schakelingen ("sea-of-gates").

In 1990 stapte hij over naar de groep "TV systems" in hetzelfde laboratorium en werkte daar vervolgens aan systeemaspekten en elektronische aansturing van veldemissie displays.

Vanaf 1994 werkt hij bij Philips Display Components, ook in Eindhoven, in de ontwikkelafdeling van afbuigspoelen. Zijn onderzoek aan het dynamisch gedrag van afbuigspoelen heeft geleid tot dit proefschrift.

